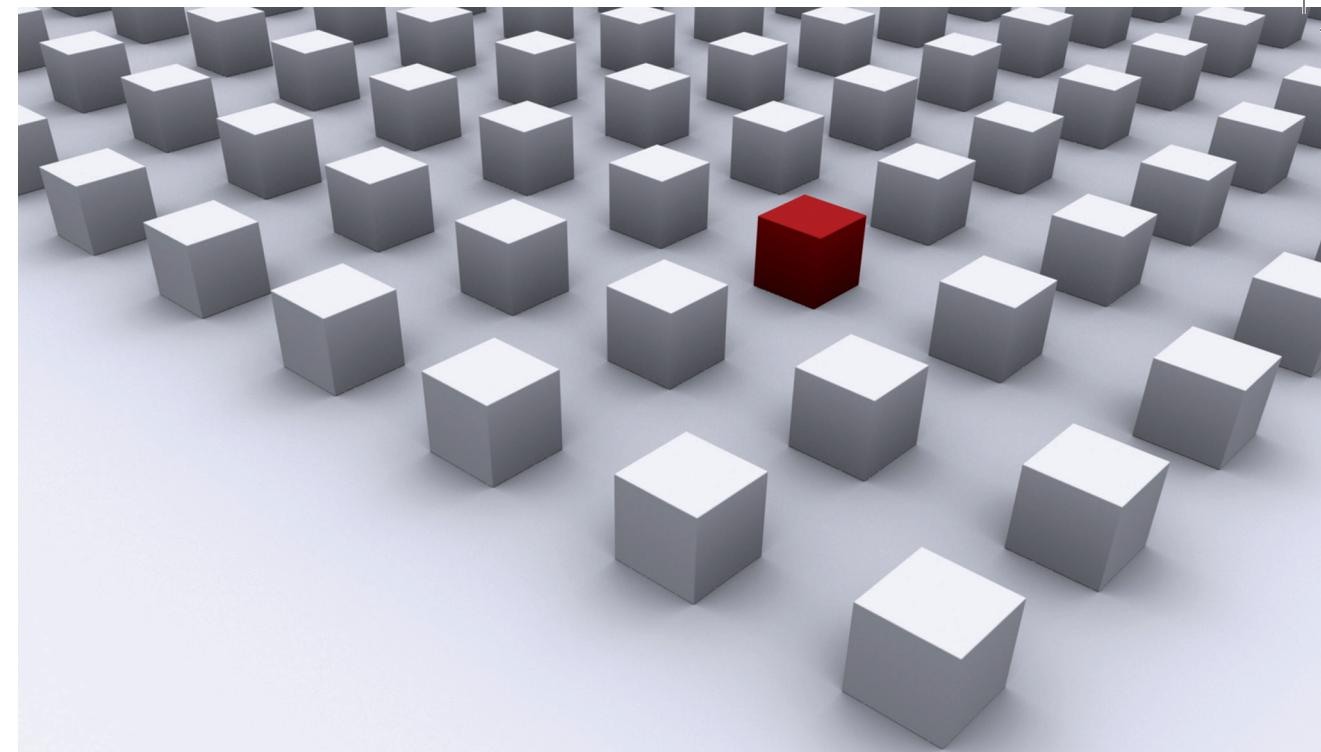


„The recent experimental advances in manipulating ultra-cold atoms make it feasible to study coherent transport of Bose-Einstein condensates (BEC) through various mesoscopic structures. In this work the quasi-stationary propagation of BEC matter waves through two dimensional cavities is investigated using numerical simulations within the mean-field approach of the Gross-Pitaevskii equation.

The focus is on the interplay between interference effects and the interaction term in the non-linear wave equation. One sees that the transport properties show a complicated behaviour with multi-stability, hysteresis and dynamical instabilities for non-vanishing interaction. Furthermore, the prominent weak localization effect, which is a robust interference effect emerging after taking a configuration average, is reduced and partially inverted for non-vanishing interaction.“

Dissertationsreihe Physik - Band 44



Timo Hartmann

Transport of Bose-Einstein
condensates through two
dimensional cavities

Universitätsverlag Regensburg

Universitätsverlag Regensburg



Universität Regensburg

Timo Hartmann

44
Dissertationsreihe
Physik



Timo Hartmann



Transport of Bose-Einstein
condensates through two
dimensional cavities

Transport of Bose-Einstein condensates through two dimensional cavities

Dissertation zur Erlangung des Doktorgrades der Naturwissenschaften (Dr. rer. nat.)
der Fakultät für Physik der Universität Regensburg
vorgelegt von

Timo Hartmann

aus Eschwege

im Juni 2014

Die Arbeit wurde von Prof. Dr. Klaus Richter angeleitet.

Das Promotionsgesuch wurde am 16.01.2012 eingereicht.

Das Promotionskolloquium fand am 05.11.2014 statt.

Prüfungsausschuss: Vorsitzender: Prof. Dr. Christian Schüller
1. Gutachter: Prof. Dr. Klaus Richter
2. Gutachter: Prof. Dr. Thomas Niehaus
weiterer Prüfer: Prof. Dr. Andreas Schäfer



Dissertationsreihe der Fakultät für Physik der Universität Regensburg, Band 44

Herausgegeben vom Präsidium des Alumnivereins der Physikalischen Fakultät:
Klaus Richter, Andreas Schäfer, Werner Wegscheider, Dieter Weiss

Timo Hartmann

**Transport of Bose-Einstein
condensates through two
dimensional cavities**

Universitätsverlag Regensburg

Bibliografische Informationen der Deutschen Bibliothek.
Die Deutsche Bibliothek verzeichnet diese Publikation
in der Deutschen Nationalbibliografie. Detaillierte bibliografische Daten
sind im Internet über <http://dnb.ddb.de> abrufbar.

1. Auflage 2015

© 2015 Universitätsverlag, Regensburg

Leibnizstraße 13, 93055 Regensburg

Konzeption: Thomas Geiger

Umschlaggestaltung: Franz Stadler, Designcooperative Nittenau eG

Layout: Timo Hartmann

Druck: Docupoint, Magdeburg

ISBN: 978-3-86845-119-1

Alle Rechte vorbehalten. Ohne ausdrückliche Genehmigung des Verlags ist es
nicht gestattet, dieses Buch oder Teile daraus auf fototechnischem oder
elektronischem Weg zu vervielfältigen.

Weitere Informationen zum Verlagsprogramm erhalten Sie unter:
www.univerlag-regensburg.de

Contents

1	Introduction	1
2	The Bose-Einstein condensate	7
2.1	The mean-field equation for condensates	7
2.1.1	Energy minimization using the Hartree ansatz	7
2.1.2	The second quantization	9
2.1.3	Particle-particle interaction	11
2.2	External potentials for Bose-Einstein condensates	12
2.2.1	Optical potentials	12
2.2.2	External potentials induced by magnetic fields	13
2.2.3	Restriction to two dimensions	14
2.3	Gauge potentials for Bose-Einstein condensates	15
2.4	Summary	17
3	Stationary scattering states of the Schrödinger equation	19
3.1	Introduction	19
3.2	The retarded Green function	20
3.3	The tight binding model	21
3.4	The tight binding model for a constant potential	22
3.4.1	Eigenfunctions for a constant potential	22
3.4.2	A source on an infinite lattice	23
3.4.3	Calculation of the current	25
3.4.4	A source in an semi-infinite strip	26
3.5	The Green function in the tight binding model	28
3.5.1	Handling of the left lead	29
3.5.2	Calculation of the self energy	30
3.5.3	Handling of the right lead	32
3.6	Generalization to two dimensions	33
3.6.1	The two dimensional leads	34
3.6.2	Current measurement in two dimensions	36
3.6.3	Magnetic gauge field	36
3.6.4	Selection of the gauge field	37
3.7	Exterior complex scaling boundary conditions	38
3.7.1	Accuracy of the exterior complex scaling boundary conditions	42
3.7.2	Resonances	43
3.8	Scattering systems of “billiard” type	47

3.8.1	\mathcal{B}_1 : An almost-closed example system	48
3.9	Computational complexity	50
3.10	Summary, outlook and open ends	52
4	Simulation of the time dependent Gross-Pitaevskii equation	53
4.1	Introduction	53
4.2	Crank-Nicholson	54
4.3	Incorporating the interaction term	56
4.4	The Taylor series method	57
4.5	The Split operator method	59
4.6	Accuracy of the exterior complex scaling boundary conditions	61
4.7	Non-adiabatic switching of the source	62
5	Stationary scattering states of the Gross-Pitaevskii equation	67
5.1	Introduction	67
5.1.1	Scaling behavior of the Gross-Pitaevskii equation	68
5.1.2	The position dependent interaction strength	69
5.2	Numerical solution of the non-linear system of equations	71
5.2.1	Calculation of the derivative	72
5.2.2	Selection of the start vector	73
5.3	The curve tracking algorithm	76
5.3.1	Calculation of the tangent vector	77
5.3.2	Critical points	78
5.3.3	Adaptive stepsize control	81
5.3.4	Artificial homotopy	82
5.4	Time dependent simulations	83
5.4.1	Time dependent population of the scattering system	83
5.4.2	Time dependent variation of μ	85
5.4.3	Time dependent variation of g and j_{in}	86
5.5	Curve tracking for various parameters	88
5.6	Perturbation theory	92
5.6.1	Perturbation theory for the wave function	92
5.6.2	Perturbation theory for the energy	94
5.7	Dynamical stability	100
5.8	Other geometries	105
5.8.1	\mathcal{B}_2 : A nearly closed system without horizontal mirror symmetry	105
5.8.2	\mathcal{B}_3 : A nearly closed system without any symmetry	108
5.8.3	\mathcal{B}_4 : Another nearly closed full symmetric system	108
5.8.4	\mathcal{B}_5 : A wide open system with classical chaotic dynamics	113
5.9	One dimensional systems with non-trivial topology	118
5.9.1	\mathcal{B}_6 : A ring with vanishing potential	119
5.9.2	\mathcal{B}_7 : A ring with a weak disorder potential	122
5.9.3	\mathcal{B}_8 : A ring with a strong disorder potential	122
5.10	Summary	122

6	Scattering states in chaotic billiards	125
6.1	Weak localization	126
6.1.1	Weak localization in the linear regime	126
6.1.2	Weak localization in the non-linear regime	132
6.1.3	Analysis of the classical dynamics	136
6.1.4	Comparison with numerical results	141
6.1.5	Direct evaluation of the semiclassical sum	147
6.2	Intensity distribution	150
6.2.1	Theoretical analysis	150
6.2.2	Comparison with numerical results	154
6.3	Other geometries	157
6.3.1	\mathcal{B}_9 : The clipped triangle	157
6.3.2	\mathcal{B}_{10} : The stomach billiard	157
6.3.3	\mathcal{B}_{11} : The half circle (narrow leads)	158
6.3.4	\mathcal{B}_{12} : The half circle (wide leads)	158
6.3.5	\mathcal{B}_{13} : The limaçon (narrow leads)	158
6.3.6	\mathcal{B}_{14} : The limaçon (wide leads)	158
6.4	Related effects in mesoscopic systems	172
6.4.1	Coherent backscattering in disordered potentials	172
6.4.2	Time-reversal mirrors in chaotic cavities	173
6.4.3	Half-period Aharonov-Bohm oscillations in disordered rings	174
6.5	Summary and outlook	175
	Appendix	177
A	The Newton method	177
B	The Onsager relations	180
B.1	Symmetries of the scattering matrix	180
B.2	The Onsager relations	183
B.3	The breakdown of the Onsager relations in the interacting case	184
B.4	The generalized continuity equation	185
C	Transparent boundary conditions	187
D	Block Gauß matrix inversion	191
E	The Dyson equation	192
F	Derivation of the Peierls phase	194
G	The stability amplitude in Birkhoff coordinates	197
H	A smooth switching function	199
	References	204

List of publications

- T. Hartmann, F. Keck, H. J. Korsch and S. Mossmann. *Dynamics of Bloch oscillations*. New Journal of Physics **6**, p. 2 (2004).
- H. J. Korsch, H.-J. Jodl and T. Hartmann. *Chaos-A Programm Collection for the PC*. (Springer, 2008), third edition.
- T. Hartmann, J. Michl, C. Petitjean, T. Wellens, J.-D. Urbina, K. Richter and P. Schlagheck. *Weak localization with nonlinear bosonic matter waves*. Annals of Physics **327**, p. 1998-2049 (2012)
- T. Hartmann, J.-D. Urbina, K. Richter and P. Schlagheck. *Intensity distribution of non-linear scattering states*. AIP Conference Proceedings, Volume 1468 - “Let’s Face Chaos through Nonlinear Dynamics” 8th International Summer School/Conference , p. 193 (2012), arXiv:1205.3067

Chapter 1

Introduction

The microscopic world at the level of individual atoms behaves fundamentally different than the macroscopic world which dominates the physics we encounter in everyday life. The first is wholly described by quantum mechanics discovered in the 20th century while the latter is wholly described by classical mechanics which was already fully developed in the 19th century. In the classical world we use the Lagrange/Hamilton point particle mechanics while in the quantum world particles are described by the Schrödinger equation. The latter is essentially a classical wave equation. Albeit wave equations are ubiquitous in classical physics, the whole interpretation and conceptual foundation of the Schrödinger equation sets it apart.

While the Schrödinger wave equation has parallels in classical physics we come now to something which is unknown to the classical world. A fundamental dictum of quantum mechanics is that several particles of the same kind should be indistinguishable. The consequence of that dictum is that the description of a system consisting of many quantum particles differs drastically depending on whether one investigates several particles of the same kind or particles of several different kinds. This behavior has no counterpart in classical mechanics and underlies many interesting physical phenomena.

Another intrinsic feature of quantum particles is their spin which also lacks a classical counterpart¹. The famous spin-statistic theorem [73, 162, 166] due to Fierz and Pauli relates the behavior of several indistinguishable particles to their spin. The many-particle wavefunction of several indistinguishable particles with half-integer spin (called fermions) changes the sign after an interchange of two particles. In contrast to that the wavefunction of particles with integer spin (called bosons) remains unchanged after any permutation of particles.

Quantum effects are very susceptible to perturbations from outside which induce decoherence destroying any quantum feature. This usually means well isolated (from the environment) systems at low temperatures² are required to observe these effects. Furthermore, at low enough temperatures one can safely assume that the observed system is near its ground state. For a system of identical bosonic particles this ground state is particularly interesting. It is called a Bose-Einstein condensate (BEC). In contrast to fermionic systems (keyword Fermi surface), the particles in

¹ The closest analogy is an intrinsic angular momentum. But the spin has several features which an intrinsic angular momentum cannot take account of.

² Low in comparison to typical excitation energies of the system.

the ground state of a many-particle bosonic system approximatively occupy all the same single particle state. For interacting particles, this results in a non-linear potential term in the effective mean field equation of motion. The influence of this non-linearity on the transport properties of a condensate will form the main topic of this thesis.

First predicted by Bose and Einstein in 1924 [25, 60, 61], it took many years to successfully create a Bose-Einstein condensate with atoms in an experiment³. The main difficulties which had to be overcome were due to the very low temperatures in the region of $10^{-8}K \dots 10^{-6}K$ which are necessary to create a condensate. New techniques as trapping potentials for neutral atoms, laser cooling and evaporative cooling had to be developed. After the first success in 1995 [7, 31, 51], many other experiments with various elements have been conducted. Bose-Einstein condensates are one of the few quantum objects which can reach macroscopic dimensions and are (in principle) visible with the naked eye. In microgravity, a condensate can reach dimensions of up to several millimeters [204]. This makes them particularly interesting.

Due to the very low temperatures, the velocity of individual atoms in the condensate is quite low. Therefore the de Broglie wavelength of the atoms is very large. Additionally, measurements give very good information about the quantum state because many coherent atoms are detected simultaneously. This makes Bose-Einstein condensates an ideal system to study matter waves. Furthermore, Bose-Einstein condensates in dilute atom gases offer a high degree of control over most experimental parameters such as external potential, particle-particle interaction and gauge potential. Therefore, condensates allow one to study many quantum effects which were originally predicted for solid state systems but are difficult to observe there due to the lack of experimental control. Examples for such effects are Bloch oscillations⁴ [22, 68, 95], Mott insulator transition [86, 115], Anderson localization [8, 20, 111, 115, 122, 178], weak localization in diffusive systems [112] and many more. Furthermore the exceptionally good experimental control allows one to use Bose-Einstein condensates (and ultra-cold atoms in general) as model system to simulate and investigate a variety of other quantum phenomena which may be inaccessible in their native environment.

The above mentioned characteristics of Bose-Einstein condensates in dilute cold atoms make interferometry experiments with them highly sensitive to measurements of inertial forces and accelerations. This opens the road to many interesting future technical applications such as high accuracy measurements of the gravitational field for prospecting, inertial navigational systems for submerged submarines or planes (as backup for satellite navigation systems such as GPS) [55, 56]⁵ various experimental tests of general relativity⁶ and many more.

Anderson localization, also called strong localization, is the effect that transport (and diffusion) in an arbitrarily weak⁷ disorder potential is totally suppressed by destructive interference

³ Some other effects like superfluid helium [137] or superconductivity can be considered to be due to a BEC. But these effects are somewhat “dirty” as only a tiny fraction of atoms are in the ground state [167] or quasi-particles are used. In this context fit also exciton BECs [117, 188]. There exists also a BEC made of photons [119] where the particle number is not conserved. We only consider here “real” BECs in dilute atom gases where a high fraction of particles occupy the ground state.

⁴ The observation of Bloch oscillations in solid state systems without any “tricks” such as semiconductor superlattices has been realized only recently as very sophisticated experimental tools are necessary [185].

⁵ Not all experiments to detect inertial forces use Bose-Einstein condensates. Many experiments use just cold uncondensed atoms [37, 41, 57, 80, 90].

⁶ Such as measurement of the Lense-Thirring (also called frame-dragging) effect in earthbound table-top experiments, precision tests of the weak equivalence principle, detection of gravitational waves and many more [155, 204].

⁷The disorder strength does not matter in one and two dimensions. Of course the length scale on which the

effects. In contrast to this, the weak localization effect only causes a relatively small correction to the transport properties. It can be thought as the precursor of Anderson localization. All these localization effects are import objects of study because they are robust interference effects which are visible even after an ensemble average. They are not exclusive to quantum matter waves, but happen also for classical waves in optics and acoustics [4, 5, 115, 200]. But it is important to check if localization also happens for quantum matter waves.

Conducting systems with a random disorder potential are called diffusive. In diffusive systems, a prominent weak localization effect is coherent backscattering [3, 190]. It is the enhancement of reflection in the incident direction in comparison to other directions when a wave hits a disorder potential. In ballistic systems the disorder potential is replaced by confining the wave to a cavity with flat potential and hard wall boundaries. The shape of the cavity is chosen such that the classical motion inside the cavity is chaotic. The chaotic multiple reflection at the boundaries in ballistic system takes the role of the disorder potential in diffusive systems. In these ballistic systems, the weak localization effect is the gauge (magnetic) field dependent enhancement of reflection of matter waves for the time reversal symmetric case in comparison to broken time reversal symmetry.

In all experimental verifications of Anderson localization [20, 111, 178] and weak localization in diffusive systems [112] using BEC matter waves, the effect of particle-particle interaction is completely neglected^{8 9}. Obviously it is of interest how well this approximation is justified. While the localization effects depend on the linear superposition of interfering waves, the particle-particle interaction introduces a non-linearity. The crucial question is now how the non-linearity affects the interference phenomena of localization. Previous studies [98, 99] have investigated this topic for weak localization in diffusive systems or for strong localization in one-dimensional systems [159–161]. This thesis now studies the influence of the non-linearity on weak localization in two dimensional ballistic billiard systems numerically. To this end, a novel computational method to calculate stationary scattering states for non-linear wave equations will be used. The numerical results are compared to a prediction based on a semiclassical perturbation theory. The final result is that the characteristic weak localization peak shape (the reflection as function of gauge field) already known for vanishing interaction is transformed into a characteristic double peak structure for non-vanishing interaction strength [96]. Similar results are obtained for the intensity distribution of the wave function.

Experiments with Bose-Einstein condensates tend to be very complicated and take a long time to properly set them up. Both facts makes them quite expensive. Therefore a theoretical study of the possible experimental outcomes it advisable. The systems studied here are *mesoscopic*¹⁰ two dimensional systems. Therefore all analytic techniques¹¹ known in one dimension to study BECs are not applicable. Neither are analytic techniques applicable which make simplifications based on the system size. The only working analytical technique is the semiclassical analysis as developed in [96]. This method is an intermediate between quantum and classical physics. The

localization happens depends on the disorder strength. In three dimensions the disorder strength has to reach a certain threshold to cause localization; this is the so-called Anderson transition.

⁸Either by diluting the atomic gas or by using Feshbach resonances (Sec. 2.1.3) to make the interaction strength negligible.

⁹Also in other technical applications (such as inertial force measurements) the non-linear interaction is often regarded as an unwanted effect which disturbs and obstructs the desired results.

¹⁰Neither very small nor very large

¹¹ These are mostly based on the solution of an ordinary second order differential equation.

quantum wave propagation is studied as perturbation (in \hbar) around the classical point particle dynamics while keeping the important interference effects but discarding most others. But the semiclassical analysis makes use of many universal assumptions whose validity in actual systems varies to some degree. Also many approximation are made whose error term is only qualitatively known. Therefore the semiclassical analysis has to be checked with numerical simulations¹². This thesis fulfills the role of checking the semiclassical prediction for the weak localization effect and shows possible outcomes of future experiments.

Successful experiments with degenerate quantum gases have studied the Anderson localization in one [20, 178] and three dimensions [111, 122]¹³, the Bloch oscillation [68], the Mott insulator transition [86], and many other basic quantum effects. Also weak localization in diffusive systems (manifest as coherent backscattering in momentum space) has been observed for a quasi two dimensional Bose-Einstein condensate in a disordered potential [112]. But no experiment has studied the effect of interaction on localization thus far. But the steady progress in experimental sophistication leads to hope that experiments to study the effect of atom-atom interaction on localization (of course from perspective of this work especially on weak localization in ballistic systems) will be possible in the near future. Examples of the necessary experimental repertoire are a guided atom laser [45, 88] (a source for “monochromatic” atoms with a well defined incoming velocity), almost arbitrarily shaped potentials for cold atoms [28, 78, 101, 105, 116, 148] and artificial gauge fields [49, 136]. The building blocks for successful experimental tests of the results of this thesis do exist; all it remains is to put them together.

Outline

The first three chapters (Chap. 2-4) provide the (more or less) well known technical foundations to simulate Bose-Einstein condensates on the basis of the mean-field description. These chapters can be skipped by readers not interested in known technical details. In the last two chapters (Chap. 5-6) a novel way to calculate stationary scattering of the Gross-Pitaevskii equation is used to investigate how the weak localization effect in ballistic billiard systems is modified by the non-linear particle-particle interaction. Readers interested in technical details should focus on Chap. 5 while Chap. 6 contains the “real physics”.

Chap. 2 provides a short overview of the mean field description of Bose-Einstein condensates and discusses how to generate artificial external and gauge potentials for neutral atoms. The final result of this chapter is the two-dimensional Gross-Pitaevskii equation (2.17) which is used in the rest of this work.

Chap. 3 is a technical introduction to the tight binding model for the linear Schrödinger equation. This model allows one to calculate stationary scattering states of a two dimensional cavity with several infinite leads attached. This is done by solving linear systems of equations and forms the foundation to investigate scattering states of the non-linear Gross-Pitaevskii equation in Chap. 5. In the tight binding model leads are incorporated using self energies. Alternative boundary conditions in the form of exterior complex scaling are also developed. These are useful to handle the leads in time dependent simulations and for the dynamical stability analysis.

Chap. 4 is a technical discussion of several methods to simulate the time propagation of the Gross-Pitaevskii equation. Each method has its advantages and disadvantages.

¹² Actually, the numerical data was available before the semiclassical analysis was completed. This data was used to determine several terms appearing in the semiclassical results.

¹³ [122] uses an ultracold Fermi gas instead of a BEC.

Chap. 5 introduces a novel way to calculate stationary scattering states of the two dimensional Gross-Pitaevskii equation. The non-linearity of this equation makes this a non-trivial and hard task but also provides interesting effects (like multi-stability, hysteresis and instabilities) not existing in linear systems. Technically the scattering states are calculated by solving a non-linear system of equations. The dynamical stability of such found stationary states is investigated using the Bogoliubov-de Gennes equation. The time-independent ansatz is compared with time-dependent simulations and a perturbative ansatz.

Chap. 6 focuses on universal transport behavior in the form of the weak localization effect which does not depend on the details of the investigated system as long as it belongs to a specific universality class. The methods discussed in the previous chapters are used to analyze how the weak localization effect in ballistic systems is modified by the particle-particle interaction. The numerical results are compared to a semiclassical theory. Furthermore the intensity distribution of the wave function is studied in a similar way. Related effects in other systems are also briefly discussed.

The appendix supplements the previous chapters with various technical details. App. A gives a short introduction into the Newton method to solve non-linear equations. App. B derives the Onsager relations which seem to be common knowledge but whose derivation is hardly found in the literature. App. C describes the “perfect” transparent boundary conditions for time simulations. App. D and App. E emphasize the technical details for the self energy calculation in the tight-binding model. App. F provides a more systematic approach to the Peierls phase which is usually introduced in some ad hoc manner. App. G calculates the semiclassical stability amplitude for ballistic two dimensional billiard systems. App. H analyzes a switching function.

Chapter 2

The Bose-Einstein condensate

This chapter provides a short overview of the mathematical description of Bose-Einstein condensates and of the possibilities to manipulate these condensates experimentally. The theory presented here is based on the assumption that we want to describe bosonic atoms in dilute gases. For experimental investigations of Bose-Einstein condensates, the alkali metals are of particular interest because of the multitude of strong spectral lines they provide which allow for manipulation (cooling and trapping) of these atoms by lasers. But other elements are possible to use, too. Successful Bose-Einstein condensation has been demonstrated using the atoms ^1H , ^7Li , ^{23}Na , ^{39}K , ^{41}K , ^{52}Cr , ^{85}Rb , ^{87}Rb , ^{133}Cs , ^{170}Yb , ^{174}Yb , $^4\text{He}^*$, ^{168}Er and a few others.

2.1 The mean-field equation for condensates

In this section we derive the mean-field description of Bose-Einstein condensates at zero temperature. The resulting equation of motion is called the Gross-Pitaevskii equation. There are many methods leading to this result and two of them are described here. The material covered here can be found in many standard references [48, 129, 167, 169].

2.1.1 Energy minimization using the Hartree ansatz

In conventional quantum mechanics a system of N identical bosonic particles is described by a wave function $\Psi(\mathbf{r}_1, \dots, \mathbf{r}_N)$ which is symmetric under any permutation of particles. The corresponding Hamilton operator can be written as [167]:

$$H = \sum_{j=1}^N \left[-\frac{\hbar^2}{2m} \Delta_j + V(\mathbf{r}_j) \right] + \sum_{1 \leq j < k \leq N} U(\mathbf{r}_j - \mathbf{r}_k) . \quad (2.1)$$

It acts on the space of all square integrable functions $\mathbb{R}^{3N} \rightarrow \mathbb{C}$ which are invariant under permutations of arbitrary coordinates.

Here $V(\mathbf{r})$ is an external potential which for example can be produced by the methods of Sec. 2.2. $U(\mathbf{r}_j - \mathbf{r}_k)$ is the two-body interaction potential which will be explained in more detail in Sec. 2.1.3. We are working in a dilute gas regime where the probability that three or more

particles collide is negligible; therefore three and more body interactions are neglected. They are unwanted anyway because they lead to the loss of particles from the condensate [167, 206].

The ground state of H can be found by minimizing the total energy

$$E[\Psi] = \int \Psi(\mathbf{r}_1, \mathbf{r}_2, \dots, \mathbf{r}_N)^* H \Psi(\mathbf{r}_1, \mathbf{r}_2, \dots, \mathbf{r}_N) \prod_{j=1}^N d\mathbf{r}_j$$

under the normalization constraint $\int |\Psi(\mathbf{r}_1, \mathbf{r}_2, \dots, \mathbf{r}_N)|^2 \prod_{j=1}^N d\mathbf{r}_j = 1$.

The Hilbert space of total symmetric functions in N variables is extremely large. Therefore we must restrict ourselves to a small portion of it. Particularly we construct the many body wave function as a simple product state of identical single particle states. This is called a Hartree ansatz:

$$\Psi(\mathbf{r}_1, \mathbf{r}_2, \dots, \mathbf{r}_N) = \prod_{j=1}^N \phi(\mathbf{r}_j). \quad (2.2)$$

Here $\phi(\mathbf{r}) \in \mathcal{L}(\mathbb{R}^3)$ is a normalized single particle wave function ($\int |\phi(\mathbf{r})|^2 d\mathbf{r} = 1$).

Inserting the Hartree ansatz into the energy functional gives

$$\begin{aligned} E[\phi] &= \int \Psi(\mathbf{r}_1, \mathbf{r}_2, \dots, \mathbf{r}_N)^* H \Psi(\mathbf{r}_1, \mathbf{r}_2, \dots, \mathbf{r}_N) \prod_{j=1}^N d\mathbf{r}_j \\ &= N \int \left[\frac{\hbar^2}{2m} |\nabla \phi(\mathbf{r})|^2 + V(\mathbf{r}) |\phi(\mathbf{r})|^2 \right] \\ &\quad + \frac{N(N-1)}{2} \int U(\mathbf{r} - \mathbf{r}') |\phi(\mathbf{r})|^2 |\phi(\mathbf{r}')|^2 d\mathbf{r} d\mathbf{r}'. \end{aligned}$$

It is more convenient to choose another normalization. The replacement $\psi(\mathbf{r}) = \sqrt{N} \phi(\mathbf{r})$ allows us to move the particle number N out of the energy functional into the normalization condition $\int |\psi(\mathbf{r})|^2 d\mathbf{r} = N$ by using $\frac{N-1}{N} \approx 1$ valid for large N .

$$E[\psi] = \int \left[\frac{\hbar^2}{2m} |\nabla \psi(\mathbf{r})|^2 + V(\mathbf{r}) |\psi(\mathbf{r})|^2 \right] + \frac{1}{2} \int U(\mathbf{r} - \mathbf{r}') |\psi(\mathbf{r})|^2 |\psi(\mathbf{r}')|^2 d\mathbf{r} d\mathbf{r}'. \quad (2.3)$$

The approximate ground state of the many particle Hamiltonian Eq. (2.2) can now be found using a variational principle. We demand that $\psi(\mathbf{r})$ minimizes the energy functional Eq. (2.3) under the normalization constraint that the particle number is fixed. Using a Lagrange multiplier μ to handle the constraint we arrive at

$$\delta E - \mu \delta N = 0 \quad (2.4)$$

This equation for the variation has to be fulfilled with respect to the independent variation of $\psi(\mathbf{r})$ and its complex conjugate $\psi^*(\mathbf{r})$. Finally the Euler-Lagrange equation for Eq. (2.4) gives us the (generalized) Gross-Pitaevskii equation [159, 167]

$$\mu \psi(\mathbf{r}) = \left[-\frac{\hbar^2}{2m} \Delta + V(\mathbf{r}) + \int U(\mathbf{r} - \mathbf{r}') |\psi(\mathbf{r}')|^2 d\mathbf{r}' \right] \psi(\mathbf{r}) \quad (2.5)$$

which is a mean-field equation describing approximatively the many particle physics. In this context μ is called the chemical potential. It describes the energy necessary to add one more particle to the system. $\psi(\mathbf{r})$ is called the condensate wave function.

The (approximative) time evolution of the many particle system Eq. (2.1) can also be derived using a variational approach [48, 169]:

$$\delta \left[-i\hbar \int \psi^*(\mathbf{r}, t) \frac{\partial}{\partial t} \psi(\mathbf{r}, t) d\mathbf{r} dt + \int E[\psi] dt \right] = 0 . \quad (2.6)$$

In this ansatz we have introduced a time dependence into ψ . The Euler-Lagrange equations for Eq. (2.6) gives us the time dependent (generalized) Gross-Pitaevskii equation:

$$i\hbar \frac{\partial \psi(\mathbf{r}, t)}{\partial t} = \left[-\frac{\hbar^2}{2m} \Delta + V(\mathbf{r}) + \int U(\mathbf{r} - \mathbf{r}') |\psi(\mathbf{r}', t)|^2 \right] \psi(\mathbf{r}, t) . \quad (2.7)$$

The mathematical rigorous results

In order to find the true ground state of the Hamiltonian Eq. (2.1) the minimization has to be done with respect to the whole set of symmetrical many particle wave functions which is much larger than the set of simple product states of the form Eq. (2.2). There exists rigorous mathematical proofs [132–134] that for a δ -interaction $U(\mathbf{r}) = a\delta(\mathbf{r})$ (see Sec. 2.1.3) in the limit $N \rightarrow \infty$ and $a_0 = Na = \text{fixed}$, the ground state many-particle wave function and the ground state energy converge in some well defined sense to the solution of the stationary Gross-Pitaevskii equation in the form of Eq. (2.5). The time dependent variant Eq. (2.7) can also be recovered [64, 168].

2.1.2 The second quantization

While in Sec. 2.1.1 we used conventional quantum mechanics to derive a mean-field approximation of the many particle dynamics there is another approach which uses the framework of second quantization [154, 156, 186]. This framework provides a better connection to quantum statistical mechanics which allows some insight into the process of condensation. Furthermore one can go beyond the mean-field approximation.

The Hamilton operator in second quantization can be written as:

$$\begin{aligned} \hat{H} = & \int d\mathbf{r} \hat{\Psi}^\dagger(\mathbf{r}) \left(-\frac{\hbar^2}{2m} \Delta + V(\mathbf{r}) \right) \hat{\Psi}(\mathbf{r}) \\ & + \frac{1}{2} \int d\mathbf{r} d\mathbf{r}' \hat{\Psi}^\dagger(\mathbf{r}) \hat{\Psi}^\dagger(\mathbf{r}') U(\mathbf{r} - \mathbf{r}') \hat{\Psi}(\mathbf{r}') \hat{\Psi}(\mathbf{r}) . \end{aligned} \quad (2.8)$$

This is a generalization of Eq. (2.1). Here the $\hat{\Psi}^\dagger(\mathbf{r})$ and $\hat{\Psi}(\mathbf{r})$ are the bosonic creation and annihilation operators in the position basis which in this representation are traditionally called field operators. Their physical interpretation is that $\hat{\Psi}^\dagger(\mathbf{r})$ creates a particle at position \mathbf{r} and that $\hat{\Psi}(\mathbf{r})$ annihilates a particle at the same position.

Working in the Heisenberg picture we get the following equation of motion for the field operator:

$$\begin{aligned} i\hbar \frac{\partial}{\partial t} \hat{\Psi}(\mathbf{r}, t) &= [\hat{\Psi}, \hat{H}] \\ &= \left[-\frac{\hbar^2}{2m} \Delta + V(\mathbf{r}) + \int d\mathbf{r}' \hat{\Psi}^\dagger(\mathbf{r}', t) U(\mathbf{r} - \mathbf{r}') \hat{\Psi}(\mathbf{r}', t) \right] \hat{\Psi}(\mathbf{r}, t) . \end{aligned} \quad (2.9)$$

The field operators are now rewritten in an orthonormal basis $\{u_j(\mathbf{r})\}_{j=0}^{\infty}$ of the single particle Hilbert space:

$$\hat{\Psi}(\mathbf{r}) = u_0(\mathbf{r})\hat{a}_0 + \sum_{j=1}^{\infty} u_j(\mathbf{r})\hat{a}_j . \quad (2.10)$$

Here the creation and annihilation $\hat{a}_j^\dagger, \hat{a}_j$ operators operate on Fock space in the usual way

$$\begin{aligned} \hat{a}_j^\dagger |n_0, n_1, \dots, n_j, \dots\rangle &= \sqrt{n_j + 1} |n_0, n_1, \dots, n_j + 1, \dots\rangle \\ \hat{a}_j |n_0, n_1, \dots, n_j, \dots\rangle &= \sqrt{n_j} |n_0, n_1, \dots, n_j - 1, \dots\rangle \end{aligned} \quad (2.11)$$

and obey the usual bosonic commutation relations

$$[\hat{a}_i, \hat{a}_j^\dagger] = \delta_{i,j} \quad [\hat{a}_i^\dagger, \hat{a}_j^\dagger] = 0 \quad [\hat{a}_i, \hat{a}_j] = 0 . \quad (2.12)$$

In a Bose-Einstein condensate the ground state $u_0(\mathbf{r})$ is assumed to be macroscopically occupied while the number of particles in the higher states is assumed to be negligible.

Comparing the expectation value of the particle number in the ground state

$$N = \langle \hat{a}_0^\dagger \hat{a}_0 \rangle$$

with the expectation value of the commutation relation

$$1 = \langle [\hat{a}_0, \hat{a}_0^\dagger] \rangle$$

we see that the latter is suppressed by a factor of $\frac{1}{N}$. Because N is assumed to be macroscopically large we can make the approximation $[\hat{a}_0, \hat{a}_0^\dagger] \approx 0$ and treat the creation and annihilation operator for the ground state like c -numbers [48]. This is analogous to the transition from quantum to classical mechanics. Using the replacement $\hat{a}_0 = \hat{a}_0^\dagger = \sqrt{N}$ we can write the field operator as¹

$$\hat{\Psi}(\mathbf{r}) = \sqrt{N}u_0(\mathbf{r}) + \sum_{j=1}^{\infty} u_j(\mathbf{r})\hat{a}_j = \sqrt{N}u_0(\mathbf{r}) + \delta\hat{\Psi}(\mathbf{r}) .$$

Here $\delta\hat{\Psi}(\mathbf{r})$ is a field operator acting only on the higher modes whose occupation is negligible compared to the ground mode: $\langle \delta\hat{\Psi}(\mathbf{r}) \rangle \approx 0$.

Adding a time dependence gives the Bogoliubov ansatz [71, 72] where one defines a (c -number) wave function ψ describing the condensate as the expectation value of the field operator

$$\psi(\mathbf{r}, t) = \langle \hat{\Psi}(\mathbf{r}, t) \rangle$$

and decomposes the field operator according to

$$\hat{\Psi}(\mathbf{r}, t) = \psi(\mathbf{r}, t) + \delta\hat{\Psi}(\mathbf{r}, t) .$$

Neglecting the term $\delta\hat{\Psi}(\mathbf{r}, t)$ which describes the non-condensed atoms and inserting this Bogoliubov ansatz into the Heisenberg equations of motion Eq. (2.9) we arrive at the usual (generalized) Gross-Pitaevskii equation (2.7)

$$i\hbar \frac{\partial \psi(\mathbf{r}, t)}{\partial t} = \left[-\frac{\hbar^2}{2m} \Delta + V(\mathbf{r}) + \int U(\mathbf{r} - \mathbf{r}') |\psi(\mathbf{r}', t)|^2 \right] \psi(\mathbf{r}, t) .$$

¹A complex phase of \hat{a}_0 can be absorbed into the definition of u_0 .

A crucial point concerning the Bogoliubov ansatz is that the system is not allowed to be in a pure number state like in Sec. 2.1.1. Otherwise the expectation value of $\hat{\Psi}$ would be zero. Therefore one works with a grand canonical ensemble and introduces an infinitely small artificial term which breaks the conservation of the particle number in order to get a non-vanishing expectation value for the field operator [211]. This is similar to the scenario of a spontaneously broken symmetry. A closely related ansatz is the assumption that the condensate is described by a coherent state [9, 16, 43, 210]. For a rigorous mathematical analysis why it is allowed to replace \hat{a}_0 and \hat{a}_0^\dagger with c -numbers and why the Bogoliubov ansatz works see the references [81, 133].

On the other hand, the fact that nature realizes a superselection rule forbidding superpositions of states with different atom numbers casts some doubt on the Bogoliubov ansatz [128]. There are some proposals to avoid the explicit symmetry breaking [39]. But in the end all approaches should give the same result in the thermodynamic limit.

The second quantization allows one to go beyond the mean-field approximation. To this end we take the expectation value of Eq. (2.9). The mean-field theory arises by replacing the expectation value of the product of field operators by a product of expectation values:

$$\langle \hat{\Psi}^\dagger(\mathbf{r}', t) \hat{\Psi}(\mathbf{r}', t) \hat{\Psi}(\mathbf{r}, t) \rangle \approx \langle \hat{\Psi}^\dagger(\mathbf{r}', t) \rangle \langle \hat{\Psi}(\mathbf{r}', t) \rangle \langle \hat{\Psi}(\mathbf{r}, t) \rangle .$$

Using cumulants one can systematically improve this approximation and go beyond the mean-field theory to describe the condensate [87, 120]. In this framework one can for example investigate the depletion of the condensate [67] and investigate the validity of the mean-field equation.

2.1.3 Particle-particle interaction

The scattering of two particles with the interaction potential $U(\mathbf{r}_j - \mathbf{r}_k)$ can be analyzed using a partial wave ansatz [154, 187, 198]. At very low energies one can show that s-wave scattering alone is sufficient to describe the scattering process [129, 167]. The p-wave scattering is forbidden because of the bosonic symmetry while higher angular momentum terms are kinetically suppressed. Therefore it is justified to approximate the interaction by a simple contact potential:

$$U(\mathbf{r}_j - \mathbf{r}_k) = \frac{4\pi\hbar^2 a_s}{m} \delta(\mathbf{r}_j - \mathbf{r}_k) . \quad (2.13)$$

Here the scattering length a_s is a parameter which depends on the type of atoms we are using.

The scattering length a_s can be changed by Feshbach resonances [44, 121, 167]. The interatomic potential depends on the electronic spin configuration. In a Feshbach scenario the scattering energy E_{scatter} of the normal configuration gets in resonance with the energy E_{bound} of a bound state in another configuration. See Fig. 2.1 for an illustration. Second order perturbation theory gives us [167]:

$$\frac{4\pi\hbar^2 a_s}{m} = \frac{4\pi\hbar^2 a_{s,0}}{m} + \frac{|\langle \psi_{\text{bound}} | H_{\text{coupling}} | \psi_{\text{scatter}} \rangle|^2}{E_{\text{scatter}} - E_{\text{bound}}} .$$

If the magnetic moments of the two states are different the value of $E_{\text{scatter}} - E_{\text{bound}}$ depends on the external magnetic field. This way we can control the scattering length a_s and even set a_s to zero by carefully tuning the magnetic field.

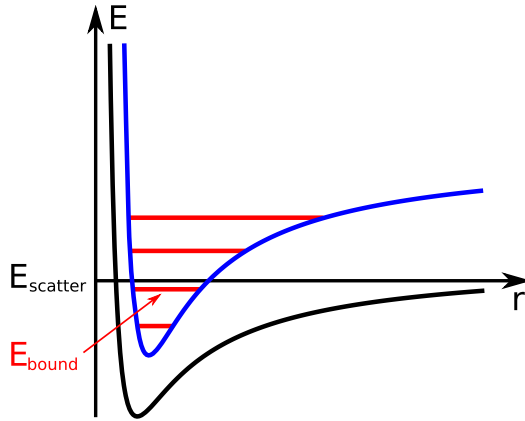


Figure 2.1: The situation in a Feshbach resonance scenario. The black potential arises in one electronic spin configuration, the blue potential arises from another electronic spin configuration. The blue potential curve allows several bound states colored in red. The energy difference between the two potentials can be controlled by applying an external magnetic field.

Inserting the approximation Eq. (2.13) into Eq. (2.5) and Eq. (2.7) we get the following stationary and time dependent (three-dimensional) Gross-Pitaevskii equation

$$\begin{aligned} \mu \psi(\mathbf{r}) &= \left[-\frac{\hbar^2}{2m} \Delta + V(\mathbf{r}) + U_0 |\psi(\mathbf{r})|^2 \right] \psi(\mathbf{r}) \\ i\hbar \frac{\partial \psi(\mathbf{r}, t)}{\partial t} &= \left[-\frac{\hbar^2}{2m} \Delta + V(\mathbf{r}) + U_0 |\psi(\mathbf{r}, t)|^2 \right] \psi(\mathbf{r}, t) \end{aligned} \quad (2.14)$$

with $U_0 = 4\pi\hbar^2 a_s/m$. These equations are only valid in the dilute gas regime where the condition $na_s^3 \ll 1$ (here n is the particle density) is satisfied [48].

2.2 External potentials for Bose-Einstein condensates

There are basically three ways to create external potentials for neutral atoms: One can use gravitational², electrical or magnetical fields. Here we discuss the latter two. The external potential based on electrical fields uses the AC Stark effect at optical frequencies. The external potential based on magnetic fields makes use of the Zeeman effect. The presentation given here is based on [48, 129, 167, 169].

2.2.1 Optical potentials

An electrical field \mathbf{E} induces an electrical dipole moment $\mathbf{p} = \alpha \mathbf{E}$ in a neutral atom. Here α is the polarizability. This dipole moment interacts with the electrical field; the value of the interaction energy is $V_{\text{pot}} = -\int_0^{\mathbf{E}} \mathbf{p} \cdot d\mathbf{E} = -\frac{1}{2} \alpha |\mathbf{E}|^2$. That is the quadratic Stark effect. The DC Stark effect is related to static electric fields while the AC Stark effect is related to electrical fields of electromagnetic waves.

The AC Stark effect is a nice way to generate external potentials for neutral atoms. One uses electromagnetic waves (generated by lasers) with frequency ω in the vicinity of an atomic transition between two states, say ground state $|g\rangle$ and excited state $|e\rangle$. The polarizability α can then be calculated in second order perturbation theory as [167]

$$\alpha = \text{Re} \frac{|\langle e | \mathbf{d} \cdot \mathbf{E} / |\mathbf{E}| | g \rangle|^2}{E_e - E_g - \hbar\omega - i\hbar\Gamma_e/2}.$$

²The gravitational field of the earth is not always wanted in experiments; hence there exists Bose Einstein condensate experiments which use microgravity in falltowers [204].

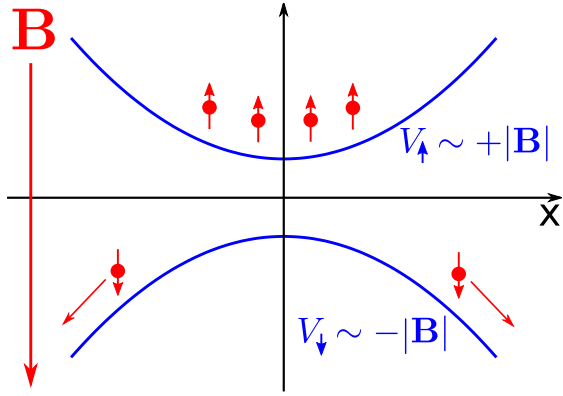


Figure 2.2: Magnetic moments \uparrow which are antiparallel to an applied magnetic field \mathbf{B} are attracted to regions where $B = |\mathbf{B}|$ is minimal. Parallel aligned magnetic moments are attracted to regions where B is larger.

Here \mathbf{d} is the electrical dipole operator and Γ_e^{-1} is the lifetime of the excited state $|e\rangle$. The external potential for the neutral atoms is then

$$V_{\text{pot}} = -\frac{1}{2} \alpha \langle |\mathbf{E}|^2 \rangle_{\text{time averaged}} .$$

The sign of the interaction energy V_{pot} depends on the detuning of the frequency ω with respect to the transition frequency. Furthermore the magnitude of the interaction energy V_{pot} depends on the intensity of the electromagnetic wave. It follows that blue detuned lasers generate a repulsive potential ejecting atoms from high intensity regions. Red detuned lasers generate an attractive potential capturing atoms inside high intensity regions. The latter effect is also used in optical tweezers (operating not on atoms but on (literally) microscopical particles).

A position dependent external potential $V_{\text{pot}}(\mathbf{r})$ can be created by varying the intensity of the laser beam with the position \mathbf{r} . This provides many ways to craft almost arbitrary external potentials for neutral atoms. The simplest example is that the beam of a red detuned (hence attractive) laser itself is used as a quasi-onedimensional waveguide [45, 88] which may be called a “guided atom laser”. As the ultracold atoms move very slowly a fast moving laser beam (deflected by acousto-optic modulators) can be used to inscribe potential landscapes on the condensate [78, 101, 105, 116, 148]. Spatial light modulators [28] can be used, too. Disordered potentials can be created using speckle patterns [3, 182].

Two counterpropagating laser beams create standing wave whose intensity varies on the scale of half a wavelength. If one uses red detuned lasers this allows one to confine a condensate to a two dimensional plane. This will be discussed in more detail in Sec. 2.2.3. Various other lattice potentials can also be created using standing waves with (two or more) laser beams in many different configurations [182].

2.2.2 External potentials induced by magnetic fields

The energy level of an atom with non-vanishing total angular momentum F split into $2F + 1$ hyperfine states $m_F = -F, -F + 1, \dots, +F$ by applying a magnetic field B . This is called the Zeeman effect. For small magnetic fields B the energy shift for each of the hyperfine states is given by [93, 167]

$$V_{\text{pot}} = -g_F \mu_B B m_F .$$

Here g_F is the Landé factor and μ_B is the Bohr magneton. The sign of g_F can be both positive or negative.

In an inhomogeneous magnetic field, magnetic dipoles experience a force. Atoms whose magnetic moment $g_F m_F$ points in the same direction as the magnetic field \mathbf{B} (i.e. $g_F m_F > 0$) are attracted to regions where $B = |\mathbf{B}|$ is large. These atoms are called high field seekers. Atoms whose magnetic moment $g_F m_F$ points in the opposite direction as the magnetic field \mathbf{B} (i.e. $g_F m_F < 0$) are attracted to regions where $B = |\mathbf{B}|$ is small. These atoms are called low field seekers. See Fig. 2.2 for an illustration. A position dependent modulus of the magnetic field can thus be used to create external potentials for neutral atoms with a non-vanishing magnetic moment m_F .

While a local maximum of $B = |\mathbf{B}|$ cannot exist in a current free region, a local minimum³ can be created. The minimum of B should not be zero because then the atoms loose their orientation. Typical experimental realizations as the Ioffe-Pritchard trap [167] use two or more superimposed magnetic fields to create such minima. Advanced designs for magnetic traps are so small that they fit on microelectronic chips [21, 35, 108].

2.2.3 Restriction to two dimensions

In this work we want to investigate the quantum transport properties of two-dimensional Bose Einstein condensates. To this end the motion in one dimension, say the z -direction, has to be restricted. Experimentally this can be done for example with a standing wave created by two counterpropagating red detuned lasers as described in Sec. 2.2.1. The following discussion is based on [98].

To investigate the restriction to two dimensions theoretically we assume a harmonic confinement $V_\perp(z) = \frac{1}{2} m \omega_\perp^2 z^2$ in z -direction. The confinement has to be strong enough that the difference between ground state and first excited state in z -direction exceeds all other relevant energy scales (for example the kinetic energy in x, y -direction and the interaction energy) of the system. Furthermore we assume that the potential in x, y -direction varies on a much larger scale than in z -direction. Under these conditions the condensate is always in the ground state in z -direction. This justifies a separation ansatz

$$\Psi(x, y, z, t) = \psi(x, y, t) \phi(z)$$

where $\phi(z)$ is a function which depends predominately on z and only weakly on x, y, t (i.e. $\frac{\partial \phi}{\partial x} \cong 0, \frac{\partial \phi}{\partial y} \cong 0, \frac{\partial \phi}{\partial t} \cong 0$). The normalization $\int |\phi(z)|^2 dz = 1$ is chosen. This ansatz inserted into the three dimensional Gross-Pitaevskii equation (2.14) gives

$$\begin{aligned} \phi(z) i \hbar \frac{\partial \psi(x, y, t)}{\partial t} = \phi(z) \left[-\frac{\hbar^2}{2m} \left(\frac{\partial^2}{\partial x^2} + \frac{\partial^2}{\partial y^2} \right) + \tilde{V}(x, y) \right] \psi(x, y, t) \\ + \psi(x, y, t) \left[-\frac{\hbar^2}{2m} \frac{\partial^2}{\partial z^2} + V_\perp(z) + U_0 |\psi(x, y, t)|^2 |\phi(z)|^2 \right] \phi(z). \end{aligned} \quad (2.15)$$

The (non-linear) equation for the ground state in z direction reads

$$\mu_\perp \phi(z) = \left[-\frac{\hbar^2}{2m} \frac{\partial^2}{\partial z^2} + V_\perp(z) + U_0 |\psi(x, y, t)|^2 |\phi(z)|^2 \right] \phi(z).$$

³ This has to be contrasted with the maximum principle [77] for the individual components of \mathbf{B} which are disallowed to have either local minima or maxima in current free regions.

For small interaction strengths U_0 this equation can be solved perturbatively using the non-interacting ground state wave function [154]

$$\phi_0(z) = (\sqrt{\pi}a_\perp)^{-1/2} e^{-x^2/(2a_\perp^2)}$$

with the harmonic oscillator length $a_\perp = \sqrt{\hbar/(mw_\perp)}$. This gives

$$\mu_\perp = \frac{1}{2}\hbar\omega_\perp + U_0|\psi(x, y, t)|^2 \langle \phi_0 | |\phi_0|^2 | \phi_0 \rangle = \frac{1}{2}\hbar\omega_\perp + \frac{\hbar^2}{m} \sqrt{8\pi} \frac{a_s}{a_\perp} |\psi(x, y, t)|^2$$

where we have used $U_0 = 4\pi\hbar^2 a_s/m$. Inserting this result into Eq. (2.14) gives the two dimensional Gross-Pitaevskii equation

$$i\hbar \frac{\partial \psi(x, y, t)}{\partial t} = \left[-\frac{\hbar^2}{2m} \left(\frac{\partial^2}{\partial x^2} + \frac{\partial^2}{\partial y^2} \right) + V(x, y) + g \frac{\hbar^2}{m} |\psi(x, y, t)|^2 \right] \psi(x, y, t)$$

with $g = \sqrt{8\pi} a_s/a_\perp$ and $V(x, y) = \tilde{V}(x, y) + \frac{1}{2}\hbar\omega_\perp$.

The theoretical discussion remains valid if we introduce an adiabatically slow position dependence (in x, y -direction) of the harmonic confinement potential in z -direction. This makes a_\perp depend on x, y and thus leads to a position dependent interaction strength $g(x, y)$.

In summary one can say that the restriction to two dimensions leads to a renormalization of the interaction strength but does not change the form of the Gross-Pitaevskii equation.

2.3 Gauge potentials for Bose-Einstein condensates

In experiments one usually uses uncharged particles whose center-of-mass motion is not affected by magnetic gauge fields⁴ to create Bose Einstein condensates. Consequently there is no gauge potential in the mean field time evolution equation (2.14). But using internal states one can simulate magnetic fields by creating artificial gauge potentials. This section describes how this is done. The presentation is based on [49].

Let $|a\rangle, |c_1\rangle, |c_2\rangle, \dots, |c_N\rangle$ be a position-dependent orthonormal basis for the $N + 1$ internal states. It is assumed that the basis changes adiabatically slowly with respect to the position. In this case one can assume that the particles stay in one internal state, say $|a\rangle$, for all relevant positions and times. The contribution from all other internal states $|c_1\rangle, \dots, |c_N\rangle$ can be neglected. The total wave function $|\Psi\rangle = \psi|a\rangle + \{\text{terms with } c\}$ can therefore be approximated by $|\Psi\rangle = \psi|a\rangle$.

We must now transform the time evolution equation for $|\Psi\rangle$ in one for ψ . For sake of simplicity we neglect the atom-atom interactions and external potentials. The time evolution for $|\Psi\rangle$ is then given by

$$i\hbar \frac{\partial}{\partial t} |\Psi\rangle = \frac{1}{2m} [-i\hbar \nabla]^2 |\Psi\rangle. \quad (2.16)$$

The action of ∇^2 on $|\Psi\rangle$ is given by

$$\begin{aligned} \nabla |\Psi\rangle &= (\nabla \psi) |a\rangle + \psi |\nabla a\rangle \\ \nabla^2 |\Psi\rangle &= (\Delta \psi) |a\rangle + 2(\nabla \psi) \cdot |\nabla a\rangle + \psi |\Delta a\rangle. \end{aligned}$$

⁴ Of course magnetic fields can be used to create external potentials as described in Sec. 2.2.2 or to manipulate internal states of the atoms.

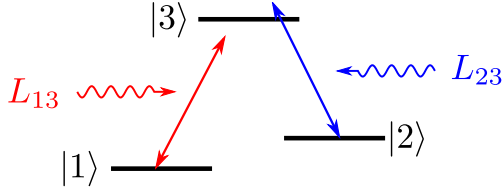


Figure 2.3: This figure shows a Λ -configuration as used in STIRAP. Three internal states $|1\rangle$, $|2\rangle$, $|3\rangle$ are coupled by two laser beams L_{13} , L_{23} with a finite detuning.

Projecting Eq. (2.16) onto $|a\rangle$ and using $\psi = \langle a|\Psi\rangle$ we arrive at

$$i\hbar \frac{\partial}{\partial t} \psi = -\frac{\hbar^2}{2m} [\Delta + 2\langle a|\nabla a\rangle \cdot \nabla + \langle a|\Delta a\rangle] \psi.$$

Comparing this with

$$\frac{1}{2m} [-i\hbar \nabla - q\mathbf{A}]^2 = -\frac{\hbar^2}{2m} \Delta + \frac{q^2}{2m} \mathbf{A}^2 + i\frac{\hbar q}{2m} [\nabla \cdot \mathbf{A}] + i\frac{\hbar q}{m} \mathbf{A} \cdot \nabla$$

we see that the artificial gauge potential \mathbf{A} (with the artificial charge q) must be given by

$$\mathbf{A} = i\frac{\hbar}{q} \langle a|\nabla a\rangle.$$

Furthermore it follows that the time evolution equation for ψ

$$i\hbar \frac{\partial}{\partial t} \psi = \frac{1}{2m} [-i\hbar \nabla - q\mathbf{A}]^2 \psi + W \psi$$

must contain a further potential term $W(\mathbf{r})$ given by

$$\begin{aligned} \frac{2m}{\hbar^2} W &= -\langle a|\Delta a\rangle + \langle a|\nabla a\rangle \cdot \langle a|\nabla a\rangle + \nabla \cdot \langle a|\nabla a\rangle \\ &= \langle a|\nabla a\rangle \cdot \langle a|\nabla a\rangle + \langle \nabla a|\nabla a\rangle. \end{aligned}$$

The term $W(\mathbf{r})$ can be rewritten by using orthonormality and completeness $\mathbb{1} = |a\rangle \langle a| + \sum_{n=1}^N |c_n\rangle \langle c_n|$ of the internal basis states as

$$\frac{2m}{\hbar^2} W = \sum_{n=1}^N \mathbf{C}_n \cdot \mathbf{C}_n^*$$

with (also note $\langle a|\nabla a\rangle = -\langle \nabla a|a\rangle$)

$$\mathbf{C}_n = \langle a|\nabla c_n\rangle = -\langle \nabla a|c_n\rangle \quad \mathbf{C}_n^* = \langle \nabla c_n|a\rangle = -\langle c_n|\nabla a\rangle.$$

A possible physical realization[49, 114] of this scheme to create artificial gauge potentials uses a Λ -type internal level structure (see Fig. 2.3) as is used in STIRAP (stimulated Raman adiabatic passage)[17]. Two laser beams L_{13} , L_{23} couple the three internal states $|1\rangle$, $|2\rangle$, $|3\rangle$ into three dressed states: a dark state $|D\rangle$ and two bright states $|B_+\rangle$, $|B_-\rangle$. The dark state $|D\rangle$ does not contain the excited state $|3\rangle$ and is therefore longlived. This would correspond to our $|a\rangle$. The coupling depends on the amplitude (this means modulus and phase) of the electric field of the laser beams and on the detuning. Therefore the creation of artificial gauge potentials works best if the photons of one of the lasers have orbital angular momentum [114] as then the phase of the electric

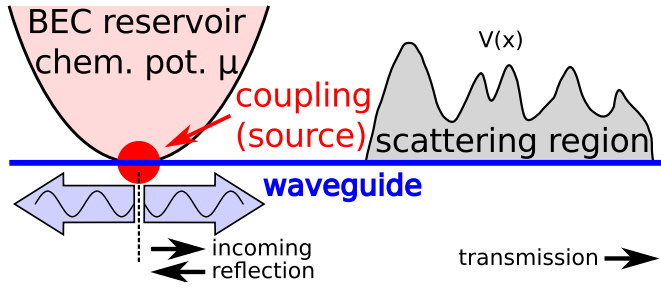


Figure 2.4: A trap containing a reservoir of atoms in a Bose-Einstein condensate is coupled to a waveguide. Inside the waveguide the atoms propagate as a plane wave. The waveguide itself is connected to a scattering region. As we are interested in transport properties, we measure reflection and transmission through the scattering region.

field is strongly position dependent. Other experimental realizations [49, 135, 136] use a spatial modulation of the intensity and/or detuning of the lasers. Using variations of these approaches allows one to simulate other kind of gauge potentials as for example spin-orbit interaction.

In summary one can say that artificial gauge potentials can be created as some kind of Berry phase. Consequently $\mathbf{A} = i\hbar \langle a | \nabla a \rangle / q$ is called a Berry-Mead connection. The potential $W(\mathbf{r})$ has to be combined with the potentials created by the methods of Sec. 2.2 to create the final potential $V(\mathbf{r})$.

2.4 Summary

In the rest of this work we use the inhomogeneous two-dimensional Gross-Pitaevskii equation

$$i\hbar \frac{\partial}{\partial t} \Psi(\mathbf{r}, t) = H \Psi(\mathbf{r}, t) + g(\mathbf{r}) \frac{\hbar^2}{m} |\Psi(\mathbf{r}, t)|^2 \Psi(\mathbf{r}, t) + S(\mathbf{r}) e^{-i\mu t/\hbar} \quad (2.17)$$

with $H = \frac{1}{2m} [-i\hbar \nabla - q\mathbf{A}(\mathbf{r})]^2 + V(\mathbf{r})$

with position $\mathbf{r}=(x, y)$, time independent Hamilton operator H , gauge potential $\mathbf{A}(\mathbf{r})$ (with charge q), external potential $V(\mathbf{r})$ and (dimensionless) position dependent interaction strength $g(\mathbf{r})$. This equation of motion is obtained by combining Sec. 2.1, Sec. 2.2 and Sec. 2.3 and describes a Bose-Einstein condensate restricted to two dimensions.

The interaction strength $g(\mathbf{r})$ can be controlled by using Feshbach resonances (see Sec. 2.1.3), by changing the transversal confinement (see Sec. 2.2.3) or by modifying the overall particle density (see Sec. 5.1.1). The gauge potential $\mathbf{A}(\mathbf{r})$ corresponds to a simulated⁵ magnetic field $\mathbf{B}(\mathbf{r}) = \nabla \times \mathbf{A}(\mathbf{r})$.

So far, the only term unaccounted for is the inhomogeneous source term $S(\mathbf{r}) e^{-i\mu t/\hbar}$. This source term models a particle reservoir which injects particles into our system as illustrated in Sec. 3.4.2 and Sec. 4.7. The physical picture is that one couples a trap containing a Bose-Einstein condensate (with chemical potential μ) to a waveguide (see Fig. 2.4). Inside the waveguide the atoms propagate as plane waves. The waveguide (and scattering potential) is modelled by H while the effect of the coupled condensate in the trap is described by the source term. A possible realization could be a condensate in a magnetic trap with a red detuned (i.e. attractive) laser beam as a waveguide. The coupling would be accomplished by using microwave radiation to change the magnetic moment of the atoms to zero. Then the atoms are not affected by the trapping potential anymore and propagate inside the waveguide. This setup is called a guided atom laser [45, 67, 88].

⁵ Not to be confused with the real magnetic field trapping potentials used in Sec. 2.2.2.

In this work we are studying open scattering systems. The Hamiltonian H describes two semi-infinite leads connected by a scattering region. The reflection and transmission through the scattering region are measured (see Fig. 2.4).

Non-linear Schrödinger equations such as Eq. (2.17) (without gauge potential) also arise in other contexts such as non-linear optics [27] and water waves in shallow waters [212].

Chapter 3

Stationary scattering states of the Schrödinger equation

3.1 Introduction

The topic of this chapter is the development of a method to numerically calculate stationary scattering states of the inhomogeneous, time-dependent Schrödinger equation

$$i\hbar \frac{\partial}{\partial t} \Psi(\mathbf{r}, t) = H \Psi(\mathbf{r}, t) + S(\mathbf{r}) e^{-i\mu t/\hbar} \quad (3.1)$$

with $H = \frac{1}{2m} [-i\hbar \nabla - q\mathbf{A}(\mathbf{r})]^2 + V(\mathbf{r})$.

where H is the time-independent Hamilton operator and S describes the spatial component of the source which is technically an element of the Hilbert space on which H acts.

Inserting the ansatz

$$\Psi(\mathbf{r}, t) = \Psi(\mathbf{r}) e^{-i\mu t/\hbar}$$

into Eq. (3.1) gives us

$$[\mu - H] \Psi(\mathbf{r}) = S(\mathbf{r}) . \quad (3.2)$$

We see that as $S(\mathbf{r})$ is given we “only” have to solve a linear equation system to calculate the stationary scattering state $\Psi(\mathbf{r})$.

Therefore we will address the following issues in this chapter:

1. In Eq. (3.2) the continuous variable \mathbf{r} has to be discretized in order to simulate it on a computer. This will be done using the finite difference method (also known as tight binding model) introduced in Sec. 3.3.
2. As it stands, Eq. (3.2) is not well-posed because appropriate boundary conditions are missing. These are necessary as we are studying open scattering systems. We will introduce two different kinds of boundary conditions: the self energy boundary conditions (Eq. (3.36))

and the exterior complex scaling boundary conditions (Eq. (3.63)). Both boundary conditions can be used to describe semi-infinite leads attached to the scattering region. Both self-energy and complex scaling approaches are suitable to Green function calculation while the complex scaling approach has further uses for resonance calculations, time dependent propagation and stability analysis.

3. We have to look into many details and technical issues to make sense of Eq. (3.2).

The material related to the tight binding model presented here follows roughly [50, 70].

3.2 The retarded Green function

In this work μ will always be located in the continuous part of the spectrum of H to excite propagating modes. Therefore Eq. (3.2) is not well posed because $[\mu - H]$ is not invertible. This problem is inherently related to the issue of finding the right boundary conditions of $\Psi(\mathbf{r})$ for $|\mathbf{r}| \rightarrow \infty$.

To remedy the situation we now use the following form of the the inhomogeneous Schrödinger equation¹:

$$i\hbar \frac{\partial}{\partial t} \Psi(t) = H\Psi(t) + Sf(t) . \quad (3.3)$$

Here $f(t)$ describes an arbitrary time behavior of the source. We regard this equation now as an initial value problem where we start at some time t_0 with the given wave function $\Psi(t_0)$ and propagate the wave function to another time t . The inhomogeneous linear ordinary differential equation (3.3) can now be solved with the method of the variation of constants (see [26, 75]):

$$\Psi(t) = e^{-i(t-t_0)H/\hbar} \Psi(t_0) - \frac{i}{\hbar} \int_{t_0}^t e^{-\frac{i}{\hbar}(t-t')H} S f(t') dt' . \quad (3.4)$$

The physical situation we want to describe now is that we start at $t_0 = -\infty$ with $\Psi(t_0) = 0$, then adiabatically slowly switch the source term on and propagate the system to $t = 0$. The source should oscillate with the (real) energy μ .

Mathematically this can be realized with the following switching function:

$$f(t) = e^{-i(\mu+i\epsilon)t/\hbar} \quad (\mu \in \mathbb{R}, \quad \epsilon \in \mathbb{R} \quad \text{and} \quad \epsilon > 0) .$$

Here ϵ is a small positive constant which switches the source on and renders the integral in Eq. (3.4) well defined. Using Eq. (3.4) we can calculate

$$\begin{aligned} \Psi(0) &= -\frac{i}{\hbar} \int_{-\infty}^0 e^{-\frac{i}{\hbar}(\mu+i\epsilon-H)t'} S dt' \\ &= (\mu + i\epsilon - H)^{-1} S . \end{aligned} \quad (3.5)$$

The adiabatically slow switching can be realized by taking the limit² $\epsilon \rightarrow 0$:

$$\Psi(0) = \lim_{\substack{\epsilon \rightarrow 0 \\ \epsilon > 0}} (\mu + i\epsilon - H)^{-1} S .$$

¹ The position variable \mathbf{r} will from now on be dropped when appropriate.

² A word of warning is justified here: As μ is usually located in the continuous part of the spectrum of H one cannot simply put $\epsilon = 0$ here because $[\mu - H]$ is not invertible. In Sec. 3.7.2 the behavior of the Green function $[\tilde{\mu} - H]^{-1}$ as a function of the complex parameter $\tilde{\mu}$ is investigated in more detail.

The operator occurring here is called the retarded Green function (see for example [50, 70, 146]):

$$G^{(r)} = \lim_{\substack{\epsilon \rightarrow 0 \\ \epsilon > 0}} (\mu + i\epsilon - H)^{-1} . \quad (3.6)$$

In the following a stationary scattering state is always understood as the result of applying the retarded Green function onto a source term:

$$\Psi = G^{(r)} S \quad (3.7)$$

which is the right way to interpret Eq. (3.2). As we will see in Sec. 3.4.2 the choice of the retarded Green function $G^{(r)}$ gives us the correct behavior of $\Psi(\mathbf{r}, t)$ as a function of \mathbf{r} for $|\mathbf{r}| \rightarrow \infty$. The wave function should consist only of outgoing plane waves there³. This is the necessary boundary condition to render Eq. (3.2) well defined.

The retarded Green function (3.6) is always well-behaved except when μ exactly equals a bound state energy. This can for example be shown by examining the behavior of the Green function $[\tilde{\mu} - H]^{-1}$ as a function of the complex variable $\tilde{\mu}$ as it is done in Sec. 3.7.2 using complex scaling.

To avoid problems with embedded bound states in the continuous part of the spectrum we therefore postulate that the overlap of $S(\mathbf{r})$ with any bound state vanishes or is at least negligible small. As we will see in Sec. 4.7 this requirement can be met by placing the source sufficient far away from the scattering region.

3.3 The tight binding model

The main part of this work is about numerical simulations of the Gross-Pitaevskii equation (2.17). The aim of this section is to introduce a framework in which this simulations are carried out.

We first consider here the (linear) one dimensional Schrödinger equation with the following Hamilton operator:

$$H\Psi(x) = -\frac{\hbar^2}{2m} \frac{\partial^2}{\partial x^2} \Psi(x) + V(x)\Psi(x) . \quad (3.8)$$

In order to carry out numerical simulations of this equation we have to use some form of discretization. In this work we choose the finite difference approximations for the first (needed later) and second derivative [1], which are correct up to order $(\Delta x)^2$:

$$\begin{aligned} \frac{\partial}{\partial x} \Psi(x) &= \frac{\Psi(x + \Delta x) - \Psi(x - \Delta x)}{2\Delta x} + \mathcal{O}((\Delta x)^2) \\ \frac{\partial^2}{\partial x^2} \Psi(x) &= \frac{\Psi(x + \Delta x) + \Psi(x - \Delta x) - 2\Psi(x)}{(\Delta x)^2} + \mathcal{O}((\Delta x)^2) . \end{aligned} \quad (3.9)$$

³ This is to be contrasted with the advanced Green function

$$G^{(a)} = \lim_{\substack{\epsilon \rightarrow 0 \\ \epsilon > 0}} (\mu - i\epsilon - H)^{-1}$$

which generates incoming plane waves at $|\mathbf{r}| \rightarrow \infty$.

In order to use this approximation, the continuous system is reduced to a lattice with regular spacing Δx . From now on we therefore use the following notation:

$$\begin{array}{lll} \text{lattice points} & x_n = n \Delta x & \text{with } n \in \mathbb{Z} \\ \text{wave function} & \Psi_n = \Psi(x_n) & = \Psi(n \Delta x) \\ \text{potential} & V_n = V(x_n) & = V(n \Delta x) \end{array}$$

For convenience we further define a lattice parameter

$$\alpha = \frac{\hbar^2}{2m(\Delta x)^2} . \quad (3.10)$$

Using the finite difference approximation (3.9) the discretized form of the Hamilton operator (3.8) reads now

$$(H\Psi)_n = (2\alpha + V_n)\Psi_n - \alpha\Psi_{n-1} - \alpha\Psi_{n+1} . \quad (3.11)$$

This discretized Hamiltonian H can also be written as the tridiagonal matrix

$$H = \begin{pmatrix} \ddots & & & & \\ & 2\alpha + V_{j-1} & -\alpha & & \\ & -\alpha & 2\alpha + V_j & -\alpha & \\ & & -\alpha & 2\alpha + V_{j+1} & \\ & & & & \ddots \end{pmatrix} \quad (3.12)$$

acting on the vector of lattice points.

The discretized Hamiltonian H as shown in Eq. (3.11) and Eq. (3.12) is also called a tight binding Hamiltonian and correspondingly the approximation is called a tight binding approximation (see [50, 70]).

In all the following numerical simulations we will use such a tight binding approximation. The lattice spacing Δx will be chosen small enough that the approximation error⁴ (which scales as $\mathcal{O}((\Delta x)^2)$) becomes negligible which is the case for roughly 30 lattice points per wavelength.

3.4 The tight binding model for a constant potential

In this section we study the tight binding Hamiltonian (3.12) for a constant potential $V_n = V$. Of special interest will be the energy dispersion relations and the behavior of a source term in Green function calculations. This information will be needed at various points, for example in the calculation of the self-energies of the leads as done in Sec. 3.5 and for proper normalization of the source term.

3.4.1 Eigenfunctions for a constant potential

Our first aim is to find eigenenergies μ and eigenfunctions Ψ of the tight binding Hamiltonian H given by Eq. (3.11) for a constant potential V :

$$H\Psi = \mu\Psi . \quad (3.13)$$

⁴also called discretization error

In components this formula looks as follows:

$$[\mu - (2\alpha + V)]\Psi_n + \alpha(\Psi_{n-1} + \Psi_{n+1}) = 0. \quad (3.14)$$

This is a linear three term recursion formula with constant coefficients. So there are two independent solutions to this problem [124].

We first assume that $\mu > V$ and make the ansatz

$$\Psi_n = e^{i k n \Delta x}.$$

Inserting this ansatz into the recursion formula (3.14) results in

$$(\mu - (2\alpha + V)) + 2\alpha \cos(k\Delta x) = 0$$

which leads to the following dispersion relation:

$$\begin{aligned} \mu &= V + 2\alpha(1 - \cos(k\Delta x)) & k &= \frac{1}{\Delta x} \arccos\left(1 - \frac{\mu - V}{2\alpha}\right) \\ &= V + 4\alpha \left(\sin \frac{k\Delta x}{2}\right)^2 & &= \frac{2}{\Delta x} \arcsin \sqrt{\frac{\mu - V}{4\alpha}}. \end{aligned} \quad (3.15)$$

The two eigenfunctions of the eigenvalue problem (3.13) for the eigenenergy μ are now given by

$$\Psi_{+,n} = C_+ e^{+i k n \Delta x} \quad \Psi_{-,n} = C_- e^{-i k n \Delta x}$$

where k is calculated from the dispersion relation (3.15). C_+ and C_- are normalization constants. The two eigenfunctions Ψ_+ and Ψ_- are right and left moving plane waves.

For the case $\mu < V$ one can make the similar ansatz

$$\Psi_n = e^{k n \Delta x}$$

giving the dispersion relations

$$\begin{aligned} \mu &= V + 2\alpha(1 - \cosh(k\Delta x)) & k &= \frac{1}{\Delta x} \operatorname{acosh}\left(1 - \frac{\mu - V}{2\alpha}\right) \\ &= V - 4\alpha \left(\sinh \frac{k\Delta x}{2}\right)^2 & &= \frac{2}{\Delta x} \operatorname{asinh} \sqrt{\frac{V - \mu}{4\alpha}} \end{aligned} \quad (3.16)$$

and the eigenfunctions

$$\Psi_{+,n} = C_+ e^{-k n \Delta x} \quad \Psi_{-,n} = C_- e^{+k n \Delta x}$$

which are exponential decaying or rising functions.

3.4.2 A source on an infinite lattice

We study now the effect of the source term $S(r)$ which was introduced in Eq. (3.1). This will allow us to select a source emitting a predefined current of particles as described in Sec. 3.4.3.

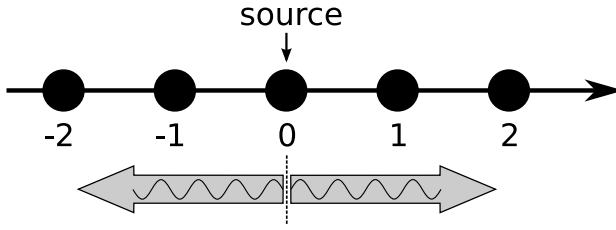


Figure 3.1: This figure illustrates Eq. (3.18). A point source is located at $n = 0$ which emits outgoing plane waves to the left and to the right.

To this end we have to explicitly calculate the effect of the retarded Green function Eq. (3.6) on a delta source:

$$\Psi = \lim_{\substack{\epsilon \rightarrow 0 \\ \epsilon > 0}} (\mu + i\epsilon - H)^{-1} S. \quad (3.17)$$

Here H is the tight binding Hamiltonian (3.11) for a constant potential V and the source term S is given by

$$S_n = \begin{cases} 1 & \text{for } n = 0 \\ 0 & \text{for } n \neq 0. \end{cases}$$

The use of the retarded Green function enforces outgoing boundary conditions onto the wave function Ψ as illustrated in Fig. 3.1. The solution of the Green function problem Eq. (3.17) is equal to the solution of

$$(\mu - H)\Psi = S \quad (3.18)$$

where we have included the infinitely small imaginary $+i\epsilon$ into the energy μ for the sake of simplicity. In components this equation reads

$$\begin{aligned} (\mu - (2\alpha + V))\Psi_0 + \alpha(\Psi_{-1} + \Psi_{+1}) &= 1 & \text{for } n = 0 \\ (\mu - (2\alpha + V))\Psi_n + \alpha(\Psi_{n-1} + \Psi_{n+1}) &= 0 & \text{for } n \neq 0. \end{aligned} \quad (3.19)$$

In order to solve this equation set we now make the ansatz

$$\Psi_n = C e^{i k \Delta x |n|}. \quad (3.20)$$

We immediately realize that this ansatz fulfills Eq. (3.19) in the region $n \neq 0$ provided that k is given by the dispersion relation (3.15).

Inserting the ansatz (3.20) and the dispersion relation (3.15) into the equation (3.19) for $n = 0$ we can conclude:

$$\begin{aligned} \underbrace{C(\mu - (2\alpha + V))}_{-2\alpha \cos(k\Delta x)} + 2\alpha C e^{ik\Delta x} &= 1 \\ \Rightarrow -C\alpha (e^{+ik\Delta x} + e^{-ik\Delta x} - 2e^{+ik\Delta x}) &= 1 \\ \Rightarrow C\alpha (e^{+ik\Delta x} - e^{-ik\Delta x}) &= 1 \\ \Rightarrow 2iC\alpha \sin(k\Delta x) &= 1 \end{aligned}$$

giving us

$$C = -\frac{i}{2\alpha \sin(k\Delta x)}.$$

So we get as solution to Eq. (3.17):

$$\Psi_n = -\frac{i}{2\alpha \sin(k\Delta x)} e^{ik\Delta x |n|}. \quad (3.21)$$

The final step is to set the imaginary part of μ to zero which corresponds to take the limit $\epsilon \rightarrow 0$ (with $\epsilon > 0$) in Eq. (3.17). This can be done without problem so in the end k in Eq. (3.21) is a real quantity. The interpretation of this term is that the source S emits outgoing plane waves to the left and to the right as seen in Fig. 3.1.

It only remains to check if the outgoing boundary conditions are fulfilled, which means to check if (3.21) is a solution of the *retarded* Green function (3.17). In practice this means we have to ensure that the proper sign of k is chosen in the ansatz (3.20)⁵.

To this end we look at the infinitesimal small positive imaginary part of μ which will introduce an infinitesimal small imaginary part in k whose sign will tell us if we have found a proper solution of Eq. (3.17) or not. Taking the derivative of the dispersion relation (3.15) with respect to k we see that

$$\frac{\partial \mu}{\partial k} = 2\alpha \Delta x \sin(k\Delta x)$$

holds. We always stay in the first Brillouin zone because we are only interested in the continuum limit $\Delta x \rightarrow 0$. So we have $0 < k\Delta x < \pi$ and therefore $\frac{\partial \mu}{\partial k} > 0$ and simultaneously $\frac{\partial k}{\partial \mu} > 0$.

Therefore a small positive imaginary part in μ induces a small positive imaginary part in k . In this case the ansatz $\Psi_n = C e^{i k \Delta x |n|}$ given in (3.20) vanishes for $n \rightarrow \pm\infty$, so Ψ_n is an element of the Hilbert space $L^2(\mathbb{Z})$ and therefore a solution to the retarded Green function problem (3.17).

The alternative ansatz $\Psi_n^{\text{alt}} = C e^{-i k \Delta x |n|}$ with the negative sign for k gives an exponential growth for $n \rightarrow \pm\infty$, so Ψ_n^{alt} is not an element of the Hilbert space $L^2(\mathbb{Z})$ and therefore is not a solution to Eq. (3.17).

3.4.3 Calculation of the current

In Green function calculations one has to normalize the source term in such a way that a plane wave of given current is emitted to the left and to the right.

From the definition of the probability current [187] (see also Eq. (B.21))

$$j(x) = \frac{\hbar}{m} \text{Im} \left[\Psi(x)^* \frac{\partial}{\partial x} \Psi(x) \right] \quad (3.22)$$

one can see that a plane wave $C e^{ikx}$ carries a current of $j = \frac{\hbar k}{m} |C|^2$. Looking at Eq. (3.21) we can now conclude that a source term S with

$$S_n = \begin{cases} \sqrt{j_0 \frac{m}{\hbar k}} 2i\alpha \sin(k\Delta x) & \text{for } n = 0 \\ 0 & \text{for } n \neq 0 \end{cases} \quad (3.23)$$

generates a plane wave carrying a current j_0 running to the left and to the right after applying the Green function (3.17) onto it. This gives us the desired normalization of the source term S .

The Green function calculation gives us a scattering state Ψ corresponding to a fixed energy μ . A non-vanishing non-constant scattering potential may generate a back reflected plane wave which we want to calculate now given Ψ . To this end we look at the wave function Ψ in the region between the source and the scattering potential. In this region the potential should still be

⁵ The ansatz would also work with k replaced by $-k$ (neglecting the boundary conditions).

constant and of the same value as at the point of the source. Therefore in this region Ψ_n is given by

$$\Psi_n = Ae^{+ink\Delta x} + Be^{-ink\Delta x} \quad (3.24)$$

where A and B are the amplitudes of the right and left moving plane waves respectively. This wave function carries the current

$$j = \frac{\hbar}{m}k \left[|A|^2 - |B|^2 \right] . \quad (3.25)$$

The goal is to calculate A and B given Ψ_n . To this end we write Eq. (3.24) as

$$\begin{bmatrix} \Psi_n \\ \Psi_{n+1} \end{bmatrix} = M \begin{bmatrix} A \\ B \end{bmatrix}$$

where M is following matrix:

$$M = \begin{bmatrix} 1 & 1 \\ e^{+ik\Delta x} & e^{-ik\Delta x} \end{bmatrix} \begin{bmatrix} e^{+ikn\Delta x} & 0 \\ 0 & e^{-ikn\Delta x} \end{bmatrix} .$$

Therefore we can calculate A and B as follows:

$$\begin{bmatrix} A \\ B \end{bmatrix} = M^{-1} \begin{bmatrix} \Psi_n \\ \Psi_{n+1} \end{bmatrix} . \quad (3.26)$$

Of course this way of calculating the back reflected part of the wave function only works at a fixed energy μ , i.e. it only works when applied to scattering states. In time dependent calculations as done in Chap. 4 the wave function will be a superposition of many different energy components in general. To calculate the current in this case we have to use a finite difference version of Eq. (3.22):

$$j(n\Delta x + \frac{1}{2}\Delta x) = \frac{\hbar}{m} \text{Im} \left[\frac{\Psi_{n+1}^* + \Psi_n^*}{2} \frac{\Psi_{n+1} - \Psi_n}{\Delta x} \right] + \mathcal{O}((\Delta x)^2) . \quad (3.27)$$

If we calculate this discrete current for the wave function (3.24) we get

$$j = \frac{\hbar}{m} \frac{\sin(k\Delta x)}{\Delta x} \left[|A|^2 - |B|^2 \right] . \quad (3.28)$$

There is a difference of order $\mathcal{O}((\Delta x)^2)$ between this result and the continuous version (3.25). But in our calculations Δx is usually so small that this difference is negligible.

A disadvantage of Eq. (3.28) is that is not possible to individually calculate the amplitude of the back reflected part as it is possible with Eq. (3.26). All we can do is to calculate the back-reflected current as we know the incident current (from the normalization of the source) and the discrete current j .

3.4.4 A source in an semi-infinite strip

In Sec. 3.4.2 we studied the effect of a source term situated on a infinite lattice. But for the calculation of the self energy in Sec. 3.5.2 we will need the effect of a source term situated on a

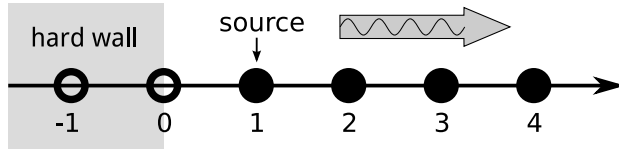


Figure 3.2: This figure illustrates Eq. (3.29). A point source is located at $n = 1$. Hard wall Dirichlet boundary conditions are applied for $n \leq 0$ while outgoing boundary conditions are applied for $n \rightarrow +\infty$ by use of the retarded Green function.

semi infinite lattice. This means hard wall Dirichlet boundary conditions are applied for $n \leq 0$ which implicates that $\Psi_n = 0$ for $n \leq 0$.

Again we have to calculate Ψ using the retarded Green function as in Sec. 3.4.2

$$\Psi = \lim_{\substack{\epsilon \rightarrow 0 \\ \epsilon > 0}} (\mu + i\epsilon - H)^{-1} S \quad (3.29)$$

where the source S is given by

$$S_n = \begin{cases} 1 & \text{for } n = 1 \\ 0 & \text{for } n \neq 1 \end{cases}$$

and H is the tight binding Hamiltonian (3.11) for a constant potential V . The boundary condition $\Psi_0 = 0$ is enforced on the left side. The whole situation is illustrated in Fig. 3.2. In components Eq. (3.29) reads:

$$\begin{aligned} (\mu - (2\alpha + V))\Psi_1 + \alpha\Psi_2 &= 1 & \text{for } n = 1 \\ (\mu - (2\alpha + V))\Psi_n + \alpha(\Psi_{n-1} + \Psi_{n+1}) &= 0 & \text{for } n > 1. \end{aligned} \quad (3.30)$$

Let us first assume that $\mu > V$. In this case we try following ansatz:

$$\Psi_n = C e^{ik\Delta x n}.$$

For $n > 1$ we can argue as in Sec. 3.4.2 that k must obey the dispersion relation (3.15). The reasoning that this ansatz fulfills the outgoing boundary conditions is also the same.

So we only have to look at $n = 1$ in Eq. (3.30):

$$\begin{aligned} \underbrace{(\mu - 2(\alpha + V))}_{-2\alpha \cos(k\Delta x)} C e^{ik\Delta x} + \alpha C e^{2ik\Delta x} &= 1 \\ \Rightarrow C \alpha e^{ik\Delta x} (-e^{-ik\Delta x} - e^{+ik\Delta x} + e^{+ik\Delta x}) &= 1 \\ \Rightarrow -C \alpha e^{ik\Delta x} e^{-ik\Delta x} &= 1 \\ \Rightarrow C &= -\frac{1}{\alpha}. \end{aligned}$$

This gives us the solution to Eq. (3.29):

$$\Psi_n = -\frac{1}{\alpha} e^{ik\Delta x n}.$$

In the case $\mu < V$ a similar ansatz results in

$$\Psi_n = -\frac{1}{\alpha} e^{-k\Delta x n}$$

where k is given by the dispersion relation (3.16).

The calculation done in this section is so useful because the result of Eq. 3.29 gives us the $(1, 1)$ -entry of the retarded Green function which we will need in Sec. 3.5.2:

$$\lim_{\substack{\epsilon \rightarrow 0 \\ \epsilon > 0}} [(\mu + i\epsilon - H)^{-1}]_{1,1} = G_{1,1}^{(r)} = \begin{cases} -\frac{1}{\alpha} e^{ik\Delta x} & \text{for } \mu > V \\ -\frac{1}{\alpha} e^{-k\Delta x} & \text{for } \mu < V \end{cases} \quad (3.31)$$

Here k is given by (3.15) for $\mu > V$ and by (3.16) for $\mu < V$.

The terms $e^{ik\Delta x}$ and $e^{-k\Delta x}$ will often be used for the self energy calculations of Sec. 3.5.2. Therefore we will give here expressions involving directly μ and V . These are obtained using the dispersion relations (3.15) and (3.16):

$$\begin{aligned} e^{ik\Delta x} &= \frac{2\alpha - (\mu - V) + i\sqrt{(\mu - V)(4\alpha - (\mu - V))}}{2\alpha} & \text{for } \mu > V, \\ e^{-k\Delta x} &= \frac{2\alpha - (\mu - V) - \sqrt{(V - \mu)(4\alpha - (\mu - V))}}{2\alpha} & \text{for } \mu < V. \end{aligned} \quad (3.32)$$

The case $\mu < V$ is of course a (properly chosen) analytic continuation of the case $\mu > V$. For the sake of simplicity we will therefore only make reference to the case $\mu > V$ in subsequent sections.

3.5 The Green function in the tight binding model

The major focus of this work are stationary scattering states. These can be calculated using the retarded Green function introduced in Sec. 3.2:

$$G^{(r)} = \lim_{\substack{\epsilon \rightarrow 0 \\ \epsilon > 0}} (\mu + i\epsilon - H)^{-1}. \quad (3.33)$$

Here H is a Hamiltonian discretized in a finite difference scheme (3.11).

The system we consider here is a one-dimensional setup with the following form (see Fig. 3.3):

- Below some position x_0 the potential is constant, so $V(x) = V_0$ for $x \leq x_0$. This we call the (semi-infinite) left lead.
- In the middle between x_0 and x_1 we have a possible non-constant potential. This we call the scattering region.
- Above some position x_1 the potential is constant. So $V(x) = V_1$ for $x \geq x_1$. This we call the (semi-infinite) right lead.

The system extends from $x = -\infty$ to $x = +\infty$. Because of its infinite size the system cannot directly be simulated on a computer. But in the end we are only interested in the restriction of the Green function (3.33) onto the scattering region. In order to calculate this restriction we handle the leads in a way which allows us to incorporate them into a modified finite (discrete) Hamiltonian for the scattering region.

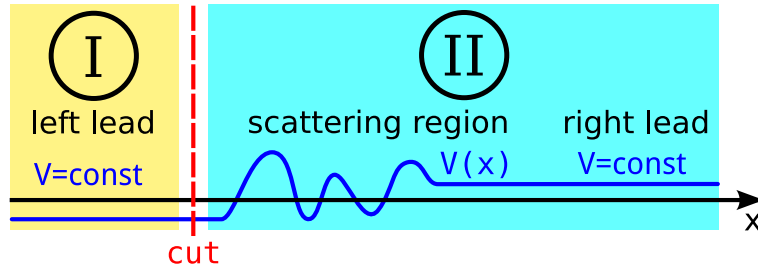


Figure 3.3: This figure shows a schematic description of our setup. In the middle we have a scattering region where the potential can be non-constant. To the left and to the right the potential is constant. These regions are called the left lead and the right lead which extend towards $-\infty$ or $+\infty$ respectively. In order to handle the left lead we cut the system into two regions called I and II. Region I consists of the left lead and region II consists of the scattering region and the right lead.

3.5.1 Handling of the left lead

We exemplarily show here how to handle the left lead. The first step is to split the system into two regions (see Fig. 3.3):

- Region I consists of the left lead.
- Region II consists of the scattering region and the right lead.

There exist two projection operators P_I and P_{II} onto these two regions I and II:

$$P_I(x) = \begin{cases} 1 & \text{for } x < x_0 \\ 0 & \text{for } x \geq x_0 \end{cases} \quad P_{II}(x) = \begin{cases} 0 & \text{for } x < x_0 \\ 1 & \text{for } x \geq x_0 \end{cases} \quad (3.34)$$

$$P_I^2 = P_I = P_I^\dagger \quad P_{II}^2 = P_{II} = P_{II}^\dagger \quad P_I + P_{II} = \mathbb{1}.$$

Using these one can split the Hamiltonian H into four parts:

$$H = \mathbb{1}H\mathbb{1} = (P_I + P_{II})H(P_I + P_{II}) = P_IHP_I + P_{II}HP_I + P_IHP_{II} + P_{II}HP_{II}.$$

We call $H_I = P_IHP_I$ the restriction of H onto region I. Similar $H_{II} = P_{II}HP_{II}$ is called the restriction of H onto region II. The operator $V = P_IHP_{II}$ is called the coupling operator. It mediates the coupling between region I and II. The adjoint operator is $V^\dagger = P_{II}HP_I$.

This splitting can be more clearly seen if we write H in matrix form:

$$H = \begin{bmatrix} H_I & V \\ V^\dagger & H_{II} \end{bmatrix}.$$

The numeration of the grid points is done in such a way that the points in region I come before the points in region II⁶.

⁶ A word of caution is warrantable here: Strictly speaking $H_I = P_IHP_I$ is a matrix of the same format as H . But from now on whenever H_I is considered as a part of a matrix it is understood as the restriction of P_IHP_I as a matrix onto region I. The same convention applies to the other matrices H_{II} , V and V^\dagger .

The ultimate goal is to calculate the retarded Green function (3.33) so the second step is to invert the matrix $(\mu - H)$. For the sake of simplicity from now on we include the small positive imaginary part ϵ of Eq. (3.33) into μ :

$$(\mu - H)^{-1} = \begin{bmatrix} \mu - H_I & -V \\ -V^\dagger & \mu - H_{II} \end{bmatrix}^{-1}. \quad (3.35)$$

We now use the formulas of App. D. Defining Schur's complement S (see [85, 179]) as

$$S = (\mu - H_{II}) - V^\dagger(\mu - H_I)^{-1}V$$

we can write the inverse of the matrix (3.35) as:

$$(\mu - H)^{-1} = \left[\begin{array}{c|c} (\mu - H_I)^{-1} & (\mu - H_I)^{-1}V S^{-1} \\ \hline +(\mu - H_I)^{-1}V S^{-1}V^\dagger(\mu - H_I)^{-1} & \left[\mu - H_{II} - V^\dagger(\mu - H_I)^{-1}V \right]^{-1} \end{array} \right]$$

So we finally can calculate the projection of $G^{(r)}$ onto region II:

$$\begin{aligned} G_{II}^{(r)} &= P_{II} G^{(r)} P_{II} = \left[\mu - H_{II} - V^\dagger(\mu - H_I)^{-1}V \right]^{-1} \\ &= [\mu - H_{II} - \Sigma_I]^{-1}. \end{aligned} \quad (3.36)$$

This projection will be called $G_{II}^{(r)}$ from now on.

Here we have introduced the so called self energy Σ_I :

$$\Sigma_I = V^\dagger(\mu - H_I)^{-1}V. \quad (3.37)$$

This is a finite matrix which encapsulates the whole effect of the semi-infinite left lead onto region II.

The fixation onto the *retarded* Green function, i.e. using an infinitely small positive part of μ as in Eq. (3.33), happens during the calculation of $(\mu - H_I)^{-1}$ which is used in the self energy (3.37). Therefore the energy μ in Eq. (3.36) can be chosen as a purely real number.

The derivation of Eq. (3.36) can be also accomplished using a Dyson equation as is shown in App. E.

3.5.2 Calculation of the self energy

In order to calculate the self energy we now make use of the tridiagonal structure of the matrix (3.12). Especially the matrix V has only one non-zero entry in the lower left as illustrated in following formula:

$$H = \begin{pmatrix} H_I & V \\ V^\dagger & H_{II} \end{pmatrix} = \begin{array}{cc} \begin{array}{c} \boxed{H_I} \\ 0 \end{array} & \begin{array}{c} 0 \\ \boxed{-\alpha} \end{array} \\ \begin{array}{c} 0 \\ \boxed{-\alpha^\dagger} \end{array} & \begin{array}{c} \boxed{H_{II}} \end{array} \end{array}$$

This simplifies the calculation of the self-energy (3.37) considerably.

$$H = \begin{pmatrix} (H_I)_{ij} & (V)_{ig} \\ (V^\dagger)_{fj} & (H_{II})_{fg} \end{pmatrix} = \begin{array}{cc} \begin{array}{c} \downarrow 1 \\ i \\ \downarrow m \\ 1 \\ f \\ \downarrow n \end{array} & \begin{array}{c} \xrightarrow{j} \xrightarrow{g} \\ 1 \quad m \quad 1 \quad n \end{array} \\ \begin{array}{cc} \boxed{(H_I)_{ij}} & \boxed{-\alpha \delta_{im} \delta_{g1}} \\ \boxed{-\alpha^\dagger \delta_{f1} \delta_{jm}} & \boxed{(H_{II})_{fg}} \end{array} \end{array}$$

We label the indices of the four parts of the matrix $\mu - H$ as shown in above formula. The indices i and j run from $1 \dots m$ and similar the indices f and g run from $1 \dots n$. Here δ_{ab} denotes the Kronecker delta symbol which is 0 for $a \neq b$ and 1 for $a = b$.

We now use Eq. (3.37) (and apply the Einstein summation convention)

$$\begin{aligned} (\Sigma_I)_{fg} &= [V^\dagger]_{fj} [(\mu - H_I)^{-1}]_{ji} V_{ig} \\ &= \alpha^\dagger \delta_{f1} \delta_{jm} [(\mu - H_I)^{-1}]_{ji} \alpha \delta_{im} \delta_{g1} \\ &= \alpha^\dagger [(\mu - H_I)^{-1}]_{mm} \alpha \delta_{f1} \delta_{g1} . \end{aligned}$$

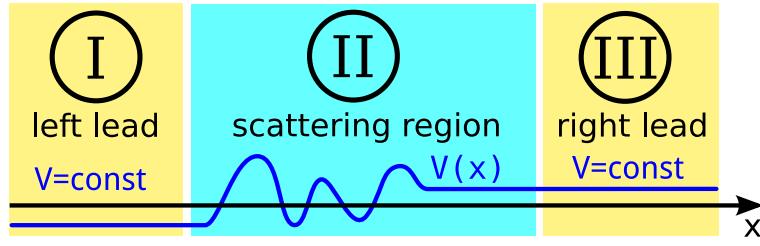


Figure 3.4: The complete system can be split into a scattering region and two attached leads which extend to $x \rightarrow +\infty$ and $x \rightarrow -\infty$ respectively. Inside the leads the potential is assumed to be constant.

This means that the self-energy matrix has only one non-zero entry in the upper left corner:

$$\Sigma_I = \begin{array}{|c|c|} \hline (\Sigma_I)_{11} & \\ \hline \hline & 0 \\ \hline \end{array}$$

We can go further and calculate $(\Sigma_I)_{11}$ explicitly using Eq. (3.31) (for $\mu > V_I$) and the fact that the lattice parameter α introduced in Eq. (3.10) is real:

$$(\Sigma_I)_{11} = \alpha^2 G_{mm}^{(r)} = -\alpha^2 \frac{1}{\alpha} e^{ik_1 \Delta x} = -\alpha e^{ik_1 \Delta x} .$$

Therefore we have now an explicit expression for the self energy:

$$(\Sigma_I)_{11} = -\alpha e^{ik_1 \Delta x} . \quad (3.38)$$

Here k_1 satisfies the dispersion relation (3.15) where the potential $V = V_I$ is the value of $V(x)$ in region I. Furthermore only the case $\mu > V_I$ is shown. In the case $\mu < V_I$ one has to use the appropriate term in Eq. (3.31).

Of special note is here that the whole effect of the left lead can be encapsulated into the self energy Σ which is essentially just a single complex number.

3.5.3 Handling of the right lead

The complete system can also be split into a scattering region, a left lead and a right lead as shown in Fig. 3.4. The same procedure which was applied to the left lead in Sec. 3.5.3 can now be applied to the right lead, too. The result is that the effect of the leads can be encapsulated into the two self energies Σ_I and Σ_{III} respectively. Using these two self energies we can now calculate the restriction of the Green function onto the scattering region:

$$G_{II}^{(r)} = P_{II} G^{(r)} P_{II} = [\mu - H_{II} - \Sigma_I - \Sigma_{III}]^{-1} .$$

Using now the explicit form of the one dimensional tight binding Hamiltonian (3.12) and the explicit form of the self energies (3.38) one arrives at following traditional matrix⁷:

$$\left[G_{\text{II}}^{(r)}\right]^{-1} = (\mu - 2\alpha)\mathbb{1} + \begin{bmatrix} -V_1 + \alpha e^{ik_I \Delta x} & \alpha & & & \\ \alpha & -V_2 & & & \\ & & \ddots & & \\ & & & -V_{n-1} & \alpha \\ & & & \alpha & -V_n + \alpha e^{ik_{\text{III}} \Delta x} \end{bmatrix}. \quad (3.39)$$

Here the self energies are colored in blue. The most important thing to note is that in order to take the effect of the leads into account we only have to modify the first and the last entry on the diagonal of the matrix. The whole effect of the leads can be encapsulated in just two complex numbers. We get k_I from dispersion relation (3.15) with the value of the potential $V = V_I$ in the left lead. k_{III} results from the same equation with the value of potential $V = V_{\text{III}}$ in the right lead.

3.6 Generalization to two dimensions

In Sec. 3.3 we described how to simulate the one dimensional Schrödinger equation. Here we apply the same principles to the two dimensional Schrödinger equation with following Hamilton operator:

$$H\Psi(x, y) = -\frac{\hbar^2}{2m} \left[\frac{\partial^2}{\partial x^2} + \frac{\partial^2}{\partial y^2} \right] \Psi(x, y) + V(x, y)\Psi(x, y). \quad (3.40)$$

The finite difference approximation (3.9) is applied once in the x -direction and once in the y -direction:

$$\begin{aligned} \left[\frac{\partial^2}{\partial x^2} + \frac{\partial^2}{\partial y^2} \right] \Psi(x, y) &= \frac{\Psi(x + \Delta x, y) + \Psi(x - \Delta x, y) - 2\Psi(x, y)}{(\Delta x)^2} \\ &+ \frac{\Psi(x, y + \Delta x) + \Psi(x, y - \Delta x) - 2\Psi(x, y)}{(\Delta x)^2} + \mathcal{O}((\Delta x)^2). \end{aligned}$$

Using this approximation we reduce the continuous system to a two dimensional rectangular lattice with the lattice spacing Δx . The discretized Hamilton operator (3.40) reads now

$$(H\Psi)_{(x,y)} = (4\alpha + V_{(x,y)}) \Psi_{(x,y)} - \alpha [\Psi_{(x+1,y)} + \Psi_{(x-1,y)} + \Psi_{(x,y+1)} + \Psi_{(x,y-1)}]. \quad (3.41)$$

Here (x, y) is an integer pair describing the point on the lattice and α is the lattice parameter (3.10). This tight binding Hamilton operator is illustrated in Fig. 3.5.

Hard wall Dirichlet boundary conditions may enforce that the wave function Ψ is zero in one or more given regions of the two dimensional plane. Therefore only lattice points where the wave function Ψ does not necessary vanish have to be taken into account in the tight binding Hamilton operator (3.39). Accordingly the lattice used in (3.39) may be of irregular shape.

As in Sec. 3.5.3 we can divide the system into a scattering region and an arbitrary number of attached leads. Again we will be only interested in projection of the Green function onto the scattering region. Therefore the leads will be again incorporated though self-energies as described in Sec. 3.6.1.

⁷Here n denotes the number of grid points inside the scattering region.

3.6.1 The two dimensional leads

In a two-dimensional system a lead is characterized by a semi-infinite propagating direction in which the transversal potential profile is constant. Therefore a separation ansatz will allow us to treat the two-dimensional lead as a superposition of one-dimensional leads.

In the framework of the tight binding Hamiltonian (3.41) there are only two natural choices for the extending direction, namely a direction parallel to the x axis or parallel to the y axis⁸. As an example in this section we look at a lead extending in the direction $x \rightarrow +\infty$. The lead is represented by a regular rectangular lattice having a finite size n in y direction and an infinite size towards $x \rightarrow +\infty$ as shown in Fig. 3.6.

We now divide the lead into vertical slabs. Each vertical slab \mathcal{H}_x (labeled by its horizontal position x) has a one-dimensional tight binding Hamiltonian given by Eq. (3.12) in y -direction attached to it:

$$\mathcal{H}_x = \begin{bmatrix} 2\alpha + V_{x,1} & -\alpha & & & \\ -\alpha & 2\alpha + V_{x,2} & & & \\ & & \ddots & & \\ & & & 2\alpha + V_{x,n-1} & -\alpha \\ & & & -\alpha & 2\alpha + V_{x,n} \end{bmatrix}. \quad (3.42)$$

Here x denotes the horizontal position of the slab and n denotes the number of lattice points in y -direction. Inside the lead the matrices \mathcal{H}_x do not depend on the index x as the vertical potential profile is assumed to be independent on x . The total two-dimensional tight binding

⁸See the notes in Sec. 3.10 for leads attached at arbitrary angles

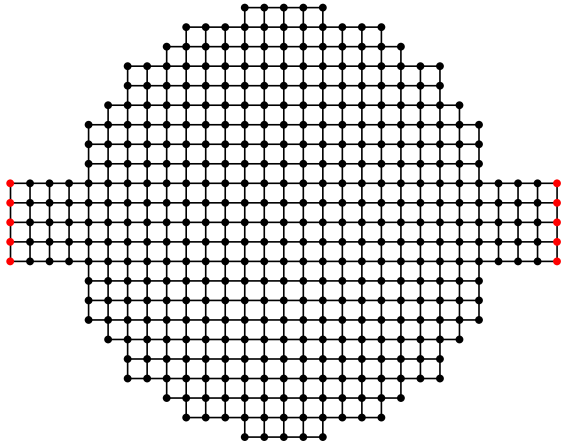


Figure 3.5: This figure illustrates the tight binding Hamilton operator (3.39). The circles represent the lattice points while the edges connecting neighboring lattice points represent non zero entries in the matrix of the Hamiltonian (3.39). The lattice may be of irregular shape due to hard wall Dirichlet boundary conditions. The red circles highlight the places where semi-infinite leads are attached using self-energies as described in Sec. 3.6.1.

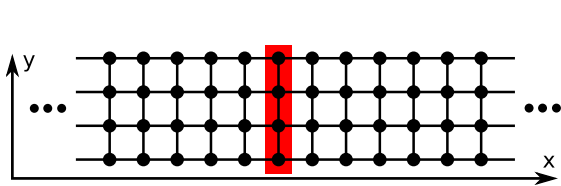


Figure 3.6: This figure illustrates a two dimensional lead extending towards $x \rightarrow +\infty$. It is represented by a regular rectangular two dimensional lattice. The lead is divided into vertical slabs; one such slab is shown here in red.

Hamiltonian (3.41) can now be build from such vertical slabs:

$$H = \begin{pmatrix} \ddots & & & & \\ & 2\alpha\mathbb{1} + \mathcal{H}_{x-1} & -\alpha\mathbb{1} & & \\ & -\alpha\mathbb{1} & 2\alpha\mathbb{1} + \mathcal{H}_x & -\alpha\mathbb{1} & \\ & & -\alpha\mathbb{1} & 2\alpha\mathbb{1} + \mathcal{H}_{x+1} & \\ & & & & \ddots \end{pmatrix}. \quad (3.43)$$

Each entry consists of a $n \times n$ matrix. The resulting matrix is block tridiagonal. Of course the form of this matrix depends on the scheme used to number the points in the regular grid. The system used here is to assign a point (x, y) the number $xn + y$ which first counts the position inside a vertical slab and then counts the position of the slab itself.

We now follow the reasoning of Sec. 3.5.1 only that now the matrix entries itself are square matrices instead of complex numbers. Attention must be paid to the non-commutativity of matrices, but this poses no problem. We can therefore calculate the projection of the retarded Green function onto the scattering region II as in Eq. (3.36):

$$G_{\text{II}}^{(r)} = [\mu - H_{\text{II}} - \Sigma_{\text{I}}]^{-1} \\ \Sigma_{\text{I}} = V^\dagger (\mu - H_{\text{I}})^{-1} V.$$

As in Sec. 3.5.2 the self-energy Σ_{I} has only one non-zero entry, only that now the entry itself is a $n \times n$ -matrix:

$$(\Sigma_{\text{I}})_{11} = \alpha^2 [(\mu - H_{\text{I}})^{-1}]_{11}.$$

In Σ_{I} the index 1 denotes the vertical slab in the scattering region neighboring the lead and in H_{I} the index 1 denotes the vertical slab in the lead neighboring the scattering region.

It remains to explicitly calculate $[(\mu - H_{\text{I}})^{-1}]_{11}$. To this end we use a separation ansatz for the wave function in the leads:

$$\Psi(x, y) = \sum_{j=1}^n a_n \chi_j(y) e^{ik_j x \Delta x}. \quad (3.44)$$

Here x and y are integer numbers labeling the horizontal and vertical position in the lead. The $\chi_j(y)$ are the eigenvectors of a vertical slab \mathcal{H} and the E_j are the corresponding eigenenergies:

$$\mathcal{H}\chi_j(y) = E_j\chi_j(y).$$

The matrix \mathcal{H} given by Eq. (3.42) is a real symmetric $n \times n$ matrix, therefore we get n real energies E_j and n corresponding real orthonormal eigenvectors $\chi_n(y)$. The normalization of the eigenvectors is chosen such that $\sum_{j=1}^n |\chi_j(y)|^2 = 1$ is satisfied.

The separation ansatz (3.44) splits the two dimensional lead into n one dimensional leads onto which the considerations of Sec. 3.4.4 and Sec. 3.5.2 can be applied separately. This gives us as a generalization of Eq. (3.38):

$$[(\Sigma_{\text{I}})_{11}]_{ab} = -\alpha \sum_{j=1}^n \chi_j(a) \chi_j(b) e^{ik_j \Delta x}. \quad (3.45)$$

We get k_j from dispersion relations (3.15) using $\mu - E_j$ instead of $\mu - V_{\text{lead}}$.

This self-energy matrix (3.45) has to be applied to the slab in the scattering region directly neighboring the lead, analogous to the considerations of Sec. 3.5.3.

3.6.2 Current measurement in two dimensions

The wave function in a region where the vertical potential profile $V(y)$ does not depend on x can be separated into vertical eigenmodes as in Eq. (3.44):

$$\Psi(x, y) = \sum_{j=1}^n \chi_j(y) \xi_j(x) . \quad (3.46)$$

For Green function calculations where the energy μ is well defined each $\xi_j(x)$ is a superposition of a left moving (e^{-ikx}) and right moving (e^{+ikx}) plane wave. Therefore the two dimensional problem splits into several one dimensional ones. Onto each eigenmode the considerations concerning the source normalization and the current measurement described in Sec. 3.4.3 can be applied separately. But we have to adjust the prefactors because in two dimensions the relevant quantity is the total current j in x direction:

$$j(x) = \frac{\hbar}{m} \int dy \operatorname{Im} \left[\Psi(x, y)^* \frac{\partial}{\partial x} \Psi(x, y) \right] .$$

Therefore a source S sitting located $x = x_0$ exciting the eigenmode l to carry the current j_0 would read (compare to Eq. (3.23))

$$S_l(x, y) = \chi_l(y) \delta_{x, x_0} \sqrt{\frac{j_0}{\Delta x} \frac{m}{\hbar k_l}} 2i\alpha \sin(k_l \Delta x) \quad (3.47)$$

using the normalization $\sum_{l=1}^n |\chi_l(y)|^2 = 1$. Similarly, the current measurement has to be adjusted.

The calculation of a wave function using a source term exciting the lead mode m and the subsequent measurement of the scattering amplitude in mode n can be summarized as the Fisher-Lee relations [50, 127] (see also Eq. (B.1))

$$\mathcal{S}_{n,m} = -\delta_{nm} + i\hbar \sqrt{v_n v_m} \int dy_m \int dy_n G^r \left(\begin{bmatrix} x_m \\ y_m \end{bmatrix}, \begin{bmatrix} x_n \\ y_n \end{bmatrix}, \mu \right) \chi_m(y_m) \chi_n(y_n) \quad (3.48)$$

here written in the continuum limit $\Delta x \rightarrow 0$ using $v = \hbar k/m$ and $\int dy |\chi(y)|^2 = 1$ and the retarded Green function G^r in the position basis. These relations describe how to calculate the scattering matrix \mathcal{S} from the Green function G^r . An in-depth discussion of the properties of the scattering matrix can be found in App. B.

3.6.3 Magnetic gauge field

In this section we will show how to describe the magnetic gauge field $\mathbf{A}(\mathbf{r})$ in the framework of the tight binding model. In the two-dimensional continuous Schrödinger operator

$$H = \frac{1}{2m} [-i\hbar \nabla - q\mathbf{A}]^2 + V , \quad (3.49)$$

this gauge field occurs through the minimal coupling replacement [186] $\mathbf{p} \rightarrow \mathbf{p} - q\mathbf{A}$ as the relation $\mathbf{p} = -i\hbar \nabla$ holds. To apply this replacement to the tight-binding model we note that \mathbf{p} is the generator of the translation operator:

$$\Psi(\mathbf{r} + \boldsymbol{\epsilon}) = \exp \left[+\frac{i}{\hbar} \boldsymbol{\epsilon} \cdot \mathbf{p} \right] \Psi(\mathbf{r}) .$$

Therefore in one dimension we can rewrite the tight binding form of the Schrödinger equation (3.11) in the following way (here p_x and A_x denote the x -component of \mathbf{p} and \mathbf{A} respectively):

$$\begin{aligned} \frac{1}{2m} [p_x]^2 \Psi(x) &= \alpha [2\Psi(x) - \Psi(x + \Delta x) - \Psi(x - \Delta x)] + \mathcal{O}((\Delta x)^2) \\ &= \alpha \left[2 - \exp \left[+\frac{i}{\hbar} \Delta x p_x \right] - \exp \left[-\frac{i}{\hbar} \Delta x p_x \right] \right] \Psi(x) + \mathcal{O}((\Delta x)^2) . \end{aligned}$$

Assuming for a moment that A_x is independent of x we can now apply the minimal coupling replacement giving us

$$\begin{aligned} \frac{1}{2m} [p_x - qA_x]^2 \Psi(x) &= 2\alpha\Psi(x) - \alpha \exp \left[-\frac{i}{\hbar} \Delta x q A_x \right] \exp \left[+\frac{i}{\hbar} \Delta x p_x \right] \Psi(x) \\ &\quad - \alpha \exp \left[+\frac{i}{\hbar} \Delta x q A_x \right] \exp \left[-\frac{i}{\hbar} \Delta x p_x \right] \Psi(x) + \mathcal{O}((\Delta x)^2) . \end{aligned}$$

Some corrections to this formula are necessary because A_x may depend on x . The details are worked out in App. F.

Applying the same considerations to the y direction we get the tight binding discretization of the continuous two dimensional Schrödinger equation (3.49) with a magnetic gauge field [50]:

$$\begin{aligned} (H\Psi)_{(x,y)} &= (4\alpha + V_{(x,y)}) \Psi_{(x,y)} \\ &\quad - \alpha \exp \left[i \frac{q}{\hbar} \int_{(x+1,y)}^{(x,y)} \mathbf{A}(\mathbf{r}) d\mathbf{r} \right] \Psi_{(x+1,y)} - \alpha \exp \left[i \frac{q}{\hbar} \int_{(x-1,y)}^{(x,y)} \mathbf{A}(\mathbf{r}) d\mathbf{r} \right] \Psi_{(x-1,y)} \\ &\quad - \alpha \exp \left[i \frac{q}{\hbar} \int_{(x,y+1)}^{(x,y)} \mathbf{A}(\mathbf{r}) d\mathbf{r} \right] \Psi_{(x,y+1)} - \alpha \exp \left[i \frac{q}{\hbar} \int_{(x,y-1)}^{(x,y)} \mathbf{A}(\mathbf{r}) d\mathbf{r} \right] \Psi_{(x,y-1)} . \end{aligned} \quad (3.50)$$

This is the most natural generalization of the tight binding Hamiltonian (3.41) to include a magnetic gauge field. Here (x, y) is a integer pair describing the point on the lattice. The integral $\int_b^a \mathbf{A}(\mathbf{r}) d\mathbf{r}$ is taken along the edge connecting the two neighboring lattice points a and b .

In Eq. (3.50) the gauge field only affects the phase of the coupling matrix elements while their modulus remains the same. This phase factor $\exp \left[i \frac{q}{\hbar} \int_b^a \mathbf{A}(\mathbf{r}) d\mathbf{r} \right]$ of the coupling matrix element (a, b) is called a Peierls phase [163].

One should mention that for a non-vanishing gauge field \mathbf{A} the definition of the probability current density (3.22) has to be modified (see also Eq. (B.21)) [50]:

$$\mathbf{j}(\mathbf{r}) = \frac{\hbar}{m} \text{Im} [\Psi(\mathbf{r})^* \nabla \Psi(\mathbf{r})] - \frac{q}{m} \mathbf{A}(\mathbf{r}) |\Psi(\mathbf{r})|^2 . \quad (3.51)$$

3.6.4 Selection of the gauge field

In three dimensions the well known relation $\mathbf{B} = \nabla \times \mathbf{A}$ holds which gives the magnetic field in terms of the gauge field. This relation can be reduced to two dimensions. It now relates the two dimensional gauge field

$$\mathbf{A}(x, y) = \begin{bmatrix} A_x(x, y) \\ A_y(x, y) \end{bmatrix} \quad (3.52)$$

to the out of plane magnetic field

$$B(x, y) = \frac{\partial A_y}{\partial x}(x, y) - \frac{\partial A_x}{\partial y}(x, y) . \quad (3.53)$$

Normally the magnetic field is given and one has to calculate a corresponding gauge field. This gauge field is not uniquely determined because one can add the gradient of an arbitrary function to the gauge field (3.52) without alternating the corresponding magnetic field (3.53). But there are two natural ways to choose a gauge field:

$$\mathbf{A}(x, y) = \begin{bmatrix} -\int_0^y B(x, y') dy' \\ 0 \end{bmatrix} \quad \mathbf{A}(x, y) = \begin{bmatrix} 0 \\ +\int_0^x B(x', y) dx' \end{bmatrix} .$$

The integrals occurring here are understood as line integrals parallel to the corresponding axes.

The self energy (3.45) cannot be used to describe a lead with a magnetic field inside it. While it is possible to derive improved self energies describing a lead with a magnetic field we have chosen not to use these improved self energies for the reasons explained in Sec. 3.10. Therefore we always switch off the magnetic field adiabatically inside the leads allowing us to use the normal self energies (3.45). This is no strong approximation as we will be always using weak magnetic fields whose influence onto the wave function in the leads is negligible because of their big cyclotron radii compared to the width of the leads.

Most systems considered in this work are orientated along the x axis. For these systems we use following functional dependence of the magnetic field:

$$B(x, y) = B\xi(x) .$$

Here B is a real number giving the strength of the magnetic field and $\xi(x)$ is the characteristic function of the scattering region constructed using the method described in App. H. $\xi(x)$ is one inside the scattering region and zero in the leads for $x \rightarrow \pm\infty$. The switching from zero to one is done over a few wavelengths of a typical wave function. This gives us two standard choices for a gauge field:

$$\mathbf{A}(x, y) = -By\xi(x) \begin{bmatrix} 1 \\ 0 \end{bmatrix} \quad (3.54)$$

$$\mathbf{A}(x, y) = B \int_0^x \xi(x') dx' \begin{bmatrix} 0 \\ 1 \end{bmatrix} . \quad (3.55)$$

While for the most part of this work we use the gauge field (3.54) the gauge field (3.55) has its use for the split operator time propagation scheme presented in Sec. 4.5.

3.7 Exterior complex scaling boundary conditions

The self-energy boundary conditions discussed in Sec. 3.5.1 work only for a given fixed energy μ . If one changes the energy μ one must change the self energy Σ (given by Eq.(3.38)) describing the infinite leads, too. A more powerful tool will be the boundary conditions discussed in this section. These new boundary conditions will be able to handle a wide interval of energies at once without need to change them when varying the energy μ . That way one can also use them as

absorbing boundary conditions for time dependent simulation of the Gross-Pitaevskii equation as we will discuss in Chap. 4. Furthermore using this boundary conditions it is possible to calculate complex resonance energies for the linear scattering problem as discussed in Sec. 3.7.2. Last but not least they are essential to determine if a non-linear scattering state is dynamically stable or unstable as discussed in Sec. 5.7.

In order to develop the new boundary conditions we note that after separation of the lead eigenmodes the leads themselves are described by the one-dimensional free particle Hamiltonian

$$H = -\frac{\hbar^2}{2m} \frac{\partial^2}{\partial x^2} . \quad (3.56)$$

Solutions of the time independent Schrödinger equation using this Hamiltonian for a fixed energy μ ($\mu \in \mathbb{R}$ and $\mu > 0$) are given by a superposition of in- and outgoing plane waves:

$$\begin{aligned} H\Psi &= \mu\Psi = \frac{\hbar^2 k^2}{2m} \Psi \quad (\text{with } k > 0) \\ \Psi(x) &= Ae^{+ikx} + Be^{-ikx} = A\Psi_{\text{out}}(x) + B\Psi_{\text{in}}(x) . \end{aligned} \quad (3.57)$$

We assume here that the lead extends towards the direction $x \rightarrow \infty$.

The leads are characterized by the condition that only outgoing plane waves are allowed as solutions. Therefore one seeks for boundary conditions enforcing $B = 0$. As in Sec. 3.4.2 the crucial idea is to transform the outgoing plane waves to decaying exponentials (for $x \rightarrow \infty$) and the ingoing plane waves to rising exponentials. While in Sec. 3.4.2 this was accomplished by making the energy μ complex we use here the method of complex scaling [2, 14] which rotates the x coordinate into the complex plane. More precisely, the complex scaling method replaces x by $e^{i\theta}x$ where θ is a real parameter in the range $0 < \theta < \frac{\pi}{2}$. This rotation transforms the plane waves from Eq. (3.57) into the functions

$$\Psi_{\text{out}}(e^{i\theta}x) = e^{+ike^{i\theta}x} \quad \text{and} \quad \Psi_{\text{in}}(e^{i\theta}x) = e^{-ike^{i\theta}x}$$

which have the desired form because the condition $\text{Im}(ke^{i\theta}) \geq 0$ is fulfilled. While the now exponential decaying outgoing solutions Ψ_{out} are elements of the Hilbert space $L^2(\mathbb{R})$ the exponential rising (for $x \rightarrow \infty$) ingoing solutions Ψ_{in} are no elements of this Hilbert space (they are not even bounded) and therefore have to be excluded which enforces $B = 0$.

Except in special cases the scattering potential cannot be evaluated at complex coordinates. Therefore we want to restrict the rotation of the x coordinate to the leads while keeping the usual x coordinate inside the scattering region. To this end we introduce a coordinate transformation from the old variable x to a new variable z (with $z \in \mathbb{R}$)

$$x = F(z)$$

where $F(z)$ is a given function with the behavior:

$$\begin{aligned} F(z) &\rightarrow e^{i\theta}z & \text{for } z \rightarrow \infty \\ F(z) &= z & \text{for } z \text{ inside the scattering region} . \end{aligned} \quad (3.58)$$

This is called the method of (smooth) exterior complex scaling [150] which is illustrated in Fig. 3.7. In this work the coordinate transformation $F(z)$ is chosen as

$$F(z) = \int_{z_0}^z f(z') dz' \quad (3.59)$$

$$\text{with} \quad f(z) = 1 + (e^{i\theta} - 1) u(z) \quad (3.60)$$

Here $u(z)$ is a switching function (as explained in App. H) smoothly rising from zero in the scattering region to one in the leads over a given distance ΔL .

The Hamiltonian (3.56) is now transformed to the variable z . Introducing the derivative of F as

$$f(z) = \frac{\partial F}{\partial z} = \frac{\partial x}{\partial z}$$

one can transform the derivative operator $\frac{\partial}{\partial x}$ to the new coordinate z :

$$\frac{\partial}{\partial x} = \frac{\partial z}{\partial x} \frac{\partial}{\partial z} = \frac{1}{f(z)} \frac{\partial}{\partial z}.$$

The second derivative $\frac{\partial^2}{\partial x^2}$ can be transformed analogously:

$$\frac{\partial^2}{\partial x^2} = \frac{1}{f(z)} \frac{\partial}{\partial z} \left(\frac{1}{f(z)} \frac{\partial}{\partial z} \right) = \frac{1}{f(z)^2} \frac{\partial^2}{\partial z^2} - \frac{f'(z)}{f(z)^3} \frac{\partial}{\partial z}.$$

This gives us the Hamiltonian (3.56) expressed in the new coordinate z :

$$H = -\frac{\hbar^2}{2m} \left[\frac{1}{f(z)^2} \frac{\partial^2}{\partial z^2} - \frac{f'(z)}{f(z)^3} \frac{\partial}{\partial z} \right]. \quad (3.61)$$

After applying this transformation we truncate the lead to a finite length L by using the hard wall Dirichlet boundary conditions $\Psi(F(L)) = 0$. This leads to some reflection as follows from

$$\Psi(F(L))=0=Ae^{+ikF(L)} + Be^{-ikF(L)} \implies B = -Ae^{2ikF(L)} \sim -A \exp[2ike^{i\theta}L]. \quad (3.62)$$

Therefore the truncated leads do not enforce $B = 0$ but nevertheless one can make the reflected part arbitrary small by increasing the length L . Thus the unwanted incoming solutions Ψ_{in} can

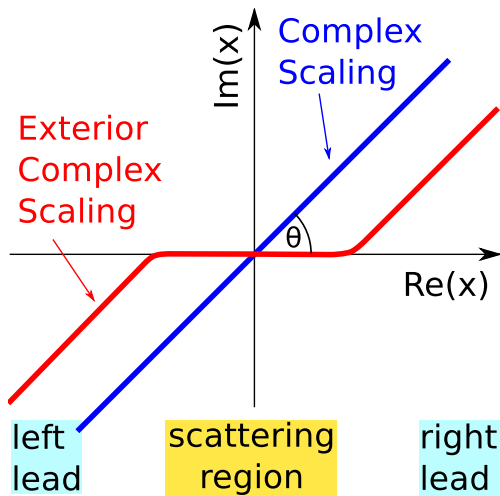


Figure 3.7: This figure illustrates the method of complex scaling. The usual complex scaling method (here shown in blue) simply rotates the whole x coordinate into the complex plane. The exterior complex scaling method (shown in red) keeps the x coordinate unchanged inside the scattering region while inside the leads the x coordinate is rotated into the complex plane, too.

be exponentially suppressed. As $0 < \theta < \frac{\pi}{2}$ this reasoning also works in the case $\mu < 0$ where we have the complex wave vector $k = i\sqrt{-\frac{2m}{\hbar^2}\mu}$. But the method ceases to be efficient for small values of the modulus of μ because the length L necessary to archive a given suppression scales as $\frac{1}{\sqrt{|\mu|}}$. This behavior is investigated in more detail in Sec. 3.7.1.

This Hamiltonian (3.61) is now discretized using the finite difference approximation for the first and second derivative as given in Eq. (3.9):

$$\begin{aligned} \{H\Psi\}_n = & \frac{\hbar^2}{2m(\Delta x)^2} \frac{1}{f(n\Delta x)^2} [2\Psi_n - \Psi_{n-1} - \Psi_{n+1}] \\ & + \frac{\hbar^2}{4m\Delta x} \frac{f'(n\Delta x)}{f(n\Delta x)^3} [\Psi_{n-1} - \Psi_{n+1}] + \mathcal{O}((\Delta x)^2). \end{aligned} \quad (3.63)$$

Inside the scattering region this is the normal tight binding approximation of the free particle Hamiltonian as given in Eq. (3.11) while inside the lead the kinetic energy term is modified in such a way that it damps outgoing plane waves and suppresses incoming plane waves and thus is able to describe the effect of the lead using only a region of finite length L . This Hamiltonian (3.63) will be henceforth denoted as the exterior complex scaling boundary conditions (abbr. “*ECSBC*” henceforth). This boundary conditions do not depend on the energy μ and therefore work simultaneously for a wide range of energies. But this flexibility comes at a price as one has to extend the lattice grid representing the system by the length L in comparison to a calculation using the self energy boundary conditions (3.36) (abbr. “*SEBC*”). Furthermore the *SEBC* work perfectly (in the framework of the tight binding model) for a fixed energy μ while the *ECSBC* work only approximatively (but this over a wide energy interval). The accuracy of the *ECSBC* will be investigated in more detail in Sec. 3.7.1.

In a two-dimensional system the *ECSBC* (3.63) is only used in the coordinate giving the direction of the lead while the transversal coordinate axes still uses the usual discretized form of the Hamiltonian as in Eq. (3.11). In such a system one can illustrate the usefulness of a boundary condition working for more than one energy at once. For example if one calculates the Green function $(\mu - H)^{-1}$ the boundary conditions have to work simultaneously for all energies $\mu - E_n$ where the E_n are the energies of the lead eigenmodes as one sees after a separation of the wave function in longitudinal and transversal components. But as we already have the perfectly working⁹ self energy boundary condition (3.36) for Green function calculations, the main use of the *ECSBC* are resonance calculations (Sec. 3.7.2), time dependent simulations (Chap. 4) and stability analysis (Sec. 5.7)¹⁰.

The Hamiltonian given in Eq. (3.63) is an asymmetric tridiagonal matrix

$$H = \begin{pmatrix} a_1 & b_2 & & \\ c_2 & a_2 & b_3 & \\ & c_3 & a_3 & \\ & & & \ddots \end{pmatrix}. \quad (3.64)$$

For certain applications (e.g. the complex symmetric Lanczos algorithm [46]) a complex sym-

⁹In the framework of the tight-binding model.

¹⁰The main points against usage of the *ECSBC* for the Green function are: They increase the lattice and thus calculation time and they are only approximatively correct.

metric form of this matrix is preferable¹¹. In this cases one defines the transformation

$$\Omega = \text{diag}(\omega_1, \omega_2, \omega_3, \dots) = \text{diag}(1, \frac{c_2\omega_1}{b_2}, \frac{c_3\omega_2}{b_3}, \dots)$$

and uses $\Omega^{-\frac{1}{2}}H\Omega^{+\frac{1}{2}}$ instead of H . This transformation only affects the grid points inside the lead.

3.7.1 Accuracy of the exterior complex scaling boundary conditions

The accuracy of the exterior complex scaling boundary conditions is now tested using a model system. One uses a one dimensional lattice of length L_0 and lattice spacing Δx representing the discretized Schrödinger equation (3.11) with a flat potential $V(x) = 0$. While on the left side of the system hard wall Dirichlet boundary conditions are imposed, one attaches a lead to the right side. A source vector S is introduced which is zero on all lattice point except the leftmost point on the lattice. This is the same system as used in Sec. 3.4.4 and shown in Fig. 3.2.

The lead is either attached using the *SEBC* (3.36) or one extends the lattice by the length L and applies the *ECSBC* (3.63) in this region. One now compares the two wave functions Ψ_{SE} and Ψ_{ECSBC} calculated as the Green function $\Psi = (\mu - H)^{-1}S$ using the two different boundary conditions. In the framework of the tight binding model the *SEBC* are exact. Therefore one introduces ε as a measure for the error of the *ECSBC*

$$\varepsilon = \max_n \frac{|\Psi_{SE,n} - \Psi_{ECSBC,n}|}{|\Psi_{SE,n}|}. \quad (3.65)$$

Here n numerates the lattice points situated in the region of length L_0 .

For small values of μ the truncation error calculated in (3.62) dominates ε

$$\varepsilon = e^{-2i\text{Im}F(L)} \sim e^{-2kL \sin \theta} \quad (3.66)$$

as shown in Fig. 3.8a and Fig. 3.9a. This means that the *ECSBC* breaks down if the wavelength $\lambda = \frac{2\pi}{k}$ becomes comparable to the size L of the exterior complex scaling region.

For large values of μ the discretization error introduced in Eq. (3.63) which is of order $\mathcal{O}((\Delta x)^2)$ dominates ε as seen in Fig. 3.8b and Fig. 3.9b.

The discretization error $\mathcal{O}((\Delta x)^2)$ is also the reason that the error ε depends for large values of μ on the length of the switching region ΔL as shown in Fig. 3.9d. The switching should be done over a region consisting of at least 30 lattice points to get good results. In connection with this one notes that for large values of μ the error shows a wrong dependence on θ as seen in Fig. 3.9c. This is also due to the discretization error because the larger θ is the larger is the change in x over the switching region ΔL . In numerical calculations one regards the error as a function of μ and optimizes the parameters θ, L and ΔL such that the exterior complex scaling boundary conditions work satisfactory over the desired energy range. This is shown in Fig. 3.9.

Special attention has to be paid that in the actual calculations the possible values of the modulus of μ do not become too small because then the *ECSBC* break down as follows from Eq. (3.66). Therefore in two dimensional systems the studied energies μ must have a certain minimal distance to the energies of the lead eigenmodes.

¹¹ Complex symmetry is defined by $H_{n,m} = H_{m,n}$. This is to be contrasted with complex hermitian symmetry which is given by $H_{n,m} = H_{m,n}^*$

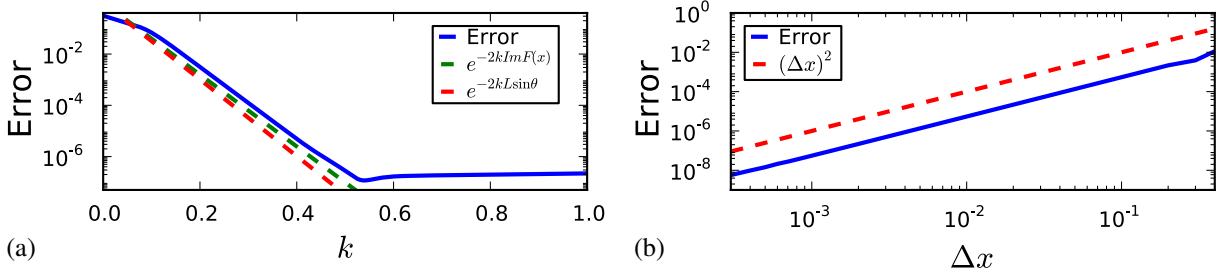


Figure 3.8: These figures show the error ε (defined in Eq. (3.65)) as a function of the wave vector k and of the lattice spacing Δx in (a) and (b) respectively. For small values of k the error ε behaves like the exponential function in k given by Eq. (3.66) and shown in (a) as a red and green dashed curve. The simple formula $\varepsilon \sim e^{-2kL\sin\theta}$ does not take the switching length ΔL into account and therefore the agreement is inferior to the other formula. For larger values of k the error ε is dominated by the discretization error which scales as $(\Delta x)^2$ (see Eq. (3.63)). Both figures use the dimensionless unit system $\hbar = m = 1$. In these units the parameters for (a) are $L = 24, \Delta L = 3, \theta = 0.8$ and $\Delta x = 0.002$. The parameters for (b) are $L = 12, \Delta L = 3, \theta = 0.8$ and $\mu = 1$. Of course one might need to transform these values into a different unit system.

On the other hand the error ε introduced in Eq. (3.65) is a relative measure which compares the error of the wave function with the wave function itself. If one introduces instead the alternative error measure

$$\tilde{\varepsilon} = \frac{\max_n |\Psi_{SE,n} - \Psi_{ECSBC,n}|}{\max_n |S_n|} \quad (3.67)$$

which compares the error of the wavefunction with the source term it is shown in Fig. 3.9a that $\tilde{\varepsilon}$ stays bounded even when $|\mu|$ becomes pretty small. Therefore one should not worry too much about the case $\mu = 0$.

The results obtained for the model system used in this section are representative for all scattering systems because in the end the only thing that matters is what fraction of a plain wave is reflected back by the exterior complex scaling boundary conditions.

3.7.2 Resonances

Transmission spectra can be best understood in terms of “resonances”. In this section we will explain what resonances are and they can be calculated. We will give here only a rough summary of the main results. See [150, 173, 198] for more details and proofs of the statements given here.

As the spectrum of the selfadjoint Hamilton operator H given by Eq. (3.1) (acting in the usual way on $L(\mathbb{R}^m)$; no complex rotation is performed at this stage) is purely real the Green function

$$G(\mu) = [\mu - H]^{-1}$$

is a holomorphic function of μ in the upper complex half plane $\mathbb{H}^+ = \{z \in \mathbb{C} | \text{Im} z > 0\}$. The continuous spectrum of H consists of $\sigma_c = \{x \in \mathbb{R} | x > 0\}$ (and zero which is excluded here for technical reasons) assuming the condition $\lim_{r \rightarrow \infty} V(r) = 0$ is fulfilled. We can now perform an analytic continuation of $G(\mu)$ coming from \mathbb{H}^+ over the semi-infinite line given by σ_c into the lower half plane $\mathbb{H}^- = \{z \in \mathbb{C} | \text{Im} z < 0\}$. This continuation will be called $G^c(\mu)$ henceforth. This G^c does not coincide with G evaluated at $\mu \in \mathbb{H}^-$, so σ_c represents a branch cut of the holomorphic function $G(\mu)$. Of course G^c evaluated at $\mu \in \sigma_c$ gives the retarded Green function G^r .

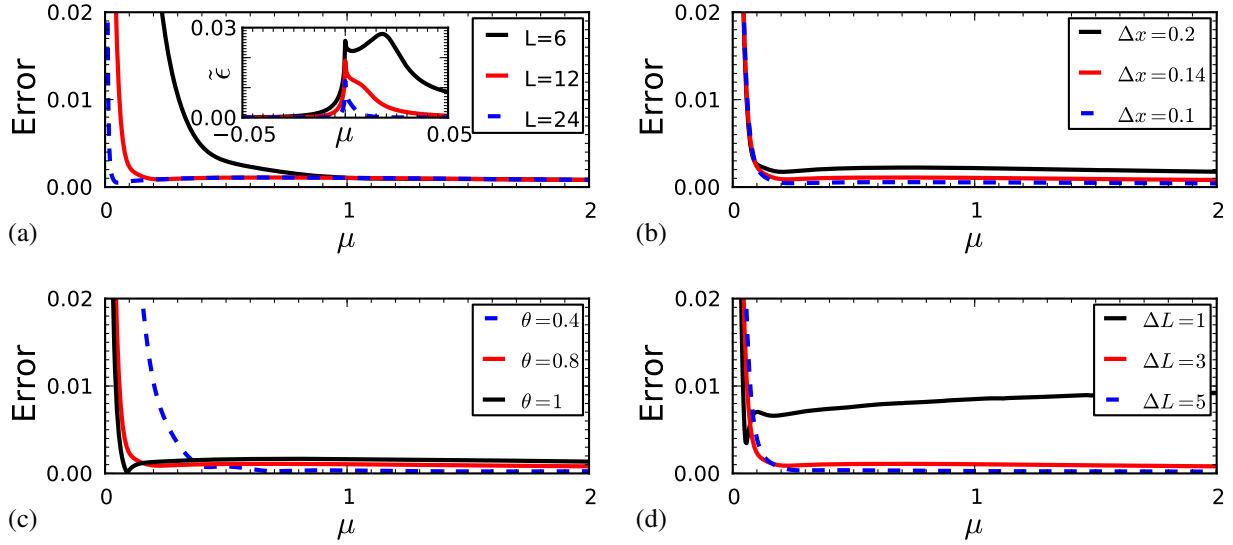


Figure 3.9: These figures show the error ε (defined in Eq. (3.65)) as a function of μ for different parameter sets. One uses here the same unit system as in Fig. 3.8. The base parameter set is $L = 12, \Delta L = 3, \theta = 0.8$ and $\Delta x = 0.14$. This set works well for $0.1 \leq \mu \leq 2$ where the error ε is always below 0.003. In each subfigure one of this parameters is varied. The inset in (a) shows $\tilde{\varepsilon}$ (defined in Eq. (3.67)) as a function of μ . One sees that $\tilde{\varepsilon}$ is always below 0.02 for this parameter set.

So one must regard $G(\mu)$ as a holomorphic function on a Riemann surface. In more complicated systems where several continua open at different thresholds the Green function $G(\mu)$ has multiple branch cuts.

The analytic continuation $G^c(\mu)$ can have poles in \mathbb{H}^- . We now define the resonances (sometimes also called Siegert resonances [192]) as the location of these poles. The method of complex scaling introduced in Sec. 3.7 can now be used to calculate these resonances. Let $\mathcal{E} = \frac{\hbar^2 \mathcal{K}^2}{2m}$ be such a resonance with the complex wave vector \mathcal{K} and the asymptotic behavior $\Psi_{\mathcal{E}}(x) \rightarrow e^{i\mathcal{K}x}$ for $x \rightarrow \infty$. \mathcal{K} can be written as $\mathcal{K} = |\mathcal{K}|e^{-i\vartheta}$ with the angle ϑ ($0 < \vartheta < \frac{\pi}{2}$) which implies $\mathcal{E} = \frac{\hbar^2 |\mathcal{K}|^2}{2m} e^{-2i\vartheta}$. If we now rotate the x-coordinate into the complex plane using the complex scaling $x \mapsto e^{i\theta} x$ the asymptotic behavior of the resonance becomes $\Psi_{\mathcal{E}}(x) \rightarrow \exp[ie^{i(\theta-\vartheta)} |\mathcal{K}| x]$. Therefore if the condition $\theta > \vartheta$ is fulfilled the resonance becomes a bound state which can be calculated as the eigenvalue of the complex scaled Hamiltonian H_{θ} . If $\theta < \vartheta$ the resonance is not visible and cannot be calculated. The continuous spectra of the complex scaled Hamiltonian H_{θ} corresponds to scattering states which stay bounded for $x \rightarrow \infty$ but do not decay which implies that the complex wave vector \mathcal{K} of these continuum states has a phase of $e^{-i\theta}$.

Therefore we have the situation depicted in Fig. 3.10. The continuous spectra of H_{θ} is rotated by the angle 2θ into the lower half of the complex plane (i.e. \mathcal{H}^-) by the complex scaling $x \mapsto e^{i\theta} x$. Only the resonances which are situated in the wedge between the rotated continuum and the real axis σ_c are visible and can be calculated as bound states of the complex scaled Hamiltonian H_{θ} . While the resonance energies do not depend on θ once they are visible, the continuum state energies vary with θ , enabling us to distinguish between resonances and continuum states. Furthermore the modulus of a resonance wavefunction is big inside the cavity and decays inside the leads; for the continuum states it is the other way round, giving us a further tool to distinguish them.

In order to calculate the resonances numerically we have to use iterative eigenvalue methods because the involved matrices are too big for direct methods to calculate the eigenvalues. For the biggest system studied here the matrices are of dimension 150000×150000 . Here we use a shift-invert method in combination with the implicit restarted Arnoldi method as realized in the software library *ARPACK* [130, 194]. This means we select a target energy \tilde{E} and apply the Arnoldi method to $(\tilde{E} - H_\theta)^{-1}$. This gives us all eigenvalues of H_θ in the vicinity of \tilde{E} . An alternative to the Arnoldi method is the complex symmetric Lanczos method [46] which is not used here because of its inferior numerical stability.

Exterior complex scaling has been used before to calculate resonances of billiard type systems [109, 165]. But in these works they use a finite element method in combination with sharp exterior complex scaling while we use the finite difference method in combination with the smooth exterior complex scaling (3.63).

The *normal* complex scaling method has been also used before in the context of Bose-Einstein condensates [183, 184, 207]. But the *normal* complex scaling method is not well suited for the Gross-Pitaevskii equation (2.17) because the interaction term $g(\mathbf{r}) |\Psi(\mathbf{r})|^2 \Psi(\mathbf{r})$ uses the complex conjugate wavefunction $\Psi(\mathbf{r})^*$. The effect of the complex rotation onto $\Psi(\mathbf{r})^*$ is hard to calculate and furthermore the procedure is numerically unstable. On the other side the *exterior* complex scaling method does not suffer from this problems because the complex rotation is done in the leads where the interaction strength $g(\mathbf{r})$ is switched off (see Sec. 5.1.2). Inside the scattering region where $g(\mathbf{r})$ is nonzero the wavefunction $\Psi(\mathbf{r})$ is not altered. Therefore the *exterior* complex scaling method is better suited for the Gross-Pitaevskii equation.

The main usefulness of the resonances stems from the fact that we can perform an eigenvector decomposition of H_θ [118]:

$$H_\theta = \sum_n \mathcal{E}_n |\Psi_n\rangle \langle \Psi_n| + \int d\mathcal{E}_\theta \mathcal{E}_\theta |\Psi_{\mathcal{E}_\theta}\rangle \langle \Psi_{\mathcal{E}_\theta}|$$

Here the \mathcal{E}_n are the bound and resonance energies and the \mathcal{E}_θ are the continuum energies. The vectors $|\Psi_n\rangle$ and $|\Psi_{\mathcal{E}_\theta}\rangle$ are the corresponding resonance wavefunctions. Because H_θ is only

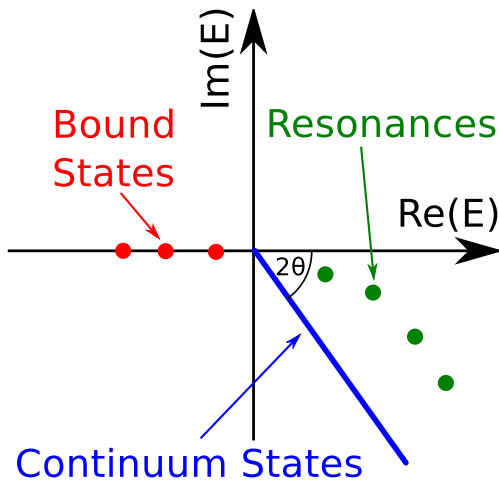


Figure 3.10: This figure illustrates the spectrum of the complex scaled Hamiltonian H_θ . The bound state energies are not affected by the complex scaling whereas the continuous part of the spectrum is rotated by an angle of 2θ into the complex plane. The resonances are located in the lower right half of the complex plane $\{z \in \mathbb{C} | \text{Re}z > 0 \text{ and } \text{Im}z < 0\}$. Only the resonances inside wedge between the rotated continua and the positive real axes are visible and have to be taken into account. Once these resonance energies are visible they do not depend on θ .

complex symmetric¹² instead of selfadjoint we have to use the indefinite inner product

$$(\psi|\chi) = \int d\mathbf{r} \psi(\mathbf{r}) \chi(\mathbf{r})$$

which has a few unpleasant mathematical properties (i.e. existence of non-zero vectors of pseudo-norm zero) but otherwise can be used similar to the usual (definite) hermitian scalar product. Similarly the (retarded) Green function can be written as

$$[\mu - H]^{-1} = \sum_n \frac{1}{\mu - \mathcal{E}_n} |\Psi_n\rangle \langle \Psi_n| + \int d\mathcal{E}_c \frac{1}{\mu - \mathcal{E}_c} |\Psi_{\mathcal{E}_c}\rangle \langle \Psi_{\mathcal{E}_c}|.$$

As the complex scaling method can be used as boundary conditions for Green function calculations as described in Sec. 3.7 we can write the solution of the retarded Green function (see Sec. 3.2)

$$\Psi = \lim_{\substack{\epsilon \rightarrow 0 \\ \epsilon > 0}} (\mu + i\epsilon - H)^{-1} S$$

as

$$\Psi = \sum_n |\Psi_n\rangle \frac{(\Psi_n|S)}{\mu - \mathcal{E}_n} + \int d\mathcal{E}_c |\Psi_{\mathcal{E}_c}\rangle \frac{(\Psi_{\mathcal{E}_c}|S)}{\mu - \mathcal{E}_c}.$$

Using the Fisher-Lee relations (3.48) this allows us to approximatively rewrite the transmission as

$$T(\mu) = \left| \sum_n \frac{A_n}{\mu - \mathcal{E}_n} + \int d\mathcal{E}_\theta A_{\mathcal{E}_\theta} [\mu - \mathcal{E}_\theta]^{-1} \right|^2$$

where the amplitudes A_n are determined by the overlap between the lead eigenfunctions and the resonance wave functions Ψ_n . The amplitudes $A_{\mathcal{E}_\theta}$ for the continuum are determined similarly but they are very small because the corresponding wave functions decay inside the cavity. Furthermore the weight factor $[\mu - \mathcal{E}_\theta]^{-1}$ is very small because usually the most continuum states have a big distance to μ . So the continuum can be normally neglected.

In case of a single well separated resonance we get the famous Breit-Wigner formula for a resonance peak [32, 198]

$$T(\mu) = \frac{|A_n|^2}{(\mu - \text{Re}\mathcal{E}_n)^2 + (\text{Im}\mathcal{E}_n)^2} \quad (3.68)$$

which is a Lorentzian function in μ .

While in principle it is possible to calculate A_n as described above, the exact values are of no direct interest in this work. Therefore if we want to examine if the transmission spectrum $T(\mu)$ calculated by the normal Green function method described in Sec. 3.5 is well described by the explicitly calculated resonances we use a different approach. We select an energy range $\mu_0 \dots \mu_1$ in which we want to check the spectrum and determine all resonances $\mathcal{E}_{n_1} \dots \mathcal{E}_{n_2}$ whose real part lies inside this range. Then we define the function

$$f(\mu, \{E_n\}_{n=n_1}^{n_2}, \{A_n\}_{n=n_1}^{n_2}, \{\beta_m\}_{m=0}^M) = \left| \sum_{n=n_1}^{n_2} \frac{A_n}{\mu - E_n} + \sum_{m=0}^M \beta_m \left(\mu - \frac{\mu_0 + \mu_1}{2} \right)^m \right|^2 \quad (3.69)$$

¹²at least for vanishing magnetic field

and minimize the function

$$F(\{E_n\}_{n=n_1}^{n_2}, \{A_n\}_{n=n_1}^{n_2}, \{\beta_m\}_{m=0}^M) = \int_{\mu_0}^{\mu_1} d\mu \left| T(\mu) - f(\mu, \{E_n\}_{n=n_1}^{n_2}, \{A_n\}_{n=n_1}^{n_2}, \{\beta_m\}_{m=0}^M) \right|^2 \quad (3.70)$$

with respect to the (complex) parameters $E_{n_1}, \dots, E_{n_2}, A_{n_1}, \dots, A_{n_2}$ and β_0, \dots, β_M . The parameters β_0, \dots, β_M are used to describe a background consisting of resonances outside the energy interval $\mu_0 \dots \mu_1$ and of the continuum states. One of the phases of the complex amplitudes A_{n_1}, \dots, A_{n_2} has to be fixed because otherwise the problem would be ill-defined. This minimization is in principle a high dimensional curve fit. After we have minimized F we can compare the resulting values of E_{n_1}, \dots, E_{n_2} with the actual resonance energies $\mathcal{E}_{n_1} \dots \mathcal{E}_{n_2}$ to evaluate the quality of the fit. Furthermore we can compare $f(\mu)$ with $T(\mu)$. An example of this fitting procedure is discussed in Sec. 3.8.1.

As explained in App. A the problem to minimize a function with respect to its parameters is closely related to the problem to find the zeros of a function of several variables (see [157] for more details), and so the Newton iteration in the form of Powell’s dog leg method can be applied successfully to such minimization problems. The actual minimization is performed using the software library *MINPACK* [151].

3.8 Scattering systems of “billiard” type

In this work we will deal mainly with two dimensional systems of billiard type. Such a system consist of a bounded region of \mathbb{R}^2 where in the inside the potential V is assumed to be zero while at the boundary we impose Dirichlet hard wall boundary conditions which correspond to $V = \infty$ outside the region. This region is called a “cavity” from now on. Besides its shape, the only relevant parameter of the cavity is its area Ω from which we can construct the Heisenberg time

$$\tau_H = \frac{m\Omega}{\hbar} \quad (3.71)$$

which is a measure of the mean density of states $\tau_H/(2\pi\hbar)$ inside the billiard¹³. Given this Heisenberg time one can define an energy scale $E_H = \hbar/\tau_H$ and measure all relevant energies with respect to this scale. But as usually the interesting processes happen at energies much bigger than the energy E_H this energy scale is quite inconvenient. Therefore for each billiard we define a typical energy scale E_0 and measure all relevant energies with respect to E_0 which itself can be given as a multiple of E_H . Another way to fix E_0 is to relate it to a wavevector k_0 using $E_0 = \frac{\hbar^2 k_0^2}{2m}$ and give k_0 as a multiple of $\Omega^{-\frac{1}{2}}$.

Using E_0 we can define an energy scale, a time scale \hbar/E_0 and a length scale k_0^{-1} . Using the area Ω we can furthermore define a scale B_0 for the magnetic field:

$$B_0 = \frac{2\pi\hbar}{q\Omega},$$

also called the flux quantum. All quantities in this work will be expressed in the units E_0, k_0 and B_0 .

¹³This fact is called Weyl’s theorem [91].

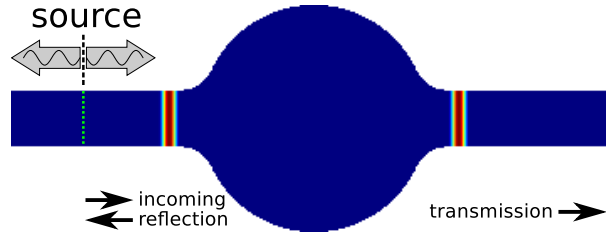


Figure 3.11: This figure illustrates the first example system \mathcal{B}_1 studied in this work. It consists of a circular cavity with a lead attached to the left and to the right. All corners are rounded. The white region corresponds to $V = \infty$ which is enforced by hard wall Dirichlet boundary conditions. The blue region corresponds to $V = 0$. Inside the leads we inserted a small potential barrier here colored in red. The lattice used to simulate the system only takes points inside the colored region into account. In transmission calculations a source (green dashed) is placed in the left lead.

The billiard geometry as described above is closed. If we attach one or more rectangular regions which extend towards infinity to this cavity we get an open system in which we can investigate scattering processes. This will be main topic of this work. The rectangular regions are called “leads” whose widths can be measured in multiples of πk_0^{-1} corresponding to the number of open channels inside the leads at the relevant energy scale.

3.8.1 \mathcal{B}_1 : An almost-closed example system

The first system studied will be an almost-closed cavity of circular shape where the leads are attached in a smooth way such that no sharp edges are created as shown in Fig. 3.11. This billiard is mirror symmetric with respect to the x axis and the y axis. The relevant energy scale to which henceforth all energies are measured is $E_0 = 336.3 \frac{\hbar}{t_H}$ which can also be written $k_0 \sqrt{\Omega} = 25.9$ as explained in Sec. 3.8. The leads have a width W of $W k_0 = 2.25\pi$. The first channel inside the lead opens at $0.19E_0$ and the second channel opens at $0.78E_0$. We will mostly measure in the region where only one channel is open.

Inside the leads a small potential barrier of height $V_0 = 0.9E_0$ and width $\sigma_0 = 1.41 k_0^{-1}$ is inserted in order to get a “nice” resonance structure of the transmission spectrum in which typical scattering processes can be analyzed most cleanly. This barrier potential makes the system almost closed. Instead of using a barrier potential, a similar effect could be created using a constriction of the leads at position where they touch the cavity.

The lattice spacing is chosen as $\Delta x = \lambda_0/30$ with the wavelength $\lambda_0 = 2\pi k_0^{-1}$. The lattice dimension is $n = 21991$. For the time propagations described in Chap. 4 we use a stepsize of $\tau = 0.025 \hbar/E_0$ and either the Crank-Nicholson method (Sec. 4.2) or the Taylor series method (Sec. 4.4). A length of $x_s = 5.4 \pi k_0^{-1}$ is used to switch on the interaction strength $g(\mathbf{x})$ inside the leads (see Sec. 5.1.2 for a detailed discussion). The parameters used are summarized in Fig. 3.12.

We now first calculate the transmission spectrum through this billiard as shown in Fig. 3.13. To this end we place a source term as given in Eq. (3.47) to the left side of the cavity, calculate the scattering state Ψ using the retarded Green function Eq. (3.6) and measure the current on the right hand side as described in Sec. 3.6.2.

Next we calculate the resonances of the system using exterior complex scaling as described in Sec. 3.7.2. The resonances are also shown in Fig. 3.13. In the energy range investigated, most

parameter	value	description
$\sqrt{\Omega}$	$8.25 \pi k_0^{-1}$	Ω is the area of the cavity
W	$2.25 \pi k_0^{-1}$	width of the leads
r	$4.5 \pi k_0^{-1}$	“radius” of the cavity
	$0.19 E_0, 0.78 E_0$	energies of the lead eigenmodes
V_0	$0.9 E_0$	height of the barrier potential
σ_0	$0.45 \pi k_0^{-1}$	width of the barrier potential
Δx	$\frac{1}{15} \pi k_0^{-1}$	lattice spacing
n	21991	lattice dimension
τ	$0.025 \hbar E_0^{-1}$	time step
x_s	$5.4 \pi k_0^{-1}$	switching length for $g(x)$

Figure 3.12: This tabular summarizes the parameters used for the system \mathcal{B}_1 shown in Fig. 3.11.

resonances are well separated, i.e. they can be well described by Breit-Wigner peaks (3.68). The criterion to decide if two resonances \mathcal{E}_a and \mathcal{E}_b are well separated is

$$|\operatorname{Re} [\mathcal{E}_a - \mathcal{E}_b]| \gg |\operatorname{Im} \mathcal{E}_a| + |\operatorname{Im} \mathcal{E}_b|$$

so that their Lorentzian curves do not overlap because their spacing exceeds their width. The overlapping resonances will show interesting behavior later in Chap. 5 (see especially Sec. 5.6.2).

The system is mirror-symmetric with respect to the reflection $y \mapsto -y$. The consequence is that the resonances can be classified according to their parity with respect to this reflection. As the ground state lead-eigenmode has positive parity we can now conclude that in the energy interval where only one channel in the leads is open the resonances with negative parity cannot couple to the leads and thus are actually bound states embedded inside the continuous spectrum corresponding to the ground state lead-eigenmode. Such negative-parity bound states will play a role in the stability analysis discussed in Sec. 5.7. In an experiment, the symmetry will be always broken by some imperfections. In such case these bound states will manifest themselves as very sharp resonances.

The mirror symmetry $x \mapsto -x$ causes the resonances to have parity $+1$ or -1 with respect to this reflection. The consequence is that almost all resonance peaks in the transmission spectrum rise up to unity as seen in Fig. 3.13.

Finally we can check if the transmission spectrum is compatible with the calculated resonance structure by the minimization of Eq. (3.70). The minimization is done over the whole energy interval shown in Fig. 3.13 using an additional polynomial of degree $M = 3$ to take the background into account. The result is that the fitted transmission (3.69) reproduces the actual transmission with a maximal error of $2 \cdot 10^{-4}$ and the fitted resonances agree with the actual resonances within an error range of 10^{-5} except for the two resonances near $\mu = 0.61$ where the error rises to $5 \cdot 10^{-4}$. These two resonances are exceptional because they have nearly equal resonance energy while belonging to different mirror symmetry classes with respect to the y axis. Therefore they nearly annihilate each other in the transmission spectrum and can for this reason not be calculated well by curve fitting. We conclude that the resonances indeed describe the transmission spectrum well.

This system will be the primary example system studied in Chap. 5.

3.9 Computational complexity

In the computation of stationary scattering states (and in the computation of resonance states) the major computational task is to solve the linear system of equations

$$[\mu - H] \Psi = S .$$

Here H is the discretized Hamiltonian in the form of Eq. (3.11) (1D) or Eq. (3.50) (2D with gauge field) supplemented by suitable boundary conditions. The operator $\mu - H$ is a matrix of

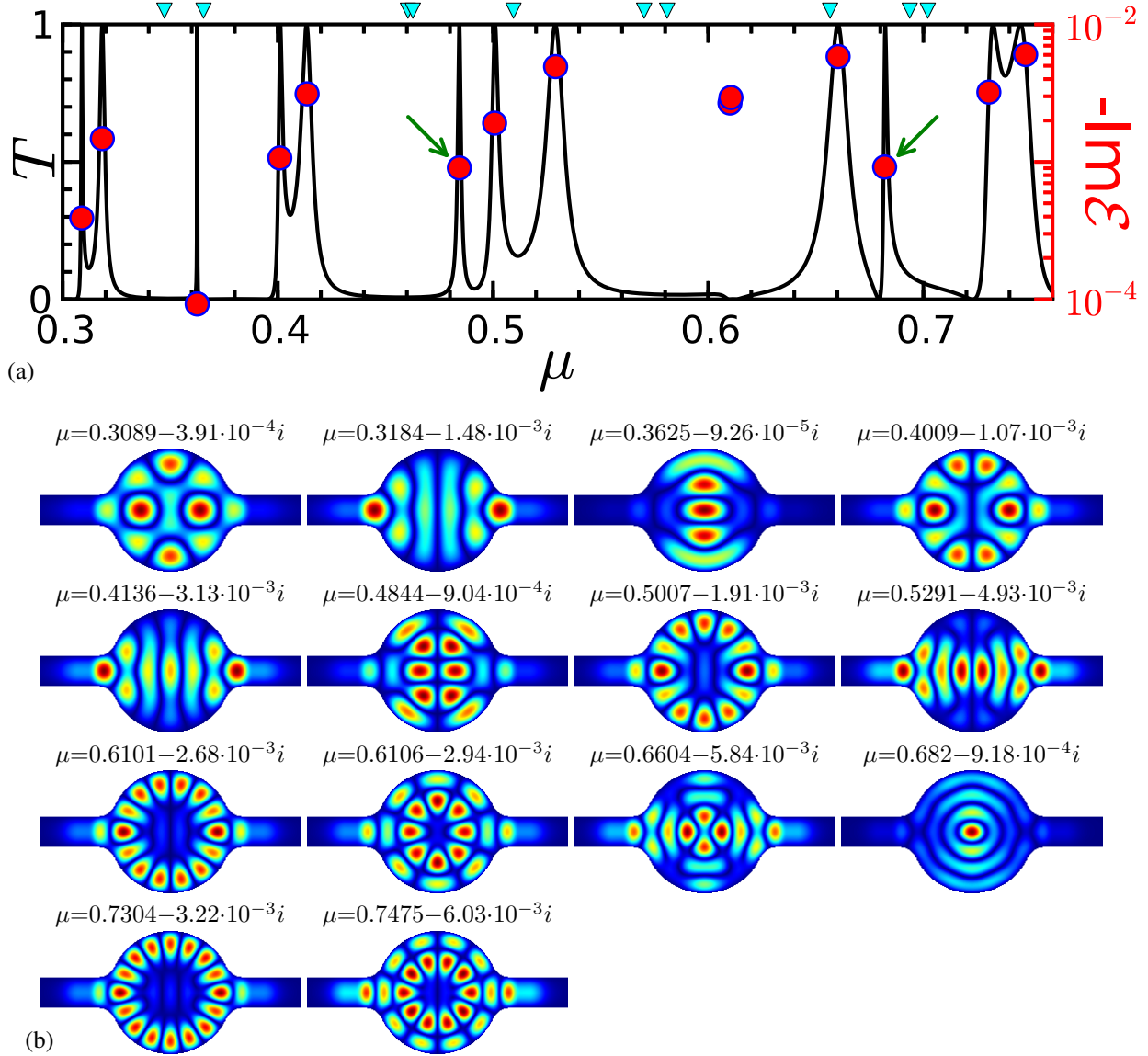


Figure 3.13: In (a) the transmission spectrum $T(\mu)$ (black curve) of the billiard \mathcal{B}_1 depicted in Fig. 3.11 is shown. Furthermore the red dots mark the position of the resonances \mathcal{E} whose real part uses the same axis as μ . The cyan triangles above the spectrum indicate the position of the bound states (negative parity $y \mapsto -y$). In (a) the corresponding resonance wavefunctions are shown. The green arrows mark the resonances which will be investigated in more detail in Fig. 5.3. All energies are measured as multiples of the relevant energy scale E_0 of the billiard.

dimension $n \times n$ where n is the number of grid points. For the biggest systems investigated in this work n is roughly as big as 150000. Any direct matrix inversion methods are not feasible for systems of this size.

But if one looks at the aforementioned discretized Hamiltonians one sees that they are very sparse (i.e. the overwhelming part of the matrix entries are zeros) as each grid point is only connected to its two (1D) or four (2D) neighbors¹⁴. Therefore an obvious idea is to take advantage of the sparsity pattern by using algorithms directly designed for sparse matrices.

In this work we will calculate the matrix inverse in form of a LU decomposition [172] using the sparse matrix computer library *UMFPACK* [52]:

$$[\mu - H] = LU \quad \Rightarrow \quad \Psi = U^{-1}L^{-1}S.$$

Here L and U are lower and upper triangular respectively. This LU decomposition is an efficient way to handle the matrix inverse because both U^{-1} and L^{-1} can be effectively applied to a vector without the need to explicitly calculate them. Furthermore L and U do only suffer moderately from the so-called “fill-in” (i.e. that entries which are zero in H become non-zero).

It is important to know the “computational cost” of calculating the the LU decomposition of the matrix $[\mu - H]$ and of the related matrices later used for solving the scattering problem for interacting systems. This “computational cost” has to take into account the running time of the algorithm (also known as computational complexity) and the amount of memory used during the calculation. Both can be estimated by following considerations.

We first look at a regular grid of size n in y direction and m in x direction as shown in Fig. 3.6. The corresponding matrix (3.39) is a block tridiagonal matrix consisting of m matrix blocks each of size n . The computational complexity to invert a single block is $\mathcal{O}(n^3)$ [172]. Albeit each single block is itself a sparse matrix the inverse of a block is a full matrix whose memory usage is n^2 . Therefore the complexity to calculate the LU decomposition of Eq. (3.43) using a block block Gauß algorithm is $\mathcal{O}(mn^3)$ giving a result occupying $\mathcal{O}(mn^2)$ memory.

In the general case of an irregular grid as shown in Fig. 3.5 and its corresponding matrix (3.41) one has to interpret n as the bandwidth of the sparse matrix which is a measure of the width of the system. Furthermore we introduce N as the total number of points on the grid (of course $N = mn$ holds in an regular grid). Then the “computational cost” of calculating the LU decomposition of the sparse matrix (3.41) is given by:

$$\begin{aligned} \text{running time} &\sim \mathcal{O}(N n^2) \\ \text{memory usage} &\sim \mathcal{O}(N n) \end{aligned} \tag{3.72}$$

If we keep the geometry fixed and introduce a length scale L then the running time scales as $\mathcal{O}(L^4)$ and the memory usage as $\mathcal{O}(L^3)$.

From Eq. (3.72) we see that the “computational cost” scales unfavorably with the width of the system. This is the main factor limiting the size of the systems which can be simulated using the methods of this work. Therefore it would be highly desirable to have an algorithm to solve linear equation systems with a better computational complexity. In principle such algorithms should exist because the matrix (3.41) has only $\mathcal{O}(N)$ non zero entries. Indeed iterative algorithms for the solution of sparse linear systems [145, 179] can archive better running times while using less

¹⁴ The only exceptions are the grid point directly adjacent to the leads which might be connected to more points if one uses the self energy boundary conditions (3.36).

memory than the LU decomposition algorithm. But their performance is very problem dependent and they are very fragile while the LU decomposition algorithm is quite robust. Furthermore the matrices of type Eq. (3.41)¹⁵ which are used extensively in this work are especially hard to handle using iterative algorithms [66]. Therefore we only use the LU decomposition in this work.

3.10 Summary, outlook and open ends

In this section we have introduced the tight binding model to numerical simulate the Schrödinger equation. Magnetic fields are incorporated using a Peierls phase into this model. Special attention has been paid how to describe semi-infinite leads attached to the scattering region. To this end the self energy and exterior complex scaling boundary conditions have been introduced. Both methods will be used in later chapters. The exterior complex scaling method allows us to study resonances, too.

The self energies introduced in Eq. (3.37) and Eq. (3.38) are used in similar form in the recursive Green function method [50, 70, 126, 138, 139] which is a block Gauß matrix inversion algorithm (similar to App. D) to invert the matrix (3.39) and its two dimensional generalization (3.43). In this work we will only use the self energy component of the recursive Green function method and calculate the matrix inverse in form of a LU decomposition of the involved sparse matrices using the sparse matrix computer library *UMFPACK* [52]. This LU decomposition is a computational efficient way to handle the inverse of a sparse matrix and can be generalized to non-square matrices. The main reason for doing this will become obvious when we deal with interacting systems as described in Chap. 5 (see especially Sec. 5.3.1). Then we have to deal with modifications of Eq. (3.39) involving non-square matrices which do not fit well into the framework of the recursive Green function method.

Furthermore the recursive Green function method can only deal with block tridiagonal matrices and therefore any irregular grid has to be transformed (i.e. by suitable renumbering of grid points) to this form [208]. This complication does not arise in our case, because *UMFPACK* is designed to handle matrices of any sparsity pattern.

In [208] improved expressions for the self energy (3.37) generalizing Eq. (3.38) and Eq. (3.45) were developed. Using this improved self energies it is possible to describe a (constant) magnetic field inside the leads or (using some tricks) leads attached at an (almost) arbitrary angle. But these improved self energies have a non trivial dependence on the energy μ and the magnetic field B making the task of calculating the derivative of the self energies with respect to μ and B very challenging. These derivatives will be needed in Sec. 5.3.1. Therefore we do not use the improved self energies in this work.

In this work we use exclusively the finite difference method introduced in Eq. (3.9) to discretize the Schrödinger equation (3.1). Another discretization scheme is the finite element method (short the FEM) [106]. This we tried out and it works quite fine for the linear Schrödinger equation. Indeed a FEM with higher order triangle elements (4th or higher) outperforms the finite difference method both with respect to accuracy as with respect to running time. But in the non-linear case the interaction term in the Gross-Pitaevskii equation (2.17) ruins this advantage because for higher triangle elements this term is cumbersome and very slow to evaluate.

¹⁵ The linear systems of equations corresponding to this matrices are known as “indefinite Helmholtz equations” in the literature.

Chapter 4

Simulation of the time dependent Gross-Pitaevskii equation

4.1 Introduction

While in Chap. 3 we described how to calculate stationary scattering states of the Schrödinger equation, we now show how to do a simulation of the time dependent inhomogeneous Gross-Pitaevskii equation:

$$i\hbar \frac{\partial}{\partial t} \Psi(\mathbf{r}, t) = H \Psi(\mathbf{r}, t) + g(\mathbf{r}) \frac{\hbar^2}{m} |\Psi(\mathbf{r}, t)|^2 \Psi(\mathbf{r}, t) + S(\mathbf{r}, t) . \quad (4.1)$$

The linear Hamilton operator

$$H = \frac{1}{2m} [-i\hbar \nabla - q\mathbf{A}(\mathbf{r})]^2 + V(\mathbf{r}) \quad (4.2)$$

is here always understood as its discretized version in position space. This means that H is a tight binding Hamiltonian of type Eq. (3.11), Eq. (3.41) or Eq. (3.50).

The basic step to simulate Eq. (4.1) is to understand how to simulate the time-dependent inhomogeneous Schrödinger equation:

$$i\hbar \frac{\partial}{\partial t} \Psi(t) = H \Psi(t) + S(t) . \quad (4.3)$$

The interaction term $g(\mathbf{r}) \frac{\hbar^2}{m} |\Psi(\mathbf{r}, t)|^2 \Psi(\mathbf{r}, t)$ in Eq. (4.1) can be built into the simulation afterwards as shown in Sec. 4.3. As in Chap. 3 we have to take care that the leads are handled appropriately.

We can integrate the time evolution (4.3) exactly:

$$\Psi(\tau) = e^{-\frac{i}{\hbar} \tau H} \Psi(0) - \frac{i}{\hbar} \int_0^\tau e^{-\frac{i}{\hbar} (\tau - \tau') H} S(\tau') d\tau' . \quad (4.4)$$

Therefore the main step is to calculate an approximation to the exponential of the linear Hamilton operator H given by Eq. (4.2). This can be done in several ways resulting in different time propagation algorithms each having special advantages and disadvantages.

The leads can be incorporated into the simulation using either transparent boundary conditions (*TBC*, see App. C) or exterior complex scaling boundary conditions (*ECSBC*, see Sec. 3.7).

For convenience we here present a short overview over the different time propagation methods:

method	advantages	disadvantages
Crank-Nicholson	<i>TBC</i> possible, unconditional stable	slow for wide systems
Taylor series	widely applicable	
split operator	very fast	only rectangular grids, potentially unstable, periodic boundary conditions

4.2 Crank-Nicholson

We first present here the Crank-Nicholson method [82, 106, 125] which replaces the exponential function by its (1,1)-Padé approximation [47, 102];

$$e^x = \frac{1 + \frac{x}{2}}{1 - \frac{x}{2}} + \mathcal{O}(x^3) .$$

In order to apply this approximation to the solution (4.4) of the Schrödinger equation we choose a small timestep τ :

$$e^{-i\tau H/\hbar} = \frac{1 - i\frac{\tau}{2\hbar}H}{1 + i\frac{\tau}{2\hbar}H} + \mathcal{O}(\tau^3) . \quad (4.5)$$

This is the defining equation for the Crank-Nicholson method for simulation of the (homogeneous) Schrödinger equation. This right hand side of Eq. (4.5) is also called the Cayley transformation of H [82].

If we want to use Eq. (4.5) to propagate the (homogeneous) Schrödinger equation from the time t_0 to the time t_1 we have to divide the interval $t_0 \dots t_1$ into n ($n \in \mathbb{N}$) subintervals of size $\tau = \frac{t_1 - t_0}{n}$ and repeatedly use Eq. (4.5) on each subinterval:

$$e^{-\frac{i}{\hbar}(t_1 - t_0)H} = \left[\frac{1 - i\frac{\tau}{2\hbar}H}{1 + i\frac{\tau}{2\hbar}H} \right]^n + \mathcal{O}(n^{-2}) . \quad (4.6)$$

Here n (or equivalently τ) determines the quality of the approximation. A higher n gives a better approximation to the exponential but the simulation takes longer.

In order to incorporate the inhomogeneous source term $S(\mathbf{r}, t)$ of the Schrödinger equation (4.3) into the simulations we now derive Eq. (4.5) in a slightly different way. We start by rewriting Eq. (4.4):

$$e^{-i\frac{\tau}{2\hbar}H}\Psi(0) = e^{+i\frac{\tau}{2\hbar}H}\Psi(\tau) + \frac{i}{\hbar} \int_0^\tau e^{-\frac{i}{\hbar}(\frac{\tau}{2} - \tau')H} S(\tau') d\tau' .$$

The exponential functions in this equation are now approximated using $e^x = 1 + x + \frac{1}{2}x^2 + \mathcal{O}(x^3)$ while the integral is approximated using the midpoint rule $\int_0^\tau f(\tau') d\tau' = \tau f(\frac{\tau}{2}) + \mathcal{O}(\tau^3)$. This

gives us

$$(1 - i\frac{\tau}{2\hbar}H)\Psi(0) = (1 + i\frac{\tau}{2\hbar}H)\Psi(\tau) + \frac{i}{\hbar}\tau S(\frac{\tau}{2}) + \frac{1}{2}\left(\frac{iH}{2\hbar}\right)^2 \tau^2 [\psi(\tau) - \psi(0)] + \mathcal{O}(\tau^3) .$$

Using the relation $\psi(\tau) - \psi(0) = \mathcal{O}(\tau)$ we can therefore deduce

$$\Psi(\tau) = \left[1 + i\frac{\tau}{2\hbar}H\right]^{-1} \left[\left(1 - i\frac{\tau}{2\hbar}H\right)\Psi(0) - \frac{i}{\hbar}\tau S(\frac{\tau}{2})\right] + \mathcal{O}(\tau^3) . \quad (4.7)$$

This is the defining equation of the Crank-Nicholson method for the inhomogeneous Schrödinger equation (4.3). As in Eq. (4.6) we have to repeatedly use Eq. (4.7) in order to do a time propagation over a larger time interval.

The advantage of the Crank-Nicholson method is that for hermitian operators H the approximation $e^{-i\frac{\tau}{\hbar}H} \approx \frac{1-i\frac{\tau}{2\hbar}H}{1+i\frac{\tau}{2\hbar}H}$ is unitary just like the exact expression $e^{-i\frac{\tau}{\hbar}H}$. This leads to a well behaved numerical simulation. Moreover for hermitian tight binding Hamiltonians like the ones that we are using in this work (see Eqs. (3.11), (3.41) and (3.50)) the Crank-Nicholson method is unconditionally stable [106, 125]. This means no matter how big τ gets there are no modes which grow exponentially.

The leads can be incorporated into the Crank-Nicholson method in a natural way using transparent boundary conditions [11] as shown in App. C. That means we can restrict the simulation to the scattering region (as shown in Fig. 3.4) almost without introducing any error. Alternatively one can use the exterior complex scaling boundary conditions introduced in Sec. 3.7 which are also needed for the split-operator and Taylor series time-propagation methods later on. These boundary conditions are not as good as the transparent boundary conditions but they can be used more flexibly as they are applicable for all time propagation methods presented here and for the dynamical stability analysis in Sec. 5.7. The accuracy of both boundary conditions is studied in Sec. 4.6.

In comparison to other methods, for example with the Chebyshev propagation method [197], the Crank-Nicholson method given in Eq. (4.5) works only well for a comparably small stepsize τ . But this is of no concern in this work because the source term and the interaction term are time dependent forbidding big stepsizes anyway.

The matrix inverse $(1 + i\frac{\tau}{2\hbar}H)$ needed in Eq. (4.6) can be calculated before the actual computation and stored as a LU factorization which will be then used at each time step. As seen in Eq. (3.72), the number of non zero entries in the LU factorization scales as $\mathcal{O}(Nn)$. From this we can deduce that the computational complexity of each time step is $\mathcal{O}(Nn)$. Here N is the number of points of the system and n is the width of the system. Therefore we see that the computational complexity of the Crank-Nicholson method scales unfavorably with the system width. While in one dimension it is competitive with the Taylor series method presented in Sec. 4.4 in two dimensions it becomes intolerable slow as the width of the system increases. Therefore we will mainly use the Crank-Nicholson method for one dimensional and narrow two dimensional systems. For those systems it is superior to the Taylor series method introduced in Sec. 4.4. Furthermore we will need the Crank-Nicholson method as a building block for the split operator method presented in Sec. 4.5.

4.3 Incorporating the interaction term

The interaction term $g \frac{\hbar^2}{m} |\Psi(\mathbf{r}, t)|^2 \Psi(\mathbf{r}, t)$ in the Gross-Pitaevskii equation (4.1) in principle has the same effect as a time dependent potential. Therefore we look first at the Schrödinger equation with a time dependent potential $\tilde{V}(t)$:

$$i\hbar \frac{\partial}{\partial t} \Psi(t) = (H + \tilde{V}(t)) \Psi(t) .$$

The solution of this equation can be given as

$$\Psi(\tau) = U(\tau) \Psi(0)$$

where we have introduced the time evolution operator [187] (\mathcal{T} is the time ordering symbol):

$$\begin{aligned} U(\tau) &= \mathcal{T} \exp \left[-\frac{i}{\hbar} \int_0^\tau d\tau' (H + \tilde{V}(\tau')) \right] \\ &= 1 - \frac{i}{\hbar} \int_0^\tau d\tau' (H + \tilde{V}(\tau')) \\ &\quad - \frac{1}{\hbar^2} \int_0^\tau d\tau' \int_0^{\tau'} d\tau'' (H + \tilde{V}(\tau')) (H + \tilde{V}(\tau'')) + \mathcal{O}(\tau^3) . \end{aligned} \quad (4.8)$$

We now apply the integration rules $\int_0^\tau f(\tau') d\tau' = \tau f(\frac{\tau}{2}) + \mathcal{O}(\tau^3)$ and $\int_0^{\frac{\tau}{2}} f(\tau'') d\tau'' = \frac{\tau}{2} f(\frac{\tau}{2}) + \mathcal{O}(\tau^2)$ on Eq. (4.8):

$$\begin{aligned} U(\tau) &= 1 - i \frac{\tau}{\hbar} \left(H + \tilde{V}(\frac{\tau}{2}) \right) - \frac{1}{\hbar^2} \tau \left(H + \tilde{V}(\frac{\tau}{2}) \right) \int_0^{\frac{\tau}{2}} d\tau'' (H + \tilde{V}(\tau'')) + \mathcal{O}(\tau^3) \\ &= 1 - i \frac{\tau}{\hbar} \left(H + \tilde{V}(\frac{\tau}{2}) \right) - \frac{\tau^2}{2\hbar^2} \left(H + \tilde{V}(\frac{\tau}{2}) \right)^2 + \mathcal{O}(\tau^3) \\ &= \exp \left[-i \frac{\tau}{\hbar} \left(H + \tilde{V}(\frac{\tau}{2}) \right) \right] + \mathcal{O}(\tau^3) \\ &= \exp \left[-i \frac{\tau}{\hbar} \left(H + \frac{1}{2} (\tilde{V}(0) + \tilde{V}(\tau)) \right) \right] + \mathcal{O}(\tau^3) . \end{aligned}$$

The interpretation of these results is that one can replace the time dependent potential \tilde{V} by its average over the interval $0 \dots \tau$ while only introducing an error of order $\mathcal{O}(\tau^3)$. So the final result is:

$$\Psi(\tau) = \exp \left[-i \frac{\tau}{\hbar} \left(H + \frac{1}{2} (\tilde{V}(0) + \tilde{V}(\tau)) \right) \right] \Psi(0) + \mathcal{O}(\tau^3) . \quad (4.9)$$

To simulate the Gross-Pitaevskii equation (4.1) one has to use:

$$\tilde{V}(\mathbf{r}, 0) = g(\mathbf{r}) \frac{\hbar^2}{m} |\Psi(\mathbf{r}, 0)|^2 \quad \tilde{V}(\mathbf{r}, \tau) = g(\mathbf{r}) \frac{\hbar^2}{m} |\Psi(\mathbf{r}, \tau)|^2 .$$

The problem now is that Eq. (4.9) has become an implicit equation for $\Psi(\mathbf{r}, \tau)$. This implicit equation is now approximatively solved through a kind of fix point iteration. From the given wavefunction $\Psi(0)$ one can calculate a first guess for $\Psi(0)$:

$$\Psi_1(\tau) = \exp \left[-i \frac{\tau}{\hbar} (H + \tilde{V}(0)) \right] \Psi(0) .$$

Using this guess one can successively generate better estimates $\{\Psi_k(\tau)\}_{k=2}^{\infty}$ of $\Psi(0)$ using following recursion¹:

$$\Psi_{k+1}(\tau) = \exp \left[-i \frac{\tau}{\hbar} \left(H + \frac{1}{2} (\tilde{V}(0) + \tilde{V}_k(\tau)) \right) \right] \Psi(0) .$$

Here we have introduced $\tilde{V}_k(\mathbf{r}, \tau) = g(\mathbf{r}) \frac{\hbar^2}{m} |\Psi_k(\mathbf{r}, \tau)|^2$. Repeating this recursion infinitely often we get $\lim_{k \rightarrow \infty} \Psi_k(\tau) = \Psi(\tau)$. In practical calculations $\Psi_2(\tau)$ is a sufficient good approximation to $\Psi(\tau)$ so we abort the recursion after $k = 2$. The bottom line of this is that for each “non-linear” time step one has to perform two “linear” time steps, each with a slightly different potential.

The method presented here was originally proposed by [40] and was used with great success in the one dimensional case in [159–161].

For the Crank-Nicholson method (4.5) literally calculating $\exp \left[-i \frac{\tau}{\hbar} (H + W) \right]$ (here $W = \frac{1}{2}(\tilde{V}(0) + \tilde{V}(\tau))$ in Eq. (4.9)) would force us to recalculate $\left[1 + i \frac{\tau}{2\hbar} (H + W) \right]^{-1}$ at every step which is prohibitively computational expensive in two dimensions. Therefore we use the Trotter-Suzuki formula (4.13) in this case:

$$e^{-i \frac{\tau}{\hbar} (H+W)} = e^{-i \frac{\tau}{2\hbar} W} e^{-i \frac{\tau}{\hbar} H} e^{-i \frac{\tau}{2\hbar} W} + \mathcal{O}(\tau^3) .$$

4.4 The Taylor series method

The Taylor series method replaces the exponential function by its truncated power series:

$$e^x = \sum_{m=0}^{\infty} \frac{x^m}{m!} = \sum_{m=0}^{M-1} \frac{x^m}{m!} + \varepsilon \quad \text{with} \quad |\varepsilon| < \frac{|x|^M}{M!} e^{|x|} . \quad (4.10)$$

In order to apply this approximation we have to choose a time step τ and the order M of the method :

$$e^{-i \frac{\tau}{\hbar} H} = \sum_{m=0}^{M-1} \frac{1}{m!} \left[-i \frac{\tau}{\hbar} H \right]^m + \mathcal{O}(\tau^M) . \quad (4.11)$$

As in Eq. (4.6) we have to repeatedly use this formula to propagate the wave function over a larger time interval.

Given a time step τ the order M follows from following considerations. According to the dispersion relations (3.15) the maximal modulus of the eigenvalue of H can be estimated as $E_{\max}^{\text{1D}} = 4\alpha$ in one dimension and as $E_{\max}^{\text{2D}} = 8\alpha$ in two dimensions. We now demand that the error term ε in Eq. (4.10) has to be always below some predefined value ε_{\max} . This gives us the relation

$$\frac{\left(\frac{\tau}{\hbar} E_{\max} \right)^M}{M!} e^{\tau E_{\max}/\hbar} < \varepsilon_{\max}$$

from which we can deduce M as the minimal integer number fulfilling this inequality. While of course M should be as small as possible, one has to note that it is not wise to choose a very small time step τ and then set $M = 2$ because then one would obtain the Euler method for time propagation [82] which has very bad numerical properties. In order to obtain numerical stability

¹ In principle we take here the average of the squared modulus of the wave functions. One could also use here the squared modulus of the average of the wave functions without altering the order $\mathcal{O}(\tau^3)$ of the error term.

one has to ensure that the spectrum of $-i\frac{\tau}{\hbar}H$ (which was estimated above) is mapped inside the unit disk $\{z \in \mathbb{C}, |z| \leq 1\}$ by the truncated power series (4.10) so that no exponential growing modes can develop. A good rule of thumb is to choose such a time step τ that the deduced value of M is bigger than 10. In actual computations we have chosen $\varepsilon_{\max} = 10^{-5}$ and $M = 15$ which proved to be sufficient.

In order to incorporate the inhomogeneous source term $S(t)$ into the time propagation scheme we apply the integration rule $\int_0^\tau f(\tau')d\tau' = \frac{\tau}{2} [f(0) + f(\tau)] + \mathcal{O}(\tau^3)$ onto the integral in Eq. (4.4):

$$\begin{aligned}\Psi(\tau) &= e^{-i\frac{\tau}{\hbar}H}\Psi(0) - \frac{i}{\hbar} \int_0^\tau e^{-i\frac{\tau-\tau'}{\hbar}H} S(\tau')d\tau' \\ &= e^{-i\frac{\tau}{\hbar}H}\Psi(0) - i\frac{\tau}{2\hbar} \left[e^{-i\frac{\tau}{\hbar}H} S(0) + S(\tau) \right] + \mathcal{O}(\tau^3) \\ &= e^{-i\frac{\tau}{\hbar}H} \left[\Psi(0) - i\frac{\tau}{2\hbar} S(0) \right] - i\frac{\tau}{2\hbar} S(\tau) + \mathcal{O}(\tau^3).\end{aligned}\tag{4.12}$$

As in Eq. (4.11) the exponential function is now replaced by its truncated power series.

While we are allowed to choose the time step τ as big as we want to propagate the homogeneous Schrödinger equation (with a time independent potential) $i\hbar\frac{\partial\Psi(t)}{\partial t} = H\Psi(t)$ we are not allowed to do so in the case of the inhomogeneous Gross-Pitaevskii equation (4.1) because the source term $S(t)$ and the interaction term $g(\mathbf{r})\frac{\hbar^2}{m}|\Psi(\mathbf{r},t)|^2\Psi(\mathbf{r},t)$ both are time dependent. The error terms in Eq. (4.9) and Eq. (4.12) limit our choice of τ .

The computational complexity to apply the Taylor series method (4.11) is $\mathcal{O}(N)$ (here N is the number of points of the lattice) and thus grows linearly with the system size. Therefore this method is much faster than the Crank-Nicholson method (4.5) for wide two dimensional systems.

The Taylor series method belongs to a more general class of time propagation methods which all replace the exponential function by some polynomial approximation. Let \mathcal{G} be a simply connected open region in \mathbb{C} . Then these methods make the replacement $e^x = P_M(x) + \varepsilon$ where $P_M(x)$ is a polynomial of degree M which is chosen in such a way that the error term ε is in some sense “optimal” over the whole region \mathcal{G} . Such polynomials can be either derived from a Faber polynomial expansion [103, 107] or from Newton interpolation polynomials at Lejá points [12].

For closed systems the spectrum of H is real and bounded. Therefore for this systems a Chebyshev propagation method [197] would be more efficient because this method is derived from a Faber polynomial expansion where the region \mathcal{G} is an ellipse in the complex plane whose longer axis includes the spectrum of $-i\frac{\tau}{\hbar}H$.

But in our case we want to simulate open systems including leads which are incorporated using the exterior complex boundary conditions as described in Sec. 3.7. Therefore a part of the spectrum of H is rotated into the lower half of the complex plane as described in Sec. 3.7.2. The optimal region \mathcal{G} to describe the system would therefore be a semi-circle (or a circle arc) in the lower half of \mathbb{C} with radius E_{\max} . Time propagation methods for such an optimal region \mathcal{G} can be developed [12, 107] but we stick here with the much simpler and more robust Taylor series method which corresponds to Faber polynomials where \mathcal{G} is the unit disk $\{z \in \mathbb{C}, |z| \leq 1\}$. The Taylor series method with approximatively $M = 15$ lies in the middle between the low order Euler method ($M = 2$) and a high order Faber polynomial expansion where one usually chooses $M \gtrsim 1000$ with correspondingly big time steps τ .

One has to stress out here that the exterior complex scaling boundary conditions used to describe the leads only work here because they can absorb more than one energy at once. This is

necessary as in two dimension even at a given fixed global energy μ each lead eigenmode (whose energy is E_k) carries a plane wave of energy $\mu - E_k$ and all these plane waves have to be absorbed simultaneously. The performance of the boundary conditions is studied in more detail in Sec. 4.6.

4.5 The Split operator method

While the Taylor series method presented in Sec. 4.4 is actually quite fast we here present a split operator method which is even faster but on the other side has several severe disadvantages.

The split operator method is developed from the Trotter-Suzuki formula [54, 196] which is presented for completeness here. Let in the following $z \in \mathbb{C}$ be a small complex number and let A and B be some possibly non-commuting operators. Then following relation holds:

$$e^{z(A+B)} = e^{\frac{z}{2}A} e^{zB} e^{\frac{z}{2}A} + \mathcal{O}(|z|^3). \quad (4.13)$$

In order to apply this formula to the Schrödinger equation we split the tight binding Hamilton operator $H = T + V$ into a kinetic and a potential term. Choosing a small time step τ this results in:

$$e^{-i\frac{\tau}{\hbar}H} = e^{-i\frac{\tau}{2\hbar}V} e^{-i\frac{\tau}{\hbar}T} e^{-i\frac{\tau}{2\hbar}V} + \mathcal{O}(|\tau|^3)$$

The operator $e^{-i\frac{\tau}{2\hbar}V}$ can be evaluated easily and fast as it is diagonal in the position basis. In order to evaluate the operator $e^{-i\frac{\tau}{\hbar}T}$ also in a fast way we have to decompose the wave function into the eigenmodes of the kinetic energy T . For a regular rectangular lattice with periodic boundary conditions these eigenmodes are plane waves similar to the considerations in Sec. 3.4.1 and therefore the eigenmode decomposition can be done by a fast Fourier transformation \mathcal{F} [172]. This is the main idea of the split operator method as described in [69].

But in our systems we are not allowed to use periodic boundary conditions in x direction because we want to attach leads for $x \rightarrow \pm\infty$. Therefore we split the kinetic energy $T = T_x + T_y$ into a horizontal and a vertical term. Applying Eq. (4.13) again we obtain:

$$e^{-i\tau H/\hbar} = e^{-i\tau V/(2\hbar)} e^{-i\tau T_y/(2\hbar)} e^{-i\tau T_x/\hbar} e^{-i\tau T_y/(2\hbar)} e^{-i\tau V/(2\hbar)} + \mathcal{O}(|\tau|^3).$$

The kinetic energy term in y direction is evaluated as in the usual split operator method but for the kinetic energy in x direction we use the Crank-Nicholson method (4.5). The leads can now be incorporated into the simulation by applying the exterior complex scaling boundary conditions (3.63) onto T_x . Here one has to stress the fact that the kinetic energy term T_x does not depend on y and therefore is quasi one dimensional and can thus be evaluated in a fast way for each horizontal slice y . Furthermore the evaluation can be done in the eigenmode space of T_y as T_x commutes with T_y . As in Sec. 4.4 it is important that the exterior complex scaling boundary conditions work for more than one energy at once because we have to absorb one plane wave in x direction for each Fourier mode in y direction, and each plane wave has a different energy.

The complete split operator method can now be written as:

$$e^{-i\tau H/\hbar} = e^{-i\tau V/(2\hbar)} \mathcal{F}_y^{-1} e^{-i\tau T_y/(2\hbar)} \left[1 + i\frac{\tau}{2\hbar} T_x \right]^{-1} \left[1 - i\frac{\tau}{2\hbar} T_x \right] e^{-i\tau T_y/(2\hbar)} \mathcal{F}_y e^{-i\tau V/(2\hbar)} + \mathcal{O}(|\tau|^3). \quad (4.14)$$

The fast Fourier transformation \mathcal{F}_y in y direction is for the sake of clarity explicitly written down here. In this Fourier basis T_y is diagonal and thus fast to evaluate. In our calculations we use the

computer library *FFTW* [79] to evaluate \mathcal{F}_y . The kinetic energy term T_x in x direction is essential one-dimensional and therefore also fast to evaluate. A source term can be incorporated into the Crank-Nicholson step as shown in Eq. (4.7).

A magnetic field can be incorporated into this formalism if one uses the gauge field (3.55). Then the eigendecomposition of the kinetic energy in y direction reads (see Eq. (F.6)):

$$T_y e^{iky\Delta x} = E(x) e^{iky\Delta x} \quad \text{with } E(x) = 2\alpha \left[1 - \cos \left[\left(k - \frac{q}{\hbar} A(x) \right) \Delta x \right] \right].$$

Therefore the eigenvectors are unchanged by the gauge field and we can still use \mathcal{F}_y to perform an eigendecomposition of T_y . But the eigenenergies $E(x)$ of T_y now depend on x . It is worth mentioning here that k is actually discretized here because of the periodic boundary conditions in y direction. For reasons of numerical stability we want to preserve the periodicity in k space; therefore we use the tight binding dispersion relations instead of their continuous counterpart.

The computational complexity to evaluate Eq. (4.14) is $\mathcal{O}(N \log n)$ where N is the number of points on the lattice and n is the width of the lattice in y direction. Here the factor $\log n$ comes from the fast Fourier transformation. This complexity is actually a bit worse than the complexity of the Taylor series method. But the constants omitted in the Landau- \mathcal{O} -notation are actually smaller for the split operator method (4.14) than for the Taylor series method (4.11). The regular structure of the split operator method improves also the memory access times and the administration overhead in comparison to the Taylor series method.

So in actual computations the split operator method is faster. But this speed comes at a price:

- The split operator method works only on a regular lattice as shown in Fig. 3.6 while the Crank-Nicholson method and the Taylor series method both work on irregular lattices as shown in Fig. 3.5.
- The split operator method becomes unstable if V has discontinuities. Therefore all potential steps V have to be smeared out over a few (roughly 10) lattice constants. Furthermore it becomes necessary to use very small time steps τ if at some points $V(\mathbf{r})$ is large in magnitude.
- Hard wall Dirichlet boundary conditions in y -direction are more involved to implement because the Fourier transformation imposes periodic boundary condition and thus the simulated system has automatically a cylinder topology. One remedy is to use a discrete sine transformation [172] instead of a Fourier transformation. Or one could use the Crank-Nicholson method for the y -direction, too. If for sake of simplicity one wants to adhere to the Fourier transformation, one has to approximate the hard walls by a finite potential barrier in y -direction which is high compared to typical energy scales of the wave function. This way we can regain the topology of a two dimensional stripe.

These disadvantages make the split operator method less suited for the simulation of cavity geometries as introduced in Sec. 3.8 than the Crank-Nicholson method and the Taylor series method. Nevertheless we performed some simulations using the split operator method because of its speed and because it was developed first.

4.6 Accuracy of the exterior complex scaling boundary conditions

In Sec. 3.7.1 we have verified that the exterior complex scaling boundary conditions (3.63) (abbr. *ECSBC*) work well for Green function calculations in the energy domain. The task is now to verify that these boundary conditions work for wave packet propagation in the time domain, too. This is to be expected as one can switch between the energy domain and the time domain by a Fourier transformation.

To this end we study the same model system as in Sec. 3.7.1, i.e. a one dimensional lattice of length L with a flat potential $V = 0$, a hard wall boundary to the left, a lead attached to the right and a source on the first point as shown in Fig. 3.2. We simulate now the inhomogeneous Schrödinger equation for this system:

$$i\hbar \frac{\partial}{\partial t} \Psi(r, t) = H\Psi(r, t) + S(r)e^{-it\mu_0/\hbar} s(t) . \quad (4.15)$$

The source term emits particles of energy μ_0 and is adiabatically ramped from $s(t) = 0$ for $t \leq 0$ to $s(t) = 1$ for $t \geq \Delta T$ over a time interval ΔT as explained in Sec. 4.7. A good choice is to set $\Delta T \geq 10 \frac{2\pi\hbar}{\mu_0}$.

The simulation is now carried out two times. One time we are using the Crank-Nicholson method (4.5) with transparent boundary conditions (C.7) (abbr. *TBC*) and the other time we are using the Taylor series method (4.11) with *ECSBC*. The wave functions obtained with these two simulations can now be directly compared as shown in Fig. 4.1. We see that both simulations give nearly identical results. From this we can draw two conclusions. Firstly we see that the error terms for both methods given in Eq. (4.5) and Eq. (4.11) are very small because both methods use completely different approximations to the exponential function and give nevertheless nearly identical results. Secondly we can conclude that the *ECSBC* are indeed working very well because they give nearly identical results as the *TBC* which are (almost) perfect in the framework of the Crank-Nicholson method.

In order to check if the *ECSBC* work well simultaneously for multiple energies μ we repeat the calculations shown in Fig. 4.1 for energies μ in the range $\frac{1}{10}\mu_0 \leq \mu \leq 2\mu_0$ while keeping all other simulation parameters fixed. Then we look for the total maximal relative error

$$\varepsilon = \max_{t, \mu} \frac{\max_x |\Psi_{\text{CK}}(x, t) - \Psi_{\text{TS}}(x, t)|}{\max_x |\Psi_{\text{CK}}(x, t)|} .$$

We have found that the error ε is always below 0.005 over the whole energy range for our configuration, so a single realization of *ECSBC* indeed work for well for multiple energies. As in Sec. 3.7.1 the error begins to rise for $\mu < \frac{1}{10}\mu_0$, so low energies are a problem and have to be avoided by restricting the energy range used in simulations.

Another good test to check the performance of the boundary conditions is to emit a strongly dispersive Gaussian wave packet

$$\Psi(x) = \frac{C}{\pi^{\frac{1}{4}} \sqrt{\sigma}} e^{-\frac{(x-x_0)^2}{2\sigma^2}} e^{ikx}$$

onto the boundary and look if anything is reflected back. In our calculations we use $k\sigma = \frac{5}{\sqrt{2}}$ so the wave packet is quite broad in k space and thus is a superposition of many different energy components. Under time evolution with the homogeneous Schrödinger equation $i\hbar \frac{\partial \Psi(t)}{\partial t} = H\Psi(t)$ the

wave packet remains Gaussian [187] but with a time dependent position $x_0(t) = x_0(0) + \frac{\hbar k}{m}t$ and a time dependent width $\sigma(t)^2 = \sigma(0)^2 + (\frac{\hbar t}{m\sigma(0)})^2$ and a phase factor for we do not care because in the following we will only look at $|\Psi(x, t)|$. Therefore we can compare the results of the simulations with an analytical result as shown in Fig. 4.2. As the agreement between the two simulations and the analytical result is quite good we can conclude that the time propagation and the boundary conditions work well.

Similar calculations as shown in Fig. 4.1 and Fig. 4.2 can be done comparing the Crank-Nicholson method using *TBC* with the Crank-Nicholson method using *ECSBC* as used in Sec. 4.5. We find that the *ECSBC* work equally well in connection with the Crank-Nicholson method.

Exterior complex scaling boundary conditions have been used before for time propagation before [100, 142–144, 213] but only in connection with a finite element discretization using sharp exterior complex scaling in position space and a Crank-Nicholson method in time space. In this work we use the smooth exterior complex scaling tight binding approach given by Eq. (3.63) in combination with the Taylor series method (4.11).

4.7 Non-adiabatic switching of the source

While in Sec. 3.2 we switched the source $S(t)$ adiabatically on in this section we want to investigate the effect of non-adiabatic switching. To this end we study the inhomogeneous Schrödinger

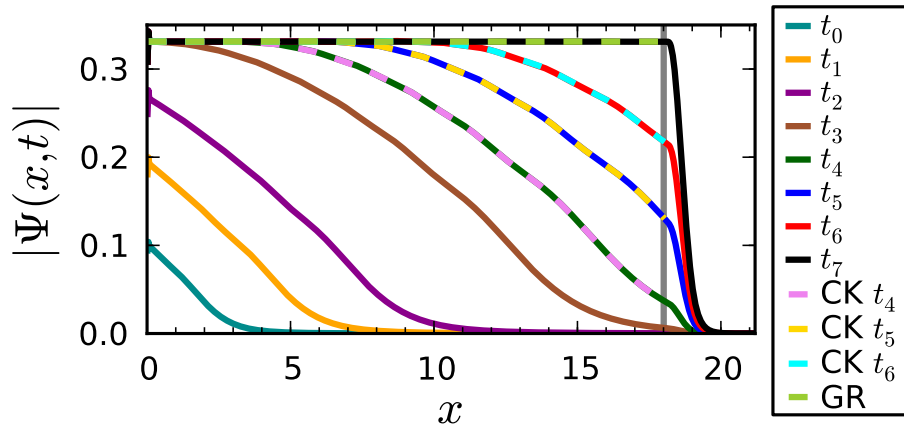


Figure 4.1: This figure illustrates the solution of the inhomogeneous Schrödinger equation Eq. (4.15) by displaying the modulus of the wave function at increasing times t_j . Here the coordinate x is measured in units of the wave length $\lambda = 2\pi\hbar(2m\mu_0)^{-\frac{1}{2}}$. The simulation is done two times. The wave functions obtained from the Taylor series method with *ECSBC* are plotted here as solid lines. On top of these results we plot the wave function obtained from the Crank-Nicholson method with *TBC* as dashed lines (labeled as CK). Furthermore we plot the stationary solution obtained from the Green function method (labeled as GR). The simulation region ends where the gray vertical line is shown. The Crank-Nicholson method and the Green function method simply stop there while the Taylor series method attaches the *ECSBC* beyond this line. The wave function in this region is rotated into the complex plane and therefore decaying. Due to the way we include the source term into the Taylor series method (see Eq. (4.12)) the wave functions obtained from this method have a small discontinuity at the point of the source. But this does not affect the rest of the scattering region.

equation

$$i\hbar \frac{\partial}{\partial t} \Psi(t) = H\Psi(t) + S(t) \quad (4.16)$$

with following time-dependence of the source term:

$$S(t) = S_0 e^{-i\mu t/\hbar} s(t + t_0) \quad (4.17)$$

Here μ is the energy of the source, S_0 is a vector describing the spatial component of the source (e.g. Eq. (3.47)) and $t_0 > 0$ denotes the period of time which passed by since we started switching the source on. The smooth function $s : \mathbb{R} \rightarrow \mathbb{R}$ defines the non-adiabatic switching of the source. It should have following properties:

- $s(t) = 1$ for $t \geq D$. Here $D > 0$ is a constant which defines the time it takes to fully switch the source on. We will keep D constant in this section so no adiabatic switching is performed.
- $s(t) = 0$ for $t \leq 0$.
- $s(t)$ rises smoothly from zero to one between 0 and D .

Such a function can be built with the methods of App. H.

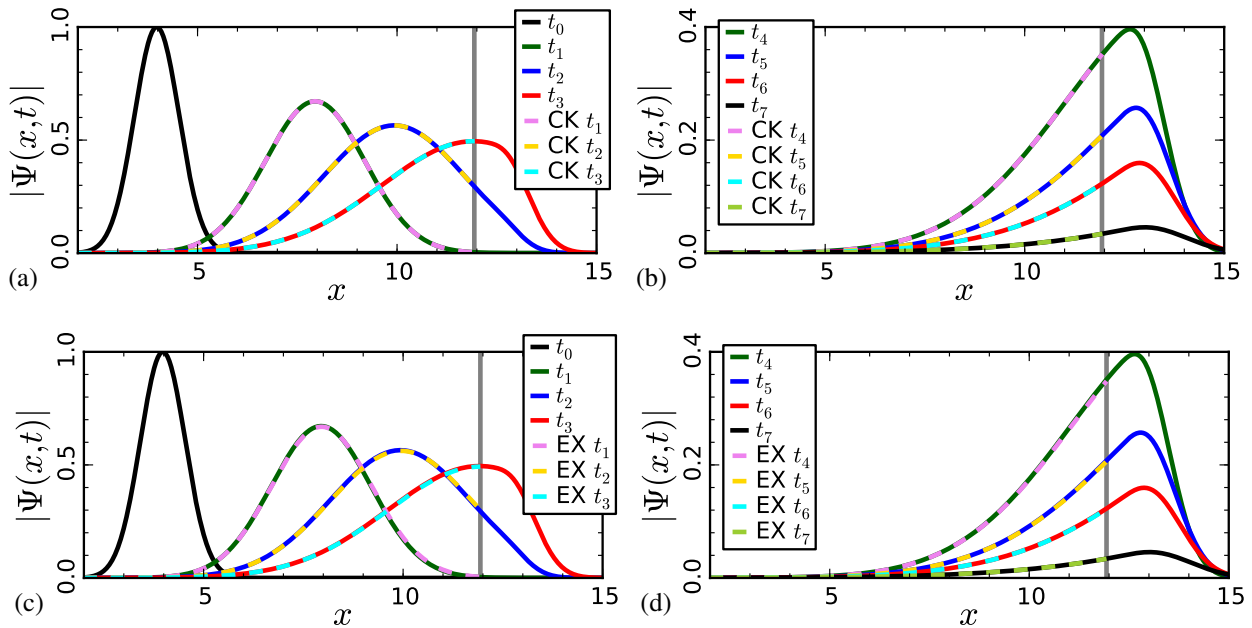


Figure 4.2: These figures illustrate what happens if we emit a strongly dispersive Gaussian wave packet onto the boundary which is presented here by a gray line. See the text in Fig. 4.1 for an explanation what happens to the right of this line. We plot the modulus $|\Psi(x, t)|$ of the wave function at increasing times t_j where x is measured in units of the wave length $\lambda = \frac{2\pi}{k}$. The simulation is again done two times. The results obtained from the Taylor series method using *ECSBC* are shown as solid lines in (a)-(d). In (a) and (b) we compare these results with results obtained using the Crank-Nicholson method with *TBC* shown here as dashed lines (labeled as CK). In (c) and (d) the results from the Taylor series method are compared with results from the exact analytical formula for the modulus of $|\Psi(x, t)|$ shown here as dashed lines (labeled as EX).

We want now to study how the wave function $\Psi(t)$ at $t = 0$ behaves as a function of t_0 . To this end we propagate the inhomogeneous Schrödinger equation 4.16 from $t = -\infty$ to $t = 0$ with the initial condition $\Psi(-\infty) = 0$. This gives us (see Eq. (3.4))

$$\Psi(0) = -\frac{i}{\hbar} \int_{-\infty}^0 e^{-\frac{i}{\hbar}(\mu-H)t'} S_0 s(t' + t_0) dt'$$

and after applying a partial integration (we assume $t_0 > D$)

$$\begin{aligned} \Psi(0) &= G^{(r)} \left[e^{-\frac{i}{\hbar}(\mu-H)t'} S_0 s(t' + t_0) \right]_{-\infty}^0 - G^{(r)} \int_{-\infty}^0 e^{-\frac{i}{\hbar}(\mu-H)t'} S_0 \frac{\partial s(t' + t_0)}{\partial t'} dt' \\ &= G^{(r)} S_0 - G^{(r)} \int_{-t_0}^{-t_0+D} e^{-\frac{i}{\hbar}(\mu-H)t'} S_0 \frac{\partial s(t' + t_0)}{\partial t'} dt' . \end{aligned}$$

Here we have used the retarded Green function $G^{(r)} = \lim_{\epsilon \rightarrow 0^+} (\mu + i\epsilon - H)^{-1}$ to get the correct behavior of $\Psi(\mathbf{r}, t)$ for $|\mathbf{r}| \rightarrow \infty$, i.e. the wavefunction should be a superposition of outgoing plane waves there. One could have introduced a small positive imaginary part into μ from the very start and then have taken the limit $\epsilon \rightarrow 0^+$ to get the same result.

We now rewrite the integral

$$\int_{-t_0}^{-t_0+D} e^{-\frac{i}{\hbar}(\mu-H)t'} S_0 \frac{\partial s(t' + t_0)}{\partial t'} dt' = e^{-\frac{i}{\hbar}(H-\mu)t_0} \int_0^D e^{-\frac{i}{\hbar}(\mu-H)t'} S_0 \frac{\partial s(t')}{\partial t'} dt'$$

and define

$$C = \int_0^D e^{-\frac{i}{\hbar}(\mu-H)t'} S_0 \frac{\partial s(t')}{\partial t'} dt'$$

which gives us

$$\Psi(0) = G^{(r)} S_0 - G^{(r)} e^{-\frac{i}{\hbar}(H-\mu)t_0} C .$$

We are interested what happens in the limit $t_0 \rightarrow \infty$, i.e. what happens if we switch the source on and then wait some time.

As we only want to excite scattering states in the continuous part of the spectrum the overlap between S_0 and any bound state should be zero or at least negligible small. This can be achieved by putting the source sufficient far into the leads because any bound state decays exponentially inside the leads. Using the ideas of Sec. 3.7.2 we can therefore decompose C into resonance states now:

$$C = \sum_n c_n \Psi_{\mathcal{E}_n} \quad \text{with} \quad H \Psi_{\mathcal{E}_n} = \mathcal{E}_n \Psi_{\mathcal{E}_n} \quad \text{and} \quad \text{Im } \mathcal{E}_n < 0 .$$

This gives us

$$\Psi(0) = G^{(r)} S_0 - G^{(r)} \sum_n e^{-\frac{i}{\hbar}(\mathcal{E}_n - \mu)t_0} c_n \Psi_{\mathcal{E}_n} .$$

We are now able to take the limit $t_0 \rightarrow +\infty$ because $\text{Re} [-i\mathcal{E}_n] < 0$:

$$\lim_{t_0 \rightarrow -\infty} \Psi(0) = G^{(r)} S_0 = \lim_{\epsilon \rightarrow 0^+} (\mu + i\epsilon - H)^{-1} S_0 .$$

The interpretation of this result is that we can regain the result of the adiabatic switching of the source (i.e. the retarded Green function (3.6)) by a nonadiabatically switching of the source if we wait long enough. The timescale on which this happens is determined by the distribution of the

imaginary parts of the resonance energies \mathcal{E}_n . What actually happens is that the unwanted vector C decays into the leads under time evolution in a similar way a wavepacket in free space decays to zero at every fixed position under time evolution.

Thus far we only studied non-interacting systems described by the (inhomogeneous) Schrödinger equation where the convergence of the time propagation to a stationary scattering solution can be guaranteed because this is a linear equation. For interacting systems we have to use the (inhomogeneous) Gross-Pitaevskii equation

$$i\hbar \frac{\partial}{\partial t} \Psi(\mathbf{r}, t) = H\Psi(\mathbf{r}, t) + g \frac{\hbar^2}{m} |\Psi(\mathbf{r}, t)|^2 \Psi(\mathbf{r}, t) + S(\mathbf{r})s(t)e^{-i\mu t/\hbar} \quad (4.18)$$

which is for $g \neq 0$ a non-linear equation where in general nothing can be said about the convergence properties of the time evolution process. The convergence behavior is strongly system and parameter dependent. A necessary condition for convergence is that a dynamically stable stationary scattering solution (see Sec. 5.7 for more details) does exist which is not always the case. If that condition fails to hold the wave function $\Psi(t)$ may slowly oscillate around the (unstable) stationary scattering solution or even turbulent behavior can be observed. This is illustrated in Fig. 4.3.

We now look at several selected case studies in more detail. To this end we propagate the (inhomogeneous) Gross-Pitaevskii equation (4.18) using the source term (4.17) starting at $t = 0$ with the initial condition $\Psi(0)=0$. We now keep $t_0 = 0$ fixed and vary t .

For $g = 0$ such a system was already used in Sec. 4.6. As Fig. 4.1 shows the source emits a plane wave whose wavefront travels with the velocity $v = \frac{\hbar k}{m}$ through the system. After the wave front has traversed the system quickly a stationary solution evolves.

For the billiard system \mathcal{B}_5 described in Sec. 5.8.4 the situation is similar. A plane wave is injected from the left lead (where the source is located) into the billiard. The wave front travels through the cavity until a boundary is hit and after a few reflections slowly a stationary scattering state evolves for $g = 0$ as shown in Fig. 4.4.

The filling of the billiard described in Sec. 3.8.1 is not shown here because it is dominated by tunneling of the wavefunction through the potential barriers which is quite slow as it happens on the timescale $\hbar/(\text{Im } \mathcal{E}) \sim 1000\hbar/E_0$. Nothing interesting happens there.

The switch time D is chosen here much larger then strictly necessary for this linear case. The reason is that by varying the source strength $s(t)$ we effectively change the interaction strength g as explained in Sec. 5.1.1 (i.e. $g_{\text{eff}} \sim s(t)$). Therefore by slowly ramping $s(t)$ up we mimic an adiabatic increase in g_{eff} . If that ramping is done slowly enough the wave function $\Psi(t)$ can follow the stationary scattering solutions corresponding to the momentary value of g . After the source is fully switched on we thus get a stationary scattering solution under suitable conditions as shown in Fig. 4.4. Of course it is also possible that the wave function becomes time dependent.

We therefore establish that the population of the scattering system happens in two steps for the interacting case $g \neq 0$: For t small and thus $g_{\text{eff}} \sim s(t) \approx 0$ firstly the linear scattering state evolves. This is then adiabatically slowly transformed into the scattering state for the non-linear case $g \neq 0$. In Sec. 5.4.3 numerical simulations confirming this view will be carried out.

In practical implementations the switch time D in which $s(t)$ rises from 0 to 1 should be made so large that the transmission T as function of the time t shows no pronounced oscillations. But for $g \neq 0$ this principally can not always be achieved, i.e. when no dynamically stable stationary solution exists (see Fig. 4.3, Fig. 5.24 and Fig. 5.39.) or if there are several branches of stationary solutions Ψ as a function of g (see Fig. 5.9).

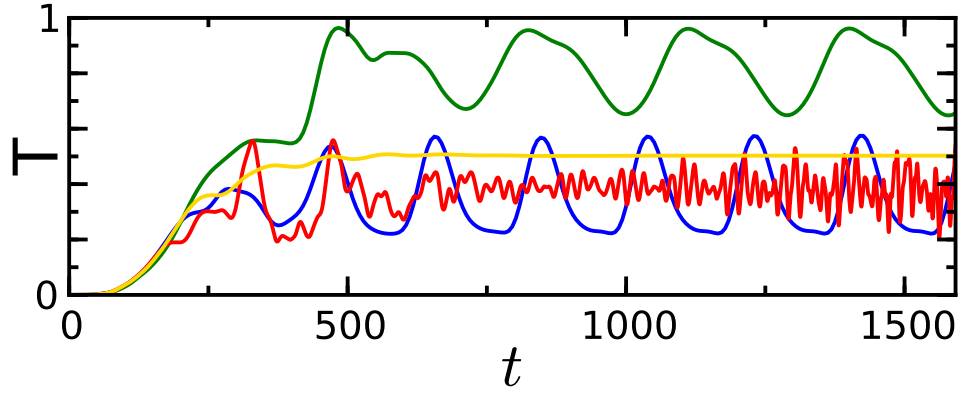


Figure 4.3: This figure displays the transmission T as a function of the time t (measured in units of $2\pi\hbar/E_0$) for different parameter sets using the annular stadium billiard \mathcal{B}_5 described in Sec. 5.8.4. The yellow curve shows for $\mu = 0.935E_0, B = -0.524B_0$ and $g = 0.04$ how a stationary solution evolves. The blue ($\mu = 0.935E_0, B = -0.419B_0$ and $g = 0.06$) and green ($\mu = 0.955E_0, B = -0.367B_0$ and $g = 0.06$) curves show how the wave function slowly oscillates around a dynamically unstable stationary scattering solution. The red curve ($\mu = 0.935E_0, B = -0.524B_0$ and $g = 0.14$) shows a turbulent flow.

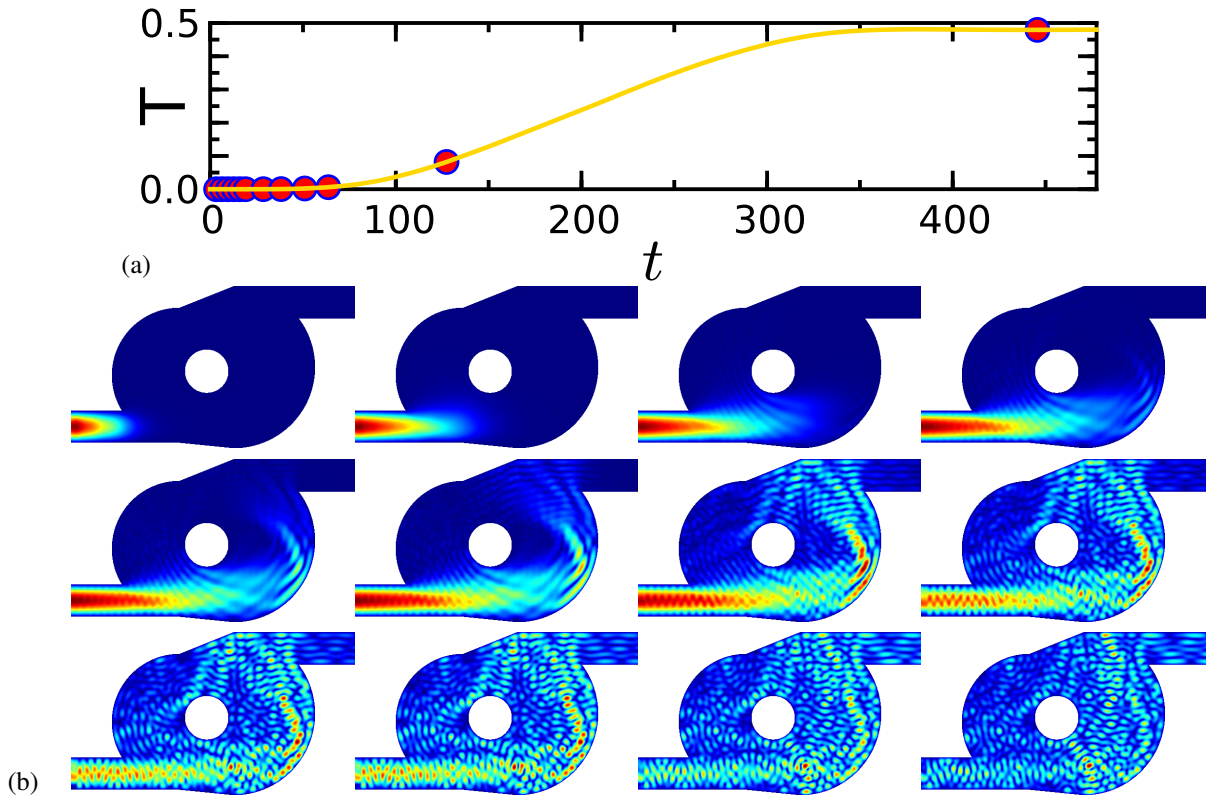


Figure 4.4: This figure illustrates how a stationary scattering solution evolves under time evolution in the annular stadium billiard \mathcal{B}_5 described in Sec. 5.8.4 for the choice of parameters $\mu = 0.93E_0, B = -0.524B_0$ and $g = 0$. Here E_0 is the typical energy of the billiard and B_0 is the typical magnetical field. The cavity is slowly filled by a source in the left lead. Fig. (a) shows the transmission T (i.e. the current inside the right lead) as a function of the time t (yellow curve) which is measured in units of $\frac{2\pi\hbar}{E_0}$. Fig. (b) illustrates $\Psi(\mathbf{r}, t)$ for the increasing times t_n which are marked in (a) as red dots. A stationary solution has evolved for $t \geq 400$.

Chapter 5

Stationary scattering states of the Gross-Pitaevskii equation

5.1 Introduction

While in Chap. 4 we studied the time dependent inhomogeneous Gross-Pitaevskii equation (4.1) the aim of this chapter is to investigate stationary solutions of this time dependent equation when the source term oscillates with the fixed energy μ :

$$i\hbar \frac{\partial}{\partial t} \Psi(\mathbf{r}, t) = H\Psi(\mathbf{r}, t) + g(\mathbf{r}) \frac{\hbar^2}{m} |\Psi(\mathbf{r}, t)|^2 \Psi(\mathbf{r}, t) + S(\mathbf{r}) e^{-it\mu/\hbar} \quad (5.1)$$

with $H = \frac{1}{2m} [-i\hbar \nabla - q\mathbf{A}(\mathbf{r})]^2 + V(\mathbf{r})$.

To this end we insert the ansatz

$$\Psi(\mathbf{r}, t) = \Psi(\mathbf{r}) e^{-it\mu/\hbar}$$

into Eq. (5.1) which gives us

$$\left[\mu - H - g(\mathbf{r}) \frac{\hbar^2}{m} |\Psi(\mathbf{r})|^2 \right] \Psi(\mathbf{r}) = S(\mathbf{r}). \quad (5.2)$$

This is the defining equation for stationary scattering states of the Gross-Pitaevskii equation. In the following we will show how to numerically calculate stationary scattering states as solutions of this equation.

In Chap. 3 we described a procedure to calculate stationary scattering states of the linear Schrödinger equation (which here corresponds to $g(\mathbf{r}) = 0$) using the retarded Green function as shown in Eq. (3.7). The recipe for this essentially was:

- discretize the system on a lattice
- represent the particle reservoir through a source term
- select some finite scattering region
- incorporate the infinite leads through self energies

- solve the resulting linear system of equations

We now have to modify this recipe to apply it to the Gross-Pitaevskii equation.

The most important change is that Eq. (5.2) is a non-linear multi-dimensional system of equations which complicates matters considerably. In Sec. 5.2 and Sec. 5.3 we will show how to solve this non-linear system of equations. We will see that in some cases there exists more than one stationary scattering state for a chemical potential μ . The interpretation of these findings will be given in Sec. 5.4. Furthermore not all solutions are dynamically stable as shown in Sec. 5.7.

The complications arising from the self energy and the source term will be addressed in Sec. 5.1.2.

In the first part all calculation use the system \mathcal{B}_1 described in Sec. 3.8.1.

5.1.1 Scaling behavior of the Gross-Pitaevskii equation

In this section we investigate the question how the strength of the incoming current j_{in} affects the stationary scattering states. To this end we multiply Eq. (5.2) by the parameter $\eta \in \mathbb{R}^+$. This results in

$$\left[\mu - H - \frac{g(\mathbf{r})}{\eta^2} \frac{\hbar^2}{m} |\eta \Psi(\mathbf{r})|^2 \right] \eta \Psi(\mathbf{r}) = \eta S(\mathbf{r}) .$$

As $S(\mathbf{r}) \sim \sqrt{|j_{\text{in}}|}$ according to Eq. (3.23), we can deduce that Eq. (5.2) is left invariant under the simultaneous replacement

$$\begin{bmatrix} g \\ j_{\text{in}} \\ \Psi(\mathbf{r}) \\ S(\mathbf{r}) \end{bmatrix} \mapsto \begin{bmatrix} g \eta^{-2} \\ j_{\text{in}} \eta^2 \\ \Psi(\mathbf{r}) \eta \\ S(\mathbf{r}) \eta \end{bmatrix} \quad (5.3)$$

In particular we have the relation

$$g j_{\text{in}} = \text{const.}$$

from which we can see that we have basically two equivalent options to study stationary scattering states in the non-linear case:

- We can keep g fixed and vary j_{in} . This is probably the preferred experimental realization because j_{in} depends on the coupling of the reservoir to the leads which is easier to change than g . Some time dependent simulations using this option will be done in Sec. 5.4.3.
- We can keep j_{in} fixed and vary g . This will be the preferred option to numerically study stationary scattering states in this chapter. It is possible to do this in an experiment by the methods described in Sec. 2.4 (Feshbach resonance, transversal confinement) but this will be harder because either the confinement potential or the (real) magnetic field has to be changed *globally*.

Two stationary scattering states Ψ_0 and Ψ_1 (corresponding to $(g_a, j_{\text{in}a})$ and $(g_b, j_{\text{in}b})$) generated using these two options can be transformed into each other using Eq. (5.3) as long as $g_a j_{\text{in}a} = g_b j_{\text{in}b}$.

From now on we always use the following normalization of the incoming current j_{in} (and so of $S(\mathbf{r})$) for stationary scattering state calculations:

$$j_{\text{in}} = \frac{E_0}{\hbar} ,$$

where E_0 is the characteristic energy scale of the system as explained in Sec. 3.8.

5.1.2 The position dependent interaction strength

In this section we will explain why we use in our simulations a position dependent interaction strength $g(\mathbf{r})$ and why this does not significantly affect our results.

The first thing to note is that the self energies (3.37) describing the infinite leads only work in the linear case with vanishing interaction. Therefore we have to switch the non-linearity $g(\mathbf{r})$ off inside the leads. The source term $S(\mathbf{r})$ also has to be placed in a region where $g(\mathbf{r})=0$ because we want to avoid the unwanted artificial non-linear feedback between the back-scattered wave and the source. Last but not least a region with $g(\mathbf{r})=0$ allows us to separate the incoming and the reflected part of the wavefunction in the region between the source and the scattering region using the superposition principle (see Sec. 3.4.3, Eq. (3.26)).

For this reasons we assume that the interaction strength $g(\mathbf{r})$ is smoothly and adiabatically switched from a constant value inside the scattering region to zero inside the leads. This situation is schematically depicted in Fig. 5.1. Such a choice of $g(\mathbf{r})$ has been used successfully in a large number of works [98, 99, 159, 160]. The function describing the switching is constructed using the methods of App. H.

In the following we will often decompose $g(\mathbf{r})=g g_0(\mathbf{r})$ where $g \in \mathbb{R}$ is a scalar and $g_0(\mathbf{r})$ is a function which is 1 inside the scattering region (i.e. the cavity) and zero inside the leads.

There are two reasons why this switching of $g(\mathbf{r})$ does hardly affect our results.

The first reason is the adiabatic principle. If we make the transition adiabatically enough the wave function $\Psi(\mathbf{r})$ inside the leads looks locally like a stationary eigenmode of the non-linear Schrödinger equation with a constant interaction strength which takes the local value $g(\mathbf{r})$. In this way unwanted scattering at the effective potential $g(\mathbf{r}) \frac{\hbar^2}{m} |\Psi(\mathbf{r})|^2$ is avoided in the region where we switch on $g(\mathbf{r})$ [159, 160]. The wave function inside the scattering region will hardly be affected by the switching of $g(\mathbf{r})$ in this adiabatic regime.

The adiabatic conditions are well fulfilled if we change $g(\mathbf{r})$ over the range of a few wavelengths of the wavefunction. This is illustrated in Fig. 5.2 where we show stationary scattering solutions (calculated with the methods of Sec. 5.2 and Sec. 5.3) of the one dimensional Gross-

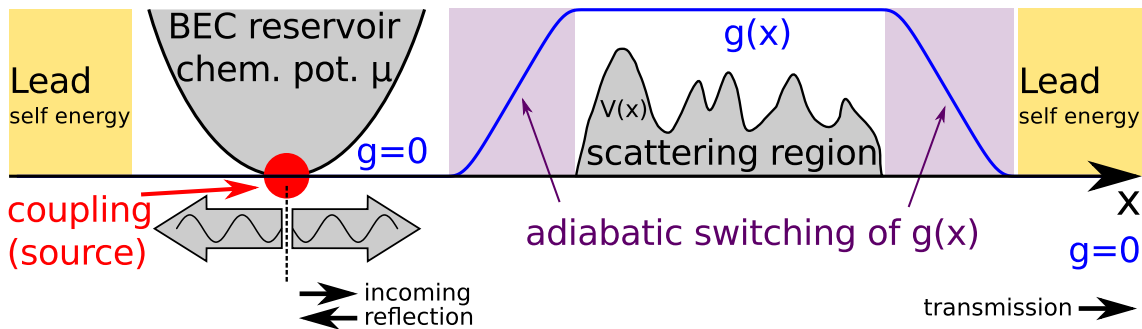


Figure 5.1: While $g(\mathbf{r})$ is assumed to be constant inside the scattering region it is adiabatically switched down to zero to the left and to the right so that it is zero inside the leads which then can be described by self energies. The source term describing a BEC reservoir coupled to the wave guide is also placed in a region where the interaction vanishes.

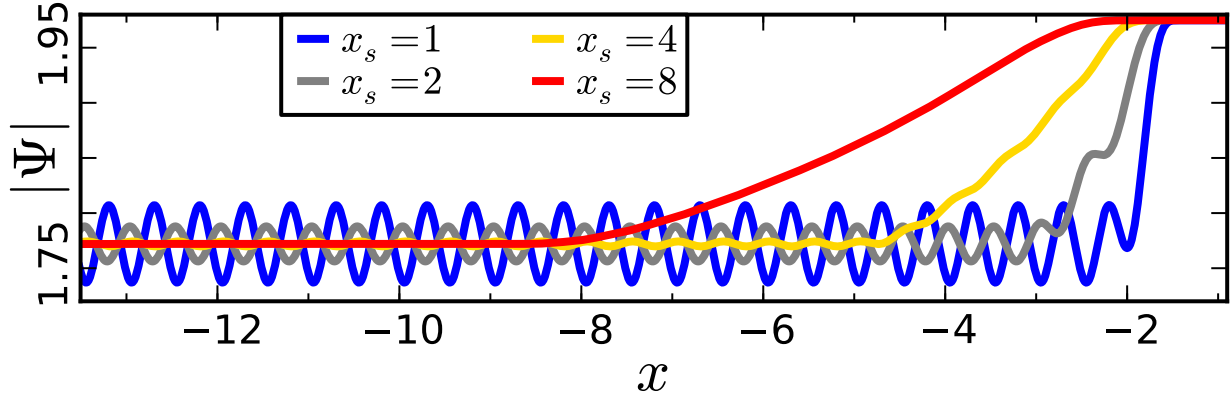


Figure 5.2: This figure illustrates solutions of the Gross-Pitaevskii equation (5.4) for different values of the length x_s over which the interaction strength is switched from zero to its full value. The interaction strength $g(x)$ has a constant non-zero value to the right of the depicted region and vanishes on the left side. The source term $S(x)$ has its support to the left side of the depicted region. All lengths occurring here are measured in units of the wave length $\lambda = \frac{2\pi\hbar}{\sqrt{2m\mu}}$. While for $x_s = 1$ strong interferences are visible indicating significant scattering of the wave function at the non-linear potential, for $x_s = 8$ no interferences are visible which shows that we have reached the adiabatic regime.

Pitaevskii equation with zero potential

$$\left[\mu + \frac{\hbar^2}{2m} \Delta \right] \Psi(\mathbf{r}) - g(\mathbf{r}) \frac{\hbar^2}{m} |\Psi(\mathbf{r})|^2 \Psi(\mathbf{r}) = S(\mathbf{r}). \quad (5.4)$$

The interaction strength is chosen as $g=0.4$ inside the scattering region while the source is normalized in such a way that a fixed incoming current of $j=\frac{\mu}{\hbar}$ is generated (see Eq. (3.23)).

The second reason why the switching of $g(\mathbf{r})$ does not affect our results is that for scattering systems of billiard type introduced in Sec. 3.8 the squared modulus of the wave function $|\Psi(\mathbf{r})|^2$ is on average much bigger inside the cavity than inside the leads¹. Furthermore the cavity has a much bigger area than the relevant region inside the leads. Therefore the interaction potential has the biggest effect inside the cavity and a negligible effect inside the leads. This will be investigated in Sec. 5.6.2 in more detail. This is to be contrasted with the situation in the scenario of coherent back-scattering (see Sec. 6.4.1) studied in [98, 99] where the distance of the region where $g(\mathbf{r})$ was switched on to the scattering region strongly influenced the results. The reason of that effect was that the modulus squared of the wave function and therefore the interaction is not negligible between the source and the scattering region.

Experimentally there are several ways to realize such a position dependent interaction parameter $g(\mathbf{r})$. The first way is a variation of the strength of the transversal confinement potential in z -direction as explained in Sec. 2.2.3. The second way is to tune $g(\mathbf{r})$ position dependently via a Feshbach resonance as explained in Sec. 2.1.3.

¹This can for example be seen by looking at the resonances in Fig. 3.13b, Fig. 5.25, Fig. 5.30 and Fig. 5.35 or by looking at the scattering states in Fig. 5.17, Fig. 5.18 and Fig. 5.19.

5.2 Numerical solution of the non-linear system of equations

While in the linear case $g(\mathbf{r})=0$ one simply has to solve the linear system of equations (3.2) (more exactly Eq. (3.7)) to calculate the stationary scattering state $\Psi(\mathbf{r})$, in the general case one has to solve the non-linear system of equations (5.2). In this section we will describe how to accomplish this.

As in the following we will need the derivative of Eq. (5.2) with respect to Ψ , the non-holomorphicity of the interaction potential $g(\mathbf{r})\frac{\hbar^2}{m}|\Psi(\mathbf{r})|^2\Psi(\mathbf{r})$ in $\Psi(\mathbf{r})$ forces us to split the wave function $\Psi(\mathbf{r})$ in real and imaginary parts² as described in Sec. 5.2.1.

Defining a function $F : \mathbb{R}^{2n} \rightarrow \mathbb{R}^{2n}$ (here n is the number of lattice points)

$$\Psi(\mathbf{r}) \mapsto [\mu - H] \Psi(\mathbf{r}) - g(\mathbf{r})\frac{\hbar^2}{m}|\Psi(\mathbf{r})|^2\Psi(\mathbf{r}) - S(\mathbf{r}), \quad (5.5)$$

we now search for a solution of $F(\Psi) = 0$ which gives us a solution to Eq. (5.2). This is done with Newton's method [157] which is presented in more detail in App. A. One selects a start vector $\Psi_0(\mathbf{r})$ and constructs a sequence of vectors $\{\Psi_k\}_{k=1}^\infty$ (here k is the iteration number) using the iteration:

$$\Psi_{k+1} = \Psi_k - (\mathcal{D}F)^{-1} F(\Psi_k). \quad (5.6)$$

Here $\mathcal{D}F$ is the derivative of F with respect to Ψ evaluated at the point Ψ_k which is calculated in Sec. 5.2.1. If the derivative $\mathcal{D}F$ at the solution is not singular and if the start vector is suitable, this iteration is guaranteed to converge quadratically to the solution of the non-linear equation.

In practice we iterate Eq. (5.6) until $\|F(\Psi)\|$ drops below some selected threshold. This gives us then a solution to the non-linear system of equations (5.2). But for unsuitable choices of the start vector this iteration may fail to converge as seen for example in Sec. 5.2.2. If this happens one has to retry the Newton iteration using a different start vector.

The possibility that the Newton method might fail is a principal problem which sets it apart from the method of solving the Green function problem in the linear case $g=0$. In that case one has to solve a linear system of equations which is always possible (with certain restrictions) as explained in Sec. 3.2.

Furthermore Eq. (5.2) may support more than one solution whereas in the linear case the solution is always uniquely determined. This poses a problem because with a given start vector Ψ_0 one can find at most one of these solutions. For different solutions one needs different start vectors and it is not a priori obvious how to choose them. Also in the case of failure of the Newton iteration the choice of an alternative starting vector is not an easy task. These issues will be addressed in Sec. 5.3.

The non-linear term $g(\mathbf{r})\frac{\hbar^2}{m}|\Psi(\mathbf{r})|^2\Psi(\mathbf{r})$ in Eq. 5.5 is evaluated in a straightforward manner: At each lattice point we simply subtract the numerical value of this expression which depends only on the numerical value of wavefunction on this lattice point. This is to be contrasted with the finite element method (FEM) mentioned in Sec. 3.10 where the evaluation of the interaction term for a specific degree of freedom involves many other degrees of freedom. Therefore in case of the FEM the non-linear term is much more complicated to evaluate. Its evaluation is especially very time consuming for higher order triangle elements which show the best performance in the linear case $g = 0$.

² The alternative would be to use the Wirtinger calculus [77] which introduces both $\Psi(\mathbf{r})$ and $\Psi(\mathbf{r})^*$ as independent variables (see Eq. (5.11) and Eq. (5.31)). The derivative $\mathcal{D}F$ used in Eq. (5.6) would then consist of both $\frac{\partial}{\partial \Psi}$ and $\frac{\partial}{\partial \Psi^*}$. But this calculus is not well suited for numerical calculations.

5.2.1 Calculation of the derivative

As F given by Eq. (5.5) is a polynomial map from \mathbb{R}^{2n} to \mathbb{R}^{2n} , taking the derivative of F with respect to Ψ poses no problem. This derivative is a linear mapping represented by a real $(2n) \times (2n)$ matrix.

In order to practically calculate $\mathcal{D}F$ one uses following splitting of $\Psi(\mathbf{r})$ in real and imaginary parts:

$$\mathbb{C}^n \ni \begin{bmatrix} \Psi_1 \\ \Psi_2 \\ \dots \\ \Psi_n \end{bmatrix} \mapsto \begin{bmatrix} \text{Re } \Psi_1 \\ \text{Im } \Psi_1 \\ \text{Re } \Psi_2 \\ \text{Im } \Psi_2 \\ \dots \\ \text{Re } \Psi_n \\ \text{Im } \Psi_n \end{bmatrix} \in \mathbb{R}^{2n} \quad (5.7)$$

Here Ψ_k denotes the value of Ψ at the lattice point k . The total number of lattice points is n .

We first look at the linear part of Eq. (5.5):

$$\Psi \mapsto [\mu - H] \Psi$$

This is a linear mapping with a matrix $(\mu - H) \in \text{Mat}(\mathbb{C}, n \times n)$ and therefore the derivative is the same mapping with the same matrix. But because we are using transformation (5.7) we have to interpret the matrix in terms of real and imaginary parts. In order to do this we look at following simple function

$$\begin{aligned} f : \mathbb{C} &\rightarrow \mathbb{C} \\ z &\mapsto az . \end{aligned}$$

Here a is a fixed complex number. We now split z and a into real and imaginary parts:

$$\begin{aligned} z &= z_0 + iz_1 && \text{with } z_0, z_1 \in \mathbb{R} \\ a &= a_0 + ia_1 && \text{with } a_0, a_1 \in \mathbb{R} \end{aligned} \quad (5.8)$$

and therefore get:

$$f : \quad z_0 + iz_1 \mapsto a_0 z_0 - a_1 z_1 + i[a_0 z_1 + a_1 z_0] .$$

Using the transformation (5.7) we arrive at

$$\begin{aligned} f : \mathbb{R}^2 &\rightarrow \mathbb{R}^2 \\ \begin{bmatrix} z_0 \\ z_1 \end{bmatrix} &\mapsto \begin{bmatrix} a_0 & -a_1 \\ a_1 & a_0 \end{bmatrix} \begin{bmatrix} z_0 \\ z_1 \end{bmatrix} . \end{aligned} \quad (5.9)$$

This example tells us how to calculate the derivative of the linear part. We take the complex $n \times n$ matrix $\mu - H$ and replace every complex entry by an appropriate real 2×2 matrix just like in Eq. (5.9). We then arrive at a real $(2n) \times (2n)$ matrix representing $\mu - H$.

In order to calculate the derivative of the non-linear part of Eq. (5.5) we first look at following simple function

$$\begin{aligned} f : \mathbb{C} &\rightarrow \mathbb{C} \\ z &\mapsto |z|^2 z . \end{aligned}$$

Again we split z into real and imaginary part as in Eq. (5.8). Applying the transformation (5.7) we arrive at:

$$f : \mathbb{R}^2 \rightarrow \mathbb{R}^2$$

$$\begin{bmatrix} z_0 \\ z_1 \end{bmatrix} \mapsto \begin{bmatrix} (z_0^2 + z_1^2) z_0 \\ (z_0^2 + z_1^2) z_1 \end{bmatrix}.$$

The derivative of this polynomial map at the position z is easily calculated:

$$\mathcal{D}f = \begin{bmatrix} 3z_0^2 + z_1^2 & 2z_0z_1 \\ 2z_0z_1 & z_0^2 + 3z_1^2 \end{bmatrix}. \quad (5.10)$$

This example tells us how to calculate the derivative of the non-linear term $g(\mathbf{r}) \frac{\hbar^2}{m} |\Psi(\mathbf{r})|^2 \Psi(\mathbf{r})$ of Eq. (5.5). We simply have to take the local value Ψ_k (k being the site index) for z and multiply this matrix with the local value $g_k \frac{\hbar^2}{m}$ (assuming that $g(\mathbf{r})$ is real). The resulting real 2×2 matrices are subtracted along the diagonal of the derivative matrix $\mathcal{D}F$.

The Wirtinger calculus [77] analogue of Eq. (5.10) is (* denotes complex conjugation):

$$\mathcal{D}f : \mathbb{C} \rightarrow \mathbb{C}, \quad u \mapsto 2|z|^2 u + z^2 u^*. \quad (5.11)$$

One conveniently summarizes Eq. (5.9) and Eq. (5.10) and writes the derivative of F (given in Eq. (5.5)) with respect to $\Psi(\mathbf{r})$ as follows:

$$\mathcal{D}F = \frac{\partial F}{\partial \Psi(\mathbf{r})} = \mu - H - g(\mathbf{r}) \frac{\hbar^2}{m} \frac{\partial [|\Psi(\mathbf{r})|^2 \Psi(\mathbf{r})]}{\partial \Psi(\mathbf{r})}. \quad (5.12)$$

Similar to the discussion in Sec. 3.9 one can see that the derivative $\mathcal{D}F$ is a sparse matrix and one can therefore use the software library UMFPACK [52] to calculate the LU decomposition [172] of it. Using this LU decomposition one can calculate the action of $\mathcal{D}F^{-1}$ on a vector as needed in the Newton iteration Eq. (5.6).

5.2.2 Selection of the start vector

In this section we calculate the stationary flow of interacting matter waves through the example system \mathcal{B}_1 (see Sec. 3.8.1) using the numerical method presented in Sec. 5.2. This system is almost closed so that the average distance between the resonances is bigger than their average width. Only the two resonance peaks marked in Fig. 3.13a are studied here while the rest of the spectrum is analyzed in Sec. 5.5. One part of the spectrum contains a single resonance well separated from other resonances while the other part contains a resonance influenced by a nearby other resonance.

In order to apply the Newton iteration Eq. (5.6) we need to choose a start vector. The most natural choice is to select the solution of the linear problem for $g = 0$ as start value of the iteration. The other natural choice would be $\Psi = 0$ but after the first iteration of the Newton method this leads to the solution of the linear equation.

The results obtained using this choice of the start vector for variable μ and fixed g are shown in Fig. 5.3. For values of μ which are far away from any resonance the Newton iteration Eq. (5.6) usually converges. But in the vicinity of the resonances the iteration might fail to converge and the success of the Newton iteration is quite random.

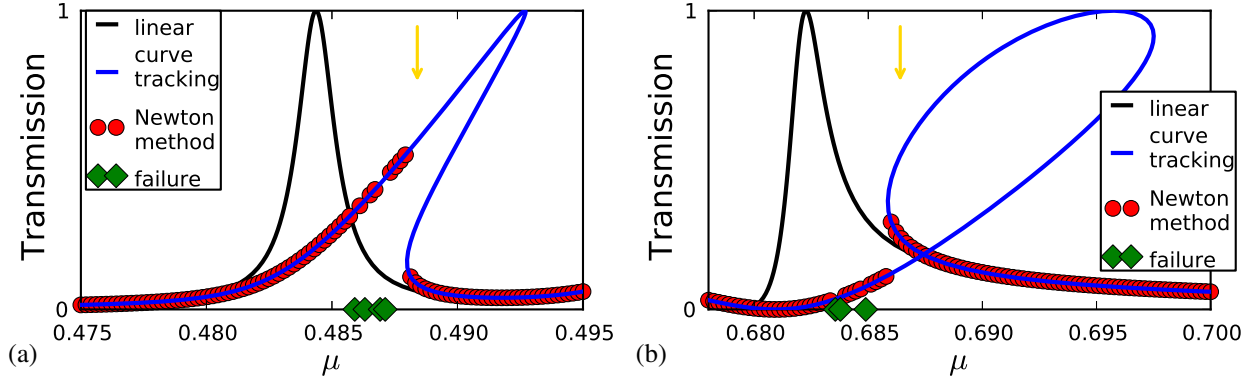


Figure 5.3: In these two figures the transmission spectrum of the billiard introduced in Sec. 3.8.1 and depicted in Fig. 3.11 is shown for a fixed value of the interaction strength g . The black curves show the transmission in the linear case $g=0$ as a reference while the blue curves show the transmission calculated using a continuation method applied to μ as described in Sec. 5.3 for $g=0.001$. The red dots describe the results of the Newton iteration Eq. (5.6) using as a start vector the wave function of the linear case. The green diamonds indicate convergence failure of the Newton method. (a) shows the transmission T in the vicinity of a well isolated resonance peak while (b) shows T in the vicinity of two overlapping resonances. The energy μ is measured with respect to the system-specific typical energy scale E_0 . These two energy intervals are marked in Fig. 3.13. The yellow arrows show the energy values μ used in Fig. 5.4.

The reason for this behavior is that in the vicinity of a resonance the interaction energy

$$g\Lambda = g \frac{\hbar^2 \int g_0(\mathbf{r})^2 |\Psi(\mathbf{r})|^4 d\mathbf{r}}{m \int g_0(\mathbf{r})^2 |\Psi(\mathbf{r})|^2 d\mathbf{r}}$$

becomes very large as we will study in more detail in Sec. 5.6.2. This implies that the effect of the interaction term is very large and therefore the solution for the linear case $g=0$ is no good initial approximation for the solution in the non-linear case. Far off from the resonances the interaction energy is smaller and the solutions of the Gross-Pitaevskii equation (5.2) for $g \neq 0$ are closer to the solution for the linear case $g=0$.

As seen in Fig. 5.3 and Fig. 5.4 we note that for some values of g and μ the system supports more than one stationary solution corresponding to different branches of Ψ as a function of μ or g . Using a single start vector we can find at most one of these solutions, so in order to find all solutions we have to use the more advanced continuation method described in Sec. 5.3.

While in Fig. 5.3 we kept g fixed and varied μ we can also keep μ fixed and vary g , as shown in Fig. 5.4. We note that Ψ as a function of g has also several branches. The Newton method using the linear solution as a start vector only works well on the branch directly connected to $g=0$ as the wave functions on this branch are quite similar to the linear wave function. But the linear wave function does not resemble the wave functions on the other branches and therefore the Newton method becomes quite erratic when the first branch ends.

The obvious way to calculate $\Psi(\mu)$ at those values of μ for which the Newton method failed in Fig. 5.3 is following simple branch tracking algorithm. For a given fixed g we use the Newton method with the linear solution as a start vector at a μ far left of the resonance. This iteration usually converges and gives us $\Psi(\mu)$. Then we increase μ in small steps and apply at the current step the Newton iteration with the solution at the previous step as a start vector. This iteration usually converges, too, as long as we can stay at the same branch. But as we see in Fig. 5.5,

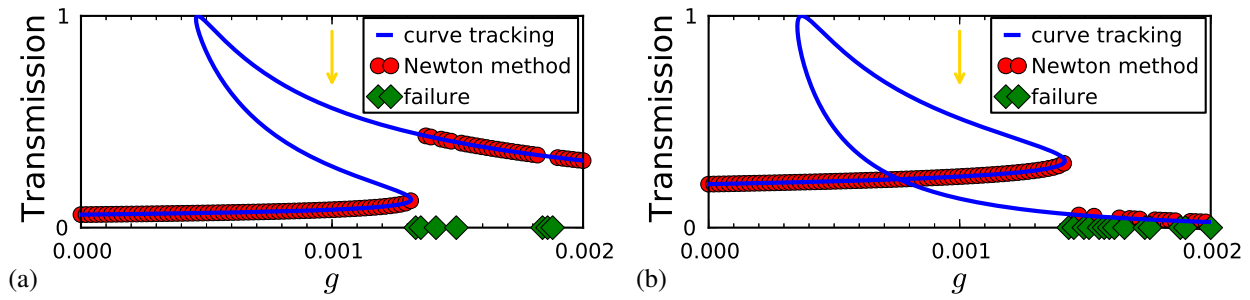


Figure 5.4: These two figures show the transmission as a function of g for a fixed value of μ using the same example system as in Fig. 5.3. (a) uses $\mu = 0.4884$ and (b) $\mu = 0.6864$ corresponding to Fig. 5.3 (a) and (b), respectively. The blue curves show the result obtained from a continuation method applied to g as described in Sec. 5.3. While the red dots show the results obtained from a Newton iteration with the wave function of the linear case as a start vector the green diamonds indicate failure of the Newton method. The yellow arrows show the interaction strengths g used in Fig. 5.3.

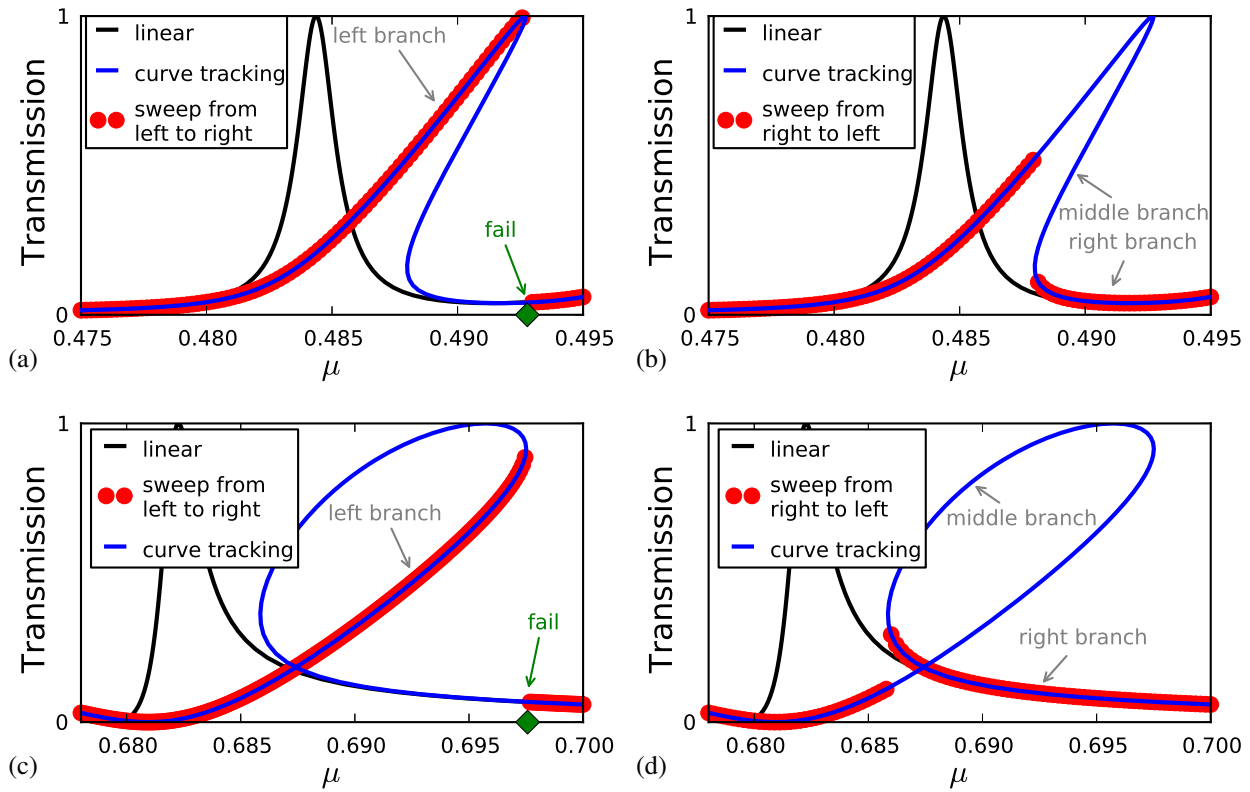


Figure 5.5: In these figures we investigate the same resonance peaks and using the same parameters as in Fig. 5.3. The energy μ is changed in small steps. We use the solution at the previous step of μ as start vector for the Newton method at the current step of μ . The thus obtained results are shown as red dots. In (a) and (c) the calculation proceeds from smaller values of μ to larger values allowing us to access the left branch, while in (b) and (d) the calculation proceeds in the opposite direction allowing us to access the right branch. The branch in the middle is inaccessible with this method. The blue and black curves are identical to those in Fig. 5.3.

Ψ as function of μ can have more than one branch and the branches may end at certain turning points. At those turning points the Newton iteration might fail and we have to restart the above described procedure by applying again a Newton iteration with the linear solution as start vector. This restarting is the main “Achilles heel” of this simple branch tracking algorithm. In more complicated systems with complex resonance structure there is no guarantee that the Newton method will converge with the linear solution as the start vector. It will usually behave quite erratic. A common outcome is a simple failure but it can also pick one of the possible existing many branches at random.

The above described method tracks the branches from left to right. Of course one can do the tracking from right to left, too. This way we can calculate two of the three branches (the left and the right) of Ψ as a function of μ as shown in Fig. 5.5. But the third branch in the middle cannot be calculated this way. Furthermore one has to do multiple sweeps to calculate at least part of the solution set Ψ at certain energies μ . This is quite inconvenient. The situation becomes worse in more complicated resonance scenarios. Therefore we will now develop a better method to calculate all branches at once.

A similar simple branch tracking algorithm can be used for μ fixed and g variable. One uses the solution at the previous step of g for the current step of g as start vector. This procedure has basically the same shortcomings as the branch tracking algorithm for μ variable and g fixed.

5.3 The curve tracking algorithm

The only way to remedy the problem faced in Sec. 5.2 and Sec. 5.2.2 is a continuation method [157, 189]. One regards one of g , B or μ as an additional free parameter³. Using this parameter we reinterpret F (defined by Eq. (5.5)) as a function $F : \mathbb{R}^{2n} \times \mathbb{R} \rightarrow \mathbb{R}^{2n}$. Now $F^{-1}(0)$ is a one dimensional manifold assuming the derivative $\mathcal{D}F$ has full rank on all solutions of $F(\tilde{\Psi}) = 0$ (here $\tilde{\Psi}$ is $\Psi(\mathbf{r})$ plus the additional free parameter). This manifold can conveniently be parametrized by the arclength s as the parametric curve $s \mapsto \tilde{\Psi}(s)$.

Assuming one has found somehow a point $\tilde{\Psi}(s_0)$ on this manifold (for example using the simple Newton iteration 5.6), one now wants to find a new point on the manifold in the vicinity of the old one. As an initial guess for the new point one now uses the linear approximation

$$\tilde{\Psi}(s_0 + \delta s) \approx \tilde{\Psi}(s_0) + \delta s \left. \frac{\partial \tilde{\Psi}(s)}{\partial s} \right|_{s=s_0} \equiv \tilde{\Psi}_{\text{prediction}} . \quad (5.13)$$

Here δs is a given stepsize which is discussed in more detail in Sec. 5.3.3 and $\left. \frac{\partial \tilde{\Psi}(s)}{\partial s} \right|_{s=s_0}$ is the tangent to the manifold which is calculated in Sec. 5.3.1.

In general the right hand side of Eq. (5.13) will not lie exactly on the manifold $F(\tilde{\Psi}) = 0$. Therefore one now applies a corrector step and uses a Newton iteration with $\tilde{\Psi}_{\text{prediction}}$ as the starting vector in order to get the new point $\tilde{\Psi}_{\text{corrected}}$ on the manifold.

The problem now is that one can not apply the Newton iteration on $F : \mathbb{R}^{2n} \times \mathbb{R} \rightarrow \mathbb{R}^{2n}$ directly because this function has the wrong format. Therefore one now chooses a component of $\tilde{\Psi}_{\text{prediction}}$ and holds this component fixed during the iteration process. This effectively reduces the number of unknowns from $2n + 1$ to $2n$ and F can now be interpreted as a function $\mathbb{R}^{2n} \rightarrow \mathbb{R}^{2n}$ (albeit

³ We set $g(\mathbf{r}) = gg_0(\mathbf{r})$ and $\mathbf{A}(\mathbf{r}) = B\mathbf{A}_0(\mathbf{r})$ with $g_0(\mathbf{r})$ and $\mathbf{A}_0(\mathbf{r})$ fixed.

a different one than defined in Eq. (5.5)). The convenient choice for the fixed component is the component of maximal modulus of the tangent vector $\frac{\partial \tilde{\Psi}(s)}{\partial s}$ at $s = s_0$.

This newly found point $\Psi_{\text{corrected}}$ can again be used to find another point on the manifold and so on. That way one can reconstruct the manifold as a sequence of points located on it. This whole procedure is called a continuation method [157, 189] used for *curve tracking* (also called *curve tracing* or *curve following*). The above described algorithm represents a predictor-corrector algorithm (depicted in Fig. 5.6) for performing this continuation procedure.

5.3.1 Calculation of the tangent vector

In order to calculate the tangent vector $\frac{\partial \tilde{\Psi}(s)}{\partial s}$ we take the derivative of $F(\tilde{\Psi}(s)) = 0$ with respect to s (here F is interpreted as $F : \mathbb{R}^{2n} \times \mathbb{R} \rightarrow \mathbb{R}^{2n}$):

$$\mathcal{D}F \frac{\partial \tilde{\Psi}(s)}{\partial s} = 0$$

This means that the tangent $\frac{\partial \tilde{\Psi}(s)}{\partial s}$ is a vector in the null space of the $(2n) \times (2n + 1)$ derivative matrix $\mathcal{D}F = \frac{\partial F}{\partial \tilde{\Psi}}$. If $\mathcal{D}F$ has full rank then the unit vector in this null space is unique except for a sign. The sign can be chosen by fixing a forward direction along the curve, for example by the condition that the scalar product of the tangent vector at the current position and the tangent vector at the previous position should be positive.

As in Sec. 5.2.1 (and similar to Sec. 3.9) the derivative $\mathcal{D}F$ is a sparse matrix which can be factored into a LU decomposition [172] using the software library UMFPACK [52]⁴. The upper triangular matrix U can then be used to calculate a vector in the null space of $\mathcal{D}F$. An alternative to the LU decomposition is the QR decomposition [172] which possesses a superior numerical stability but is more expensive to evaluate. It can be calculated using the sparse matrix library “SuiteSparseQR” [53]. This QR decomposition is not used in this work at the moment but it is an option should the LU decomposition ever prove itself to be insufficient.

⁴ In order to calculate the LU decomposition it is important that the sparse matrix software library can handle non-square matrices. UMFPACK is one of the few which can do so. In case no such library is available one can add as a workaround one further row (non-orthogonal to the null vector) to the matrix in order to make it square again.

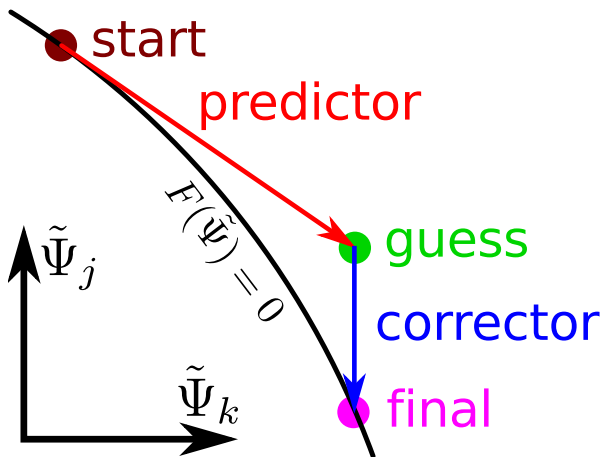


Figure 5.6: This figure explains the predictor-corrector algorithm used to perform the curve tracking. One starts with a known starting point on the manifold (brown). Then one uses the tangent vector as a predictor (red) to get an initial guess (green) for a new point on the manifold. This initial guess is corrected (blue) using a Newton method to get a new final point (magenta) on the manifold $F(\tilde{\Psi}) = 0$. During the Newton iteration we fix the component $\tilde{\Psi}_k$ while correcting all other components $\tilde{\Psi}_j$.

It remains to actually calculate the derivative $\mathcal{D}F$ of F with respect to $\tilde{\Psi}$ for concrete choices of the additional free parameter. If one chooses the chemical potential μ as additional free parameter one has

$$\tilde{\Psi} = \begin{bmatrix} \Psi \\ \mu \end{bmatrix}$$

and the derivative is calculated as follows:

$$\mathcal{D}F = \frac{\partial F}{\partial \tilde{\Psi}(\mathbf{r})} = \left[\frac{\partial F}{\partial \Psi(\mathbf{r})} \mid \frac{\partial F}{\partial \mu} \right] = \left[\mu - H - g(\mathbf{r}) \frac{\partial(|\Psi(\mathbf{r})|^2 \Psi(\mathbf{r}))}{\partial \Psi(\mathbf{r})} \mid \Psi - \frac{\partial \Sigma}{\partial \mu} \Psi - \frac{\partial S}{\partial \mu} \right]$$

Here $\frac{\partial F}{\partial \Psi(\mathbf{r})}$ is calculated as in Eq. (5.12). H depends on μ via the self energy Σ introduced in Eq. (3.37) describing the leads. To calculate $\frac{\partial \Sigma}{\partial \mu}$ one has mainly to differentiate Eq. (3.32) with respect to μ . The source term S depends on μ through the normalization condition (3.23) which has to be differentiated with respect to μ . The derivatives are calculated analytically.

For the choice of the interaction strength g as additional free parameter one has

$$\tilde{\Psi} = \begin{bmatrix} \Psi \\ g \end{bmatrix}$$

and

$$\mathcal{D}F = \frac{\partial F}{\partial \tilde{\Psi}(\mathbf{r})} = \left[\frac{\partial F}{\partial \Psi(\mathbf{r})} \mid \frac{\partial F}{\partial g} \right] = \left[\mu - H - g(\mathbf{r}) \frac{\partial(|\Psi(\mathbf{r})|^2 \Psi(\mathbf{r}))}{\partial \Psi(\mathbf{r})} \mid -g_0(x)|\Psi(\mathbf{r})|^2 \Psi(\mathbf{r}) \right]$$

Here we use the splitting $g(\mathbf{r}) = gg_0(\mathbf{r})$ with $g_0(\mathbf{r})$ fixed as explained in Sec. 5.1.2.

Finally the choice of the magnetic field B as additional free parameter gives us

$$\tilde{\Psi} = \begin{bmatrix} \Psi \\ B \end{bmatrix}$$

and

$$\mathcal{D}F = \frac{\partial F}{\partial \tilde{\Psi}(\mathbf{r})} = \left[\frac{\partial F}{\partial \Psi(\mathbf{r})} \mid \frac{\partial F}{\partial B} \right] = \left[\mu - H - g(\mathbf{r}) \frac{\partial(|\Psi(\mathbf{r})|^2 \Psi(\mathbf{r}))}{\partial \Psi(\mathbf{r})} \mid -\frac{\partial H}{\partial B} \Psi \right]$$

To calculate $\frac{\partial H}{\partial B}$ we have to take the derivative (with respect to B) of the Peierls phase describing the magnetic gauge field in the tight binding Hamiltonian (3.50). Using the splitting $\mathbf{A}(\mathbf{r}) = B\mathbf{A}_0(\mathbf{r})$ with $\mathbf{A}_0(\mathbf{r})$ fixed this reads

$$\frac{\partial}{\partial B} \exp \left[i \frac{q}{\hbar} \int_b^a \mathbf{A}(\mathbf{r}) d\mathbf{r} \right] = i \frac{q}{\hbar} \left[\int_b^a \mathbf{A}_0(\mathbf{r}) d\mathbf{r} \right] \exp \left[i \frac{q}{\hbar} \int_b^a \mathbf{A}(\mathbf{r}) d\mathbf{r} \right]$$

5.3.2 Critical points

The continuation method breaks down if $\mathcal{D}F$ fails to have full rank. Then the tangent vector is not uniquely defined as the null space of $\mathcal{D}F$ has dimension bigger than one. The points at which this happens are called critical points. Typical examples for critical points are bifurcations and cusps.

Luckily critical points are quite rare. This is a consequence of Sard's theorem [141] which says that the measure of vectors y for which $F^{-1}(y)$ contains critical points is zero. Therefore in

practice one rarely encounters critical points except for special values of μ, g and B or in specially crafted example systems.

As usually the critical points are isolated (see above), it is highly unlikely that the continuation method exactly hits a critical point and thus the determination of a tangent vector is not possible. More often the continuation method will simply not work satisfactory in the vicinity of such critical points. We now investigate the behaviour of the continuation method in the vicinity of critical points in two typical case scenarios. Instead of F we use here simpler functions $\mathbb{R}^2 \rightarrow \mathbb{R}$ onto which the continuation method can be naturally also applied.

The first example system is the twice iterated logistic map $g_x(y)$ [123]:

$$\begin{aligned} g_x(y) &= xy(1 - y) \\ f(x, y) &= g_x(g_x(y)) - y = -x^3y^4 + 2x^3y^3 - x^3y^2 - x^2y^2 + x^2y - y \end{aligned} \quad (5.14)$$

We are interested in the curve (x, y) with $f(x, y) = 0$ (see Fig. 5.7a). This curve has a critical point at $(x, y) = (3, \frac{2}{3})$ as there the derivative of f vanishes: $\frac{\partial f}{\partial x} = \frac{\partial f}{\partial y} = 0$. The curve tells us that at this point two branches intersect, that the tangents of these branches are not parallel and that one of the two branches only exists for $x \geq 3$. Such a point is called a pitchfork bifurcation [123, 189].

If we start at one of the branches the continuation method will usually pass through the critical point without problem and trace out the whole branch it started on. The problem is that the continuation method does not notice that it has passed a critical point and that it has missed the other branch. This behaviour is unsatisfactory as information about bifurcation points is important to understand the dynamics of the system [189] since they are one route to chaos [123]. Furthermore the missing branch might be of importance.

The best way [189] to detect critical points during the continuation process would be to monitor the eigenvalues of the square matrix $\mathcal{D}_\perp F$ (which is defined the restriction of $\mathcal{D}F$ to the orthogonal complement of the current one-dimensional kernel) and look for sign changes as at critical points at least one eigenvalue of this matrix is zero. But in our case this is not possible because usually the system size is too big to calculate all the eigenvalues. There are other simpler ways to detect critical points [189] but they only work under certain circumstances and can fail. In this work no critical point detection algorithm has been used and information about such critical points are only obtained indirectly as for example in Fig. 5.15. But as explained above, critical points are quite rare, therefore this is not such a big issue. A further research direction would be to monitor the continuation method for critical points, perhaps first for small systems (for example the systems described in Sec. 5.9) where one can diagonalize $\mathcal{D}_\perp F$ explicitly.

The second example system will be the so called cardioid (a special case of the limaçon of Pascal) [33] given by $h(x, y) = 0$ with h defined as

$$h(x, y) = (x^2 + y^2 - x)^2 - (x^2 + y^2). \quad (5.15)$$

This curve has a cusp [189] at $(x, y) = (0, 0)$, i.e. a critical point $\frac{\partial h}{\partial x} = \frac{\partial h}{\partial y} = 0$ where the tangents of the two branches become parallel. If the continuation method is applied to such a system it will behave highly problematic at the critical point. It will approach the critical point in smaller and smaller steps (using the stepsize control introduced in Sec. 5.3.3), until the accuracy of the Newton method is exhausted (the iteration will be stopped when $|f(x, y)| < \epsilon$ with a given $\epsilon \in \mathbb{R}^+$). Then it will randomly wander around the critical point until the corrector step hits by

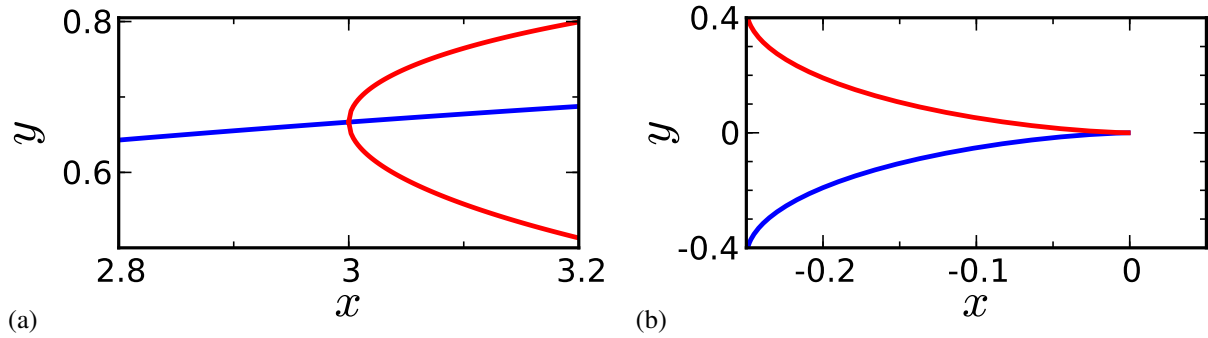


Figure 5.7: (a) shows a pitchfork bifurcation in the curve $f(x, y) = 0$ where f is given by Eq. (5.14). Two branches (here colored red and blue) are visible. They intersect at the critical point $(x, y) = (3, \frac{2}{3})$. (b) shows a cusp in the curve $h(x, y) = 0$ where h is given by Eq. (5.15). Again one can define two branches which touch each other tangentially at the critical point $(x, y) = (0, 0)$.

chance one of the two branches in the outward direction. The continuation method will now trace out the rest of the curve. This behaviour is highly erratic and unwanted. The only option is to monitor the diagonal entries of the U matrix and issue a warning or abort when they behave badly (i.e. drop below some predefined threshold).

The reason why the analysis of such behaviour is important is that under certain conditions the singular values of $\mathcal{D}F$ might become small so that the whole continuation process becomes ill-conditioned. At such points $\mathcal{D}F$ is near critical and the continuation process can show similar behaviour as at cusps. In such situations the only remedy is to improve all numerical parameters which control the Newton method and the stepsize control and repeat the continuation process.

One further possible option to treat such near singular problems would be to use a QR decomposition [172] of $\mathcal{D}F$ instead of a LU decomposition to calculate the tangent vector. The QR decomposition is numerically better behaved than the LU decomposition but is also more expensive, especially for sparse matrices⁵.

It is proper to mention here another principal problem of the continuation method unrelated to critical points. The one dimensional manifold $F^{-1}(\tilde{\Psi})=0$ (where F is defined as in Sec. 5.3) might have several disconnected components. In such a case the continuation method will always stay on the component it started on. There is no way to reach or even detect another component with the continuation method. The only remedy in such a situation is to somehow find a point on the other component and from there on use the continuation method to trace out this component. There are several ways to find points on the disconnected components:

- One can repetitively use the Newton iteration Eq. (5.6) with random start vectors and look if it converges to an interesting solution, i.e. a solution on a previously unknown component. This only works in low dimensional systems because in higher dimensions the probability to hit the convergence region of an interesting solution is too low.
- The continuation method fixes two of the parameters μ, g and B and regards the third parameter as a free variable. A natural generalization is to regard all three parameters as free variables. Thus we can interpret F (defined by Eq. (5.5)) as a function $F : \mathbb{R}^{2n} \times \mathbb{R}^3 \rightarrow \mathbb{R}^{2n}$.

⁵ A software library for sparse matrices is “SuiteSparseQR” [53] which is created by the same author as UMF-PACK.

Neglecting for the moment critical points we now can study the three dimensional manifold $F^{-1}(0)$. The continuation applied to μ, g or B traces out a specific one dimensional section on this manifold where two of the parameters are fixed. Whereas this specific one dimensional sections can show multiple disconnected components in all examples studied in this work the three dimensional manifold is simple connected (i.e. it has only one component). We can therefore reach any point on the three dimensional solution manifold using a series of one dimensional sections on to which the continuation method can be applied. This means that in order to reach a disconnected component we first have to use the continuation method applied on one parameter and then switch to another parameter and so on. Examples of such a situation will be encountered in Fig. 5.15 and Sec. 5.9.

- One can repetitively use the artificial homotopy described in Sec. 5.3.4 with different auxiliary functions until it converges to an interesting branch.

In order to apply these methods one has to make a guess where to expect other components. This can be done by looking at the three different sections in μ, g and B . If the number of different solutions a specific parameter set do not match there have to exist undiscovered components.

An illustrative example for a manifold with multiple disconnected components is the elliptic curve $j(x, y)=0$ (depicted in Fig. 5.8) where j is given by

$$j(x, y) = x^3 - 3x + 1 - y^2. \quad (5.16)$$

Other elementary examples are the hyperbolas $x^2 - y^2=1$ and $xy=1$.

5.3.3 Adaptive stepsize control

The stepsize δs is automatically adjusted to balance between good progress along the manifold and exactness of the initial guess. The algorithm presented here is in close analogy to the adaptive stepsize control for Runge-Kutta ordinary differential equation integrators as presented in [172].

The stepsize adjustment is controlled by two given numerical parameters ε_{abs} and ε_{rel} describing the absolute and relative tolerance of the stepsize control algorithm. Using this two parameters one can introduce a measure ε for the error we made in the predictor step:

$$\varepsilon = \sqrt{\frac{1}{2n+1} \sum_{k=1}^{2n+1} \left[\frac{\tilde{\Psi}_{\text{prediction},k} - \tilde{\Psi}_{\text{corrected},k}}{\varepsilon_{\text{abs}} + \varepsilon_{\text{rel}} \max(|\tilde{\Psi}_{\text{prediction},k}|, |\tilde{\Psi}_{\text{corrected},k}|)} \right]^2}.$$

One now adjusts the stepsize δs in such a way that the error ε is always below one while keeping the stepsize as large as possible.

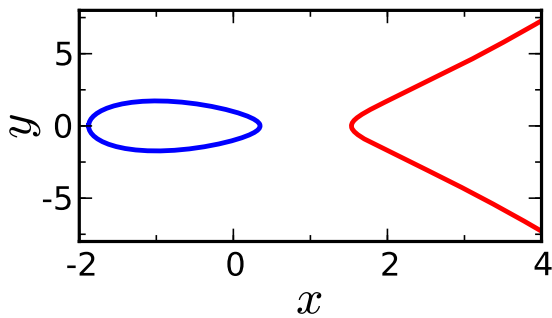


Figure 5.8: This figure displays the elliptic curve $j(x, y)=0$ where j is given by Eq. (5.16). This curve has two disconnected components, here colored in blue and red.

We first notices here that the error one made with the initial guess $\Psi_{\text{prediction}}$ is of order $(\delta s)^2$ because of the relation

$$\tilde{\Psi}(s_0 + \delta s) = \tilde{\Psi}(s_0) + \delta s \left. \frac{\partial \tilde{\Psi}(s)}{\partial s} \right|_{s=s_0} + \mathcal{O}((\delta s)^2) = \tilde{\Psi}_{\text{prediction}} + \mathcal{O}((\delta s)^2).$$

Therefore the error ε roughly scales as $(\delta s)^2$ with the stepsize δs . This scaling behavior is now used in the stepsize control mechanism.

If the error is smaller than or equal one ($\varepsilon \leq 1$) we accept the predictor-corrector step and adjust the stepsize δs as follows:

$$\delta s_{\text{new}} = \delta s_{\text{old}} \min\left(\frac{0.9}{\sqrt{\varepsilon}}, 2\right)$$

This choice has the effect that the stepsize δs_{new} of the next step is as large as possible while still keeping the error of the next step below one. Of course there is no guarantee that the next step will be accepted with this choice of δs_{new} . But it works most of the time; in typical cases more than 90% of the steps using the thus chosen new stepsize are accepted in the first try.

If the error is bigger than one ($\varepsilon_{\text{new}} > 1$) we repeat the predictor-corrector step with the new stepsize

$$\delta s_{\text{new}} = \delta s_{\text{old}} \max\left(\frac{0.9}{\varepsilon}, \frac{1}{10}\right).$$

One uses here the factor $\frac{1}{\varepsilon}$ instead of the factor $\frac{1}{\sqrt{\varepsilon}}$ to be on the safe side. The predictor-corrector step is then repeated until the error ε is smaller than one. If the Newton iteration for the calculation of $\Psi_{\text{corrected}}$ fails we also retry the predictor-corrector step with a reduced value of δs .

For most simulations the choice $\varepsilon_{\text{abs}} = \varepsilon_{\text{rel}} = 0.001$ is sufficient. But in some hard cases⁶ the curve tracking algorithm takes the wrong turn. If that happens we have to repeat the simulation with a smaller error tolerance, for example $\varepsilon_{\text{abs}} = \varepsilon_{\text{rel}} = 0.0001$.

5.3.4 Artificial homotopy

In the previous section we applied the continuation method using parameters naturally occurring in the Gross-Pitaevskii equation, i.e. μ, g and B . But there are further possibilities as described in [152, 157]. One can introduce an artificial parameter λ inducing a homotopy from an easily solvable system of equations to the non-linear equation (5.2). This can be done as follows. Let $F : \mathbb{R}^{2n} \rightarrow \mathbb{R}^{2n}$ be the function defined in Eq. (5.5). Let $G : \mathbb{R}^{2n} \rightarrow \mathbb{R}^{2n}$ be an auxiliary function whose solution to $G(\Psi_0)=0$ can be easily calculated. Then define the function H as:

$$\begin{aligned} H : \mathbb{R}^{2n} \times \mathbb{R} &\rightarrow \mathbb{R}^{2n} \\ (\Psi, \lambda) &\mapsto \lambda F(\Psi) + (1 - \lambda)G(\Psi). \end{aligned}$$

We start at $\lambda=0$. Here the equation $H(\Psi, 0)=0$ is solved by Ψ_0 with $G(\Psi_0)=0$. We can now use the curve tracking algorithm to follow the manifold $H(\Psi, \lambda)=0$ until we reach $\lambda=1$ which gives us $H(\Psi_1, 1)=0$. Thus we have found a stationary scattering state because now we have $F(\Psi_1)=0$.

A simple choice for the auxiliary function G is

$$G : \quad \Psi \mapsto \Psi - A$$

⁶This happens if the solution manifold is close to a critical point as discussed in Sec. 5.3.2.

where $A \in \mathbb{R}^{2n}$ is a given fixed vector. The solution to $G(\Psi_0)=0$ is $\Psi_0 = A$ and therefore this method can be easily implemented. Sard's theorem mentioned in Sec. 5.3.2 tells us that for almost all choices of A the set $H^{-1}(0)$ will be free of critical points and thus a one dimensional manifold. If the path emanating from $\lambda=0$ is bounded, then Watson's theorem [157] tells us that there is a well behaved path from $\lambda=0$ to $\lambda=1$. But for some choices of A this path might be unbounded and then there is no connection between $\lambda=0$ and $\lambda=1$. In this case the manifold $H^{-1}(0)$ consists of several disconnected components, a possibility already mentioned in Sec. 5.3.2. If this happens one has to choose another vector A or one has to switch to a better auxiliary function G .

As Eq. (5.5) is a third degree polynomial equation system in Ψ there exists a function (suitably parametrized) which is guaranteed to produce all solutions of $F(\Psi)=0$ [152]. Let $A, B \in \mathbb{R}^{2n}$ be two given predefined vectors. Let $\Psi \in \mathbb{R}^{2n}$ be understood as a real vector. Now we can define following auxiliary function:

$$G : [\Psi_s]_{s=1}^{2n} \mapsto [A_s \Psi_s^3 - B_s]_{s=1}^{2n}.$$

Here Ψ_s denotes the s th component of the vector Ψ . If one allows A and B to become complex all isolated solutions of $F(\Psi)=0$ are guaranteed to be reached by a path in $H^{-1}(0)$ emanating from $\lambda=0$ for suitable choices of A and B . The only problem with this approach is that such solution might be complex, i.e. that they are elements of \mathbb{C}^{2n} . Such solutions are of no interest to us. If we want to stay entirely in \mathbb{R}^{2n} (i.e. $A, B \in \mathbb{R}^{2n}$), therefore even this auxiliary function might fail to produce all solutions of $F(\Psi)=0$ with $\Psi \in \mathbb{R}^{2n}$, but it is still much better then the simple function $G : \Psi \mapsto \Psi - A$.

This artificial homotopy is very useful if we cannot find a suitable starting vector to make the Newton iteration converge and if the natural homotopies (i.e. μ, g and B) cannot be applied, for example if we want to go to a disconnected branch.

5.4 Time dependent simulations

5.4.1 Time dependent population of the scattering system

Already in Fig. 5.3 we have seen that for a fixed non-vanishing interaction strength g the stationary scattering state Ψ can have more than one branch as a function of μ . Similar effects happen for some fixed values of the chemical potential μ if we regard Ψ as a function of g as seen in Fig. 5.4.

The question is how to interpret these findings. To answer this question one must keep in mind the experimental realisation. At the beginning of an experiment the scattering region will be empty. Then it will be slowly populated by the particle reservoir. Therefore we now perform time dependent simulations in which the source term describing this reservoir slowly populates the scattering region as described in Sec. 4.7:

$$i\hbar \frac{\partial}{\partial t} \Psi(\mathbf{r}, t) = H\Psi(\mathbf{r}, t) + g \frac{\hbar^2}{m} |\Psi(\mathbf{r}, t)|^2 \Psi(\mathbf{r}, t) + S(\mathbf{r}) s(t) e^{-i\mu t/\hbar} \quad (5.17)$$

Here again $s(t)$ is a switching function which rises from zero to one in the interval $0 \dots D$.

For fixed parameters μ and t we start at time $t = 0$ with $\Psi = 0$ and propagate Eq. (5.17) until a time $t_1 \gg D$ at which a stationary scattering state has evolved. Then the transmission (defined as $j_{\text{out}}/j_{\text{in}}$) is measured and compared with the results from the direct computation of the

stationary scattering state using the non-linear equation solver. This calculation is repeated for many different choices of μ and g . The results are presented in Fig. 5.9.

One can see that the time dependent simulation always populates one of the branches calculated with the continuation method. For parameters where the currently populated branch ends the time dependent simulation jumps to another branch. At those points the convergence of the time dependent simulation towards a stationary state is very slow but for the other values of the parameters examined here we usually have fast convergence.

The crucial question is now which branch will be populated. The answer is that one must regard Ψ as a (multivalued) function of g . At a fixed energy μ , time dependent simulations will usually populate that value of $\Psi(g)$ for which the arclength of the path from $(\Psi(0), 0)$ to $(\Psi(g), g)$ along the manifold $F(\Psi, g) = 0$ is smallest. In order to avoid repetition we will postpone the detailed explanation to Sec. 5.4.3.

If we only look at the transmission T as function of μ we have to invoke the perturbation theory developed in Sec. 5.6.2 to answer the question which branch will be populated. Usually it is the branch which is the least shifted by the interaction energy $g\Lambda$. In practice the criterion for T as function of g is of more use.

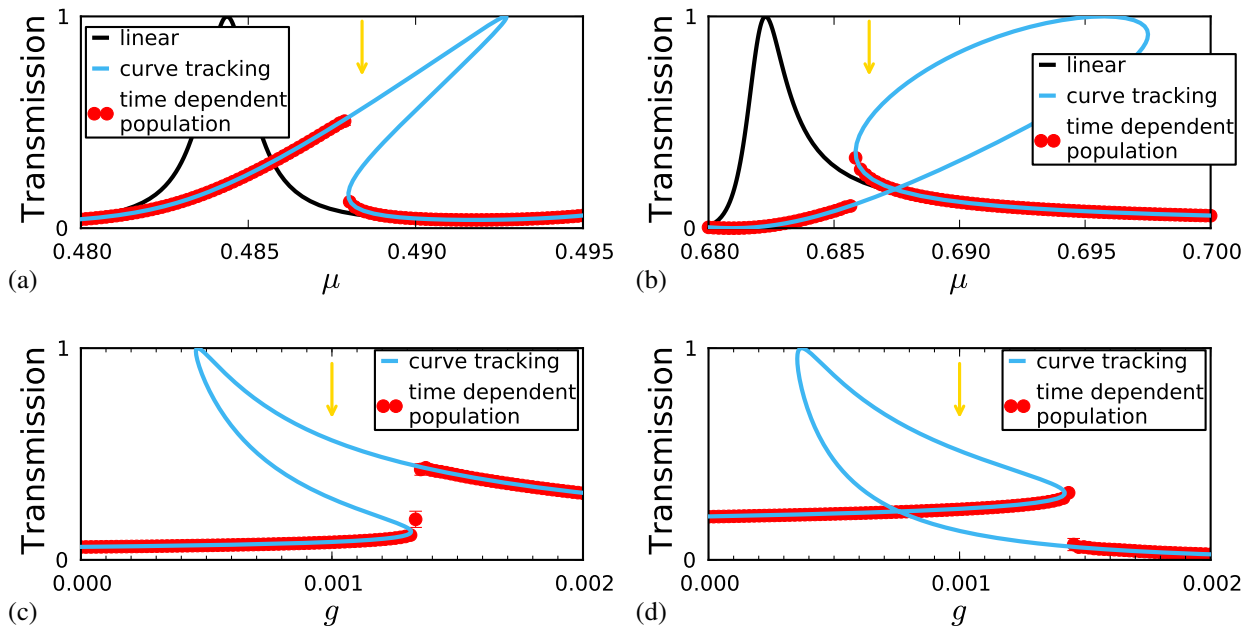


Figure 5.9: These figures compare the transmissions obtained by the curve tracking method with the results obtained with time dependent simulations. The parameters are the same as in Fig. 5.3 and Fig. 5.4. (a) and (c) show the behaviour in the vicinity of one of the resonances. The yellow arrow in one figure denotes the value of the parameter which was fixed in the other figure. Likewise (b) and (d) form one pair. The error bars of the time dependent simulation results (which are for the most parameters invisible small) indicate if the time dependent simulation has converged to a stationary scattering state. In these simulations we used the switch time $D = 3000\hbar E_0^{-1}$ and performed a time propagation until $t_1 = 12000\hbar E_0^{-1}$ where E_0 is the typical energy scale. The magnitude of D and t_1 is roughly determined by the width of the resonances.

5.4.2 Time dependent variation of μ

In Sec. 5.4.1 we have seen that always only one of the branches will be populated. What is the interpretation of the other branches which are not populated ? To answer this question we note that the chemical potential μ was fixed during the simulation of Eq. (5.17). If we allow the chemical potential μ to change with time we will see that we are now able to populate other branches. To this end we study the Gross-Pitaevskii equation with following time dependence of the source term:

$$i\hbar \frac{\partial}{\partial t} \Psi(\mathbf{r}, t) = H\Psi(\mathbf{r}, t) + g \frac{\hbar^2}{m} |\Psi(\mathbf{r}, t)|^2 \Psi(\mathbf{r}, t) + S(\mathbf{r}) s(t) \exp \left[-\frac{i}{\hbar} \int_0^t \mu(t') dt' \right] . \quad (5.18)$$

Here $\mu(t)$ is the desired time dependence of the chemical potential and $s(t)$ is a switching function only different from 1 at the very beginning of the simulation. If $\mu(t)$ changes adiabatically slowly with time, at the time t the source approximately oscillates with the energy $\mu(t)$ and the wave function $\Psi(t)$ will adapt itself to the stationary scattering solution corresponding to the momentary value of μ . This is shown in Fig. 5.10. We used following time dependence of the chemical potential:

$$\mu(t) = \mu_0 + (\mu_1 - \mu_0) \frac{t}{t_A} .$$

The simulation can be done by starting left of the resonance and then increasing μ or by starting right of the resonance and then decreasing μ . Each time the wave function Ψ follows the branch it is currently located on until that branch ends. Then Ψ jumps to another branch and for a short time shows strong time dependence (i.e. not only the trivial $e^{-\frac{i}{\hbar}\mu t}$ time dependence) until it is converged to that branch. These findings can be interpreted as a kind of hysteresis effect, i.e. the behaviour of the system depends on its history in the regime where there are several branches. In contrast to Sec. 5.4.1 the time propagation of Eq. (5.18) has only to be done twice, i.e. once for each direction.

Similar results have been found in [38, 67, 159–161] for one dimensional systems.

So we have found a method to populate one of the branches which is not reached by the population method described in Sec. 5.4.1. But there is still one branch which cannot be populated by Eq. (5.17) and Eq. (5.18), i.e. the middle branch in Fig. 5.10a and the top branch in Fig. 5.10b. In order to reach these “missing” branches one would need to vary an additional parameter besides μ with time, for example g or j_{in} . Such simulations have not been carried out. Indeed they would be problematic because as we will see in Sec. 5.7, the middle branch is dynamically unstable. Therefore during a simulation the wave function $\Psi(t)$ will after some time t_u start to deviate from this branch. Any switching of μ and j has to be done faster than t_u and then the adiabaticity condition might be violated.

Similar problems are visible in Fig. 5.29 and Fig. 5.40 in regions where no dynamically stable stationary solution exists. The wavefunction cannot follow the stationary solution in this regions for arbitrary long times even if the adiabaticity condition is met.

In actual experiments the change of the chemical potential μ with time might be not so easily carried out. But the same results can be obtained by adding a time dependent shift to the scattering potential which is perhaps easier to realize.

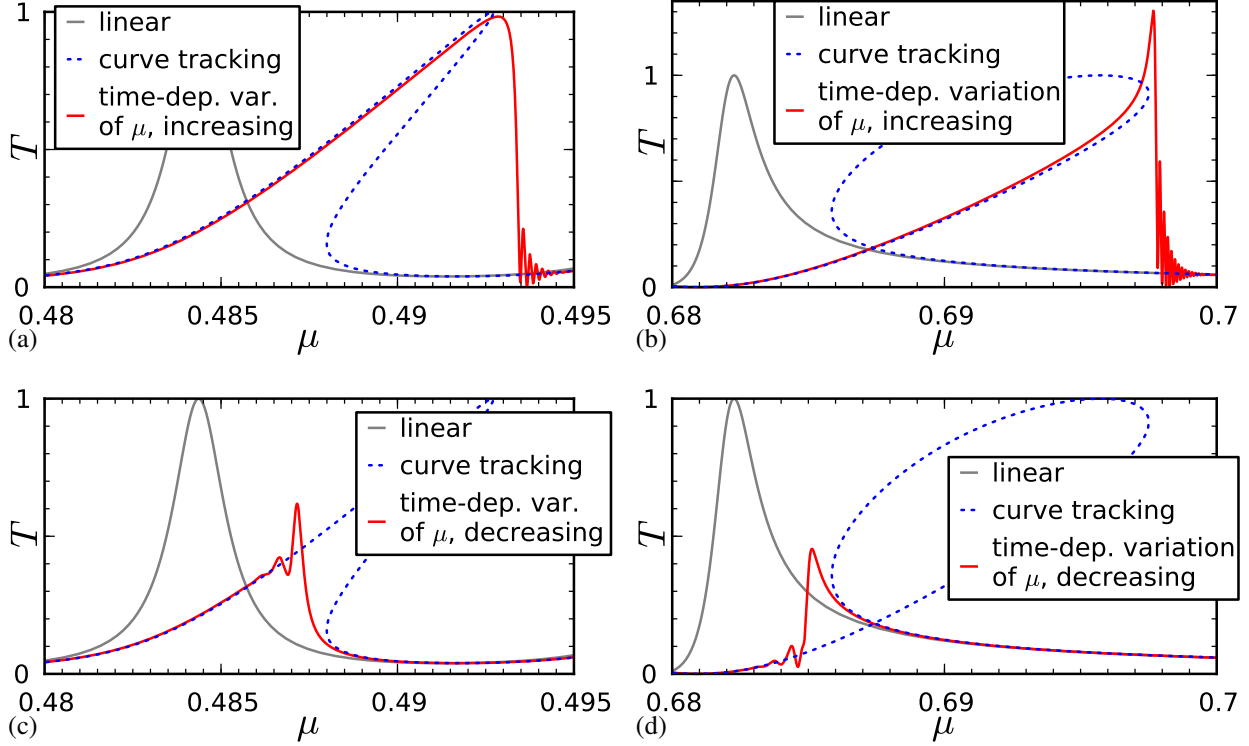


Figure 5.10: These plots compare the results obtained from the propagation of Eq. (5.18) with the stationary scattering states. Plotted is $T(t)$ vs. $\mu(t)$ (red curve) where the transmission is defined as $T(t) = j_{\text{out}}(t)/j_{\text{in}}$. As the wave function $\Psi(t)$ shows strong time dependence when it jumps from one branch to another, $T(t)$ can eventually become larger than one. The system is the same as in Fig. 5.3. In all plots the shown energy range was passed in $t_A = 60000 \hbar/E_0$ with the typical energy scale E_0 .

5.4.3 Time dependent variation of g and j_{in}

In Sec. 5.4.2 we kept g fixed during the time propagation and varied μ . Now we keep μ fixed and vary g :

$$i\hbar \frac{\partial}{\partial t} \Psi(\mathbf{r}, t) = H\Psi(\mathbf{r}, t) + g(t)g_0(\mathbf{r}) \frac{\hbar^2}{m} |\Psi(\mathbf{r}, t)|^2 \Psi(\mathbf{r}, t) + S(\mathbf{r})s(t)e^{-i\mu t/\hbar}. \quad (5.19)$$

For the time dependence of g we use the function

$$g(t) = t \frac{g_A}{t_A} \text{h}(t_A - t) + (2g_A - t \frac{g_A}{t_A}) \text{h}(t - t_A)$$

where h is the Heaviside step function [33]. g is first linearly ramped up and afterwards linearly ramped down. This way we obtain both the behaviour of $\Psi(t)$ for increasing g and for decreasing g in one simulation as shown in Fig. 5.11. If $g(t)$ changes adiabatically slowly with time, then $\Psi(t)$ can follow the stationary solution for the momentary value of g . The wave function will stay on the branch it is currently located on until that branch ends. Then it will jump to another branch. This behaviour is equivalent to the results obtained for variation of μ in Sec. 5.4.2.

In Sec. 5.1.1 we have seen that a change in g is effectively equivalent to a change in the incoming current j_{in} . Therefore Eq. (5.19) is equivalent to following equation:

$$i\hbar r \frac{\partial}{\partial t} \Psi(\mathbf{r}, t) = H\Psi(\mathbf{r}, t) + g_f g_0(\mathbf{r}) \frac{\hbar^2}{m} |\Psi(\mathbf{r}, t)|^2 \Psi(\mathbf{r}, t) + S(\mathbf{r})\tilde{s}(t)e^{-\frac{i}{\hbar}\mu t}. \quad (5.20)$$

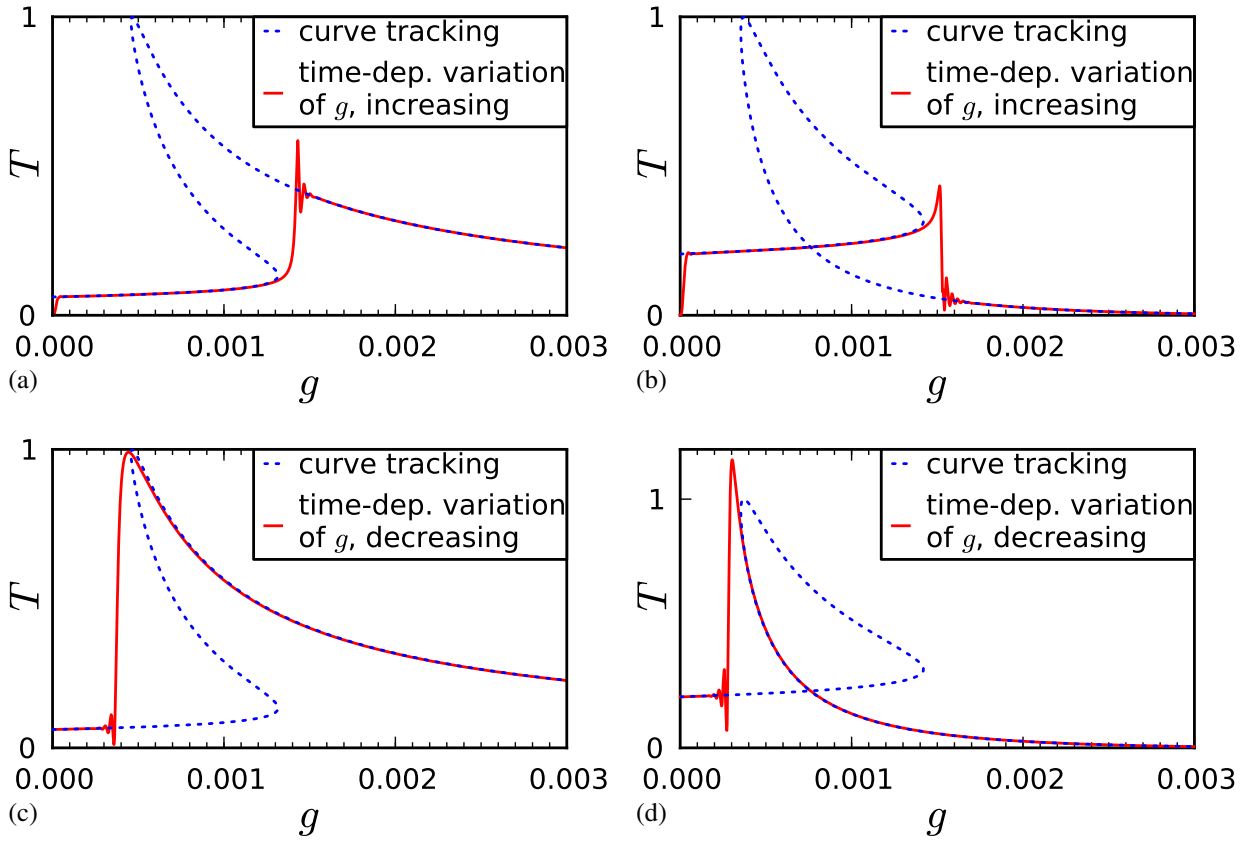


Figure 5.11: In these figures the stationary scattering states are compared with the results obtained from propagation of Eq. (5.19). We plot here $T(t) = j_{\text{out}}(t)/j_{\text{in}}$ vs. $g(t)$. The shown range of g is traversed in the time $t_A = 150000 \hbar/E_0$ (i.e. $g_A = 0.003$). The parameters are the same as in Fig. 5.4.

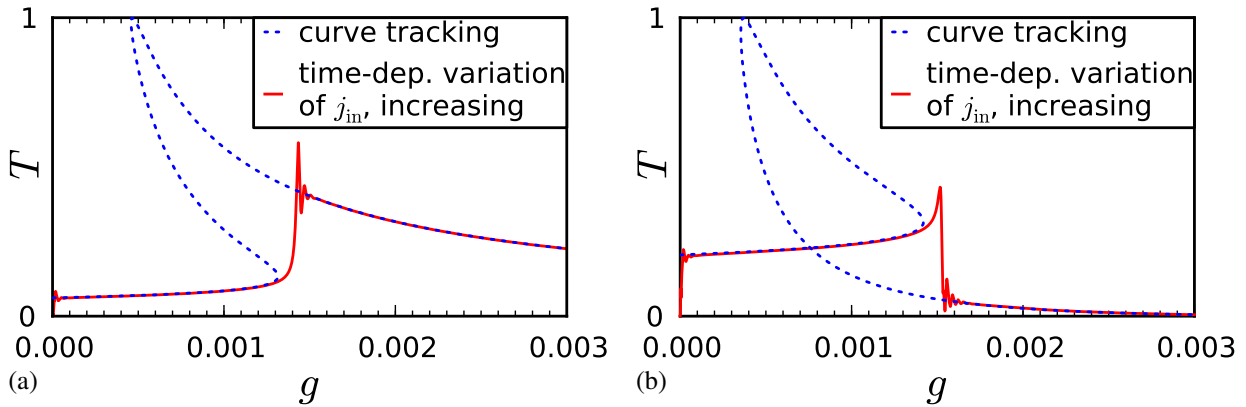


Figure 5.12: These graphs show the comparison of the the results obtained from Eq. (5.20) with the stationary solutions. According to Eq. (5.21) we plot here $T(t)$ vs. $g_{\text{eff}}(t)$. As parameters for the simulation we use $j_{\text{in},0} = 1 E_0/\hbar$, $g_0 = 0.001$ and $t_B = 50000 \hbar E_0^{-1}$, i.e. we traverse the shown range of g in the time $t = 150000 \hbar E_0^{-1}$.

Here $S(\mathbf{r})$ is normalized to create the fixed incoming current $j_{\text{in},0}$ (see Eq. (3.23) or Eq. (3.47)) while g_f is kept fixed with $g_f \neq 0$. The incoming current j_{in} should raise linearly with time, so we use following time dependence of the source term:

$$\tilde{s}(t) = \sqrt{\frac{t}{t_B}} \quad \Rightarrow \quad j_{\text{in}}(t) = \frac{t}{t_B} j_{\text{in},0}$$

To compare the results obtained using this equation (5.20) with the stationary scattering states we have to plot

$$T(t) = \frac{j_{\text{out}}(t)}{j_{\text{in}}(t)} \quad \text{vs.} \quad g_{\text{eff}}(t) = g_f \frac{j_{\text{in}}(t)}{j_{\text{in},0}} = g_f \frac{t}{t_B}. \quad (5.21)$$

The results are shown in Fig. 5.12. We restrict ourselves to increasing values of j_{in} because the results obtained by variation of j_{in} are nearly identical to the results obtained by variation of g . As mentioned in Sec. 5.1.1, a variation in j_{in} should be easier to realize experimentally than a variation of g , but because of the evident equivalence it does not matter which variant we choose.

In Sec. 4.7 and Sec. 5.4.1 we described how to populate a stationary scattering state for fixed parameters g, μ and j_{in} by propagating Eq. 5.20 using instead of $\tilde{s}(t)$ a switching function $s(t)$ rising slowly from 0 to 1. In the adiabatic regime the exact functional form of $s(t)$ or $\tilde{s}(t)$ does not matter, all that is important is that the functions rise adiabatic slowly so that the wave function can adapt itself to the momentary stationary solution. So the population of the scattering system in the aforementioned sections happens as described above and shown in Fig. 5.11 and Fig. 5.12. The only difference is that there we rise j_{in} faster than in this section and then wait some time until all unwanted components have decayed.

This insight also answers the question raised in Sec. 5.4.1 which branch will be populated. The population process starts at $g_{\text{eff}} = 0$ and then follows this branch until it ends. Then it jumps to the branch which exist for bigger $g_{\text{eff}} = 0$ and follows that branch. So in the end that branch will be populated where the point $(\Psi(g), g)$ has the shortest arclength to the point $(\Psi(0), 0)$ along the manifold $F(\Psi, g)=0$. Of course complications can arise, for example if there exists more than one branch when the old branch ends. Also then it is likely that the branch with the shortest arclength will be populated because this branch will probably be the most similar to the old one. Another possible complication is that there might exist no dynamically stable branch as seen in Sec. 5.7. Then no stationary solution will evolve during time propagation. Examples for this behaviour can be seen in Fig. 4.3, Fig. 5.24, Fig. 5.39 and Sec. 5.9.

5.5 Curve tracking for various parameters

In the previous sections we have only shown the behaviour of the transmission as a function of the chemical potential μ in the linear case and for a single fixed value of the interaction strength g . Likewise the transmission as function of g was only shown for two values of μ . Now we study the behaviour of the transmission a more diverse parameter choice as shown in Fig. 5.13. All stationary solutions were calculated using the continuation method introduced in Sec. 5.3. The billiard system used here is \mathcal{B}_1 (see Sec. 3.8.1).

In Fig. 5.13a we show the transmission as function of μ for various values of the interaction strength g . We see that the single resonance peak is tilted more and more to increasing values of μ for increasing values of the interaction strength g . For small values of g the transmission is single valued as function of μ but for larger values of g it tips over and the transmission shows

three branches as function of μ . Similar behaviour was observed in one dimension in [67, 159–161]. The physical reason responsible for this behaviour will be given by the perturbation theory developed in Sec. 5.6.2. In this work we focus mostly on a repulsive interaction $g > 0$. For an attractive interaction $g < 0$ the peak would be tilted to the left. Fig. 5.13c shows the transmission as function of g for various fixed values of μ . These curves reflect the tilting over of the resonance peak in the μ coordinate. Also as function of g the transmission can show multiple branches for

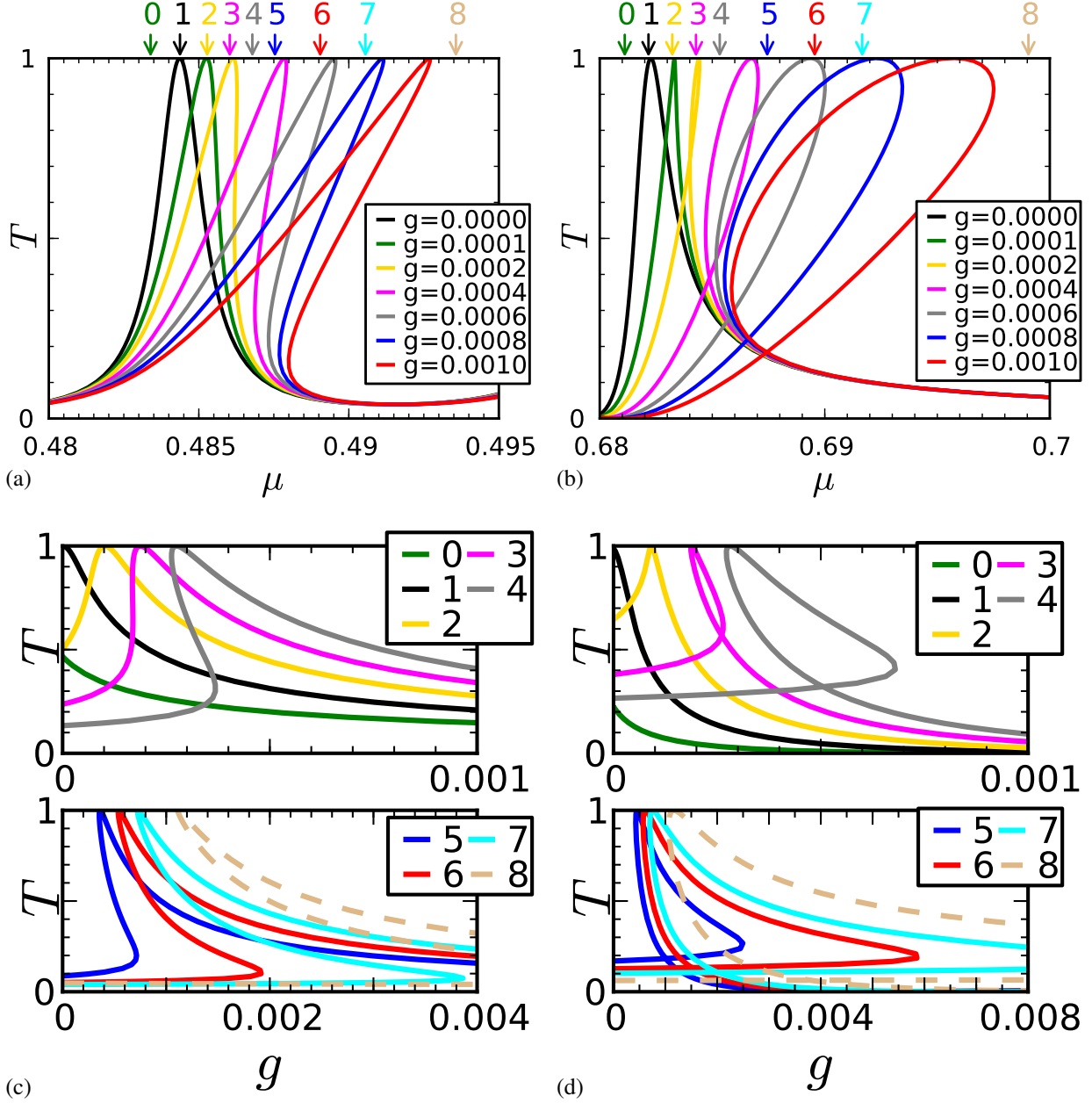


Figure 5.13: (a) and (b) show the transmission as function of μ for various values of g . The system and the energy range shown are the same as in Fig. 5.3. Likewise (c) and (d) show the transmission as function of g for various values of μ . The values of the chemical potential used in (c) are marked in (a) by the arrows above the plot. Similarly the arrows above (b) mark the values of μ used in (d).

The two energy intervals corresponding to (a) and (b) are marked in Fig. 5.14 by yellow arrows.

some values of μ . To understand the figures Fig. 5.13a and Fig. 5.13c one has to interpret these figures as one dimensional sections of the two dimensional surface $F(\Psi, \mu, g)=0$ embedded in $\mathbb{R}^{2n} \times \mathbb{R}^2$ where F is given by Eq. (5.5).

Likewise Fig. 5.13b shows how the other resonance structure winds around itself and forms a loop structure for increasing values of g . An explanation of this behaviour will be given in Sec. 5.6.2 using a perturbative ansatz.

Up to now we only inspected two parts of the spectrum for the interacting case $g \neq 0$. Fig. 5.14 shows how the rest of the spectrum is affected by the interaction term. Most resonance structures show similar behaviour as the one depicted in Fig. 5.13, i.e. one has either a peak which is tilted or a formation of a loop structure. The rapidity with which the tilt or the loop structure forms with increasing g varies from resonance to resonance. Generally one can say that sharp resonances (i.e. resonances with $\text{Im } \mathcal{E}$ small) are more strongly effected by the interaction then broad resonances. An explanation for this behaviour will be given in Sec. 5.6.2.

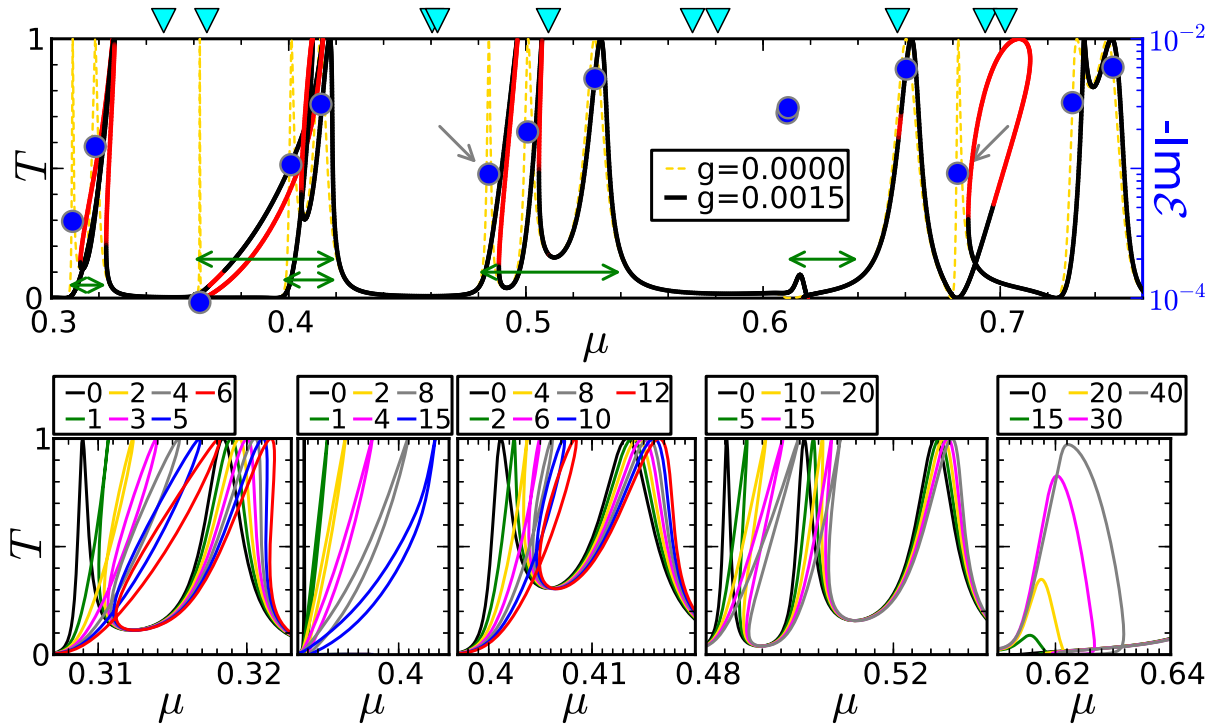


Figure 5.14: These figures illustrate the transmission spectrum of the example system \mathcal{B}_1 described in Sec. 3.8.1 for various values of the interaction strength g for diverse energy ranges. The upper figure shows the transmission spectrum for $g=0$ and $g=0.0015$ over the whole energy range studied in this work. The dynamical stability (see Sec. 5.7) is color-encoded: black and red denote stable and unstable respectively. As before in Fig. 3.13 the blue circles indicate the real and imaginary parts of the resonances and the cyan triangles indicate the position of the bound states (negative parity $y \mapsto -y$). The gray arrows indicate the resonances studied in Fig. 5.13 and in the previous sections.

The lower panel features some resonance structures (marked in the upper figure by green arrows) in more detail. The values of g used here are indicated by the color code shown above the figures. One must multiply the numbers given in the legend by 0.0001 in order to get the corresponding value of g (i.e. 8 means $g=0.0008$).

Some resonances show a deviating behaviour, i.e they do not form loops or tilted peaks. For example the resonance $\mathcal{E}=0.3625-9.26\cdot 10^{-5}i$ is not simply tilted for large g but forms a “nose like” structure. A similar “nose like” resonance was also found in one dimension in [159, 160]. While the tilt can be explained by the perturbation theory described in Sec. 5.6.2, the “nose” goes beyond this perturbative ansatz. The double resonance around $\mu=0.61$ shows also a deviating behaviour which cannot be explained by the perturbation theory.

As already mentioned in Sec. 5.3.2 there might be multiple disconnected components in the one dimensional sections $F(\tilde{\Psi})=0$. Such a scenario is shown in Fig. 5.15. Here the manifold $F(\Psi, g)=0$ consists of two disconnected components for some values of μ while the manifold $F(\Psi, \mu)=0$ for the corresponding fixed value of g is single connected. The situation is that the “nose like” resonance at $\mathcal{E}=0.3625-9.26\cdot 10^{-5}i$ overlaps with the two resonances around $\mu = 0.4$. As μ increases from 0.36 to 0.40 the g sections of the “nose like” resonance first show a normal behaviour similar to Fig. 5.13c. Then they split in two independent components. A time dependent simulation as done in Sec. 5.4.1 reveals that only the component of $F(\Psi, g)=0$ directly connected to $g=0$ is populated. The results are similar to that of Fig. 5.9. The other component is of no physical relevance in such a scenario and can be only reached by the methods of Sec. 5.4.2, i.e. a time dependent variation of μ applied to the “nose like” resonance.

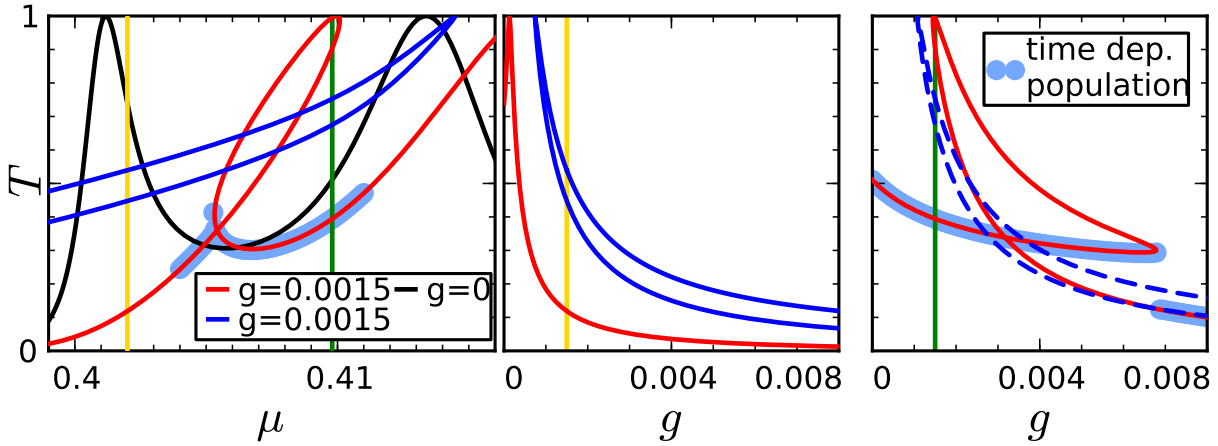


Figure 5.15: These figures show that the solution manifold $F(\Psi, g)=0$ for g variable and μ and B fixed can consist of multiple disconnected components. In the middle and right figure these two components are colored in red and blue. The left figure shows the corresponding manifold $F(\Psi, \mu)=0$ for μ variable and g and B fixed. Here the two components are connected but we used again the colors red and blue to distinguish them from another. The yellow and green line in the left figure indicate the value of μ used for the middle and right figure respectively. Similarly the yellow and green line in the middle and right figure indicate the value of g used in the left figure. The results of a time dependent population (as described in Sec. 5.4.1) are shown here as light blue dots.

5.6 Perturbation theory

5.6.1 Perturbation theory for the wave function

In order to explain the behaviour of the stationary scattering states of the Gross-Pitaevskii equation described in the previous section we now develop a perturbation theory in the parameter g . To this end we rewrite the defining equation (5.2) for the stationary scattering states in the following way (here $*$ denotes complex conjugation):

$$[\mu - H] \Psi - gg_0 \frac{\hbar^2}{m} \Psi^* \Psi^2 = S. \quad (5.22)$$

All dependencies on the position variable \mathbf{r} have been dropped here for the sake of simplicity. Furthermore we use the notation $g(\mathbf{r}) = g g_0(\mathbf{r})$ where $g \in \mathbb{C}$ is a dimensionless scalar and $g_0(\mathbf{r})$ is a function which takes the value 1 inside the scattering region and the value 0 inside the leads as explained in Sec. 5.1.2.

To derive the perturbation theory we make the ansatz that Ψ is a power series in g and g^* :

$$\Psi = \Psi_0 + g\Psi_1 + g^*\check{\Psi}_1^* + \mathcal{O}(g^2).$$

A priori it is necessary to introduce a term with g^* because of the non-holomorphy of the term Ψ^* in Eq. (5.22). The vector $\check{\Psi}_1$ is independent from Ψ_1 . We will see later that this term vanishes.

We now insert this ansatz into Eq. (5.22):

$$\begin{aligned} [\mu - H] [\Psi_0 + g\Psi_1 + g^*\check{\Psi}_1^* + \mathcal{O}(g^2)] \\ - gg_0 \frac{\hbar^2}{m} [\Psi_0^* + g^*\Psi_1^* + g\check{\Psi}_1 + \mathcal{O}(g^2)] [\Psi_0 + g\Psi_1 + g^*\check{\Psi}_1^* + \mathcal{O}(g^2)]^2 = S. \end{aligned}$$

which results in

$$[\mu - H] \Psi_0 + [\mu - H] [g\Psi_1 + g^*\check{\Psi}_1^*] - gg_0 \frac{\hbar^2}{m} \Psi_0^* \Psi_0^2 = S + \mathcal{O}(g^2).$$

The zeroth order term in g is just the scattering equation for the linear case:

$$[\mu - H] \Psi_0 = S \quad \implies \quad \Psi_0 = [\mu - H]^{-1} S.$$

The first order term in g reads as:

$$[\mu - H] [g\Psi_1 + g^*\check{\Psi}_1^*] = gg_0 \frac{\hbar^2}{m} \Psi_0^* \Psi_0^2.$$

We now insert $g=1$ and $g=i$ into this equation which leads us to:

$$\begin{aligned} [\mu - H] [\Psi_1 + \check{\Psi}_1^*] &= g_0 \frac{\hbar^2}{m} \Psi_0^* \Psi_0^2 \\ [\mu - H] [i\Psi_1 - i\check{\Psi}_1^*] &= i g_0 \frac{\hbar^2}{m} \Psi_0^* \Psi_0^2. \end{aligned}$$

Adding and subtracting this two equation results in:

$$\begin{aligned} [\mu - H] \Psi_1 &= g_0 \frac{\hbar^2}{m} \Psi_0^* \Psi_0^2 \\ [\mu - H] \check{\Psi}_1 &= 0 \end{aligned}.$$

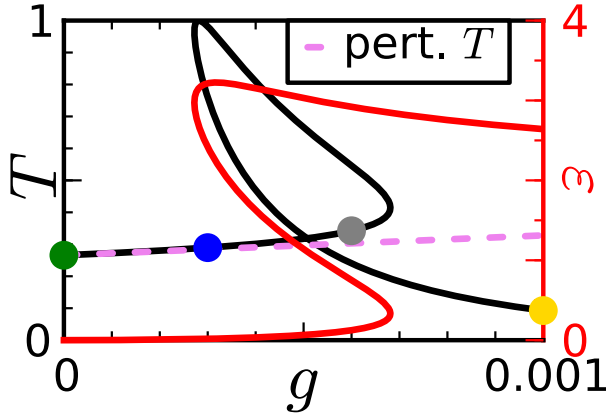


Figure 5.16: This figure illustrates the performance of the perturbation theory for the wave function. The exact transmission is displayed as a black curve. The transmission calculated using the first order perturbation theory Eq. (5.23) is shown as the dashed violet line. The red curve displays the relative error $\varepsilon = \|\Psi_{\text{pert}} - \Psi_{\text{exact}}\| / \|\Psi_{\text{exact}}\|$. We used here $\mu = 0.685332$ and the same system as in Fig. 5.14.

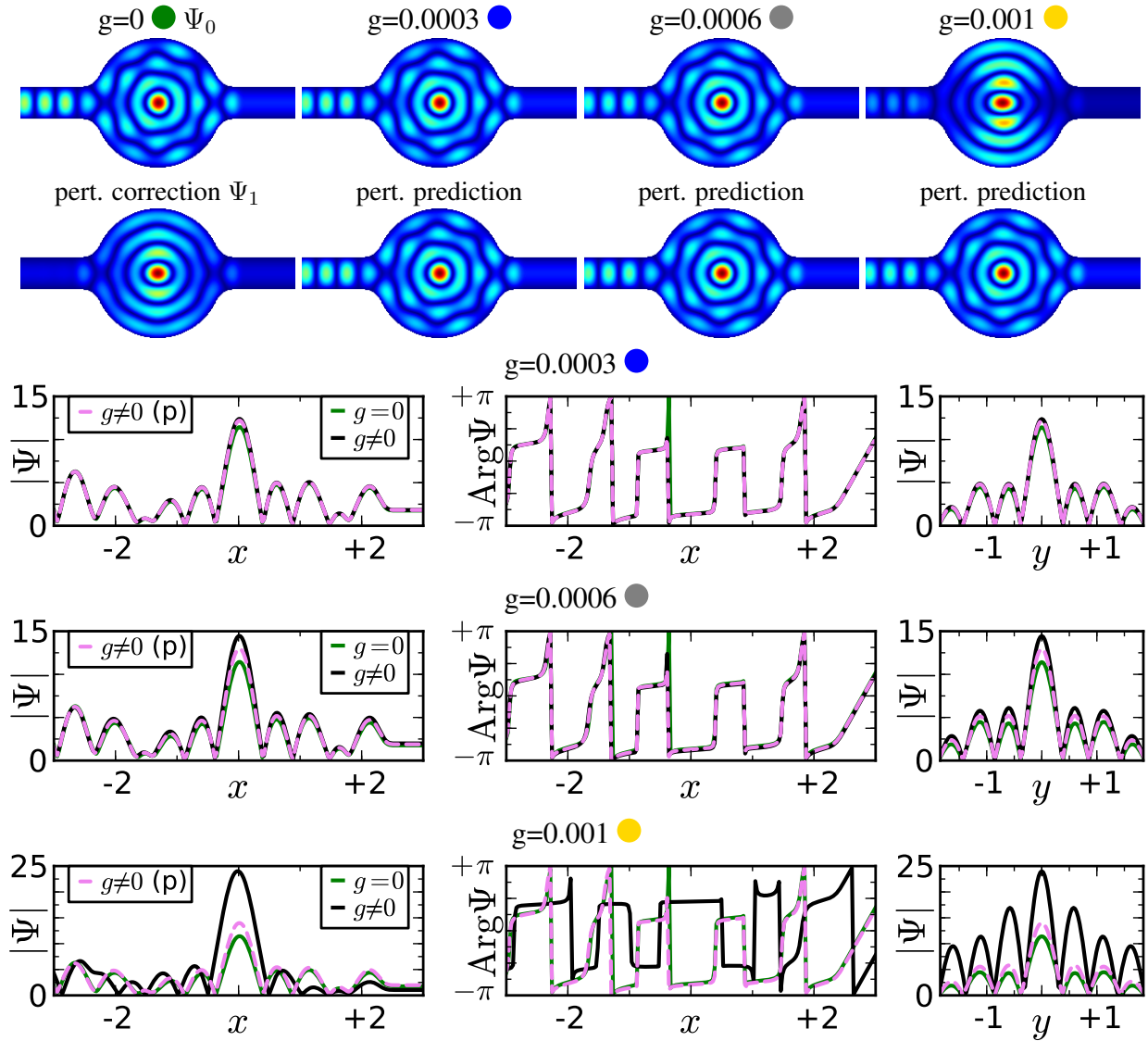


Figure 5.17: These figures compare the exact wave function with the perturbative results. The values of g used here are indicated in Fig. 5.16 as green, blue, gray and yellow dots respectively. The upper figures display a two dimensional plot of $|\Psi|^2$ (upper row: exact, lower row: perturbative) while the lower figures display one dimensional sections of $|\Psi|$ and $\arg \Psi$ ($g=0$: green, $g \neq 0$: black, perturbative: dashed violet). x and y are measured in units of the wavelength $\lambda = 2\pi\hbar/\sqrt{2m\mu}$.

This gives us a perturbation formula for the stationary scattering states correct up to first order in g :

$$\Psi = \Psi_0 + g\Psi_1 + \mathcal{O}(g^2)$$

with $\Psi_0 = [\mu - H]^{-1} S$ and $\Psi_1 = [\mu - H]^{-1} \left[g_0 \frac{\hbar^2}{m} \Psi_0^* \Psi_0^2 \right]$. (5.23)

The performance of this first order perturbation theory can be studied in Fig. 5.16 (we used $T \sim \Psi \partial_x \Psi = \Psi_0 \partial_x \Psi_0 + g(\Psi_0 \partial_x \Psi_1 + \Psi_1 \partial_x \Psi_0) + \mathcal{O}(g^2)$ there) and Fig. 5.17. For small g , Eq. (5.23) works well but as soon as the branch (of Ψ as a function of g) which is connected to $g=0$ ends, the perturbation theory fails to work. This is a principal failure which cannot be overcome by simply using a higher order series development in g because any theory of this kind regards Ψ as a (single valued) function of g and therefore cannot describe multiple branches. This is the reason why we have not studied the effect of higher order terms in the series development for Ψ here. We will continue this considerations in Sec. 6.1 where essentially a higher order perturbation theory is used to develop a semiclassical theory of the weak localisation effect.

5.6.2 Perturbation theory for the energy

A better perturbative description of the transmission of interacting matter waves through tightly confined two dimensional cavities can be developed if we assume that the interaction potential induces an energy shift but otherwise leaves the wave function Ψ approximatively unchanged from the linear case $g=0$. This is the complementary approach to Sec. 5.6.1 where Ψ was assumed to depend on the interaction strength g but μ was kept fixed.

The starting point is the defining equation (5.2) for stationary scattering states of the Gross-Pitaevskii equation:

$$[\mu - H] \Psi - gg_0 \frac{\hbar^2}{m} |\Psi|^2 \Psi = S(\mu) . \quad (5.24)$$

We now make the approximation that the *position dependent* interaction potential $\frac{\hbar^2}{m} |\Psi|^2 \Psi$ can be replaced by a *position independent* constant potential Λ which acts as a simple energy shift. This is a kind of mean field approximation for the interaction potential.

To numerically determine the energy shift Λ we rewrite Eq. (5.24) as follows:

$$[\mu - \Lambda gg_0 - H] \Psi + gg_0 \left[\Lambda - \frac{\hbar^2}{m} |\Psi|^2 \right] \Psi = S(\mu) . \quad (5.25)$$

The parameter Λ is now adjusted in such a way that the term $gg_0 \left[\Lambda - \frac{\hbar^2}{m} |\Psi|^2 \right] \Psi$ becomes negligible small. To this end we minimize the square of the L^2 -norm

$$\begin{aligned} \left\| g_0 \left[\Lambda - \frac{\hbar^2}{m} |\Psi|^2 \right] \Psi \right\|^2 = \\ \Lambda^2 \langle g_0 \Psi, g_0 \Psi \rangle - 2\Lambda \frac{\hbar^2}{m} \langle g_0 \Psi, g_0 |\Psi|^2 \Psi \rangle + \frac{\hbar^4}{m^2} \langle g_0 |\Psi|^2 \Psi, g_0 |\Psi|^2 \Psi \rangle \end{aligned}$$

with respect to the parameter Λ . This determines the energy shift as

$$\Lambda = \frac{\hbar^2 \langle g_0 \Psi, g_0 |\Psi|^2 \Psi \rangle}{m \langle g_0 \Psi, g_0 \Psi \rangle} = \frac{\hbar^2 \int g_0(\mathbf{r})^2 |\Psi(\mathbf{r})|^4 d\mathbf{r}}{m \int g_0(\mathbf{r})^2 |\Psi(\mathbf{r})|^2 d\mathbf{r}} .$$

This quantity Λ is also known as inverse participation ratio [24, 83].

This energy shift $g\Lambda$ is (approximatively) equal to the expectation value of the interaction potential and thus determines the fraction of the energy μ which is due to the particle-particle interaction. This can be seen by taking the scalar product of $g_0(\mathbf{r})\Psi(\mathbf{r})$ with Eq. (5.24) ($S(\mathbf{r})$ has support in the leads)

$$\mu \langle g_0 \Psi, \Psi \rangle = \langle g_0 \Psi, H \Psi \rangle + g \frac{\hbar^2}{m} \langle g_0 \Psi, g_0 |\Psi|^2 \Psi \rangle$$

and making the approximation $g_0(\mathbf{r})^2 \approx g_0(\mathbf{r})$ which is correct except for a negligible transition region inside the leads:

$$\mu = \frac{\langle g_0 \Psi, H \Psi \rangle}{\langle g_0 \Psi, g_0 \Psi \rangle} + g\Lambda .$$

As we have minimized the unwanted term we are now allowed to approximatively rewrite Eq. (5.25) as follows:

$$[\mu - \Lambda g g_0 - H] \Psi = S(\mu) . \quad (5.26)$$

The function $g_0(\mathbf{r})$ is one inside the cavity and zero inside the leads. The transition happens adiabatically slowly so can safely assume that inside the transition region the wave function continuously adapt to the local energy $\mu - \Lambda g g_0$ without any unwanted scattering. This allows us to rewrite Eq. (5.26) as follows:

$$[\mu - \Lambda g - H] \Psi = S(\mu - \Lambda g) .$$

This means that the stationary scattering state for energy μ and interaction strength g is approximatively equal to the stationary scattering state for energy $(\mu - \Lambda g)$ and vanishing interaction. The quality of this approximation can be seen in Fig. 5.18 and Fig. 5.19.

In the following we will always use the wave function of the non-interacting case $g=0$

$$\Psi_{g=0}(\mu) = [\mu - H]^{-1} S(\mu)$$

for the calculation of the energy shift:

$$\Lambda(\mu) = \frac{\hbar^2 \int g_0(\mathbf{r})^2 |\Psi_{g=0}(\mu, \mathbf{r})|^4 d\mathbf{r}}{m \int g_0(\mathbf{r})^2 |\Psi_{g=0}(\mu, \mathbf{r})|^2 d\mathbf{r}} . \quad (5.27)$$

The wave function in the interacting case $g \neq 0$ is now approximated as follows:

$$\Psi_g(\mu + g\Lambda(\mu)) \approx \Psi_{g=0}(\mu)$$

and equivalently for the transmission $T_g(\mu)$:

$$T_g(\mu + g\Lambda(\mu)) \approx T_g^{(p)}(\mu + g\Lambda(\mu)) = T_{g=0}(\mu) . \quad (5.28)$$

This gives us a perturbative expression $T_g^{(p)}$ for the transmission for interacting matter waves. The quality of this approximation is shown in Fig. 5.20 and Fig. 5.22 for the example system introduced in Sec. 3.8.1. For almost all resonance structure the qualitative agreement is very good. Quantitatively the agreement is naturally better for smaller values of g than for larger values g .

The perturbation theory for the energy explains finally why tilted peak and loop structures emerge in the transmission spectrum for non-vanishing interaction strength g as shown in Fig. 5.20.

At a single well-separated resonance peak the transmission $T(\mu)$ has a maximum as function of μ . As depicted in Fig. 5.22, the energy shift $\Lambda(\mu)$ assumes also a maximum at approximately the position of the resonance peak. In case of overlapping resonances this two maxima do not need to coincide. If the maximum of $\Lambda(\mu)$ is to the left of the maximum of $T(\mu)$, loop structures form while otherwise tilted peak structures emerge.

The perturbation theory performs worst for very sharp resonances (for example the resonance marked with “A” in Fig. 5.22) as at these the energy shift $\Lambda(\mu)$ becomes extremely large and thus the interaction potential $g \frac{\hbar^2}{m} |\Psi|^2 \Psi$ is responsible for a significant part of the energy μ . Under these condition the simple perturbative ansatz that the wave function is not changed from the

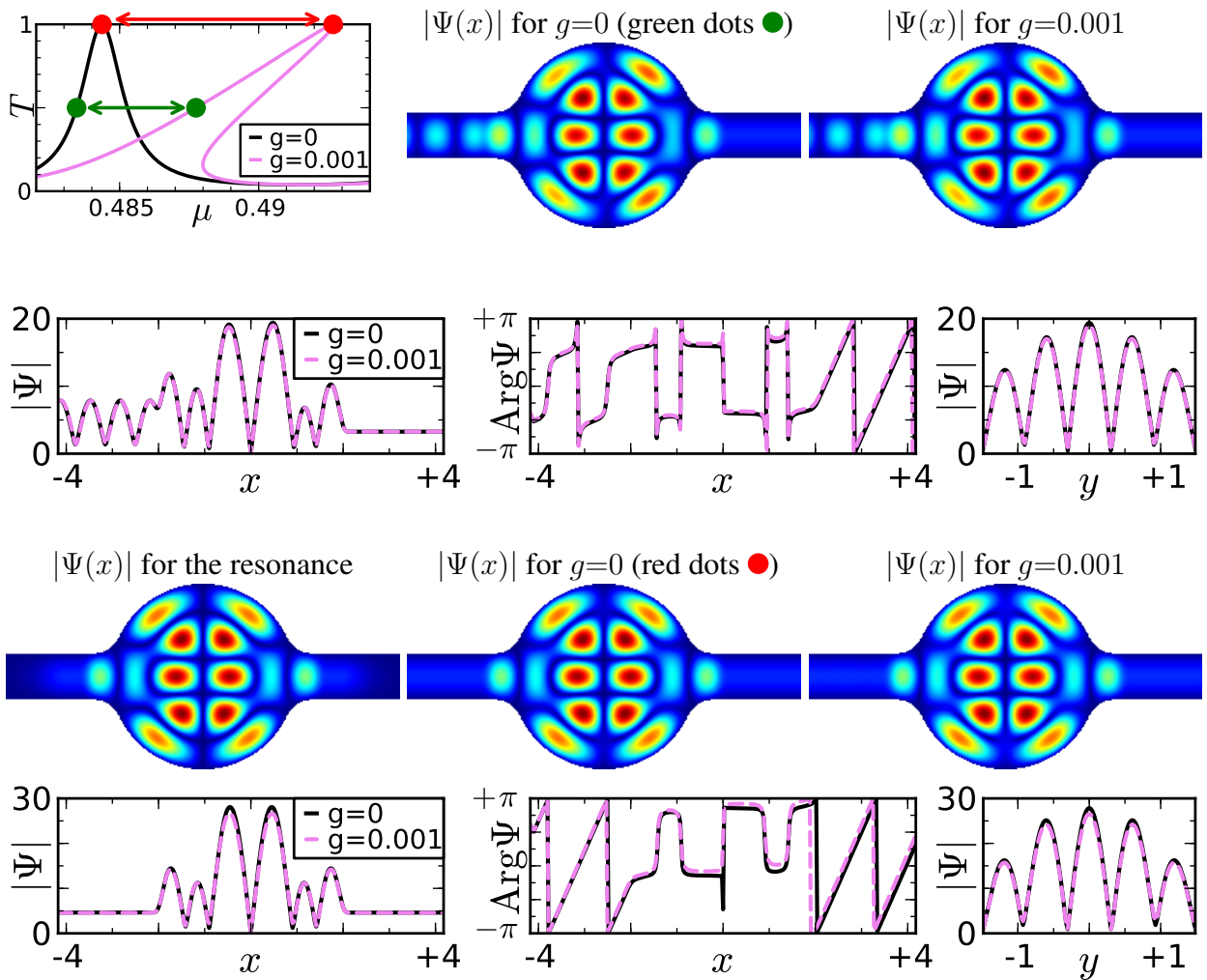


Figure 5.18: These figures compares the wavefunction for the linear case $g=0$ to the wavefunction in the interacting case $g=0.001$ for the same system as studied in Fig. 5.3. The upper part shows the wavefunction at half transmission $T=0.5$ (green circles in the transmission plot) corresponding to $\mu=0.48345$ (for $g=0$) and $\mu=0.48777$ (for $g=0.001$). The lower part shows the wavefunction at full transmission $T=1$ (red circles in the transmission plot) corresponding to $\mu=0.48437$ (for $g=0$) and $\mu=0.49268$ (for $g=0.001$). The resonance wavefunction (for $g=0$) is shown, too.

linear case cannot be expected to hold. A variety of such sharp resonances can be seen in the system \mathcal{B}_4 introduced in Sec. 5.8.3.

The interaction can also lift degeneracies existing in the linear case. For example the resonances marked with “B” in Fig. 5.22 form a degenerate pair for $g = 0$ because both have approximately the same real part and overlap strongly. They have different parity with respect to the reflection $x \mapsto -x$ and thus they interfere destructively in the transmission spectrum forcing a vanishing transmission. For non-vanishing interaction strength this degeneracy and destructive interference is lifted as seen in Fig. 5.21 resulting in a non-vanishing transmission. The perturbative ansatz cannot reproduce this behaviour for obvious reasons.

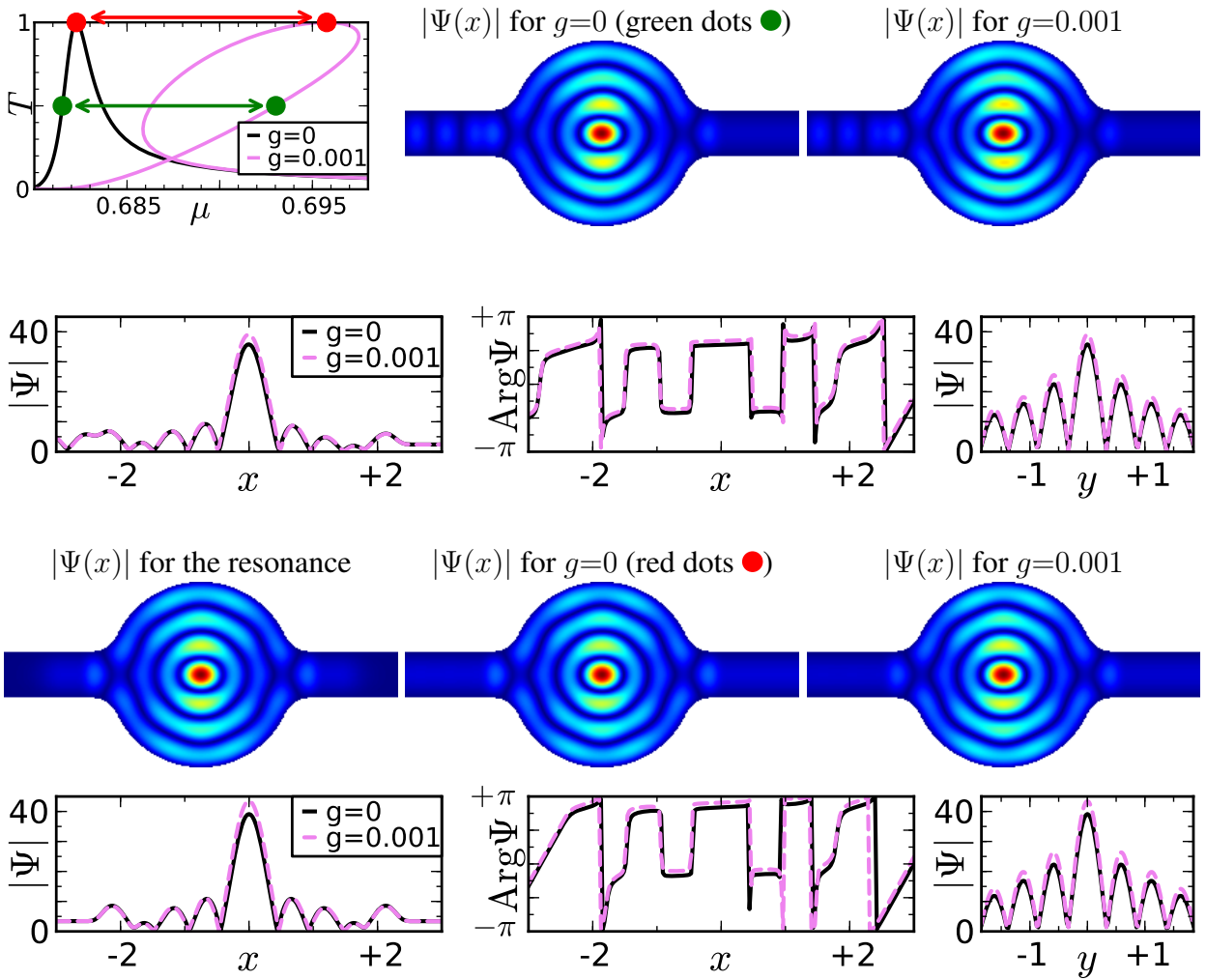


Figure 5.19: These figures compares the wavefunction for the linear case $g=0$ to the wavefunction in the interacting case $g=0.001$ for the same system as studied in Fig. 5.3. The upper part shows the wavefunction at half transmission $T=0.5$ (green circles in the transmission plot) corresponding to $\mu=0.68151$ (for $g=0$) and $\mu=0.69303$ (for $g=0.001$). The lower part shows the wavefunction at full transmission $T=1$ (red circles in the transmission plot) corresponding to $\mu=0.68227$ (for $g=0$) and $\mu=0.69577$ (for $g=0.001$). The resonance wavefunction (for $g=0$) is shown, too.

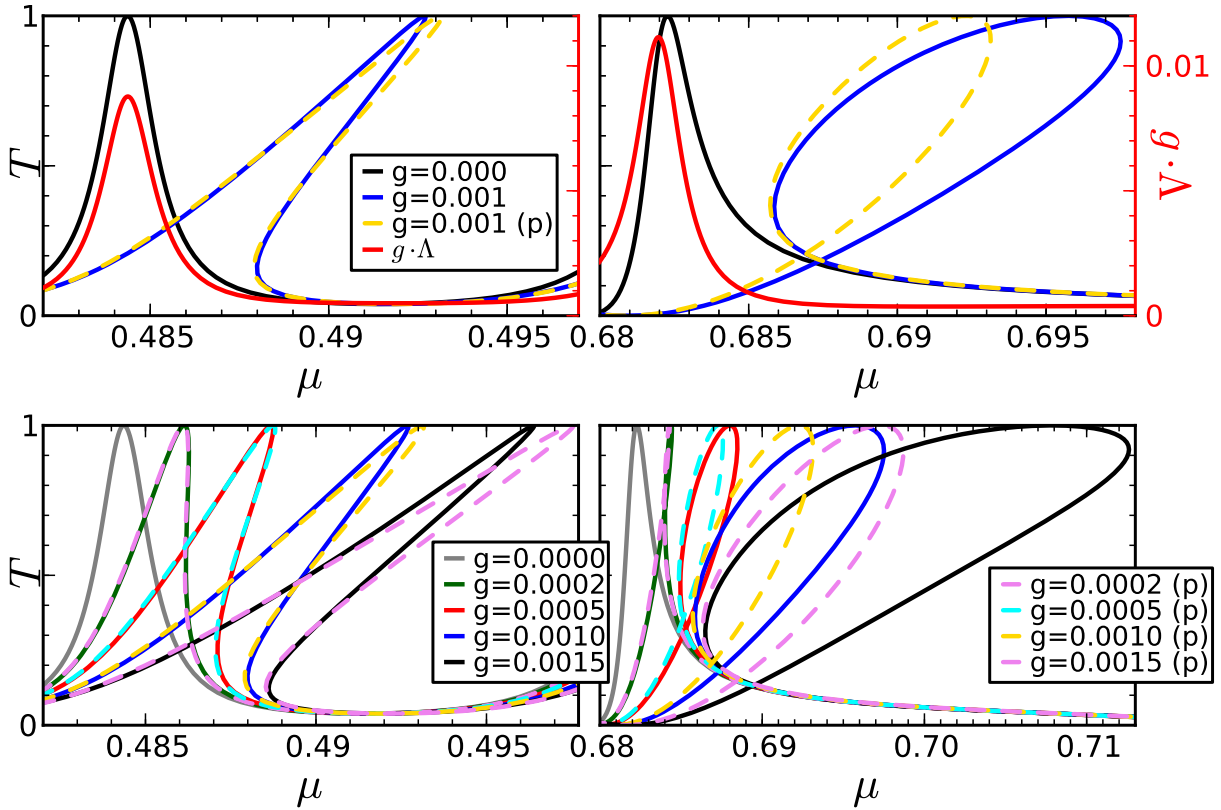


Figure 5.20: These figures show the performance of the perturbation theory for the energy using the same resonance peaks as in Fig. 5.3. All perturbative transmission curves are marked by a “(p)”. The upper panel shows the both the transmission (left axis) and the energy shift $g \cdot \Delta$ (right axis) for a single value of g . Loop structures form if the maximum of the energy shift is to the left of the maximum of the linear transmission while otherwise tilted peak structures form. The lower panel depicts the transmission for several values of g .

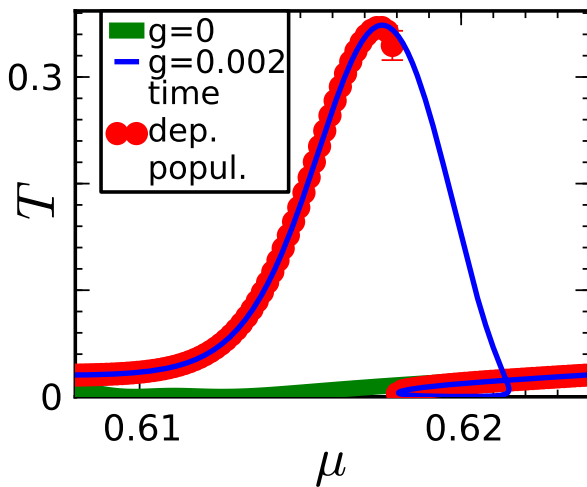


Figure 5.21: This figure shows the deviating behaviour of the degenerate resonance pair marked in Fig. 5.22 by “B”. While for $g = 0$ the transmission is approximatively zero due to destructive interference for $g \neq 0$ this effect is lifted and a non-zero transmission results. Time dependent population of the cavity as done in Sec. 5.4.1 confirm this effect. The perturbation theory for the energy can principally not reproduce this effect.

Finally we note that the perturbation theory for the energy works exceptional well for the system introduced in Sec. 3.8.1 because it is nearly closed and possesses the mirror symmetry $x \mapsto -x$. For the nearly closed example system \mathcal{B}_2 without this mirror symmetry studied in Sec. 5.8.1 the perturbation theory also works satisfactory but the heights of the transmission curves do not work out so well. For wide open systems (see for example \mathcal{B}_5 in Sec. 5.8.4) the perturbation theory for the energy works only to some degree. Here better results can be obtained by studying the energy-averaged transmission using a sophisticated version of the perturbation theory for the wave function as explained in Sec. 6.1.

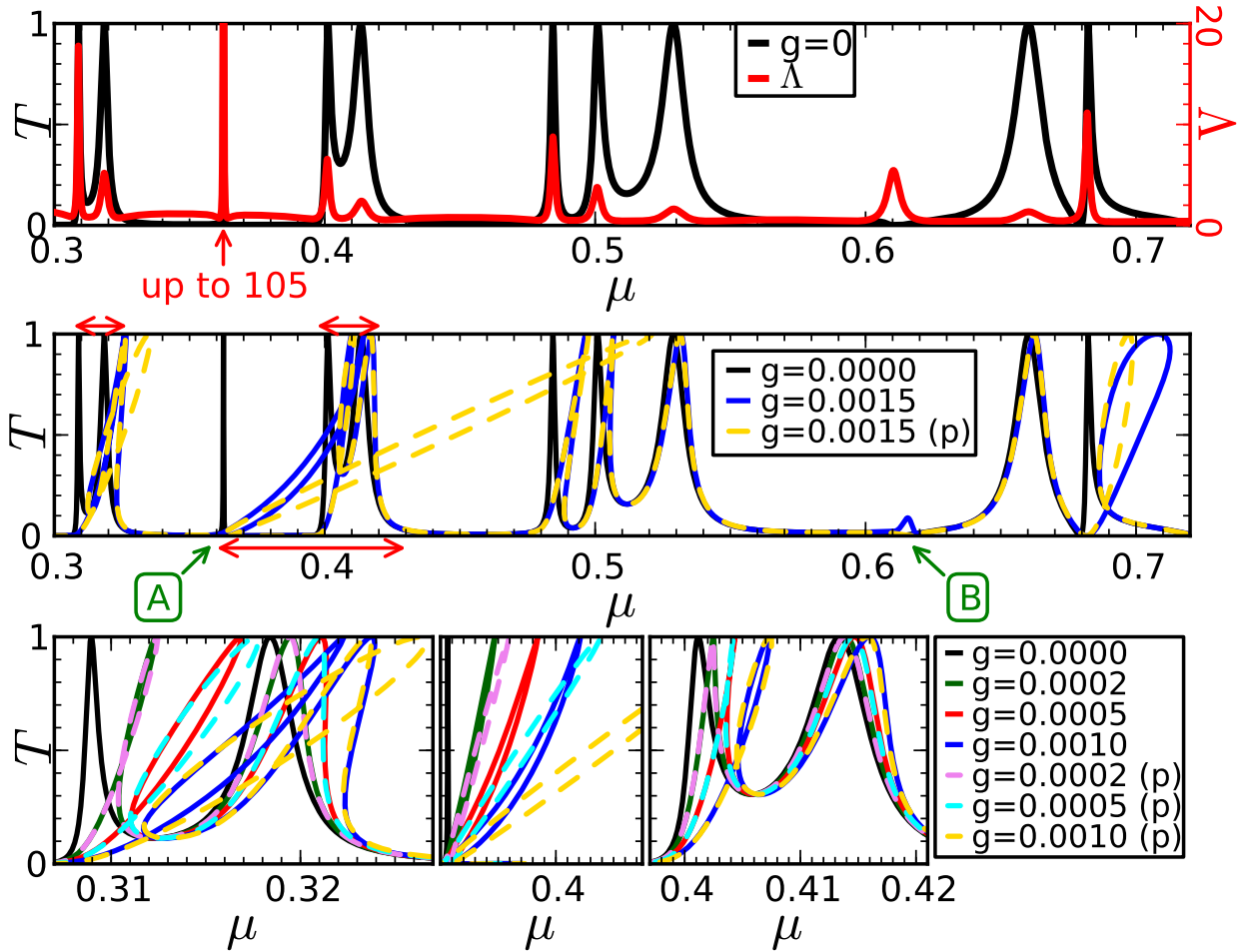


Figure 5.22: Here we show the performance of the perturbation theory for the energy for the system \mathcal{B}_1 (see Sec. 3.8.1) over the whole investigated energy range. All perturbative transmission curves are marked by a “(p)”. The upper panel depicts the energy shift Δ . While the middle panel shows the transmission for a single non-zero value of g the lower panel shows the transmission for multiple values of g for selected energy ranges which are indicated in the middle panel by red arrows. The green annotations “A” in the middle panel marks a very sharp resonance for which the perturbation theory does not work well. The green annotations “B” marks another structure for which the perturbation theory fails for a different reason and which is investigated in more detail in Fig. 5.21.

5.7 Dynamical stability

Let us assume we have found a stationary scattering state of the Gross-Pitaevskii equation using the methods of Sec. 5.2 and Sec. 5.3. The next logical step is to determine if it is stable under temporal evolution, i.e. if it is dynamical stable. Dynamical stability means that small deviations from the stationary solution do not exponentially grow during time evolution but instead are exponentially suppressed. This question is now investigated by linearizing the time-dependent Gross-Pitaevskii equation (5.1) around the stationary solution. This section follows roughly [167].

Let $\Psi_0(\mathbf{r})$ be the stationary solution (for the energy μ) whose dynamical stability we want to determine. This means $\Psi_0(\mathbf{r})$ is a solution of Eq. (5.2):

$$[H - \mu] \Psi_0(\mathbf{r}) + g(\mathbf{r}) \frac{\hbar^2}{m} |\Psi_0(\mathbf{r})|^2 \Psi_0(\mathbf{r}) + S(\mathbf{r}) = 0 . \quad (5.29)$$

The corresponding time-dependent wave function $\Psi(\mathbf{r}, t) = \Psi_0(\mathbf{r})$ naturally fulfills the time-dependent Gross-Pitaevskii equation (5.1):

$$i\hbar \frac{\partial}{\partial t} \Psi(\mathbf{r}, t) = [H - \mu] \Psi(\mathbf{r}, t) + g(\mathbf{r}) \frac{\hbar^2}{m} |\Psi(\mathbf{r}, t)|^2 \Psi(\mathbf{r}, t) + S(\mathbf{r}) . \quad (5.30)$$

The time dependence related to $e^{-it\mu/\hbar}$ has been split off.

We now add a small disturbance to $\Psi_0(\mathbf{r})$:

$$\Psi(\mathbf{r}, t) = \Psi_0(\mathbf{r}) + \epsilon \Psi_1(\mathbf{r}, t) + \mathcal{O}(\epsilon^2) .$$

Here ϵ is a small development parameter. Inserting this ansatz into Eq. (5.30) gives us in zeroth order in ϵ the stationary equation (5.29) and in first order following time evolution equation for $\Psi_1(\mathbf{r}, t)$ (here $*$ denotes complex conjugation):

$$i\hbar \frac{\partial}{\partial t} \Psi_1(\mathbf{r}, t) = [H - \mu] \Psi_1(\mathbf{r}, t) + g(\mathbf{r}) \frac{\hbar^2}{m} \left[2|\Psi_0(\mathbf{r})|^2 \Psi_1(\mathbf{r}, t) + \Psi_0(\mathbf{r})^2 \Psi_1(\mathbf{r}, t)^* \right] . \quad (5.31)$$

This is an homogeneous \mathbb{R} -linear first-order ordinary differential equation in $\Psi_1(\mathbf{r}, t)$. Therefore its general solution is a superposition of exponential modes. To determine these modes we make following ansatz (sometimes called Bogoliubov ansatz) for $\Psi_1(\mathbf{r}, t)$:

$$\Psi_1(\mathbf{r}, t) = u(\mathbf{r}) e^{-i\xi t/\hbar} + v(\mathbf{r})^* e^{+i\xi^* t/\hbar} .$$

This ansatz is nothing else than an exponential mode whose unusual form is due to the fact that Eq. (5.31) contains both $\Psi_1(\mathbf{r}, t)$ and $\Psi_1(\mathbf{r}, t)^*$. For the sake of clarity we will from now on drop all dependencies on the position variable \mathbf{r} . Inserting this ansatz into Eq. (5.31) and collecting the summands belonging to $e^{-i\xi t/\hbar}$ and $e^{+i\xi^* t/\hbar}$ we obtain following eigenequation which the exponential mode has to fulfill:

$$\begin{aligned} +\xi u &= [H - \mu] u + g \frac{\hbar^2}{m} \left[2|\Psi_0|^2 u + \Psi_0^2 v \right] \\ -\xi^* v^* &= [H - \mu] v^* + g \frac{\hbar^2}{m} \left[2|\Psi_0|^2 v^* + \Psi_0^2 u^* \right] . \end{aligned}$$

This can be written more nicely by taking the complex conjugate of the second equation (assuming $\mu \in \mathbb{R}$):

$$\xi \begin{pmatrix} +1 & 0 \\ 0 & -1 \end{pmatrix} \begin{pmatrix} u \\ v \end{pmatrix} = \begin{pmatrix} H - \mu + 2g \frac{\hbar^2}{m} |\Psi_0|^2 & g \frac{\hbar^2}{m} \Psi_0^2 \\ g \frac{\hbar^2}{m} \Psi_0^{*2} & H^* - \mu + 2g \frac{\hbar^2}{m} |\Psi_0|^2 \end{pmatrix} \begin{pmatrix} u \\ v \end{pmatrix}. \quad (5.32)$$

This generalized eigenvalue problem is called the Bogoliubov-de Gennes equation [167]. If an eigenmode with $\text{Im } \xi > 0$ exists then the stationary solution is dynamical unstable because this eigenmode will exponentially grow during under time evolution. If no such eigenmode exists the stationary solution is called dynamical stable. The timescale on which the instability manifests itself is given by $\frac{\hbar}{\text{Im } \xi}$.

In actual computations we are only record $\max \text{Im } \xi$ and use a color encoding of the transmission curve to illustrate the stability as otherwise the figures become very complicated (see Fig. 5.23). The eigenfunctions $u(\mathbf{r})$ and $v(\mathbf{r})$ belonging to such unstable mode are very similar to resonances and bound states of the billiard in the linear case $g=0$ as shown in Fig. 5.23 and Fig. 5.24. We note that the spectrum contains regions where no stable stationary solution exists as well as regions where multiple stationary solutions exists. In the latter situation the result of time dependent simulations depend on the history of the system as shown in Sec. 5.4.2 and Sec. 5.4.3. This is a hysteresis effect. Even in situations where no stable solution exists the wavefunction will oscillate around the stationary solution for not to large values of g as seen for example in Fig. 4.3, so the stationary solution have some physical significance. Furthermore the wavefunction can stay on an instable state for times shorter than $\frac{\hbar}{\max \text{Im } \xi}$.

Symmetries of the billiard system (for example $y \mapsto -y$) can induce bound states inside the continuous spectrum as shown in Fig. 3.13 or Fig. 5.24. These bound states are invisible in the transmission spectrum but affect the dynamical stability. Therefore one can sometimes see instabilities in regions of the transmission spectrum where one would normally expect a stable state. These complications can be avoided by using a completely asymmetric cavity as \mathcal{B}_3 (Sec. 5.8.2) or \mathcal{B}_5 (Sec. 5.8.4).

We will now rewrite this equation (5.32) in a form better suited to numerical calculations. To this end we introduce following shorthand notations:

$$\sigma_3 = \begin{pmatrix} +1 & 0 \\ 0 & -1 \end{pmatrix} \quad J = \begin{pmatrix} 0 & -1 \\ +1 & 0 \end{pmatrix} \quad w = \begin{pmatrix} u \\ v \end{pmatrix}$$

$$T = \begin{pmatrix} H - \mu + 2g \frac{\hbar^2}{m} |\Psi_0|^2 & g \frac{\hbar^2}{m} \Psi_0^2 \\ g \frac{\hbar^2}{m} \Psi_0^{*2} & H^* - \mu + 2g \frac{\hbar^2}{m} |\Psi_0|^2 \end{pmatrix}$$

This allows us to rewrite the Bogoliubov-de Gennes equation (5.32) compactly as

$$Tw = \xi \sigma_3 w. \quad (5.33)$$

We now apply a unitary transformation

$$Z = \frac{1}{\sqrt{2}} \begin{pmatrix} +1 & +1 \\ -i & +i \end{pmatrix}$$

corresponding to the splitting in real and imaginary parts onto Eq. (5.33):

$$ZTZ^{-1}\tilde{w} = \xi Z\sigma_3 Z^{-1}\tilde{w}.$$

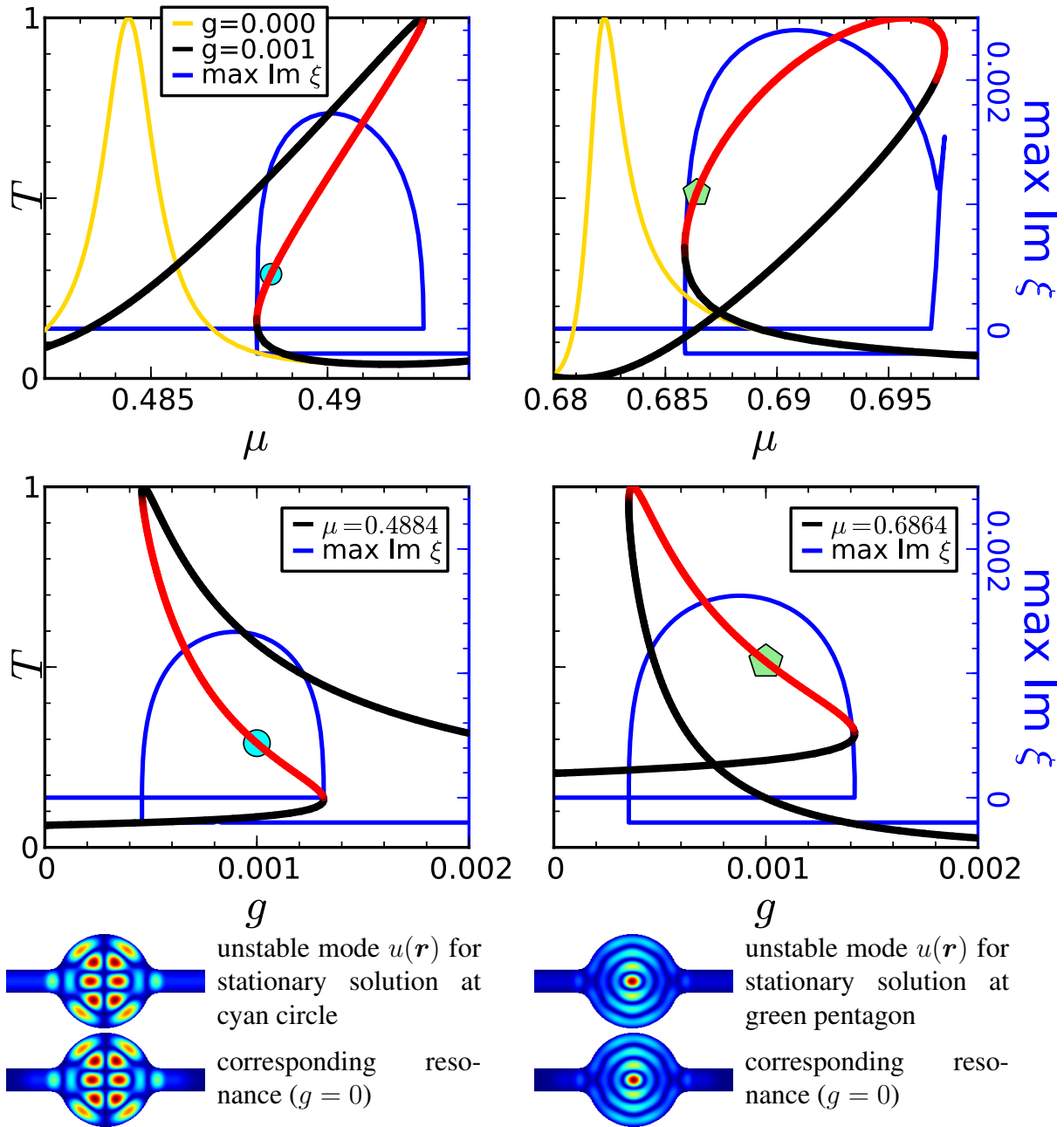


Figure 5.23: These figures illustrate the stability $\max \text{Im } \xi$ (shown in blue) for the resonance structures studied in Fig. 5.3 and Fig. 5.4. In all four plots the rightmost branch of the stability was shifted down to enhance visibility. The stability would be 0 there otherwise. Furthermore the stability is color-encoded in the transmission curves (shown in black/red). Black means that the stationary solution is stable ($\max \text{Im } \xi \leq 0$) and red means that the stationary solution is unstable ($\max \text{Im } \xi > 0$). The eigenfunction $u(\mathbf{r})$ corresponding to the unstable $\max \text{Im } \xi$ for the indicated values of g and μ is shown, too. They are closely related to the resonances (for $g=0$) belonging to the transmission peaks. The dynamical stability over the whole energy range is shown in Fig. 5.14.

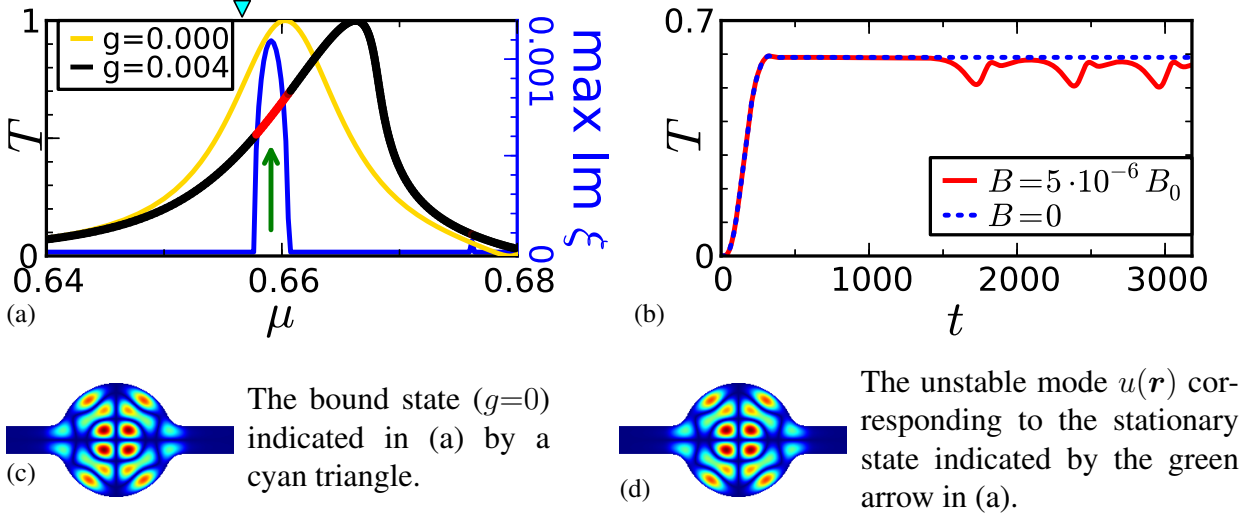


Figure 5.24: (a) shows a region in the spectrum of the example system \mathcal{B}_1 (see Sec. 3.8.1) where no stable solution exists. (b) shows a time dependent population of the cavity as done in Sec. 5.4.1 and Sec. 4.7 for the value of μ indicated in (a) by a green arrow for $g=0.004$. As the unstable eigenmode has parity -1 (see (d)) with respect to the reflection $y \mapsto -y$ it cannot be excited by the lowest lead eigenmode and thus a small symmetry breaking magnetic field is necessary to reveal the instability. The wavefunction starts to oscillate after some time (t is measured in units of $2\pi\hbar/E_0$). In experiments this symmetry breaking would be unnecessary as some imperfection will be always present. The unstable eigenmode shown in (d) is caused by the bound state shown in (c).

Here we have set $\tilde{w} = Zw$. Using $Z\sigma_3 Z^{-1} = -iJ$ and defining $\tilde{T} = ZTZ^{-1}$ we can now rewrite Eq. (5.33) as:

$$\tilde{T}\tilde{w} = -i\xi J\tilde{w}. \quad (5.34)$$

The main improvement over (5.32) is now that \tilde{T} contains only real entries:

$$\tilde{T} = \begin{pmatrix} +\text{Re } H & -\text{Im } H \\ +\text{Im } H & +\text{Re } H \end{pmatrix} - \begin{pmatrix} \mu & 0 \\ 0 & \mu \end{pmatrix} + g \frac{\hbar^2}{m} \begin{pmatrix} 3(\text{Re } \Psi_0)^2 + (\text{Im } \Psi_0)^2 & 2(\text{Re } \Psi_0)(\text{Im } \Psi_0) \\ 2(\text{Re } \Psi_0)(\text{Im } \Psi_0) & (\text{Re } \Psi_0)^2 + 3(\text{Im } \Psi_0)^2 \end{pmatrix}.$$

Furthermore an inspection of Eq. (5.9) and Eq. (5.10) reveals that \tilde{T} is nothing else than the derivative of the function

$$F : \mathbb{R}^{2n} \rightarrow \mathbb{R}^{2n}, \quad \Psi(\mathbf{r}) \mapsto [H - \mu] \Psi(\mathbf{r}) + g(\mathbf{r}) \frac{\hbar^2}{m} |\Psi(\mathbf{r})|^2 \Psi(\mathbf{r})$$

with respect to $\Psi(\mathbf{r})$ at the position $\Psi_0(\mathbf{r})$. This is to be expected as one can rewrite Eq. (5.30) as follows:

$$i\hbar \frac{\partial}{\partial t} \Psi(\mathbf{r}, t) = F(\Psi(\mathbf{r}, t)) + S(\mathbf{r}).$$

A linearization of this equation around the stationary solution $\Psi_0(\mathbf{r})$ and a subsequent exponential mode ansatz directly leads to Eq.(5.34) after splitting everything in real and imaginary parts as done in Sec. 5.2.1.

In the notation of Eq. (5.12) we can conveniently write

$$\tilde{T} = \mathcal{D}F = H - \mu + g(\mathbf{r}) \frac{\hbar^2}{m} \frac{\partial [|\Psi_0(\mathbf{r})|^2 \Psi_0(\mathbf{r})]}{\partial \Psi_0(\mathbf{r})} \quad (5.35)$$

and use the same methods already developed in Sec. 5.2.1 to calculate \tilde{T} .

To numerically solve the generalized eigenvalue problem Eq. (5.34) we first transform it into an ordinary eigenvalue problem:

$$J^{-1}\tilde{T}\tilde{w} = -i\xi\tilde{w} . \quad (5.36)$$

Any dynamical unstable mode fulfills $\text{Re}(-i\xi) > 0$. Therefore we now use the Cayley transformation (with the parameter $\beta \in \mathbb{R}^+$)

$$f_C(z) = \frac{z + \beta}{z - \beta}$$

which maps the half-plane $\{z \in \mathbb{C}, \text{Re } z > 0\}$ onto the complement of the unit-circle $\{z \in \mathbb{C}, |z| > 1\}$. That means that all eigenvalues of $J^{-1}\tilde{T}$ with $\text{Re}(-i\xi) > 0$ are transformed in eigenvalues of $f_C(J^{-1}\tilde{T})$ with magnitude larger than one. Hence we can now apply the implicit restarted Arnoldi method [193, 194] as realized in the software library ARPACK [130] onto the linear mapping

$$f_C(J^{-1}\tilde{T}) = [J^{-1}\tilde{T} - \beta]^{-1} [J^{-1}\tilde{T} + \beta] = [\tilde{T} - \beta J]^{-1} [\tilde{T} + \beta J] \quad (5.37)$$

to finally solve the eigenvalue problem Eq. (5.36) and therefore also the eigenvalue problems Eq. (5.33) and Eq. (5.32). Eq. (5.37) is some kind of twisted form of the Crank-Nicholson method Eq. (4.6).

Up to now we have completely neglected the topic of boundary conditions. For the calculation of stationary scattering solutions by Eq. (5.29) we used the self-energy boundary conditions⁷ introduced in Eq. (3.36). But because the stability analysis is based on the time dependent Gross-Pitaevskii equation (5.30) we have to use the exterior complex scaling boundary conditions⁸ defined by Eq. (3.63) in the Bogoliubov-de Gennes equation (5.32), especially in Eq. (5.35). These boundary conditions are applicable for the stability analysis because

- they work for the time propagation as explained in Sec. 4.6.
- they are able to absorb more than one energy component at once as explained in in Sec. 3.7 and Sec. 4.6.
- they are simply an (energy independent) modification of the Hamiltonian H .

For the stability analysis in practical calculations the lattice is enlarged and exterior complex scaling boundary conditions are applied in the prolonged leads. The wavefunction $\Psi_0(\mathbf{r})$ can be transferred from the original lattice to the extended lattice without problems because the prolonged part does not contribute to \tilde{T} as $g(\mathbf{r})$ is zero in the extended leads.

The stability analysis here works on the level of the Gross-Pitaevskii equation. But this equation is only a mean field approximation of the true many body dynamics. The next logical step is to ask under which circumstances this mean field approximation itself breaks down. This question

⁷ Technically we could also use the exterior complex scaling boundary conditions for the stationary scattering solutions as they can also be used for calculation of the retarded Green function as explained in Sec. 3.7. But for different reasons (*ECSBC* requires more grid points and has problems with long wavelengths) this is not the way how it is implemented.

⁸ One can use any working boundary conditions for simulation of Eq. (5.30) but for the stability analysis one has to use exterior complex scaling boundary conditions.

can be answered using the Hartree-Fock-Bogoliubov theory [67, 120] which uses higher order cumulants⁹. But this approach is prohibitive computational expensive for two dimensional systems as it requires four dimensional simulations even if one goes only one step beyond the mean field approach.

5.8 Other geometries

We now apply the numerical methods of the previous section to other billiard geometries. Overall the findings for almost closed billiard systems are similar to the observations made using the example geometry \mathcal{B}_1 introduced in Sec. 3.8.1. But systems strongly coupled to the leads show a different behaviour which will be investigated more closely in Chap. 6.

5.8.1 \mathcal{B}_2 : A nearly closed system without horizontal mirror symmetry

The first billiard system studied here is a slight variation of the billiard \mathcal{B}_1 . While that system was mirror symmetric with respect to the x - and the y -axis, we now break the symmetry $x \mapsto -x$. To this end we use the limaçon of Pascal [33] as boundary of our system. In polar coordinates this curve is given by

$$r(\phi) = r_0 (1 + e_0 \cos \phi) . \quad (5.38)$$

Otherwise the setup is analogous to \mathcal{B}_1 . Two potential barriers of height V_0 and width σ_0 ensure that the system is almost closed. An illustration of the billiard is shown in Fig. 5.25 and the parameters used can be found in Fig. 5.27.

Due to the broken symmetry the resonances (also shown in Fig. 5.25) do not couple equally into the left and right lead. The consequence is that most resonance peaks in the transmission spectrum (shown in Fig. 5.26) do not reach $T = 1$. This is in contrast to the symmetric billiard \mathcal{B}_1 whose resonance peaks reach $T = 1$ except when overlapping resonances prevent perfect transmission¹⁰ (see Fig. 3.13). Moreover in the interacting case $g \neq 0$ the resonance peaks vary in height in contrast to the symmetric case shown in Fig. 5.13 and Fig. 5.14 where the height of most peaks remains at $T = 1$ even in the interacting case. This is a consequence of the fact that the interaction potential $g(\mathbf{r}) \frac{\hbar^2}{m} |\Psi(\mathbf{r})|^2 \Psi(\mathbf{r})$ is now an asymmetric function which effectively changes the coupling into the leads. The perturbation theory for the energy μ introduced in Sec. 5.6.2 is by design unable to predict this change in height of the deformed resonance structures for $g \neq 0$. Apart from this defect it works quite nicely as seen in Fig. 5.28. Of course very sharp resonances remain a problem for the perturbation method.

In Fig. 5.26 shows also resonance structures which do not fall in neither of the categories “titled peak” or “loop” introduced in Sec. 5.5 for $g \neq 0$. This happens in the case of overlapping resonances which show a complicated behaviour in the non-linear case.

The results of time dependent simulations and of a dynamical stability analysis for the limaçon billiard are shown in Fig. 5.29. Both methods work in the same way as for the symmetric billiard \mathcal{B}_1 .

⁹ The wavefunction described by the Gross-Pitaevskii equation can be defined as $\Psi(\mathbf{r}, t) = \langle \hat{\Psi}(\mathbf{r}, t) \rangle$ using the many-particle field operator $\hat{\Psi}(\mathbf{r}, t)$. A second order cumulant is then defined as $\Phi(\mathbf{r}_1, \mathbf{r}_2, t) = \langle \hat{\Psi}(\mathbf{r}_1, t) \hat{\Psi}(\mathbf{r}_2, t) \rangle - \langle \hat{\Psi}(\mathbf{r}_1, t) \rangle \langle \hat{\Psi}(\mathbf{r}_2, t) \rangle$.

¹⁰ Different resonances can interfere destructively when they overlap.

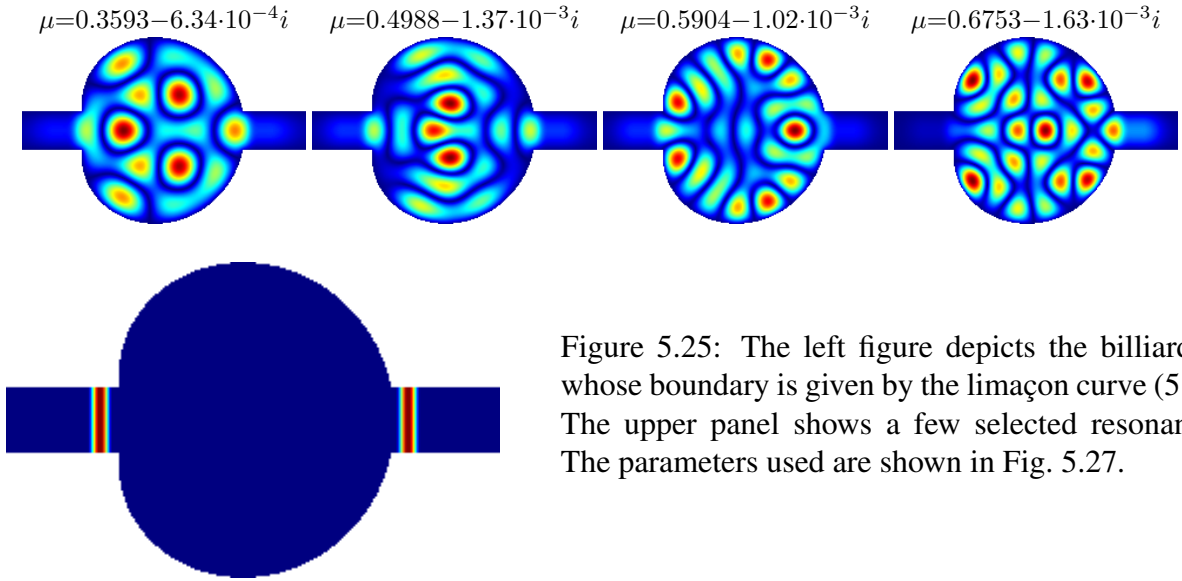


Figure 5.25: The left figure depicts the billiard \mathcal{B}_2 whose boundary is given by the limaçon curve (5.38). The upper panel shows a few selected resonances. The parameters used are shown in Fig. 5.27.

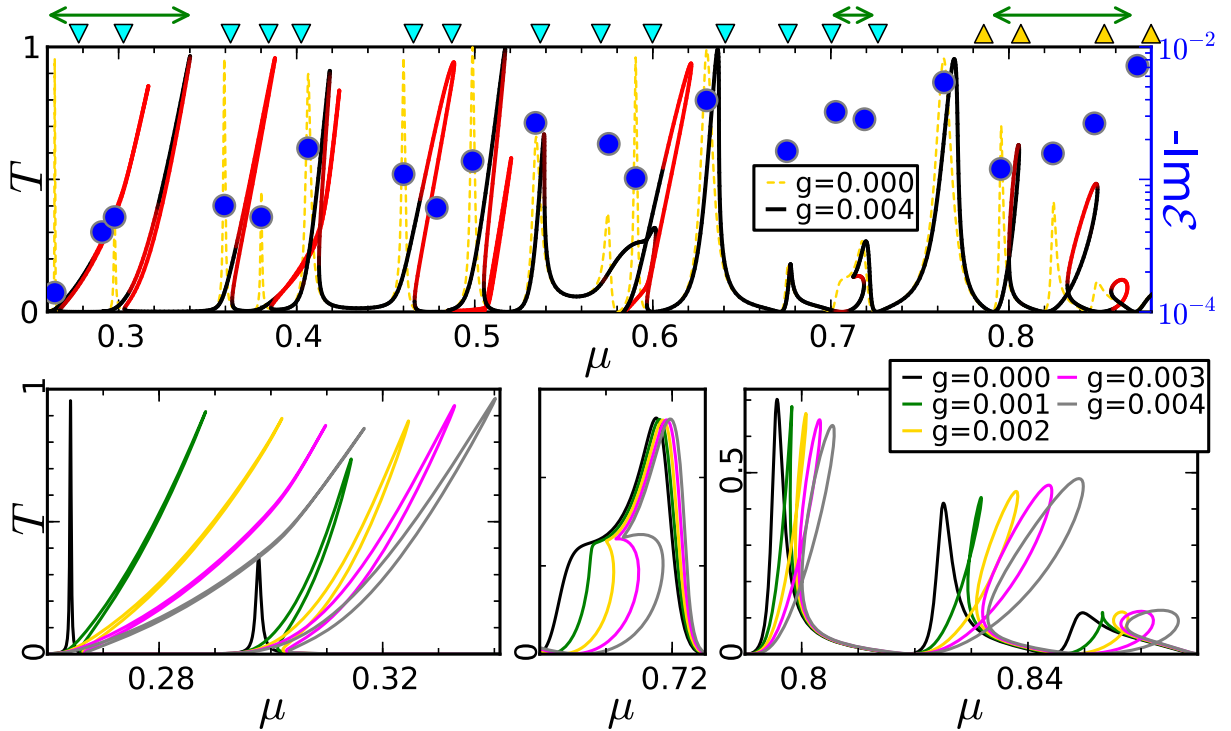


Figure 5.26: The upper panel shows the transmission spectrum for $g=0$ and $g=0.004$ for the limaçon billiard \mathcal{B}_2 . The dynamical stability is color-encoded. The blue dots show the real (horizontal axis) and imaginary part (right axis) of the resonance energies. The blue triangles on top indicate the position of bound states which cannot couple into the leads because they do not have the right parity with respect to the symmetry $y \rightarrow -y$. The yellow triangle indicate resonances (coupling into the leads) which have the same parity as the aforementioned bound states but which are not excited because the source mode is orthogonal to them. The lower panel shows the transmission spectrum for various values of g for selected ranges of μ indicated in the upper panel through green arrows. All energies are measured as multiples of the characteristic energy E_0 .

parameter	value	description
$\sqrt{\Omega}$	$8.9 \pi k_0^{-1}$	Ω is the area of the cavity
W	$2.25 \pi k_0^{-1}$	width of the leads
r_0	$4.5 \pi k_0^{-1}$	“radius” of the limaçon
e_0	0.7	parameter of the limaçon
V_0	$0.19 E_0, 0.78 E_0$	energies of the lead eigenmodes
σ_0	$1 E_0$	height of the barrier potential
Δx	$0.45 \pi k_0^{-1}$	width of the barrier potential
n	$\frac{1}{15} \pi k_0^{-1}$	lattice spacing
τ	24702	lattice dimension
τ	$0.025 \hbar E_0^{-1}$	time step
x_s	$5.4 \pi k_0^{-1}$	switching length for $g(x)$

Figure 5.27: This table shows the parameters used for the billiard \mathcal{B}_2 depicted in Fig. 5.25.

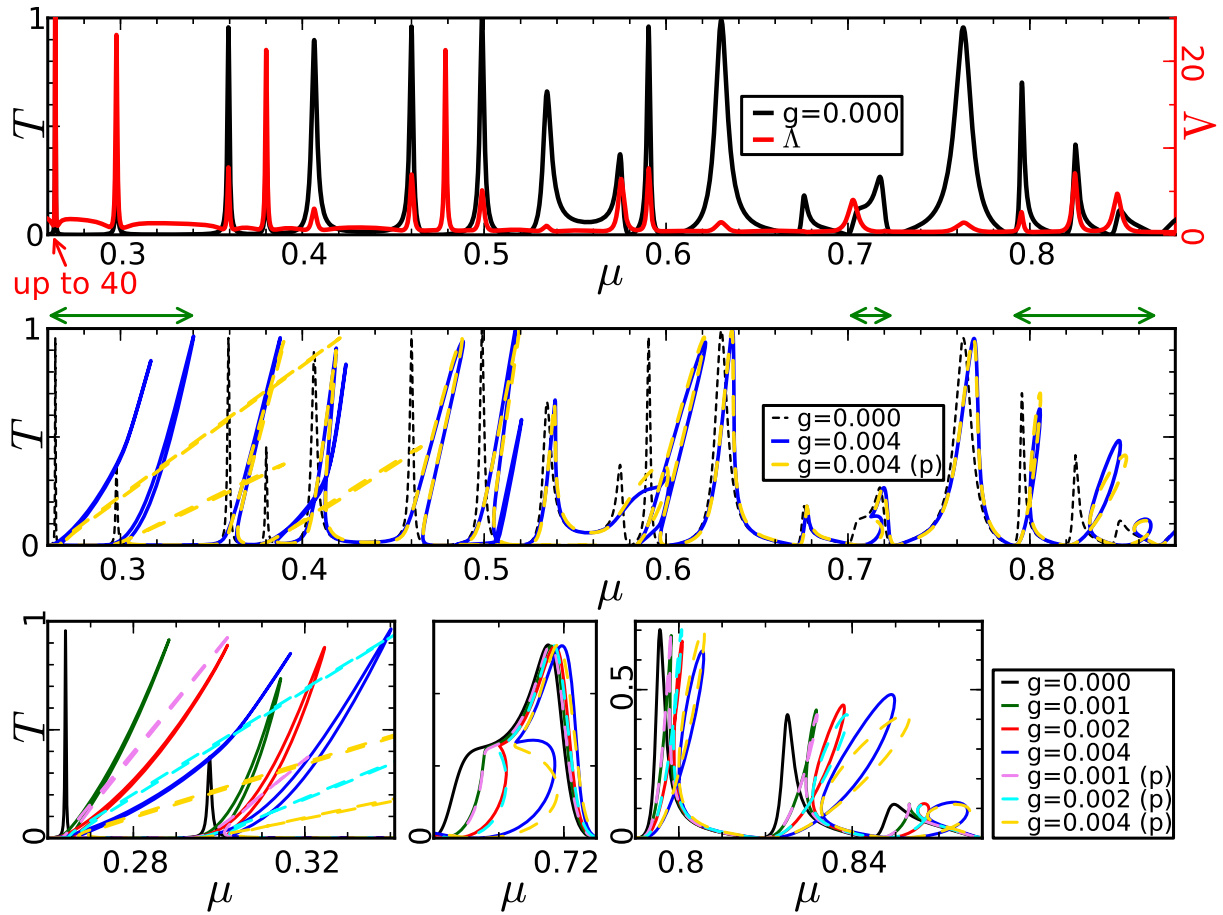


Figure 5.28: These figures illustrate how the perturbation theory for the energy μ developed in Sec. 5.6.2 works for the billiard \mathcal{B}_2 shown in Fig. 5.25. The upper panel shows the transmission spectrum in the linear case along with the energy shift Λ given by Eq. (5.27). The middle panel compares the numerical obtained transmission spectrum for $g=0.004$ with the perturbation theory Eq. (5.28) (marked by “(p)”). The lower panel does the same for selected energy ranges (illustrated in the middle panel by green arrows) and various values of g .

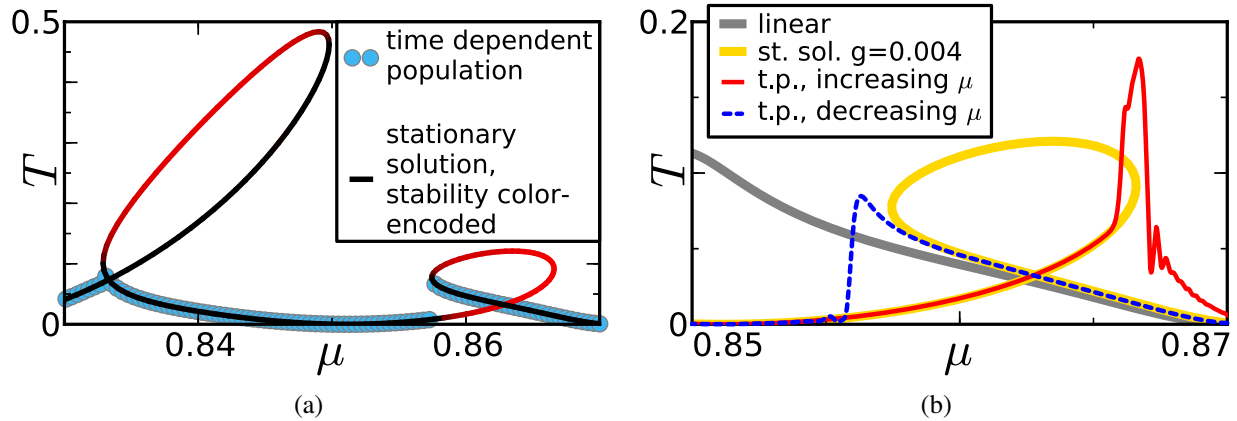


Figure 5.29: These two figures show a part of the transmission spectrum for $g=0.004$ for the billiard \mathcal{B}_2 depicted in Fig. 5.25. In Fig. (a) the stability ξ introduced in Sec. 5.7 is color-encoded into the transmission spectrum (black is stable, red is unstable). Furthermore Fig. (a) shows the results obtained through a time dependent population of the cavity as described in Sec. 5.4.1 (switch time $t_s=500\hbar E_0^{-1}$, halt time $t_h=6000\hbar E_0^{-1}$). In Fig. (b) we show the transmission obtained through a time-dependent adiabatic variation of μ as described in Sec. 5.4.2 (adiabatic passage $t_a=20000\hbar E_0^{-1}$).

5.8.2 \mathcal{B}_3 : A nearly closed system without any symmetry

In order to break the remaining symmetry of billiard \mathcal{B}_2 we now rotate the limaçon Eq. (5.38) by an angle ϕ_0 . Furthermore we use here a constriction inside the leads instead of a confinement potential to make the system almost closed. The resulting shape is shown in Fig. 5.30

The effects of the non-linearity on the transmission for this billiard \mathcal{B}_3 shown in Fig. 5.31 are similar to the findings obtained using \mathcal{B}_2 : The transmission does not always reach $T = 1$ and the interaction can change the height of the peaks. The perturbation theory works satisfactory except for very sharp resonances.

The major difference between \mathcal{B}_3 and the other systems is that \mathcal{B}_3 does not have bound states embedded inside the continuous spectrum as all resonances couple more or less to the leads. No symmetry is preventing this. For the transmission these bound states are irrelevant but the bound states affect the dynamical stability. In the systems with embedded bound states (due to symmetry) the stationary scattering states might become dynamically unstable in regions of the spectrum where it is not expected. This instability arises because of such bound states. This can be seen in Fig. 5.24, Fig. 5.29 and Fig. 5.34.

5.8.3 \mathcal{B}_4 : Another nearly closed full symmetric system

In this section we investigate a billiard whose boundary is not given by a hard wall but instead is defined by a smooth potential barrier of height $V_0 = 3 E_0$. Basically the shape of the cavity is a circle (radius r_0) with a tiny barrier at the openings of the leads. Numerical the potential has been calculated by convoluting a step potential ($V = 0$ inside the circle and in the leads and $V = V_0$ outside) with a Gaussian curve of width σ_0 . The grid is rectangular. The reason for this choice of setup is that the very first numerical method developed by me was an inferior version of the split operator method introduced in Sec. 4.5. And the split operator method only works

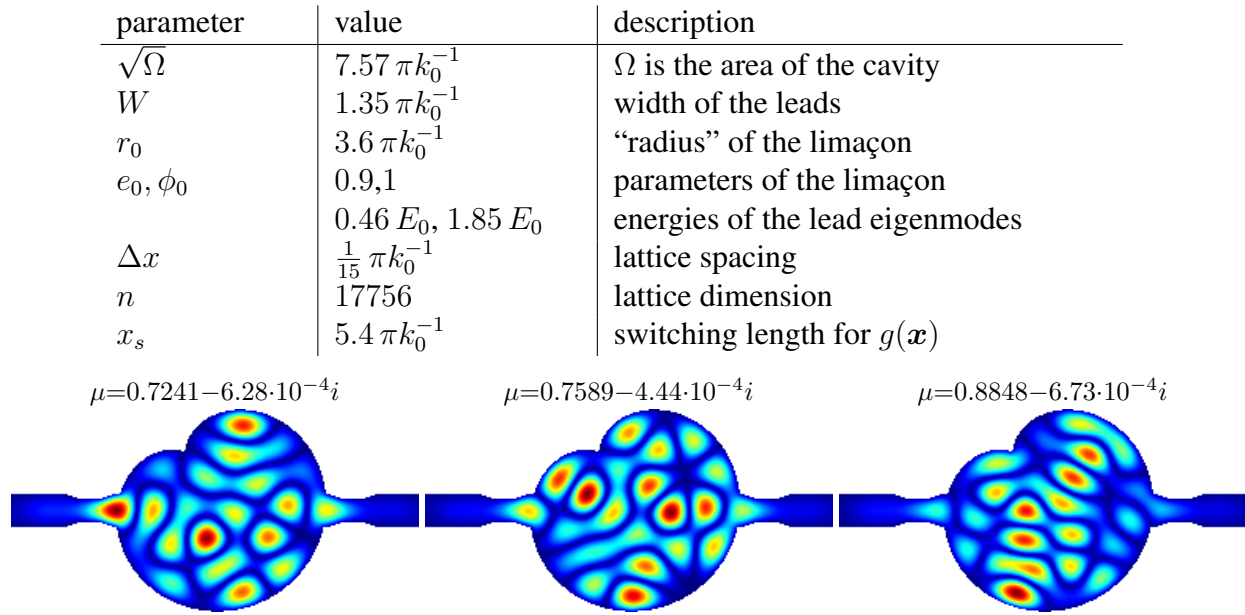


Figure 5.30: These pictures show a few selected resonances of the billiard \mathcal{B}_3 whose parameters are displayed in the upper tabular.

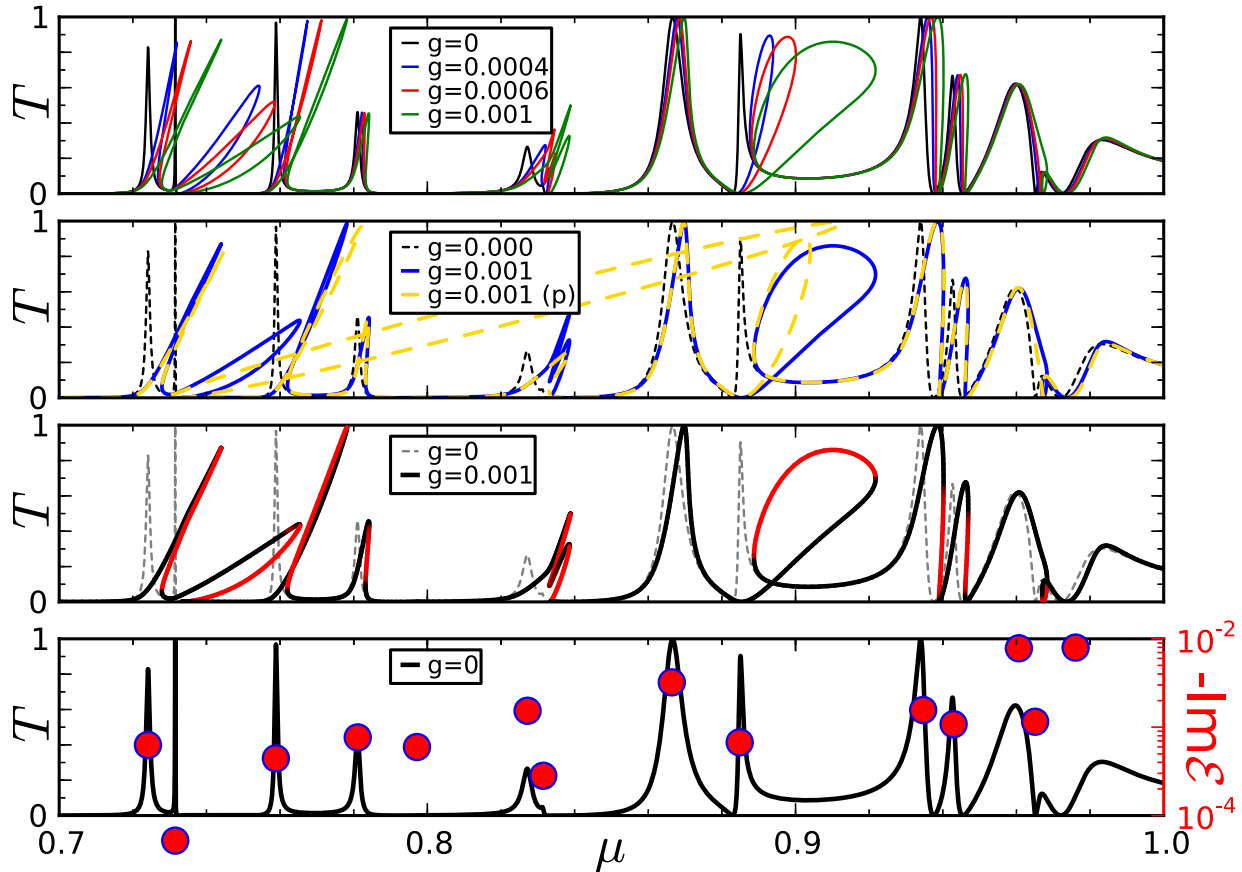


Figure 5.31: These figure shows the transmission properties of billiard \mathcal{B}_3 . The lower panel shows the resonances and the linear transmission. The two panels in the middle show the dynamical stability ξ (color encoded in black(stable) and red(unstable)) and the performance of the perturbation theory for μ (see Sec. 5.6.2, marked by (p)) for $g = 0.001$. The upper panel shows the transmission for various values of the interaction strength g .

parameter	value	description
$\sqrt{\Omega}$	$15.98 \pi k_0^{-1}$	Ω is the area of the cavity
W	$1.62 \pi k_0^{-1}$	width of the leads
r_0	$9 \pi k_0^{-1}$	radius of the cavity
V_0	$3 E_0$	confinement potential
σ_0	$0.45 \pi k_0^{-1}$	width of the Gaussian
	$0.46 E_0, 1.39 E_0$	energies of the lead eigenmodes
Δx	$\frac{1}{15} \pi k_0^{-1}$	lattice spacing
n	141600	lattice dimension
τ	$0.025 \hbar E_0^{-1}$	time step
x_s	$4.5 \pi k_0^{-1}$	switching length for $g(x)$

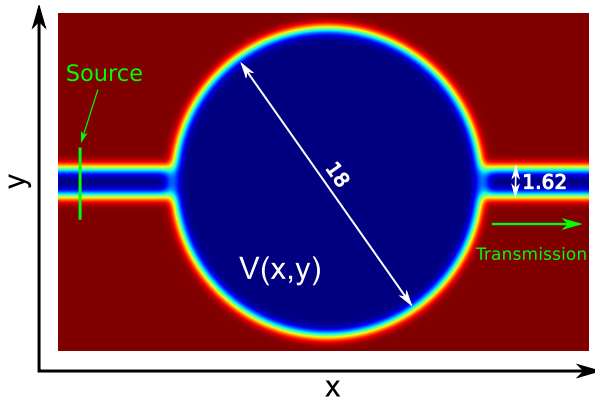
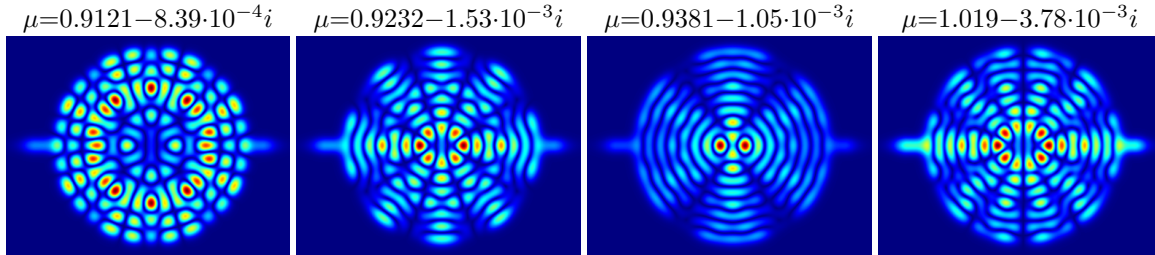


Figure 5.32: The left figure illustrates the potential used for \mathcal{B}_4 . Blue denotes $V = 0$ and brown denotes $V = V_0$. The potential is a step function smoothed by a Gaussian curve of width σ_0 . The upper tabular shows the parameters used for the simulation. The lower panel depicts a few selected resonances.



on rectangular grids with a finite and smoothed potential. The split operator method is naturally the most efficient time propagation method for this billiard while the performance of the Crank-Nicholson and Taylor-series methods is worse (both have roughly the same performance).

This billiard \mathcal{B}_4 has the same symmetries as the billiard \mathcal{B}_1 (namely $x \mapsto -x$ and $y \mapsto -y$) and therefore the transmission shows for most energies μ a very similar behaviour as seen in Fig. 5.34.

The major difference is that there exists some very sharp resonances¹¹ (i.e. the imaginary part of \mathcal{E} is very small) which are strongly deformed in the non-linear case $g \neq 0$ as seen in Fig. 5.33. The reason is that the interaction energy Λ defined by Eq. (5.27) becomes extremely large for such resonances as seen in Fig. 5.33. Therefore the non-linear interaction potential has a dominant effect on those resonances. The deformed branches of those resonances cannot be populated by time propagation methods with a fixed energy μ as described in Sec. 5.4.1. Only by adiabatic variation of μ as described in Sec. 5.4.2 one is able to populate a small part of those branches using time propagation simulations. But the overwhelming part of those strongly deformed branches

¹¹Such resonances couple only very weakly to the leads.

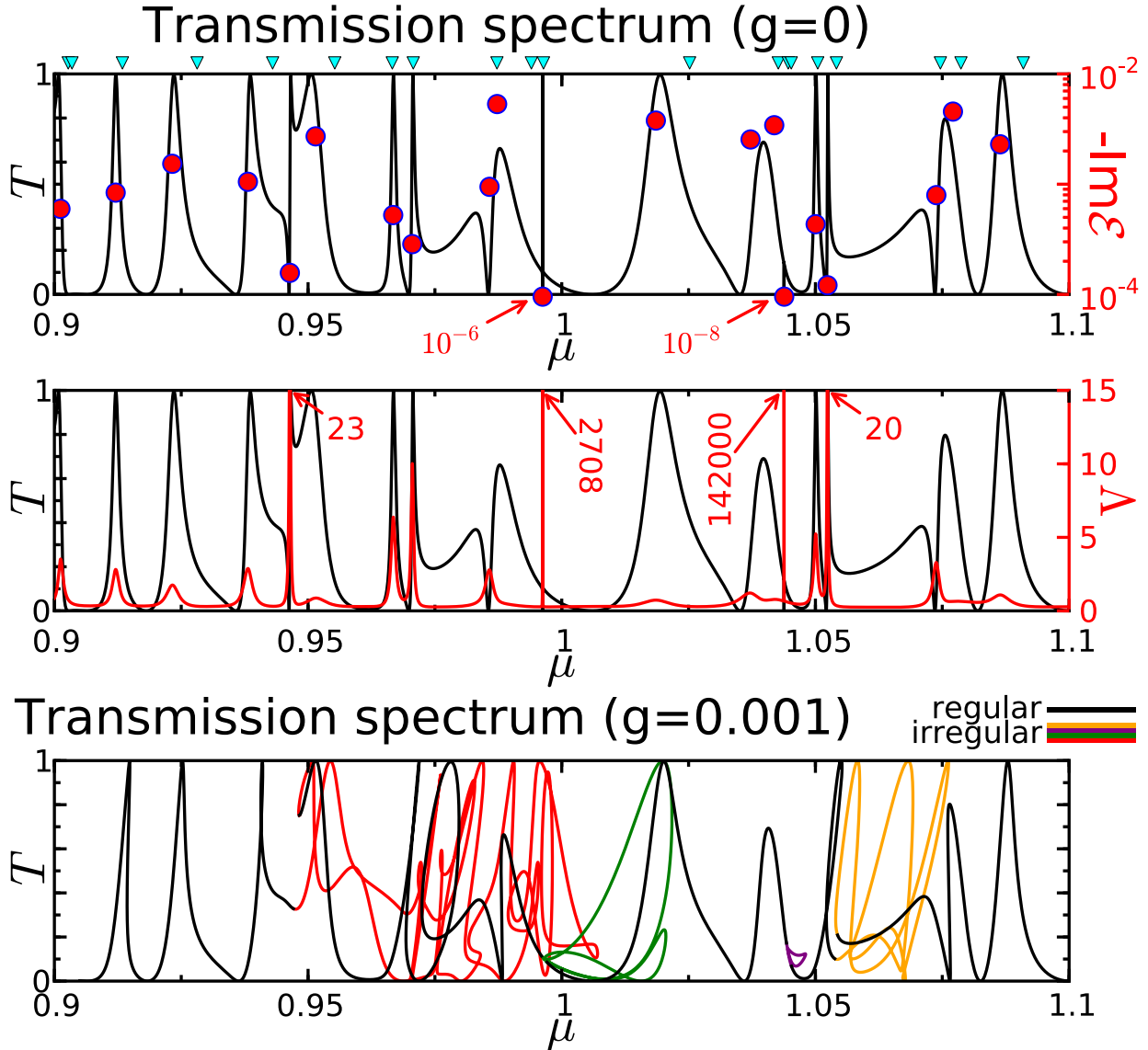


Figure 5.33: These figures show the transmission spectrum for the billiard \mathcal{B}_4 . The upper panel shows the resonances (red dots) along with the linear spectrum ($g=0$). Blue triangles indicate bound states which cannot couple into the leads because of the wrong parity. The middle panel shows the interaction energy Λ (defined by Eq. (5.27)) which can reach enormous values for some sharp resonances.

The lower panel shows the transmission spectrum for $g=0.001$. For better presentation the curve is split into several parts shown in different colors. The black part behaves regular for $g \neq 0$, i.e. it is not so strongly deformed and the perturbation theory for the energy developed in Sec. 5.6.2 works just fine. The colored parts correspond to single sharp resonances where the interaction potential strongly deforms the transmission curve. Here the perturbation theory does not work. These parts are mostly highly dynamical unstable and therefore of no practical physical importance.

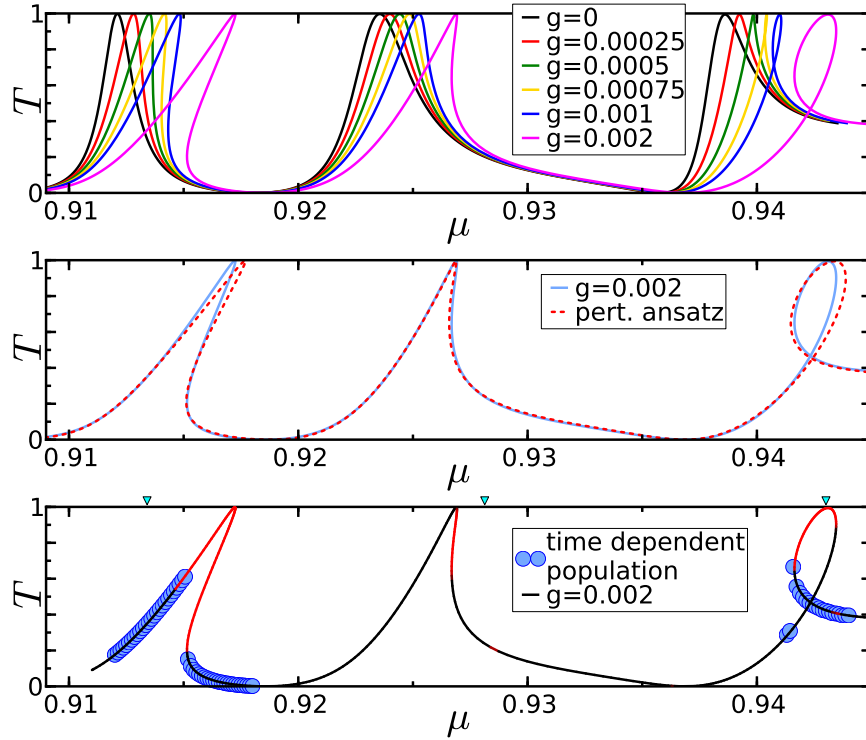
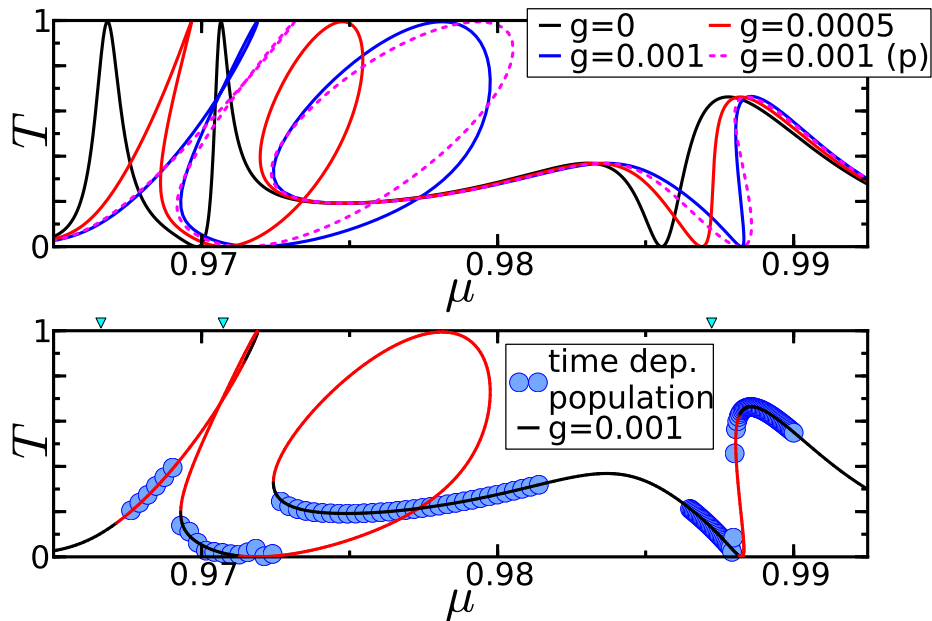


Figure 5.34: In the upper figures a selected energy range of the spectrum of billiard B_4 is closer examined. The upper panel depicts the transmission for various values of the interaction strength g . One can see tilted peak and loop structures similar to Sec. 5.5. The middle panel shows the good performance of the perturbation theory for μ developed in Sec. 5.6.2 for this part of the spectrum. The lower panel shows the result of time dependent populations as described in Sec. 5.4.1. The dynamical stability ξ is color encoded into the transmission curve. Bound states with the wrong parity (blue triangles) lead to positive values of ξ in regions where the time dependent population works just fine. The reason is that the symmetric ($y \rightarrow -y$) source term does not excite those bound states. The lower figures analyze a different energy range in the same way. The perturbation theory is marked there by (p).



is highly dynamical unstable and thus cannot be populated in any way. Therefore these branches are of no practical physical importance.

5.8.4 \mathcal{B}_5 : A wide open system with classical chaotic dynamics

After having studied only almost closed systems we now investigate a wide open system depicted in Fig. 5.35. This is a completely desymmetrized stadium billiard with a hole in the middle. No kind of barrier potential is applied, so we have a vanishing potential $V = 0$ except for the hard wall boundaries ($V = \infty$).

The hole is there for two reasons. The first reason is that it prevents direct classical paths from one lead to the other which leads to a better performance of the diagrammatic semiclassical perturbation theory developed in Sec. 6.1. The second reason is that one can move the hole around (in some limits) and calculate the transmission properties for different geometries. In this way one can calculate a geometry average of the transmission which will provide better results in Sec. 6.1.4.

In this work we studied the energy range $\mu \in 0.84 E_0 \dots 1.21 \dots E_0$ where five modes in each lead are open. This is the range where the effect of the interaction on the weak localization is seen most clearly as explained in Sec. 6.1.4. The resonances can couple well into these wide open leads which results in broad resonances.

The major difference between the wide open billiard \mathcal{B}_5 and the systems studied in the previous sections is that the resonances of \mathcal{B}_5 are not well separated anymore but are overlapping heavily as their width exceeds their spacing (see Fig. 5.36). Therefore the spectrum does not consist of simple well separated resonance peaks but instead shows a widely fluctuating behaviour known as Ericson fluctuations [65, 146] (see Sec. 6.1.3).

The effect of the interaction g on this fluctuating spectrum is highly irregular and much more complicated than in the case of an almost closed system as seen in Fig. 5.38. Especially one cannot categorize the resonance structures into “tilted peaks” or “loops”. The perturbation theory for the energy μ developed in Sec. 5.6.2 works only rudimentary as seen in Fig. 5.36. While the energy shift $g\Lambda$ fits relatively well the height of the transmission curve varies wildly. In order to describe this variation of the height the more sophisticated semiclassical perturbation theory presented in Sec. 6.1 has to be employed.

The transmission T as function of g follows also no observable pattern as seen in Fig. 5.39. Time-dependent population in the spirit of Sec. 5.4.1 of the billiard always populates the first encountered branch as explained in Sec. 5.4.3. This fact will be used in Sec. 6.1.4 to select states for the calculation of the weak localization effect. Time dependent variation of g works also nicely as seen in Fig. 5.40. The wavefunction stays always on the branch it is currently located on and jumps to another branch as soon as the current branch ends. For large values of g there exists no stable solution. This can be seen from the dynamical stability analysis (Fig. 5.39) as well as from the fact that time dependent methods reach no stationary solution (Fig. 4.3, Fig. 5.39 and Fig. 5.40).

Another important observation can be made by studying the averaged total transmission $T_{2 \leftarrow 1}$ of the annular stadium billiard \mathcal{B}_5 . This is defined as the transmission from lead no. 1 (left) to lead no. 2 (right) averaged over all incoming channels (see also Eq. (B.13))

$$T_{2 \leftarrow 1} = \frac{1}{N_1} \sum_{m,n} |\mathcal{T}_{2 \leftarrow 1, (m,n)}|^2 \quad (5.39)$$

parameter	value	description
$\sqrt{\Omega}$	$25.84 \pi k_0^{-1}$	Ω is the area of the cavity
	5	number of open channels in the leads
W	$5.4 \pi k_0^{-1}$	width of the leads
	$0.84 E_0, 1.21 E_0$	energies of the lead eigenmodes no. 5 and 6
Δx	$0.081 \pi k_0^{-1}$	lattice spacing
n	121202	lattice dimension
τ	$0.025 \hbar E_0^{-1}$	time step
x_s	$5.4 \pi k_0^{-1}$	switching length for $g(x)$
τ_D	$240.8 j_{\text{in}}^{-1} = 0.79 \tau_{D,u}$	classical dwell time
B_w	$0.22 B_0$	
	25	no. of geom. conf.
	50	in energy average
	$(0.93, 1.18) E_0$	

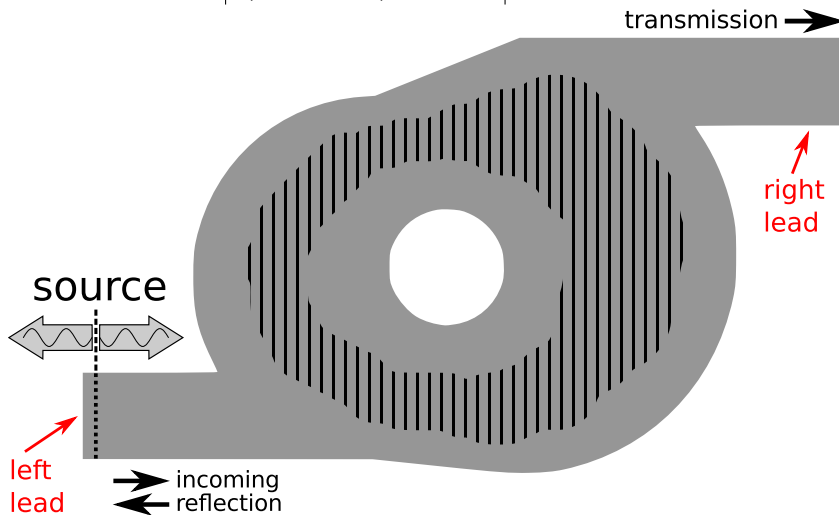
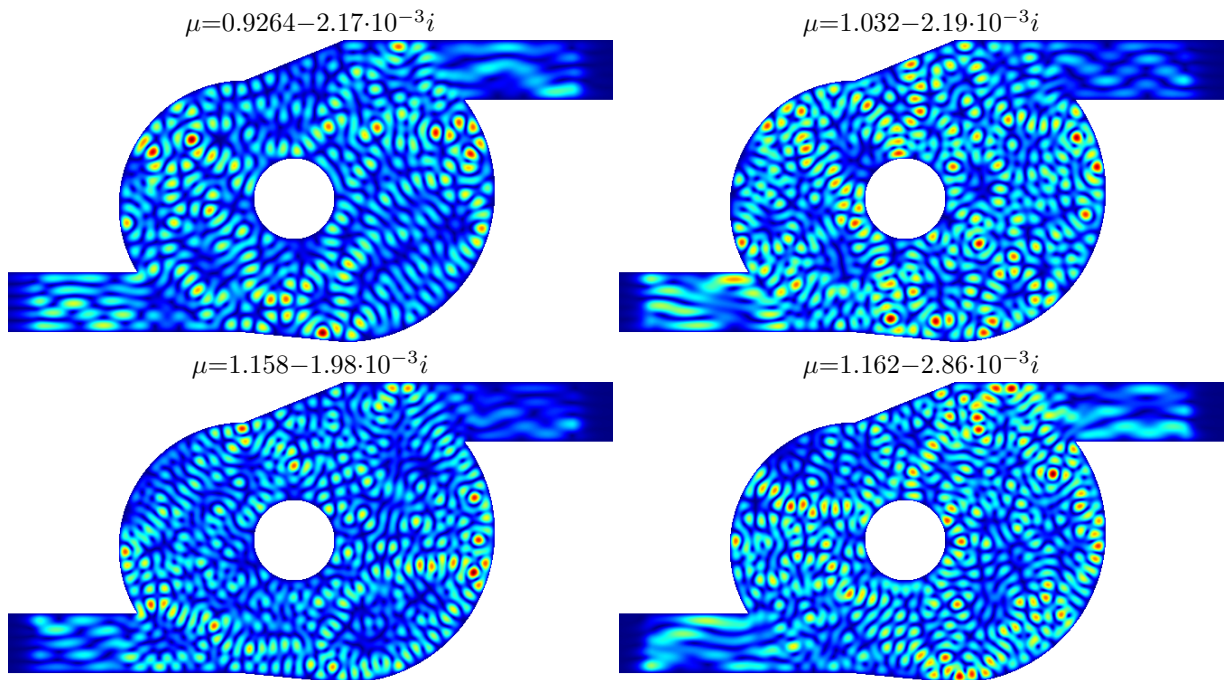


Figure 5.35: The left figure shows the annular stadium billiard \mathcal{B}_5 . The hatched area is used in Sec. 6.1.4 to calculate the wave function intensity distribution. The upper tabular shows the parameters used for this billiard. The lower figures show some selected resonances.



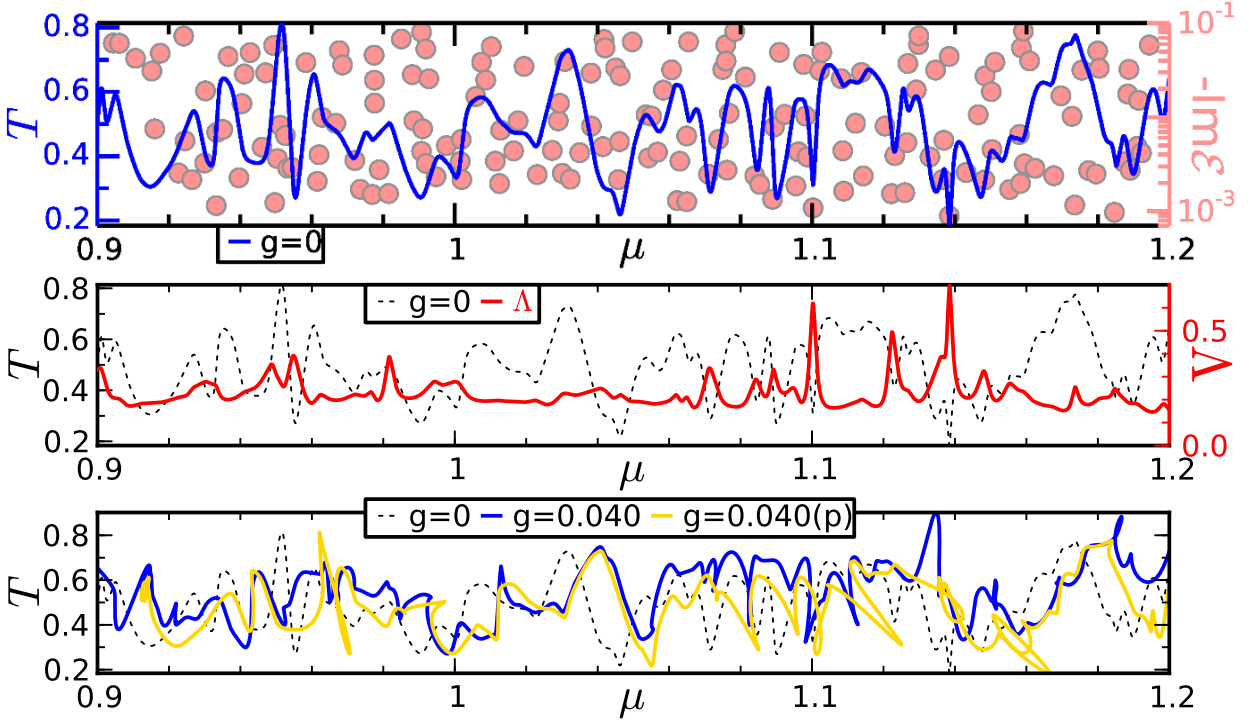


Figure 5.36: These figures illustrate the transmission properties of the annular stadium billiard \mathcal{B}_5 . The upper panel shows the transmission T (summed over all channels of the right lead) using a source term exciting mode no. 1 (the ground mode) in the left lead and a vanishing magnetic field $B = 0$ and a vanishing interaction strength $g = 0$. The red dots mark the position of the resonances. The middle panel displays the energy shift Δ given by Eq. (5.27). The lower panel shows the transmission for $g = 0.04$ along with the predictions from the perturbation theory Eq. (5.28) (marked by “(p)”).

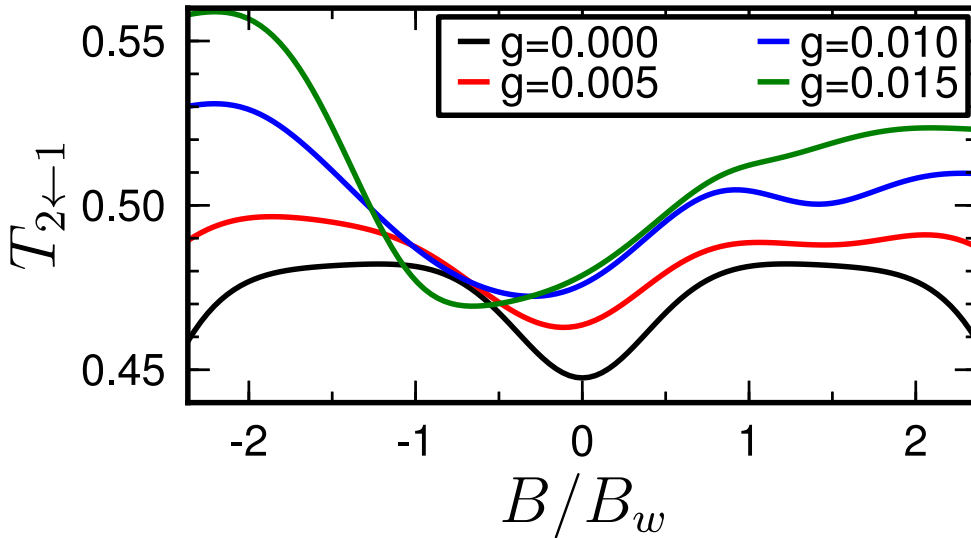


Figure 5.37: This figure shows the averaged total transmission $T_{2\leftarrow 1}$ defined by Eq. (5.39) as function of the magnetic field B for various values of the interaction strength g for the annular stadium billiard \mathcal{B}_5 using $\mu = 1.08306 E_0$. For vanishing interaction $g=0$ the total transmission is a symmetric function of B . This fact is called the Onsager relation [70] (see App. B). For $g \neq 0$ this symmetry is broken and the asymmetry increases with g . For better comparison with Sec. 6.1.4 we measure the magnetic field B in units of B_w (see Eq. (6.16)); numerically we have $B_w = 0.22 B_0$.

for a fixed energy μ and a fixed magnetic field B . Here $\mathcal{T}_{2\leftarrow 1,(m,n)}$ is the corresponding transmission amplitude, i.e. the entry of the scattering matrix \mathcal{S} , where m denotes the outgoing mode in lead no. 2 and n denotes the incoming mode in lead no. 1.

For vanishing interaction $g=0$ the total transmission $T_{2\leftarrow 1}$ is a symmetric function of the magnetic field B . This fact is called the Onsager relation [70] (see App. B, especially Eq. (B.16)). For a non-vanishing interaction strengths g this Onsager relation is broken as seen in Fig. 5.37. The reason for this breaking of the symmetry (explained in detail in App. B) is that the interaction destroys the unitarity of the scattering “matrix”¹² \mathcal{S} on which the derivation of the Onsager relation is based. Similar findings have been reported before in electronic transport through mesoscopic structures for strong bias voltages leading to non-linear effects [89, 180, 181].

One should note that after taking the energy and configuration average the Onsager relations are restored to some extent as seen in Fig. 6.9. This is because in a cavity with chaotic classical

¹² \mathcal{S} is in this case a non-linear mapping and not a linear mapping representable by a matrix.

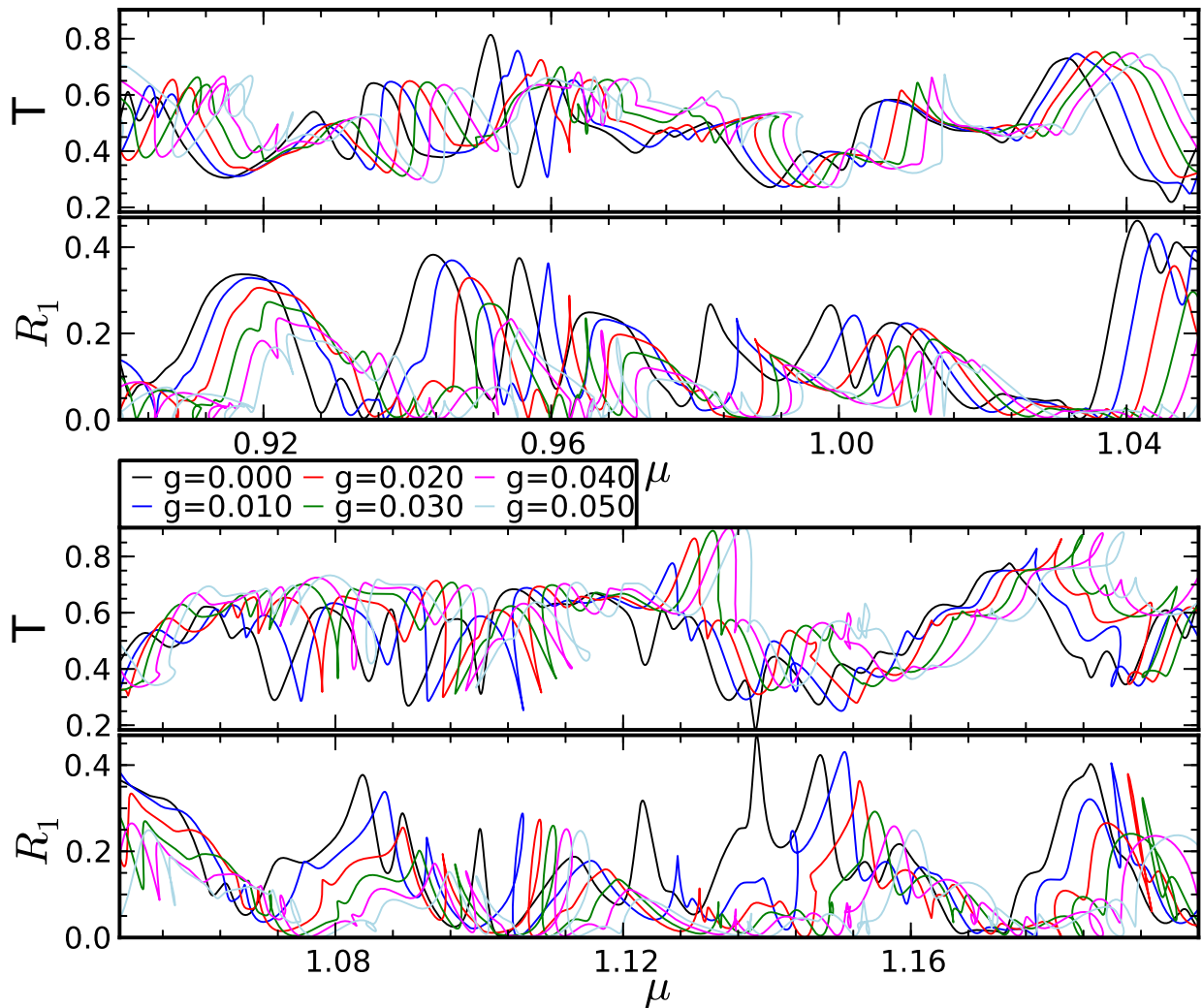


Figure 5.38: These figures show the transmission T (summed over all modes of the right lead) and the reflection R_1 into mode no. 1 of the left lead for the annular stadium billiard \mathcal{B}_5 for various values of the interaction strength g . The source term excites mode no. 1 (the ground mode) in the left lead.

dynamics there is (usually) no preferred direction and therefore the magnetic fields B and $-B$ are expected to have the same effect.

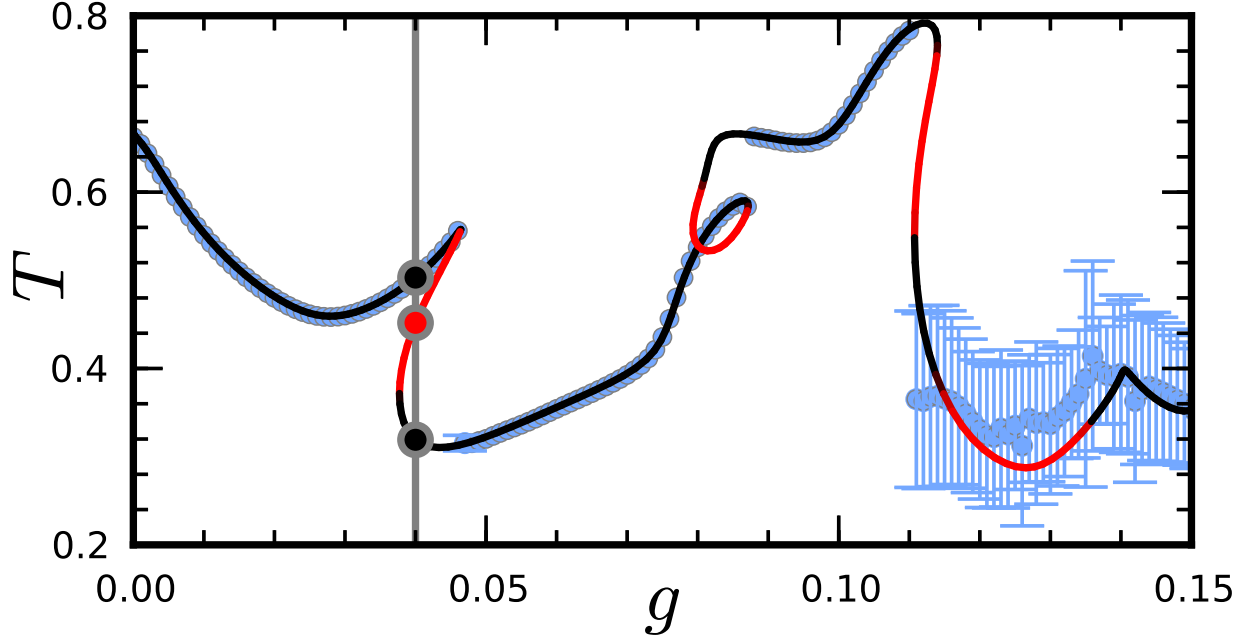


Figure 5.39: This figure shows the transmission T as a function of g using $\mu = 0.935 E_0$, $B = -0.524 B_0$ and the incoming lead mode no. 1 (the ground mode) for the billiard \mathcal{B}_5 . The dynamical stability ξ is color encoded into the transmission curve: black is stable and red is unstable. The blue dots show the transmission calculated by populating the billiard using time propagation as described in Sec. 5.4.1. The error bars of the blue dots indicate that the wave function does not reach a stationary state during time propagation. Some corresponding transmission curves as function of time can be seen in Fig. 4.3. The gray line illustrates how the states are selected for the investigation of the weak localization effect in Sec. 6.1.4. In this case we would select the upper black dot.

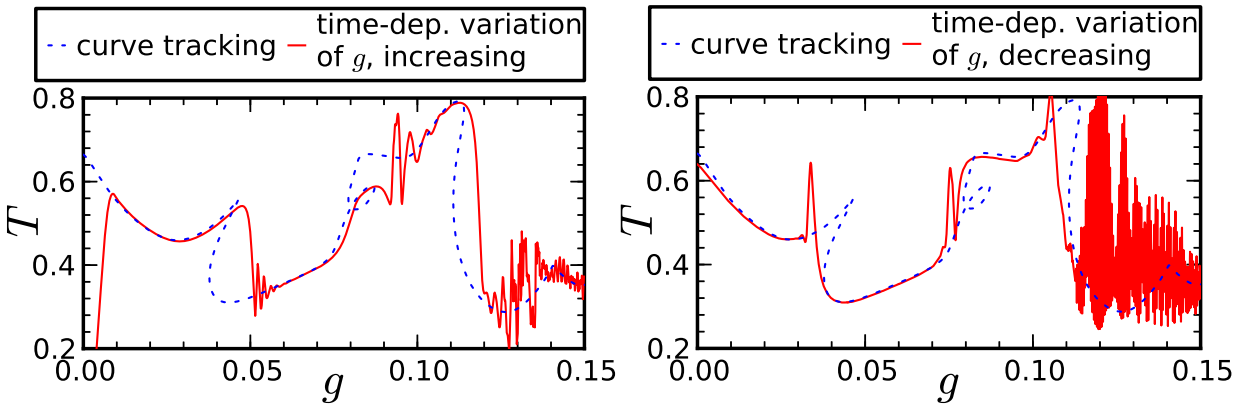


Figure 5.40: This two figures show the transmission T calculated using a time propagation with an adiabatic variation of the interaction strength g as explained in Sec. 5.4.3. The parameters used here are the same as in Fig. 5.39. Hysteresis effects are visible nicely.

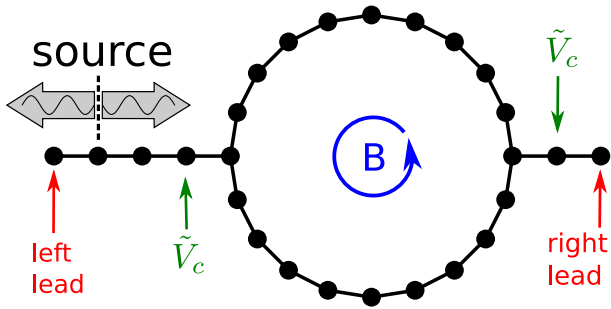


Figure 5.41: This figure illustrates the tight-binding model for ring systems. Two leads are connected by a ring through which a (dimensionless) magnetic flux B flows. The non-linear interaction g_n is restricted to the ring. A confinement potential \tilde{V}_c is applied to the first grid points outside the ring.

5.9 One dimensional systems with non-trivial topology

The main focus of this work are two-dimensional systems. But of course the techniques developed here can also be applied to one dimensional systems. These systems (with trivial topology) have already been extensively analyzed¹³ in [159–161].

In this section we are now applying our methods to one-dimensional systems with non-trivial topology. These systems consist of several one-dimensional chains connected in a non-trivial manner. The tight-binding model of such systems is a generalization of Eq. (3.50) and Eq. (5.1):

$$i\hbar \frac{\partial}{\partial t} \Psi_n = (H\Psi)_n + g_n \frac{\hbar^2}{m} |\Psi_n|^2 \Psi_n + S_n e^{-it\mu/\hbar}$$

$$\text{with} \quad (H\Psi)_n = \left[\alpha \left(\sum_{m \text{ neighbor}} 1 \right) + V_n \right] \Psi_n - \alpha \sum_{m \text{ neighbor}} e^{iBA_{nm}} \Psi_m.$$

The summation is performed over all neighbors m of n . The (dimensionless) phase BA_{nm} (a kind of “gauge potential”) allows us to study the response of the system to a magnetic flux. The condition $A_{nm} = -A_{mn}$ ensures that the Hamiltonian H is hermitian. The source S_n populates the system with particles.

The simplest examples are ring systems as depicted in Fig. 5.41. Two one-dimensional leads are connected by a ring. The source S_n is located inside the left lead; the transmission is measured to the right lead. The (dimensionless) phase A_{nm} is chosen inside the ring as $\pm 2\pi/N$ (– for clockwise connection, + for anticlockwise connection) where N is the number of grid points forming the ring. Outside the ring A_{nm} vanishes. This choice makes the transmission a periodic function¹⁴ of the (dimensionless) “magnetic field” B with period one: $T(B) = T(B + 1)$. This periodicity is called the Aharonov-Bohm effect [50]. The interaction g_n is only non-vanishing on points forming the ring and vanishes outside the ring.

The potential V_n vanishes inside the leads. In order to increase the time a particle spends inside the ring, a confinement potential \tilde{V}_c can be applied to the first grid points outside the ring which then becomes a kind of Sagnac/Fabry-Perot interferometer. Inside the ring we choose the potential to be either zero (\mathcal{B}_6) or to be a disorder potential ($\mathcal{B}_7, \mathcal{B}_8$).

All energies are measured in multiples of E_0 . With our choice of the tight-binding Hamiltonian the magnetic field B is dimensionless.

¹³ In one-dimensional systems (with trivial topology) the non-linear stationary scattering states can be simply calculated by solving a differential equation.

¹⁴ The replacement $B \rightarrow B + 1$ corresponds to the gauge change $\Psi_n \rightarrow e^{2\pi i n/N} \Psi_n$.

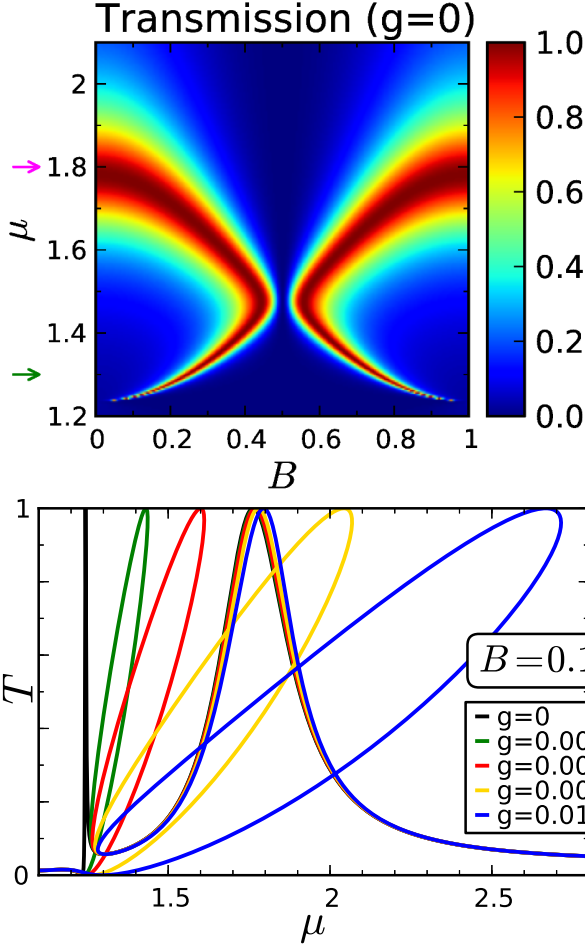


Figure 5.42: The left panel shows the transmission of \mathcal{B}_6 (Sec. 5.9.1) as function of μ and B for vanishing interacting strength g . The green (magenta) arrow marks the energy $\mu = 1.3$ ($\mu = 1.8$) used in Fig. 5.43. The lower two panels show the transmission as function of μ for a fixed value of B (g) for various values of g (B).

5.9.1 \mathcal{B}_6 : A ring with vanishing potential

The first ring system studied here is a ring with flat potential $V=0$ of following dimensions:

parameter	value	description
L_0	$1.8 \pi k_0^{-1}$	circumference of the ring
N	400	number of grid points forming the ring
Δx	L_0/N	spacing between grid points
\tilde{V}_c	$-5E_0$	confinement potential

As shown in Fig. 5.42, we see for small B two resonances in our spectral range in the non-interacting case $g = 0$. The narrow resonance at $\mu = 1.23$ is just a standing wave whose wavelength matches the ring circumference ($\text{Re } \Psi_n \sim \sin 2\pi n/N$). For zero magnetic field this becomes a bound state due to symmetry. The width of this resonance depends on the magnetic field. The broad resonance at $\mu = 1.77$ is a mixture of a ring-bound state and a state trapped at the confinement potential ($\text{Re } \Psi_n \sim |\sin 2\pi n/N|$ except for gridpoints near the leads).

If we regard the transmission as a function of μ the narrow resonance is transformed into a loop structure for finite value of the interaction g (see Fig. 5.42) similar to the scenario presented in Sec. 5.5. The only complication present here is that the width of the resonance (and hence the size of the loop) depends on the magnetic field. The broad resonance is hardly affected by the interaction g . The seemingly complicated behaviour of the transmission as function of B for fixed μ and g can be understood in terms of resonances whose widths vary with the magnetic

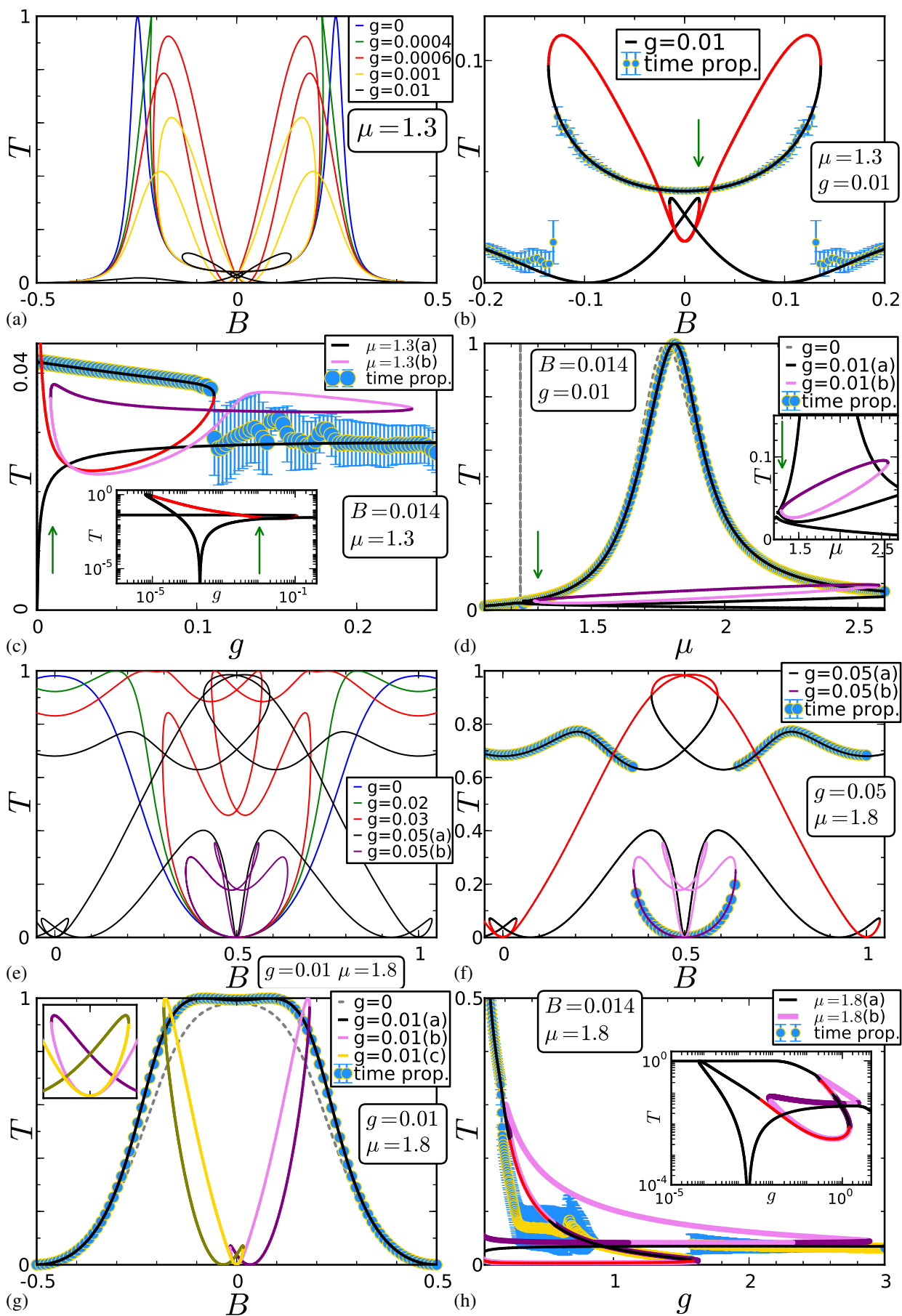


Figure 5.43: The figures on the previous page show the transmission properties of \mathcal{B}_6 (Sec. 5.9.1). (a)-(c) use $\mu = 1.3$ while (e)-(h) use $\mu = 1.8$. In (b)-(d) we study the parameter set $\mu=1.3, B=0.014, g=0.01$. In each plot two variables are fixed and one is free. The green arrow marks the value of the free variable in the other plots. The inlets show magnifications. Time propagation simulations (as done in Sec. 5.4.1) show which branches can be populated. The existence of another branch might slow the convergence of the time propagation to the stationary solution. Dynamical stability is color-encoded. (a) shows how the transmission as function of B undergoes a bifurcation for increasing values of the interaction strength g . (e) shows how complicated (loops, disconnected components) the transmission as function of B might become for non-vanishing interaction strengths. (f) shows that both disconnected branches can be populated by time-dependent simulations (as done in Sec. 5.4.1). In (g)-(h) we study the parameter set $\mu=1.8, B=0.014, g=0.01$. As function of B for fixed g only the trivial branch is populated. But we see that as function of g the time dependent population is complicated by the fact that there are many branches which might be all dynamically unstable.

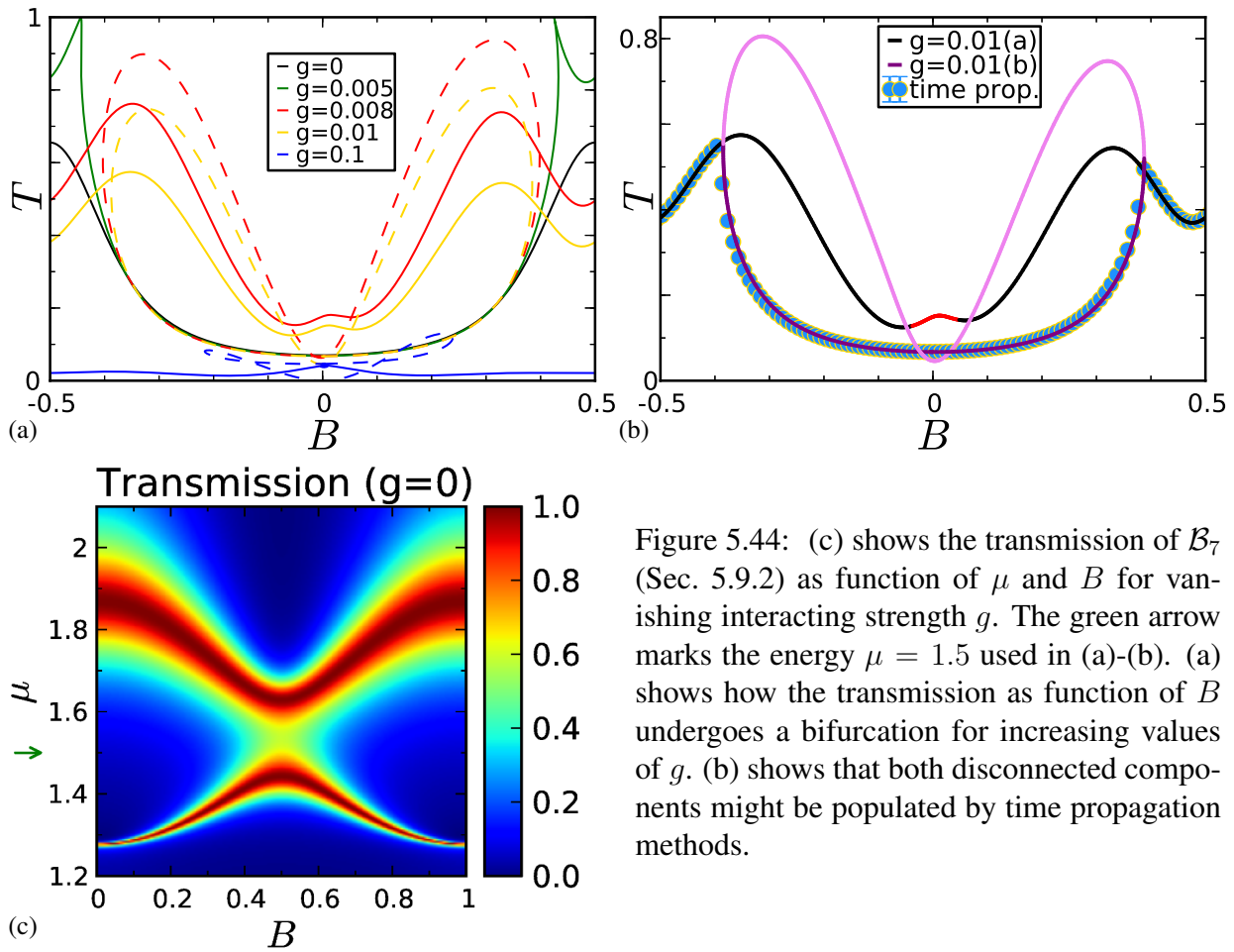


Figure 5.44: (c) shows the transmission of \mathcal{B}_7 (Sec. 5.9.2) as function of μ and B for vanishing interacting strength g . The green arrow marks the energy $\mu = 1.5$ used in (a)-(b). (a) shows how the transmission as function of B undergoes a bifurcation for increasing values of g . (b) shows that both disconnected components might be populated by time propagation methods.

field strength. Then one can use the perturbation theory for the energy developed in Sec. 5.6.2 to calculate the transmission as function of μ and intersect the result with the plane $[\mu, g = \text{fixed}, B = \text{variable}]$.

As function of μ, B and g the non-linear scattering states form a complicated three-dimensional manifold as shown in Fig. 5.43. A restriction to a one-dimensional manifold by fixating two of the tree parameters might produce two or more unconnected components. But components which are unconnected in one parameter might be connected in another parameter.

The whole discussion presented here (except for the symmetry considerations) for \mathcal{B}_6 is also valid for \mathcal{B}_7 and \mathcal{B}_8 .

5.9.2 \mathcal{B}_7 : A ring with a weak disorder potential

We now use a ring of the same dimensions as in Sec. 5.9.1 but now with a δ -correlated disorder potential $\langle V_n \rangle = 0$, $\langle V_n V_m \rangle = \tilde{V}^2 \delta_{nm}$; the V_n themselves are Gaussian-distributed. We use $\tilde{V} = 0.1 E_0$ for the disorder strength. The disorder potential breaks the perfect symmetry of \mathcal{B}_6 , but otherwise the results are comparable (see Fig. 5.44). For non-vanishing interaction strength g the Onsager relations (see also Fig. 5.37 and App. B) are violated.

5.9.3 \mathcal{B}_8 : A ring with a strong disorder potential

We now investigate the ring \mathcal{B}_7 (Sec. 5.9.2) with a stronger disorder strength $\tilde{V} = 1 E_0$. For $g \neq 0$ the Onsager relations are more strongly violated than in \mathcal{B}_7 . Various disconnected components and branches are visible. As function of g the transmission might have many branches as shown in Fig. 5.45c. For large values of g all branches are dynamically unstable.

5.10 Summary

In this chapter we have seen that the stationary scattering states of the non-linear wave equation (5.2) show a wide variety of phenomena such as multistability (more than one solution for a given set of parameters such as μ, B, g), hysteresis behavior (in time dependent simulation the currently occupied state depends on the history of the simulation) and dynamical instabilities (stationary states may not be stable under time evolution). All this phenomena are typical for non-linear wave equations.

Similar findings have been numerically observed for Bose-Einstein condensates (on the mean field level) in one dimensional systems [38, 159–161]. Related phenomena are also known in non-linear optics [27, 174, 175] and interacting electron systems [13, 171].

The stationary scattering states of the non-linear wave equation show a complicated behaviour as function of a control parameter such as the energy μ , gauge field B or interaction strength g . In order to calculate this function, a curve tracking algorithm has to be applied. Afterwards the dynamical stability of the such found solutions has to be investigated.

The results obtained by calculating stationary scattering states have to be complemented by time dependent simulations which provide a physical interpretation of stationary scattering states in the interacting case $g \neq 0$. The stationary method supplemented by a dynamical stability analysis provides similar information as time dependent simulations.

For almost closed systems, a perturbation theory in the energy allows us to understand the results well and describes most numerical findings. This theory is applicable as long as the resonances are well separated. For wide open systems with overlapping resonances this perturbation theory fails.

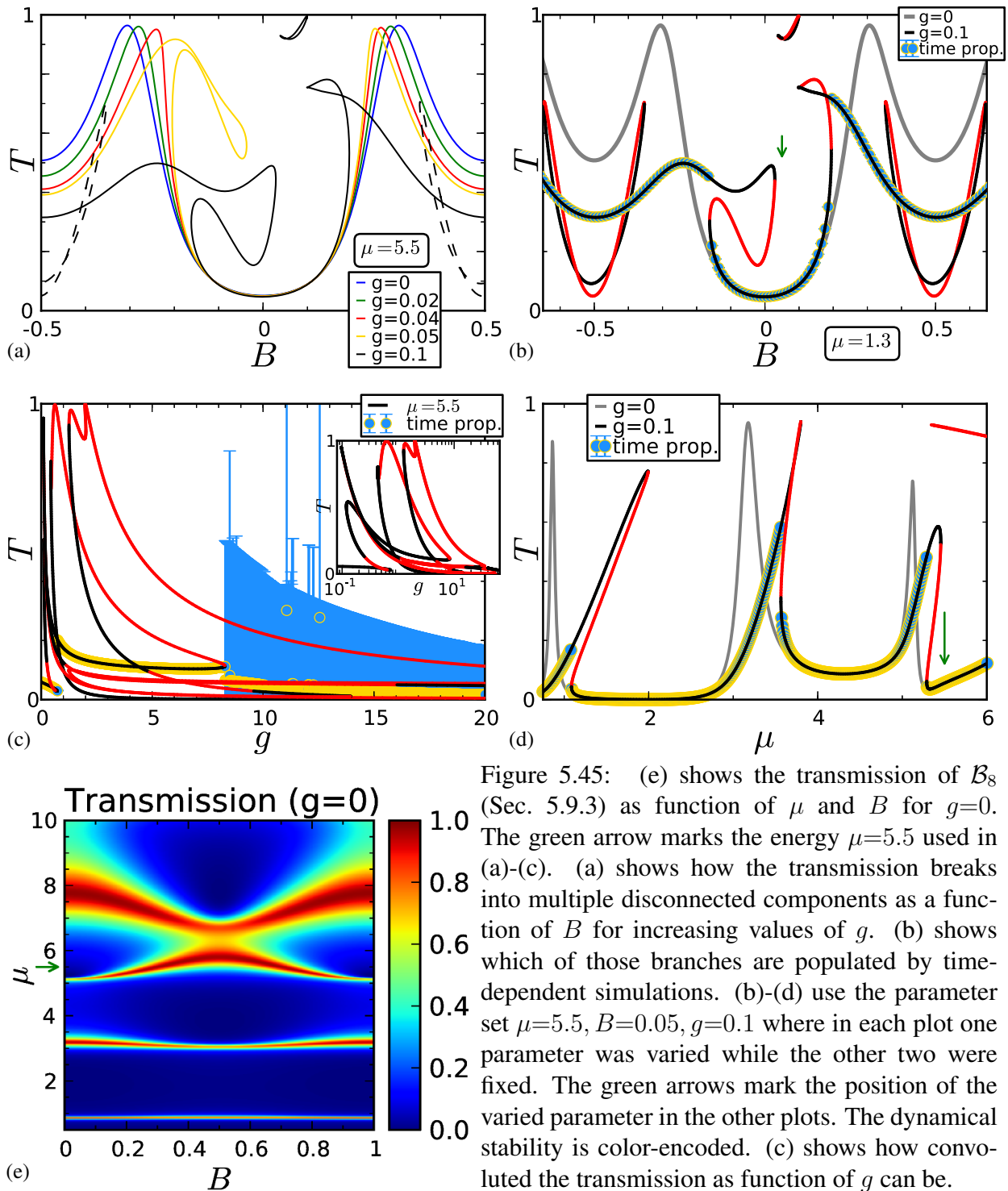


Figure 5.45: (e) shows the transmission of \mathcal{B}_8 (Sec. 5.9.3) as function of μ and B for $g=0$. The green arrow marks the energy $\mu=5.5$ used in (a)-(c). (a) shows how the transmission breaks into multiple disconnected components as a function of B for increasing values of g . (b) shows which of those branches are populated by time-dependent simulations. (b)-(d) use the parameter set $\mu=5.5$, $B=0.05$, $g=0.1$ where in each plot one parameter was varied while the other two were fixed. The green arrows mark the position of the varied parameter in the other plots. The dynamical stability is color-encoded. (c) shows how convoluted the transmission as function of g can be.

Chapter 6

Scattering states in chaotic billiards

In the previous chapters we have studied the transport properties of billiard systems for specific potentials and specific values of the control parameters (like the energy μ). This chapter focuses on universal transport properties which do not depend on the explicit details of a given system. The observables will be quantities averaged over many different parameter configurations. The value of these observables will only depend on a very few key parameters (like area or leadwidth) of the billiard and not on the detailed potential shape as long as the classical dynamics inside the billiard is chaotic. For this reason one says that these observables show an *universal* behavior.

By averaging we discard most of the information contained in the full solution of the (non-linear) wave equation (5.2). Almost all wave interference effects are cancelled out. But there are some robust interference effects which survive the averaging. One of these effects is called the *weak localization*. In the non-interacting case $g = 0$ this is the enhancement of the reflection as compared to the naive guess that the particles are scattered in all outgoing channels (of both leads) equally. This enhanced reflection is due to constructive interference of a scattering path and its time reversed counterpath. In presence of a large magnetic field this time reversal symmetry is broken and consequently no enhancement is detectable, i.e. the results are described by the naive guess in this case.

The focus of this chapter is how the weak localization effect is modified by a finite interaction between the particles. As a byproduct we can also study the distribution of intensities inside the billiard. Results of numerical simulations performed by me are compared to an analytical prediction based on the semiclassical Green function (this is due to my coworkers, see [96, 97]¹). Several different billiard systems are investigated. These are all ballistic systems. The related weak localization effect in diffusive systems will be briefly discussed, too.

For our studies we use systems of billiard type (Sec. 3.8). This means we use a flat potential $V = 0$ everywhere² while imposing hard wall boundary conditions to describe the shape of the cavity. The classical dynamics inside the cavity is assumed to be chaotic. Throughout the cavity the magnetic field B and the interaction strength g are assumed to be constant while they are switched off inside the leads. In order to study transport properties two leads are attached to the cavity. Only stationary transport will be investigated.

¹ The g used in [96] is a factor of two larger than the g used here. The convention for B_w and B_0 is also different.

² also inside the leads; no kind of barrier is used.

6.1 Weak localization

The weak localization effect is semiclassically analyzed first in the non-interacting case $g = 0$ and second in the interacting case $g \neq 0$. Afterwards the analytical prediction is compared to the numerical results.

6.1.1 Weak localization in the linear regime

The aim of this section is to *analytically* (in contrast to *numerically*) study the ballistic transport of non-interacting matter waves (which means transport in the linear regime $g = 0$) through chaotic cavities. The key ingredient to facilitate this analysis is to assume that the cavities are large with respect to the typical wavelength of the incident matter wave. This is equivalent to taking the formal limit $\hbar \rightarrow 0$ and in this limit the wave scattering of quantum systems can be approximated by classical dynamics. The same principle is used in the transition from electromagnetic wave scattering to ray optics.

In this section I only present a short overview over the semiclassical theory of the weak localization effect. A more thorough presentation is available in our paper [96] whereas a gentler introduction is available in [15, 110].

The semiclassical Green function

In order to get a quantitative description one starts with the usual Hamilton operator

$$H = \frac{1}{2m} [-i\hbar \nabla - q\mathbf{A}(\mathbf{r})]^2 + V(\mathbf{r})$$

and represents the propagator $e^{-itH/\hbar}$ as Feynman's path integral. Then one evaluates the formal limit $\hbar \rightarrow 0$ using the stationary phase method. This transforms the sum over all paths in a sum over all classically allowed paths. The result is the semiclassical Van Vleck propagator whose Fourier transform is then taken (again using the stationary phase method). This gives the semiclassical Green function [30, 91, 92, 176, 195]

$$G_{\text{sc}}(\mathbf{r}, \mathbf{r}') = \sum_{\gamma(\mathbf{r}, \mathbf{r}')} A_{\gamma} \exp \left[\frac{i}{\hbar} S_{\gamma} - \frac{i}{\hbar} \phi_{\gamma} - i \frac{\pi}{2} u_{\gamma} \right] \quad (6.1)$$

which under our assumptions (formal limit $\hbar \rightarrow 0$) is a good approximation to the exact Green function $G(\mathbf{r}, \mathbf{r}')$ in the position basis:

$$G_{\text{sc}}(\mathbf{r}, \mathbf{r}') \cong G(\mathbf{r}, \mathbf{r}') = \langle \mathbf{r} | (\mu - H)^{-1} | \mathbf{r}' \rangle.$$

The meaning of the different terms in the semiclassical Green function Eq. (6.1) is now explained.

- $\gamma(\mathbf{r}, \mathbf{r}')$ is a classical path (of a point particle) moving from \mathbf{r}' to \mathbf{r} subject to the classical Hamiltonian $H(\mathbf{p}, \mathbf{q}) = \frac{\mathbf{p}^2}{2m} + V(\mathbf{q})$ and possessing the energy μ . We use the convention $\mathbf{r} \equiv \mathbf{q}$. The sum in Eq. (6.1) is taken over all classical allowed paths.

The magnetic field is assumed to be so weak that it hardly affects the classical path, i.e. the classical path approximatively follows straight lines in regions where the potential $V(\mathbf{q})$ vanishes. Instead, the effect of magnetic field is perturbatively incorporated into the theory through the phase ϕ_{γ} .

- S_γ is the classical action³ taken along the path $\gamma(\mathbf{r}, \mathbf{r}')$:

$$S_\gamma = \int_0^{t_\gamma} \mathbf{p}_\gamma(t) \cdot \dot{\mathbf{q}}_\gamma(t) dt .$$

For a vanishing potential $V = 0$ this can be expressed using the path length L_γ as

$$S_\gamma = \hbar k L_\gamma$$

where k is determined by $\mu = \frac{\hbar^2 k^2}{2m}$.

- $\phi_\gamma = -\varphi_\gamma - \tilde{\varphi}_\gamma$ is a phase arising from the magnetic field. It is calculated as an integral along the classical path $\gamma(\mathbf{r}, \mathbf{r}')$:

$$\varphi_\gamma = \frac{q}{m} \int_0^{t_\gamma} \mathbf{p}_\gamma(t) \cdot \mathbf{A}(\mathbf{q}_\gamma(t)) dt \quad \tilde{\varphi}_\gamma = -\frac{q^2}{2m} \int_0^{t_\gamma} \mathbf{A}^2(\mathbf{q}_\gamma(t)) dt .$$

For a constant magnetic field B with vector potential $\mathbf{A}(\mathbf{r}) = \frac{B}{2} \mathbf{e}_z \times \mathbf{r}$ the phase φ_γ is proportional to the directed area \mathcal{A}_γ the path encloses:

$$\varphi_\gamma = qB\mathcal{A}_\gamma \quad \text{with} \quad \mathcal{A}_\gamma = \frac{1}{2} \mathbf{e}_z \cdot \int_0^{t_\gamma} \mathbf{q}(t) \times \dot{\mathbf{q}}(t) dt .$$

The phase $\tilde{\varphi}_\gamma$ usually drops out of the final formulas for transport properties.

- A_γ is the stability amplitude

$$A_\gamma = \frac{2\pi}{(2\pi i\hbar)^{3/2}} \sqrt{\left| \det \frac{\partial(\mathbf{p}', \mathbf{r}', T)}{\partial(\mathbf{r}, \mathbf{r}', E)} \right|} .$$

- u_γ is the Maslow index. This is an integer which counts the number of conjugate points along the path $\gamma(\mathbf{r}, \mathbf{r}')$ (i.e. points where $\det \frac{\partial(\mathbf{p}', \mathbf{r}', T)}{\partial(\mathbf{r}, \mathbf{r}', E)}$ is singular) and twice the number of reflections at hard wall boundaries.

The stationary scattering state Ψ can now be calculated as (see also Sec. 3.2 and App. B)

$$\Psi(\mathbf{r}) = \int G_{\text{sc}}(\mathbf{r}, \mathbf{r}') S(\mathbf{r}') d\mathbf{r}' .$$

We now assume that the source $S(\mathbf{r})$ injects the matter wave in lead mode χ_n and the reflected (or transmitted) part of the wave function is measured in lead modes χ_m . This amounts to calculate the scattering matrix (from now on called \mathcal{S} -matrix)⁴ [50] as in the Fisher-Lee relations Eq. (3.48)

$$\mathcal{S}_{nm} = i\hbar\sqrt{v_m} \int \Psi(\mathbf{r})\chi_m(\mathbf{r})d\mathbf{r} = i\hbar\sqrt{v_n v_m} \int \int G_{\text{sc}}(\mathbf{r}, \mathbf{r}') S_0\chi_n(\mathbf{r}')\chi_m(\mathbf{r}) d\mathbf{r}' d\mathbf{r} . \quad (6.2)$$

³Be aware that the symbol “S” is used for both the source term and the classical action, furthermore \mathcal{S} is the scattering matrix. Note also the difference between symbols for the charge q and for the position \mathbf{q} . The letter “A” is used as \mathbf{A} for the vector potential, as A for the stability amplitude and as \mathcal{A} for the directed area.

⁴ We implicitly remove the direct contribution of the incoming channel χ_n to the outgoing channel χ_n “by hand”, i.e we later remove zero length paths in the semiclassical scattering amplitude. Therefore the term $-\delta_{nm}$ in Eq. (3.48) is neglected here. The term $v_n v_m$ is used to normalize the currents in the lead modes.

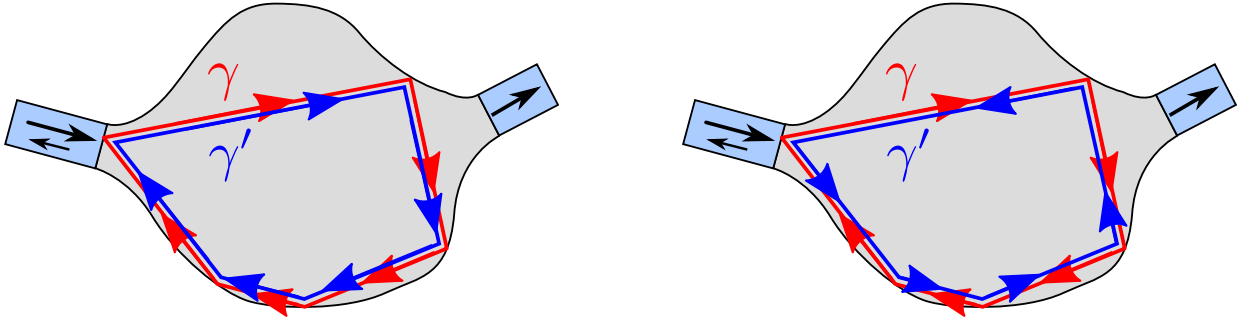


Figure 6.1: This figure illustrates the diagonal approximation to the squared moduli of the \mathcal{S} -matrix Eq. (6.4). In the left picture a path γ is paired with itself (i.e. $\gamma' = \gamma$). In the right picture a path γ is paired with its time reversed path (i.e. γ' is the time reversal of γ).

As the lead modes χ_m and χ_n are essential sinus functions (for constant potential V) the integrals over the position variables can be treated using the stationary phase method in the formal limit $\hbar \rightarrow 0$. This results in a boundary condition to all allowed classical paths: The particles can only enter or exit through a lead if the angle between the trajectory and the lead assumes certain discrete values.

We are now able to calculate the transmission (or reflection) as⁵:

$$|\mathcal{S}_{nm}|^2 \sim \sum_{\gamma} \sum_{\gamma'} A_{\gamma} A_{\gamma'}^* e^{i(S_{\gamma} - S_{\gamma'})/\hbar - i(\phi_{\gamma} - \phi_{\gamma'})/\hbar - i\pi(u_{\gamma} - u_{\gamma'})/2}. \quad (6.3)$$

These are the squared moduli of the semiclassical \mathcal{S} -matrix^{6 7}.

Because of the classically chaotic dynamics the action S_{γ} varies wildly between different paths. Furthermore we are assuming the formal limit $\hbar \rightarrow 0$. The result is that the term $e^{i(S_{\gamma} - S_{\gamma'})/\hbar}$ oscillates wildly and the contributions from most pair of paths (γ, γ') will cancel out after an energy average. Only paths (γ, γ') whose action difference $S_{\gamma} - S_{\gamma'}$ is very small (of the order of magnitude of \hbar) are still relevant after the average.

Therefore energy averaging reduces the double sum in the squared moduli of the semiclassical \mathcal{S} -matrix \mathcal{S}_{nm} Eq. (6.3) into a single sum of correlated pairs of paths. γ given, γ' can only be one of the following paths:

- γ itself (diagonal contribution, insensitive to a magnetic field)
- the time reversal of γ (diagonal contribution, only for reflection, sensitive to a magnetic field)
- loop contributions (off-diagonal contributions)

Diagonal contributions to the weak localization

In the diagonal approximation we either pair a path γ with itself or with its time reversed counter path. The last pairing is only relevant if the outgoing channel is the same as the incoming channel, i.e. for back-reflection into the same channel which was used to insert the matter wave into the cavity. This part of the reflection will be called “self-reflection” later on.

⁵ See the paragraph at the end of this section for attempts to directly evaluate this sum.

⁶ Our scattering matrix \mathcal{S} will always be normalized with respect to the incoming current, i.e. a total transmission from n to m would be $|\mathcal{S}_{nm}|^2 = 1$.

⁷ For the sake of simplicity we neglected a prefactor here related to the normalization of the incoming current.

Applying an energy average (denoted by $\langle \dots \rangle$) we arrive at

$$\begin{aligned} \langle |\mathcal{S}_{nm}|^2 \rangle_{\text{diag}} &\sim \left\langle \sum_{\gamma} |A_{\gamma}|^2 \right\rangle && \text{for } n \neq m \\ \langle |\mathcal{S}_{nn}|^2 \rangle_{\text{diag}} &\sim \left\langle \sum_{\gamma} |A_{\gamma}|^2 \right\rangle + \left\langle \sum_{\gamma} |A_{\gamma}|^2 e^{2i\varphi_{\gamma}/\hbar} \right\rangle. \end{aligned} \quad (6.4)$$

The term $\langle \sum_{\gamma} |A_{\gamma}|^2 \rangle$ originates from pairing a path γ with itself and is insensitive to a magnetic field because both paths enclose the same directed area as they are identical. The term $\langle \sum_{\gamma} |A_{\gamma}|^2 e^{2i\varphi_{\gamma}/\hbar} \rangle$ pairs a path γ with its time reversed counterpart and is sensitive to a magnetic field as the directed areas of both path have opposite sign. See Fig. 6.1 for an illustration.

Using generalized Hannay-Ozorio de Almeida sum rules [94] (which are valid for systems supporting classical chaotic dynamics), one can now evaluate the diagonal part of the reflection as:

$$\begin{aligned} \langle |\mathcal{S}_{nm}|^2 \rangle_{\text{diag}} &= \frac{1}{N_1 + N_2} && \text{for } n \neq m \\ \langle |\mathcal{S}_{nn}|^2 \rangle_{\text{diag}} &= \frac{1}{N_1 + N_2} + \frac{1}{N_1 + N_2} \left[1 + (B/B_w)^2 \right]^{-1}. \end{aligned} \quad (6.5)$$

Here B_w is a measure for the directed area distribution of the classical paths which is described in more details in Sec. 6.1.3 (see Eq. (6.16)). N_1, N_2 are the number of open channels in the left or right lead respectively (assuming a two lead setup as depicted in Fig. 5.35 or Fig. 6.1). This is the result on the level of [15, 110] whose reasoning is briefly reproduced in Sec. 6.1.3 (see Eq. (6.15)).

For a vanishing magnetic field $B = 0$ we see that the self-reflection (the reflection into the incident channel) $\langle |\mathcal{S}_{nn}|^2 \rangle_{\text{diag}}$ is twice as large as the reflection into the other channels. This is due to constructive interference between a path and its time reversed counterpart and is called the weak localization effect. For large magnetic field this time reversal symmetry is destroyed and the enhancement vanishes consequently.

Loop contributions to the weak localization

The first off-diagonal contribution to squared moduli of the semiclassical \mathcal{S} -matrix Eq. (6.3) comes from paths γ which have one self intersection at a small angle ϵ (see Fig. 6.2 and Fig. 6.3). Such a path γ forms therefore a loop. In the case of classical chaotic dynamics one can show that such a path γ has a companion path γ' which avoids this crossing but otherwise follows the original path closely except that the loop is traversed in the opposite direction. Obviously such path pairs (γ, γ') (called “Richter-Sieber pairs” [177, 191]) have similar classical actions ($S_{\gamma}, S_{\gamma'}$) (as they have nearly equal length) and are sensitive to a magnetic field (as the directed area they enclose differs by twice the loop area).

One can now evaluate the energy average for the loop contributions in a similar way as for diagonal contributions (for the details see [96]):

$$\langle |\mathcal{S}_{nm}|^2 \rangle_{\text{loop}} = -\frac{1}{(N_1 + N_2)^2} \left[1 + (B/B_w)^2 \right]^{-1}.$$

Adding the diagonal part of the reflection and the loop contribution we arrive at following

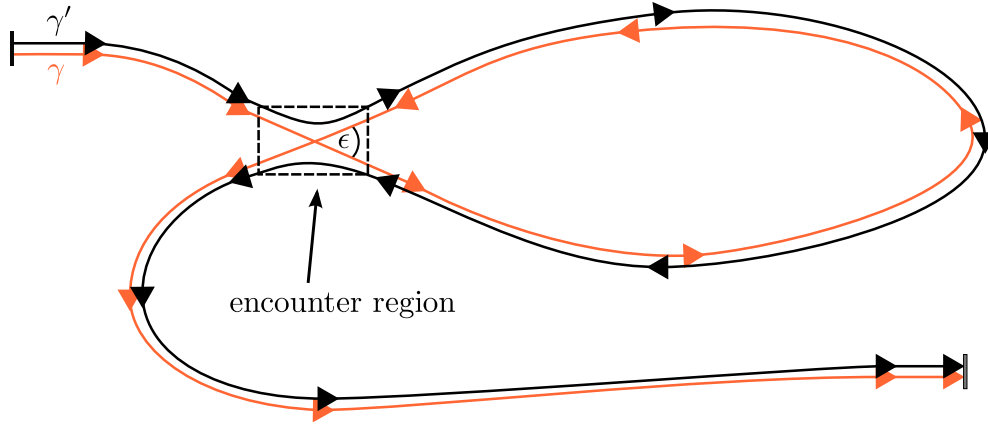


Figure 6.2: This figure schematically depicts a Richter-Sieber pair. The path γ has a self intersection at a small angle ϵ . For systems with classical chaotic dynamics there exists a companion path γ' which follows γ closely but does not intersect itself and which consequently traverses the loop in opposite direction. Fig. 6.3 shows a real-life example.

formula for the squared moduli of the semiclassical \mathcal{S} -matrix⁸:

$$\begin{aligned} \langle |\mathcal{S}_{nm}|^2 \rangle_{\text{full}} &= \langle |\mathcal{S}_{nm}|^2 \rangle_{\text{diag}} + \langle |\mathcal{S}_{nm}|^2 \rangle_{\text{loop}} \\ &= \frac{1}{N_1 + N_2} + \left[\frac{\delta_{n,m}}{N_1 + N_2} - \frac{1}{(N_1 + N_2)^2} \right] \left[1 + (B/B_w)^2 \right]^{-1}. \end{aligned}$$

In our two lead setup (as depicted in Fig. 5.35 or Fig. 6.1) we now assume that the lead modes (i.e. the channels) in the left lead are $n = 1 \dots N_1$ and that the lead modes in the right lead are $n = N_1 + 1 \dots N_1 + N_2$.

We now consecutively inject particles into all different channels of the left lead. The total reflection R is defined as the fraction of particles reflected into the left lead whereby we use an average over all incoming channels:

$$\begin{aligned} R &= \frac{1}{N_1} \sum_{n=1}^{N_1} \sum_{m=1}^{N_1} \langle |\mathcal{S}_{nm}|^2 \rangle_{\text{full}} = \frac{N_1}{N_1 + N_2} + \left[\frac{1}{N_1 + N_2} - \frac{N_1}{(N_1 + N_2)^2} \right] \left[1 + (B/B_w)^2 \right]^{-1} \\ &= \frac{N_1}{N_1 + N_2} + \frac{N_2}{(N_1 + N_2)^2} \left[1 + (B/B_w)^2 \right]^{-1}. \end{aligned}$$

Similarly the total transmission is defined as the average of the fraction of particles transmitted to the right lead:

$$T = \frac{1}{N_1} \sum_{n=1}^{N_1} \sum_{m=N_1+1}^{N_1+N_2} \langle |\mathcal{S}_{nm}|^2 \rangle_{\text{full}} = \frac{N_2}{N_1 + N_2} - \frac{N_2}{(N_1 + N_2)^2} \left[1 + (B/B_w)^2 \right]^{-1}.$$

Current conservation, i.e. unitarity of the scattering matrix (see also Sec. B), is fulfilled:

$$R + T = 1.$$

⁸Here $\delta_{n,m}$ is the Kronecker delta, i.e. $\delta_{n,n} = 1$ and $\delta_{n,m} = 0$ for $n \neq m$.

It is worth mentioning that the current conservation is only fulfilled if one takes loop contributions into account. The diagonal terms alone are not enough to ensure current conservation. Furthermore the semiclassical predictions for the reflection R and transmission T including the loop corrections match the random matrix theory (RMT) prediction⁹ [146] for zero ($B = 0$, orthogonal ensemble) or large ($B = \infty$, unitary ensemble) magnetic field.

The average of the reflection into the same channel which was used to inject particles into the cavity is still another quantity of interest:

$$R_s = \frac{1}{N_1} \sum_{n=1}^{N_1} \langle |\mathcal{S}_{nn}|^2 \rangle_{\text{full}} = \frac{1}{N_1 + N_2} + \left[\frac{1}{N_1 + N_2} - \frac{1}{(N_1 + N_2)^2} \right] \left[1 + (B/B_w)^2 \right]^{-1}. \quad (6.6)$$

Henceforth we will call R_s “self-reflection”. For this quantity the signal-to-noise ratio (i.e. weak-localization to background) is much bigger than in R or T . Also the signal-to-noise ratio does not degenerate for large lead openings (i.e. large N_1, N_2). If we assume $N_1 = N_2$ (this is always the case in the numerical examples presented in this work) the absolute magnitude of the weak localization effect is nearly twice as big in R_s as in R or T (see Eq. (6.7)). Therefore it is no surprise that the numerical values of R_s fit much better to their semiclassical predictions than the numerical values of R and T as we will see later. The loop contributions to R_s are one order of magnitude smaller than the diagonal contributions. Albeit our expression contains these contribution, one could also safely neglect them.

Summary

The weak localization in the linear case $g = 0$ effect can be summarized in following three formulas for R, T and R_s :

$$\begin{aligned} R &= \frac{N_1}{N_1 + N_2} + \frac{N_2}{(N_1 + N_2)^2} \left[1 + (B/B_w)^2 \right]^{-1} \\ T &= \frac{N_2}{N_1 + N_2} - \frac{N_2}{(N_1 + N_2)^2} \left[1 + (B/B_w)^2 \right]^{-1} \\ R_s &= \frac{1}{N_1 + N_2} + \frac{N_1 + N_2 - 1}{(N_1 + N_2)^2} \left[1 + (B/B_w)^2 \right]^{-1}. \end{aligned}$$

This is the result presented in our paper [96] for the transmission and reflection in the non-interacting case.

For $N = N_1 = N_2$, as it is always the case in the numerical examples studied in this work, we have (see Eq. (6.11) for the nonlinear case):

$$\begin{aligned} R &= \frac{1}{2} + \frac{1}{4N} \left[1 + (B/B_w)^2 \right]^{-1} \\ T &= \frac{1}{2} - \frac{1}{4N} \left[1 + (B/B_w)^2 \right]^{-1} \\ R_s &= \frac{1}{2N} + \frac{2N - 1}{4N^2} \left[1 + (B/B_w)^2 \right]^{-1}. \end{aligned} \quad (6.7)$$

⁹ The one loop semiclassical theory reproduces the RMT predictions only approximatively for small N ; for large N both theories give asymptotically the same results. The work [153] goes beyond the one loop semiclassical approximation and takes higher order contributions into account by considering paths with more than one encounter. Then the RMT prediction is also matched exactly for small N .

6.1.2 Weak localization in the non-linear regime

In the following I will only present a rough scratch of the semiclassical evaluation of the weak localization effect in the non-linear case $g \neq 0$. For a more detailed discussion see [96]. For the semiclassical analysis we assume that $g(\mathbf{r}) = g$ is constant throughout the cavity.

We start with the defining equation for non-linear stationary scattering states Eq. (5.2)

$$\left[\mu - H - g \frac{\hbar^2}{m} |\Psi(\mathbf{r})|^2 \right] \Psi(\mathbf{r}) = S(\mathbf{r})$$

and transform it into a Dyson equation

$$\Psi(\mathbf{r}) = [\mu - H]^{-1} S(\mathbf{r}) + g \frac{\hbar^2}{m} [\mu - H]^{-1} |\Psi(\mathbf{r})|^2 \Psi(\mathbf{r})$$

which is a shorthand notation for the integral equation

$$\Psi(\mathbf{r}) = \int G(\mathbf{r}, \mathbf{r}') S(\mathbf{r}') d\mathbf{r}' + g \frac{\hbar^2}{m} \int G(\mathbf{r}, \mathbf{r}') |\Psi(\mathbf{r}')|^2 \Psi(\mathbf{r}') d\mathbf{r}'$$

using the Green function in the position basis $G(\mathbf{r}, \mathbf{r}') = \langle \mathbf{r} | (\mu - H)^{-1} | \mathbf{r}' \rangle$.


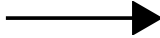


This Dyson equation can now be iterated, i.e. the left side can be plugged into the right side ad infinitum. This gives a power series for $\Psi(\mathbf{r})$ in terms of g and g^* .

$$\Psi(\mathbf{r}) = \sum_{m=0}^{\infty} \sum_{n=0}^{\infty} g^m g^{*n} \Psi_{m,n}(\mathbf{r})$$

with

$$\begin{aligned} \Psi_{0,0}(\mathbf{r}) &= [\mu - H]^{-1} S(\mathbf{r}) \\ \Psi_{1,0}(\mathbf{r}) &= \frac{\hbar^2}{m} [\mu - H]^{-1} |\Psi_{0,0}(\mathbf{r})|^2 \Psi_{0,0}(\mathbf{r}) \\ \Psi_{0,1}(\mathbf{r}) &= \Psi_{0,2}(\mathbf{r}) = 0 \\ &\dots \end{aligned}$$

This power series is best studied through a diagrammatic representation. To this end we will use the following symbols:

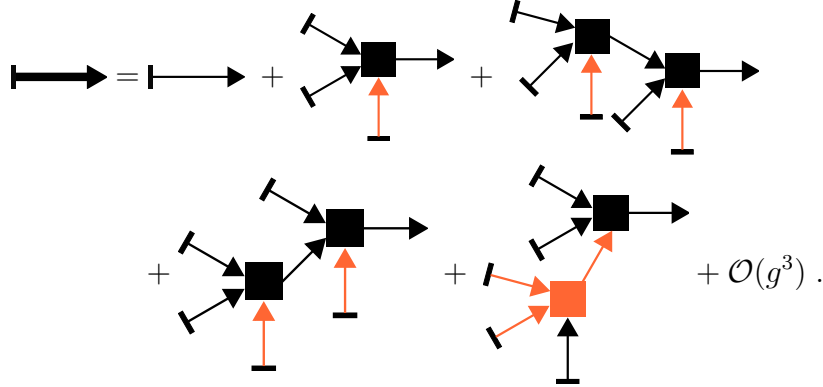
	the source $S(\mathbf{r})$
	the linear Green Function $G = (\mu - H)^{-1}$
	the solution of the non-linear scattering problem $\Psi(\mathbf{r})$
	non-linear scattering event, i.e. a factor of g

whereby an orange color denotes complex conjugation.

This allows us to express the Dyson equation in diagrammatic form:

$$\text{thick arrow} = \text{thin arrow} + \text{thin arrow} \rightarrow \text{black square} \left(\begin{array}{l} \text{thin arrow from top-left} \\ \text{orange arrow from bottom} \end{array} \right) \rightarrow \text{thin arrow}$$

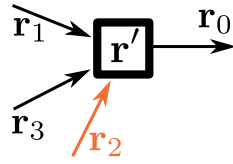
Iterating of the Dyson equation leads to following diagrammatic expression for the power series of the nonlinear scattering state $\Psi(\mathbf{r})$:



Semiclassical evaluation

Up to now we have not used any semiclassical approximations, i.e. the power series expansion is valid exactly. But the individual terms of the power series are susceptible to semiclassical tools.

The basic building block in the diagrammatic power series expansion



represents following integral

$$\int G(\mathbf{r}_0, \mathbf{r}') G(\mathbf{r}', \mathbf{r}_1) G^*(\mathbf{r}', \mathbf{r}_2) G(\mathbf{r}', \mathbf{r}_3) d\mathbf{r}' .$$

Here \mathbf{r}' is the position of the nonlinear interaction, \mathbf{r}_0 is the final position and $\mathbf{r}_1, \mathbf{r}_2, \mathbf{r}_3$ are the initial positions. $G(\mathbf{r}, \mathbf{r}') = \langle \mathbf{r} | (\mu - H)^{-1} | \mathbf{r}' \rangle$ is the ordinary Green function in the position basis.

The next step is to replace $G(\mathbf{r}, \mathbf{r}')$ with the semiclassical Green function $G_{\text{sc}}(\mathbf{r}, \mathbf{r}')$ Eq. (6.1):

$$\begin{aligned} & \int \sum_{\gamma_0, \gamma_1, \gamma_2, \gamma_3} A_{\gamma_0} A_{\gamma_1} A_{\gamma_2}^* A_{\gamma_3} e^{-i[\phi_{\gamma_0} + \phi_{\gamma_1} - \phi_{\gamma_2} + \phi_{\gamma_3}]/\hbar - i\pi[u_{\gamma_0} + u_{\gamma_1} - u_{\gamma_2} + u_{\gamma_3}]/2} \\ & \times \exp \left\{ \frac{i}{\hbar} [S_{\gamma_0}(\mathbf{r}_0, \mathbf{r}') + S_{\gamma_1}(\mathbf{r}', \mathbf{r}_1) - S_{\gamma_2}(\mathbf{r}', \mathbf{r}_2) + S_{\gamma_3}(\mathbf{r}', \mathbf{r}_3)] \right\} d\mathbf{r}' . \end{aligned}$$

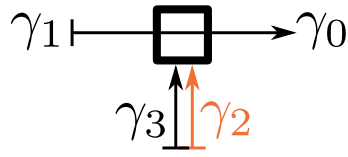
This integral is now evaluated using the stationary phase method

$$\frac{\partial}{\partial \mathbf{r}'} [S_{\gamma_0}(\mathbf{r}_0, \mathbf{r}') + S_{\gamma_1}(\mathbf{r}', \mathbf{r}_1) - S_{\gamma_2}(\mathbf{r}', \mathbf{r}_2) + S_{\gamma_3}(\mathbf{r}', \mathbf{r}_3)] = 0$$

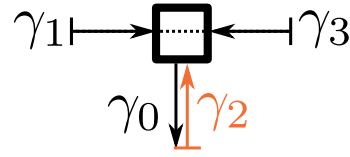
giving us the condition

$$\mathbf{p}_{\gamma_0} + \mathbf{p}_{\gamma_2} = \mathbf{p}_{\gamma_1} + \mathbf{p}_{\gamma_3}$$

for the momenta of the four paths at position \mathbf{r}' . This condition is only fulfilled for two kinds of diagrams:



ladder diagram



crossed diagram.

In the ladder type diagrams γ_0 is the continuation of γ_1 whereas γ_2 is parallel to γ_3 , i.e. $\mathbf{p}_{\gamma_0} = \mathbf{p}_{\gamma_1}$ and $\mathbf{p}_{\gamma_2} = \mathbf{p}_{\gamma_3}$. Obviously we can interchange γ_1 and γ_3 without changing the overall picture, therefore the ladder type diagrams come with a multiplicity of two.

In the crossed diagrams the time reversal of γ_1 is the continuation of γ_3 and the time reversal of γ_0 follows γ_2 , i.e. $-\mathbf{p}_{\gamma_1} = \mathbf{p}_{\gamma_3}$ and $-\mathbf{p}_{\gamma_0} = \mathbf{p}_{\gamma_2}$. In particular this means that the final vector \mathbf{r} has to be along the path γ_2 . Therefore crossed diagrams are only relevant for reflection.

All the ladder type diagrams are now combined into a ladder Green function G_l which is defined by the following Dyson equation:

$$\Rightarrow = \rightarrow + 2 \Rightarrow \text{[diagram of a square with two vertical arrows]} \rightarrow$$

The iteration of this Dyson equation

$$\begin{aligned} \Rightarrow &= \rightarrow + 2 \text{[diagram of a square with two vertical arrows]} \rightarrow + 4 \text{[diagram of two squares in series with two vertical arrows]} \rightarrow \\ &+ 4 \text{[diagram of a square with two vertical arrows]} \rightarrow + 4 \text{[diagram of a square with two vertical arrows]} \rightarrow + \mathcal{O}(g^3) \end{aligned}$$

shows that G_l can be evaluated as [96]:

$$G_l = \sum_{\gamma} A_{\gamma} e^{i[S_{\gamma} - \phi_{\gamma} - \chi_{\gamma}]/\hbar - i\pi u_{\gamma}/2} \quad \text{with} \quad \chi_{\gamma} = 2g \frac{\hbar^2}{m} \int_0^{t_{\gamma}} |\Psi[\mathbf{q}_{\gamma}(t)]|_d^2 dt.$$

Therefore at the level of the ladder diagrams the influence of the nonlinear interaction can be expressed through a phase factor. This is an implicit evaluation as the phase factor depends on the full solution $\Psi(\mathbf{r})$ of the non-linear scattering equation. Its meaning is that the diagonal terms where a path is paired with itself are not affected by the interaction g as the phase factor cancels out, i.e. the magnetic field independent background of R, T and R_s does not depend on g :

$$\langle |\mathcal{S}_{nm}|^2 \rangle_{\text{diag}} = \frac{1}{N_1 + N_2} \quad \text{for } n \neq m$$

The diagonal terms in which a path is paired with its time reversed counterpath are contained in the crossed diagrams which describe the reflection $\langle |\mathcal{S}_{nn}|^2 \rangle_{\text{diag}}$ into the same channel which was used to inject the particles. This reflection can now be calculated using the crossed diagrams

and G_I :

$$\begin{aligned}
 \langle |\mathcal{S}_{nn}|^2 \rangle_{\text{diag}} = & \text{[Diagram: A horizontal line with a double-headed arrow, representing a reflection.] } = \text{[Diagram: A horizontal line with a double-headed arrow, representing a reflection.] } + \text{[Diagram: A horizontal line with a double-headed arrow, a vertical line with a double-headed arrow, and a square with a double-headed arrow.] } + \text{[Diagram: A horizontal line with a double-headed arrow, a vertical line with a double-headed arrow, and a square with a double-headed arrow.] } + \text{[Diagram: A horizontal line with a double-headed arrow, a vertical line with a double-headed arrow, and a square with a double-headed arrow.] } + \text{[Diagram: A horizontal line with a double-headed arrow, a vertical line with a double-headed arrow, and a square with a double-headed arrow.] } \\
 & + 2 \text{[Diagram: A horizontal line with a double-headed arrow, a vertical line with a double-headed arrow, and a square with a double-headed arrow.] } + 2 \text{[Diagram: A horizontal line with a double-headed arrow, a vertical line with a double-headed arrow, and a square with a double-headed arrow.] } + \mathcal{O}(g^3) .
 \end{aligned} \tag{6.8}$$

In order to evaluate this expression we introduce the crossed density C_g

$$\text{[Diagram: A horizontal line with a double-headed arrow, representing a reflection.] } = \text{[Diagram: A horizontal line with a double-headed arrow, representing a reflection.] } + 2 \text{[Diagram: A horizontal line with a double-headed arrow, a vertical line with a double-headed arrow, and a square with a double-headed arrow.] }$$

which allows us to write the reflection as

$$\text{[Diagram: A horizontal line with a double-headed arrow, representing a reflection.] } = \text{[Diagram: A horizontal line with a double-headed arrow, representing a reflection.] } + \text{[Diagram: A horizontal line with a double-headed arrow, a vertical line with a double-headed arrow, and a square with a double-headed arrow.] } + \text{[Diagram: A horizontal line with a double-headed arrow, a vertical line with a double-headed arrow, and a square with a double-headed arrow.] } + \text{[Diagram: A horizontal line with a double-headed arrow, a vertical line with a double-headed arrow, and a square with a double-headed arrow.] } .$$

The crossed density C_g can be evaluated using the stationary phase method and semi-classical sum rules as [96]

$$\langle C_g \rangle = \frac{\langle C_0 \rangle}{1 + i2g\tau_D \frac{\hbar}{m} \langle C_0 \rangle} .$$

This finally allows us to calculate the reflection $\langle |\mathcal{S}_{nn}|^2 \rangle_{\text{diag}}$ in the diagonal approximation for non-vanishing interaction:

$$\langle |\mathcal{S}_{nn}|^2 \rangle_{\text{diag}} = \frac{1}{N_1 + N_2} + \frac{(N_1 + N_2) [1 + (B/B_w)^2]}{(N_1 + N_2)^2 [1 + (B/B_w)^2]^2 + (2gj\tau_d)^2} . \tag{6.9}$$

Here τ_d is the classical dwell time described in more detail in Sec. 6.1.3 and j is the incoming current measured in particles per seconds.

Summary

Loop contributions for non-vanishing interaction can be handled in a similar way, but the details are formidable [96] and therefore omitted here. The final result including diagonal and loop terms

is given by

$$\begin{aligned}
R &= \frac{N_1}{N_1 + N_2} + \frac{N_2 [1 + (B/B_w)^2]}{(N_1 + N_2)^2 [1 + (B/B_w)^2]^2 + (2gj\tau_d)^2} \\
T &= \frac{N_2}{N_1 + N_2} - \frac{N_2 [1 + (B/B_w)^2]}{(N_1 + N_2)^2 [1 + (B/B_w)^2]^2 + (2gj\tau_d)^2} \\
R_s &= \frac{1}{N_1 + N_2} + \frac{(N_1 + N_2 - 1) [1 + (B/B_w)^2]}{(N_1 + N_2)^2 [1 + (B/B_w)^2]^2 + (2gj\tau_d)^2} .
\end{aligned} \tag{6.10}$$

Current conservation is also fulfilled for non-vanishing interaction:

$$R + T = 1 .$$

For the important case $N = N_1 = N_2$ (used exclusively in this work) the relevant expressions are

$$\begin{aligned}
R &= \frac{1}{2} + \frac{1}{4N} \frac{[1 + (B/B_w)^2]}{[1 + (B/B_w)^2]^2 + (gj\tau_d/N)^2} \\
T &= \frac{1}{2} - \frac{1}{4N} \frac{[1 + (B/B_w)^2]}{[1 + (B/B_w)^2]^2 + (gj\tau_d/N)^2} \\
R_s &= \frac{1}{2N} + \frac{2N - 1}{4N^2} \frac{[1 + (B/B_w)^2]}{[1 + (B/B_w)^2]^2 + (gj\tau_d/N)^2} .
\end{aligned} \tag{6.11}$$

For vanishing interaction $g = 0$ these expressions reduce to the results obtained using the linear semiclassical scattering theory, see Eq. (6.7).

6.1.3 Analysis of the classical dynamics

The classical dwell time τ_D and the parameter B_w are entirely determined by the classical dynamics of the billiard system. This section describes how to compute these quantities.

As we assume a flat potential $V = 0$ inside the cavity with hard wall boundary conditions the classical trajectories inside the billiard are straight paths between reflections at the boundaries. Therefore we can employ a ray-tracing algorithm to analyze the classical dynamics. Trajectories are started in the left lead at a fixed longitudinal coordinate x and at a varying transverse coordinate y chosen from an uniform random distribution. Furthermore the total momentum $p = \sqrt{p_x^2 + p_y^2}$ is fixed (determined by $\mu = p^2/(2m)$) while the transverse momenta p_y are chosen from an uniform random distribution. The simulation is continued until the trajectory leaves through one of the leads. See Fig. 6.3 for an illustration.

The billiard is chosen such that the classical dynamics is chaotic. Therefore a particle bounces more or less randomly inside the billiard. All memory of the initial conditions are soon lost after a few bounces because of the exponential spread due to classical chaos. After a short transient region it is therefore expected that the probability per unit time interval of the particle hitting the leads becomes constant. This results in an exponential distribution [113]

$$P(t_\gamma) = \tau_D^{-1} e^{-t_\gamma/\tau_D} \tag{6.12}$$

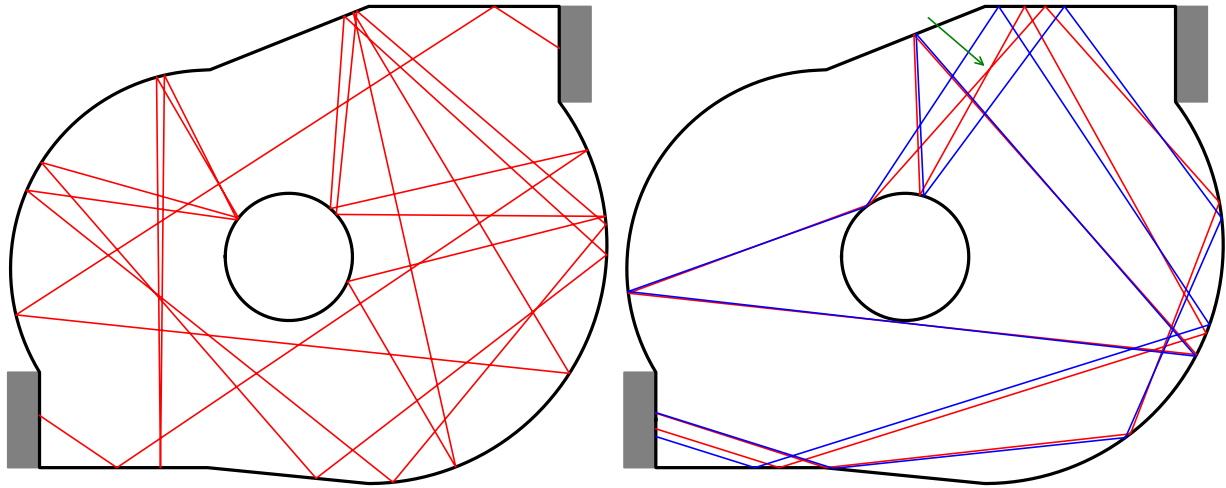


Figure 6.3: The left panel shows a long trajectory inside the billiard calculated using a ray-tracing algorithm. The right panel shows a Richter-Sieber pair; the self-crossing is marked by the green arrow.

for the time t_γ a trajectory spends inside the cavity. Here τ_D is the classical dwell time. Equivalently we can talk about the distribution $P(L) = L_0^{-1} e^{-L/L_0}$ of paths of given length L with $vt_\gamma = L, v\tau_D = L_0$ and $v = p/m$. Therefore we can use an exponential fit (shown in Fig. 6.4) to the numerical obtained path-length distribution to determine the classical dwell time τ_D .

The average time between two hits on the boundary becomes also a constant; and at each hit the particle is reflected into a “random” direction. We can now apply the central limit theorem to obtain a Gaussian distribution for the directed areas \mathcal{A} for paths of a given length L [177]:

$$P(L, \mathcal{A}) = \frac{1}{\sqrt{2\pi L\eta}} \exp\left(-\frac{\mathcal{A}^2}{2L\eta}\right). \quad (6.13)$$

Here η is system-dependent parameter which can be determined using the total distribution of the directed areas \mathcal{A} :

$$P(\mathcal{A}) = L_0^{-1} \int_0^{+\infty} P(L, \mathcal{A}) e^{-L/L_0} dL = \frac{1}{\sqrt{2\eta L_0}} \exp\left[-\sqrt{\frac{2}{\eta L_0}} |\mathcal{A}|\right]. \quad (6.14)$$

This is an exponential distribution, too, allowing us to compute η using an exponential fit to the numerical obtained distribution for \mathcal{A} as shown in Fig. 6.4.

The logical connection between η and B_w is best illustrated using the method of [15, 110] to investigate the weak localization effect. Starting with Eq. (6.4) we calculate the general form of

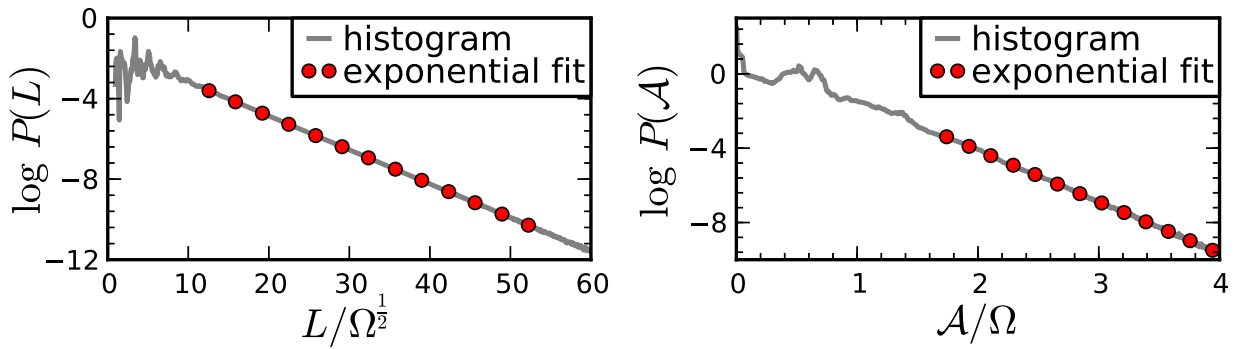


Figure 6.4: This figure shows the numerical obtained probability distribution of path lengths L and directed areas \mathcal{A} of the billiard \mathcal{B}_5 (Sec. 5.8.4) with area Ω . After a short transient region an exponential function is fitted (dots) onto both distributions yielding the parameters τ_D and B_w .

the weak localization effect as an expectation value:

$$\begin{aligned}
 \langle |\mathcal{S}_{nn}|^2 \rangle_{\text{diag}} &= c + c \left\langle \exp \left[i \frac{2}{\hbar} \varphi_\gamma \right] \right\rangle_\gamma = c + c \left\langle \exp \left[i \frac{2qB}{\hbar} \mathcal{A}_\gamma \right] \right\rangle_\gamma \\
 &= c + c \int_{-\infty}^{+\infty} \exp \left[i \frac{2qB}{\hbar} \mathcal{A} \right] P(\mathcal{A}) d\mathcal{A} \\
 &= c + c \int_{-\infty}^{+\infty} \exp \left[i \frac{2qB}{\hbar} \mathcal{A} \right] \frac{1}{\sqrt{2\eta L_0}} \exp \left[-\sqrt{\frac{2}{\eta L_0}} |\mathcal{A}| \right] d\mathcal{A} \\
 &= c + c \left[1 + \left(\frac{2qB}{\hbar} \sqrt{\frac{\eta L_0}{2}} \right)^2 \right]^{-1} = c + c [1 + (B/B_w)^2]^{-1}.
 \end{aligned} \tag{6.15}$$

Here $c = \langle \sum_\gamma |A_\gamma|^2 \rangle = (N_1 + N_2)^{-1}$ is a constant which does not depend on the magnetic field and is evaluated using the Hannay-Ozorio de Almeida sum rule [94, 96].

This finally allows us to determine B_w as

$$B_w = \frac{\hbar}{q} \frac{1}{\sqrt{2\eta L_0}}. \tag{6.16}$$

The universal prediction for the dwell time

There exists also an universal prediction [15, 113] for the classical dwell time τ_D based on ergodic arguments. Every trajectory is determined by a point and an angle. Therefore the whole phase space has “volume” $V_{\text{all}} = 2\pi\Omega$ and we can assume an uniform distribution of the trajectories in this phase space. Only particles being in front of a lead and having a suitable angle can escape the cavity in the unit time interval. The “volume” of phase space allowing escape is $V_{\text{esc}} = (W_1 + W_2) \int_{-\pi/2}^{\pi/2} \cos \alpha d\alpha$ where W_1 and W_2 are the widths of the two leads. This gives us the universal prediction for the dwell time as $v\tau_{D,u} = V_{\text{all}}/V_{\text{esc}}$ or

$$L_{0,u} = v\tau_{D,u} = \frac{\pi\Omega}{W_1 + W_2}$$

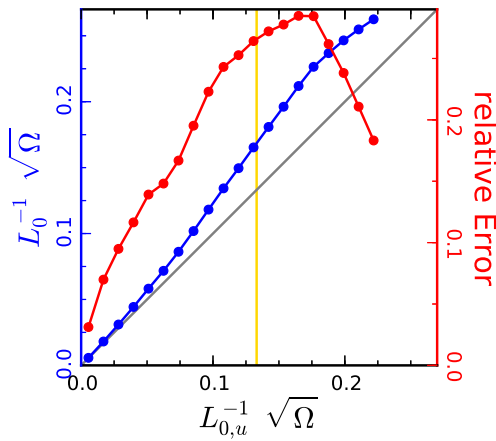


Figure 6.5: This figure compares the numerical values of $L_0 = v\tau_D$ (blue line) to the universal prediction $L_{0,u} = v\tau_{D,u}$ (gray line) for various lead widths. The relative error is shown in red. The relevant values for \mathcal{B}_5 are highlighted by the yellow line.

In practice the quality of this universal prediction is not so good. For the billiard \mathcal{B}_5 (Sec. 5.8.4) we have $\tau_D = 0.79\tau_{D,u}$ for the classical dwell time τ_D obtained by the numerical fitting procedure shown in Fig. 6.4. This deviation is probably due to the relatively large widths of the leads which compromises the ergodic argument in the derivation of $\tau_{D,u}$; furthermore in actual systems the phase space distribution is not so uniform and a particle at a given point can have more than one angle under which it is able to escape. Therefore $V_{\text{all}}, V_{\text{esc}}$ are only approximatively given by the expressions above. I have checked (see Fig. 6.5) that the agreement between universal prediction and numerics improves for smaller lead widths. But for reasons detailed in Sec. 6.1.4 we must stick to relative large lead widths.

Finally we have to mention here the Heisenberg time $\tau_H = m\Omega/\hbar$ introduced in Eq. (3.71) whose inverse \hbar/τ_H is a measure for the mean energy spacing between the eigenstates of the closed system and therefore also for the resonances. In [96] the relation

$$\frac{\tau_{D,u}}{\tau_H} = \frac{\pi\hbar}{mv(W_1 + W_2)} = \frac{1}{N_1 + N_2} \quad (6.17)$$

is often applied which uses the relation $W_1 \approx \frac{\pi\hbar}{mv}N_1$ based on plane wave transversal eigenfunctions in the leads. In the semiclassical prediction Eq. (6.10) we use $(N_1 + N_2)^{-1}$ instead of the other possibilities $\tau_{D,u}/\tau_H$ or τ_D/τ_H because that gives the random matrix theory results. In Sec. 6.2.2 we will prefer to use τ_D/τ_H over $(N_1 + N_2)^{-1}$.

Universal conductance fluctuations

There exists a method to determine the classical value of $L_0 = v\tau_D$ through quantum mechanical transport calculations. To this end we analyze now the universal conductance fluctuations (also called Ericson fluctuations [65]) semiclassically. These fluctuations exist because in wide open billiard systems many resonances overlap leading to an unpredictable spectrum (see Fig. 5.36). The presentation here is based on [15, 23, 110]. We restrict ourselves to zero magnetic field $B = 0$; for simplicity the Maslov phases are incorporated into A_γ . The whole following semiclassical analysis is only valid for the non-interacting case $g = 0$. Numerically we also only consider the linear case as calculations for $g = 0$ are quite fast. This allows us to include a vast number of parameter configurations for the statistical average which produces small statistical error bars. Sadly the data used to study the transport properties for $g \neq 0$ as done in Sec. 6.1.4 is not well suited (wrong sampling) to study the conductance fluctuations.

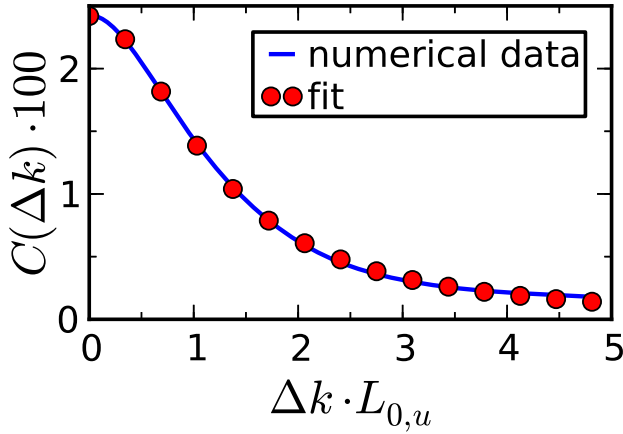


Figure 6.6: This figure shows the transmission correlation function. We fit Eq. (6.18) with C_0 and L_0 as free parameters to the numerical data.

The transmission $T(k)$ is viewed as a function of the wavevector k . Then the correlation function of the transmission can be semiclassical evaluated as

$$\begin{aligned}
 C(\Delta k) &= \langle (T(k + \Delta k) - \langle T \rangle) (T(k) - \langle T \rangle) \rangle = \langle T(k + \Delta k) T(k) \rangle - \langle T \rangle^2 \\
 &= \left\langle \sum_{\gamma_0, \gamma_1, \gamma_2, \gamma_3} A_{\gamma_0} A_{\gamma_1}^* A_{\gamma_2} A_{\gamma_3}^* e^{ik(L_{\gamma_0} - L_{\gamma_1} + L_{\gamma_2} - L_{\gamma_3})} e^{i\Delta k(L_{\gamma_0} - L_{\gamma_1})} \right\rangle - \langle T \rangle^2 \\
 &= \left\langle \sum_{\gamma, \gamma'} |A_\gamma|^2 |A_{\gamma'}|^2 e^{i\Delta k(L_\gamma - L_{\gamma'})} \right\rangle = \left\langle \sum_{\gamma, \gamma'} |A_\gamma|^2 |A_{\gamma'}|^2 \right\rangle \left| \int_0^\infty e^{i\Delta k L_\gamma} P(L) \right|^2 \\
 &= C_0 \frac{1}{1 + (\Delta k L_0)^2} .
 \end{aligned}$$

Here the average $\langle \dots \rangle$ is done over many different wavevectors k . In the diagonal approximation (which is used above) this average forces $L_{\gamma_0} - L_{\gamma_1} + L_{\gamma_2} - L_{\gamma_3} = 0$ which is systematically fulfilled for $\gamma_0 = \gamma_1, \gamma_2 = \gamma_3$ (this gives $\langle T \rangle^2$) or for $\gamma_0 = \gamma_3, \gamma_1 = \gamma_2$. We see that the correlation function has a Lorentzian shape whose width is determined by L_0 . Sadly the diagonal approximation is insufficient to correctly calculate the amplitude C_0 . For the full semiclassical evaluation of C_0 one needs higher order loop contributions [34, 203] with two or more crossings. Therefore we simply use here the random matrix theory (RMT) prediction [146]. The value of C_0 depends crucially on the details of the averaging procedure. The convention used here is

$$\begin{aligned}
 \langle T \rangle &= \frac{1}{N_1} \sum_{n=1}^{N_1} \sum_{m=N_1+1}^{N_1+N_2} \langle |S_{nm}|^2 \rangle_k \\
 \langle T(k + \Delta k) T(k) \rangle &= \frac{1}{N_1} \sum_{n=1}^{N_1} \left\langle \left[\sum_{m=N_1+1}^{N_1+N_2} |S_{nm}(k + \Delta k)|^2 \right] \left[\sum_{m=N_1+1}^{N_1+N_2} |S_{nm}(k)|^2 \right] \right\rangle_k .
 \end{aligned}$$

For this convention the prediction is [146]

$$C(\Delta k) = \frac{C_0}{1 + (\Delta k L_0)^2} \quad \text{with} \quad C_0 = \frac{(N + 1)^2}{(2N + 1)^2 (2N + 3)} . \quad (6.18)$$

In Fig. 6.6 we use C_0, L_0 as free parameters and fit $C(\Delta k)$ to the numerical data. This gives us

$$\begin{aligned}
 L_{0,\text{correlation num. fit}} &= 1.060 \, L_{0,\text{classical path length fit}} \\
 L_{0,\text{correlation num. fit}} &= 0.838 \, L_{0,\text{universal prediction}} \\
 C_{0,\text{correlation num. fit}} &= 1.057 \, C_{0,\text{RMT}} .
 \end{aligned}$$

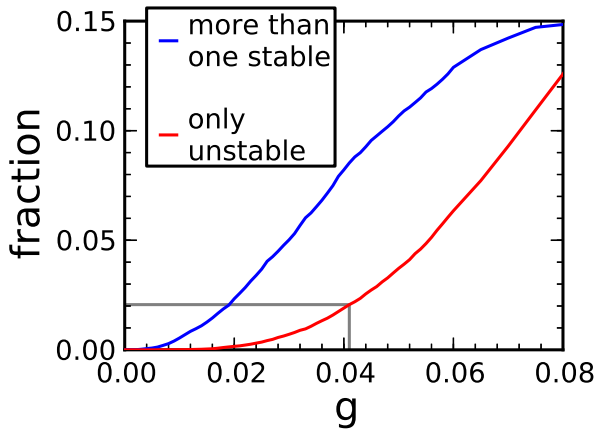


Figure 6.7: This figure shows the fraction of parameter configurations (μ, B, n_i) (here n_i is the incoming mode number) supporting only dynamically unstable solutions (red curve) or supporting more than one solution (blue curve). For $g \leq 0.04$ the fraction of configurations supporting only unstable solutions is less than 0.02 (gray lines).

We see that C_0 matches nicely to the RMT prediction. The value of L_0 matches better to the value obtained by fitting an exponential distribution to the classical path length distribution (Fig. 6.4) than to the universal prediction. This is another confirmation that the universal prediction is of inferior quality.

6.1.4 Comparison with numerical results

In this section we use the system \mathcal{B}_5 introduced in Sec. 5.8.4 to compare the numerical obtained reflection and transmission to the semiclassical prediction Eq. (6.11). The equivalent results for other systems will be discussed in Sec. 6.3.

The relevant system parameters of \mathcal{B}_5 are summarized in Fig. 5.35 (see also Sec. 3.8 for the basic units E_0, k_0, B_0), especially we have $N = 5$ open channels in both the left and right lead. The incident current is $j_{\text{in}} = E_0/\hbar$ (see Sec. 5.1.1). Using the methods of Sec. 6.1.3 the classical dwell time τ_D is calculated as $\tau_D j_{\text{in}} = 240.8$ while a similar calculation produces $B_w = 0.22 B_0$.

The numerics

In order to calculate the reflection and transmission numerically we solve the stationary scattering problem Eq. (5.2) using the curve tracing (in g) combined with Newton's method as described in Chap. 5. We thus get the pair (g, Ψ) , i.e. the interaction strength and a stationary scattering state, as a parametric curve as shown in Fig. 5.39. As is characteristic for nonlinear wave equations, for some values of g there might be more than one stationary scattering state. As we follow the parametric curve we usually select the first encountered solution Ψ for a given g as this models the adiabatic population of the cavity by the source as explained in Sec. 5.4.3 (see also Fig. 5.40).

Having found a stationary scattering state, a stability analysis using the Bogoliubov-de Gennes equation (5.32) is carried out as explained in Sec. 5.7. It might happen that no stationary solution for a given g is dynamically stable. In that case the solution with the smallest Lyapunov exponent is chosen, the latter being defined as the largest imaginary part of the eigenvalues ξ of Eq. (5.32). This choice is supported by selected case studies where we have simulated a time dependent population of the cavity as explained in Sec. 5.4.1. In these simulations we have found that for not too large values of g the time-dependent current in the transmission lead shows regular oscillations around the current of the stationary solution with the smallest Lyapunov exponent (see also Fig. 4.3 and Fig. 5.39). The experimental relevant time-averaged transmission is then

correctly reproduced by our choice. But for larger values of g the flow through the cavity might become turbulent which means that any stationary scattering state loses its significance. Therefore it is necessary to limit the range of allowed g .

As shown in Fig. 6.7, the fraction of parameter configurations (μ, B, n_i) (here n_i is the incoming mode number) supporting no dynamically stable stationary scattering state increases rapidly with g . In order to study the weak localization effect for the system \mathcal{B}_5 we always restrict g to values smaller than 0.04 which means that the fraction of configurations with only unstable solutions remains below 0.02.

For narrow leads with only a few open channels the fraction of unstable configurations rises much more rapidly than for wide leads. The reason is that for nearly closed systems the resonances are very sharp (i.e. have very small imaginary part, see Sec. 3.7.2); therefore the interaction energy $\frac{\hbar^2}{m} \int g(\mathbf{r}) |\Psi(\mathbf{r})|^4 d\mathbf{r}$ assumes to very large values (see also Sec. 5.6.2). On the other hand the visibility (i.e. magnitude) of the weak localization effect is best for narrow leads and decreases inversely proportional to the width of the leads. We therefore have to find a delicate balance between the size of the system and the width of the leads to fulfill the two contradicting requirements concerning the fraction of unstable configurations and the visibility of the weak localization effect.

The weak localization effect can only be seen in the averaged transmission and reflection. In order to get good statistics, for each fixed magnetic field B and interaction strength g we use three separate averaging procedures:

- We use 50 different energies μ regular spaced in the range $0.93E_0 \dots 1.18E_0$ where $N = 5$ modes are open in the leads. More than 50 energy steps are not advisable as the spacing between the different energies should be larger than the correlation length of the transmission which is quite large as the resonances are very broad.
- We use 25 different stopper positions, i.e. the hole in the middle is moved a little bit (on the order of a wavelength) in vertical or horizontal position. This geometrical average is necessary as we cannot increase the energy average.
- We use all $N = 5$ open modes in the left lead as incident channel (one after another).

The error bars shown in the numerical obtained transmission and reflection (for example in Fig. 6.8) indicates the size of the statistical standard deviation resulting from this averages.

The semiclassical prediction

The top right panels of Fig. 6.9 and Fig. 6.8 show the semiclassical prediction Eq. (6.11) for the transmission and the self-reflection R_s .

We first focus on R_s . For $g = 0$, the semiclassical analysis predicts a Lorentzian peak as function of the magnetic field B on top of a constant background. This Lorentzian shape is characteristic for weak localization. For increasing values of g the height of this peak is reduced, but the reduction is more efficient at the center than at the flanks, therefore at intermediate values of g we obtain a double peak structure with a dip in the middle. For $g \rightarrow \infty$ the Lorentzian peak vanishes completely, but this is of no physical relevance as then time dependence sets in and no stationary scattering states are possible (see Fig. 5.39).

For the transmission T the situation is inverted, i.e. we have a Lorentzian dip which gets flattened until a double dip structure with a peak in the middle emerges.

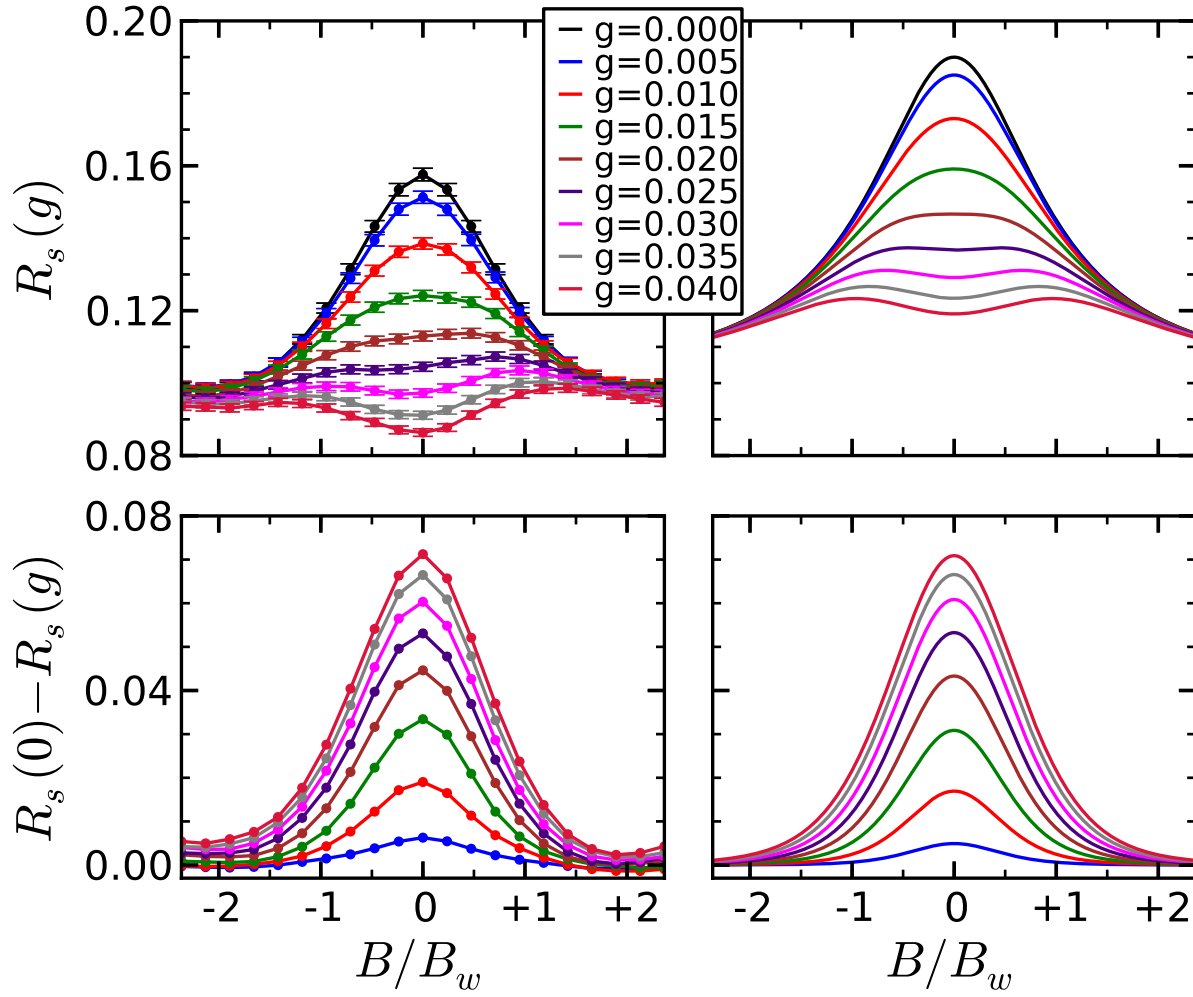


Figure 6.8: These figures display the self-reflection R_s as function of the magnetic field B and the interaction strength g . The two right panels show the semiclassical prediction Eq. (6.11), the two left panels show the corresponding numerical results. The two upper panels show R_s while the two lower panels show the difference $R_s(0) - R_s(g)$.

The results

We first focus on R_s in the linear case $g = 0$. In the top left panel of Fig. 6.8 we see that the numerical reflection shows a Lorentzian peak as predicted by the semiclassical analysis. In particular the width of the peak fits quite well, but the amplitudes (the height of the background and of the peak) are not well reproduced. The reason for this are fourfold:

- We might not have averaged over enough different configurations. This reason is of lesser importance for the system \mathcal{B}_5 studied here, but might be relevant for the systems studied in Sec. 6.3. As computations may take very long, the configuration space used for the averaging procedure is subject to patience and available computer power.
- The wavelength might not be small enough in comparison with the system size as seen in Fig. 5.35. This compromises the limit $\hbar \rightarrow 0$ on which the semiclassical Green function is based. But the above mentioned restriction concerning the ratio between the size of the

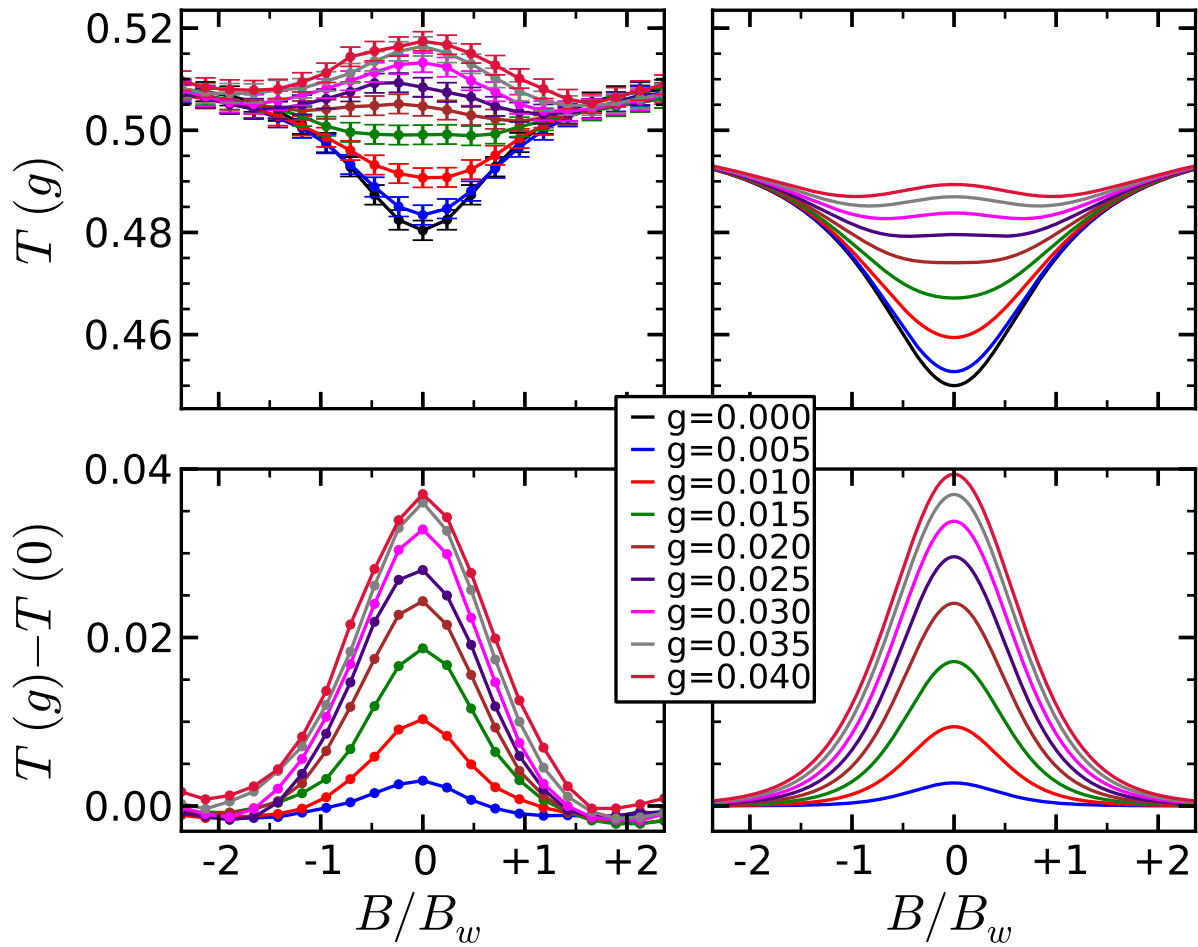


Figure 6.9: These figures display the transmission T as function of the magnetic field B and the interaction strength g . The two right panels show the semiclassical prediction Eq. (6.11), the two left panels show the corresponding numerical results. The two upper panels show T_s while the two lower panels show the difference $T_s(0) - T_s(g)$.

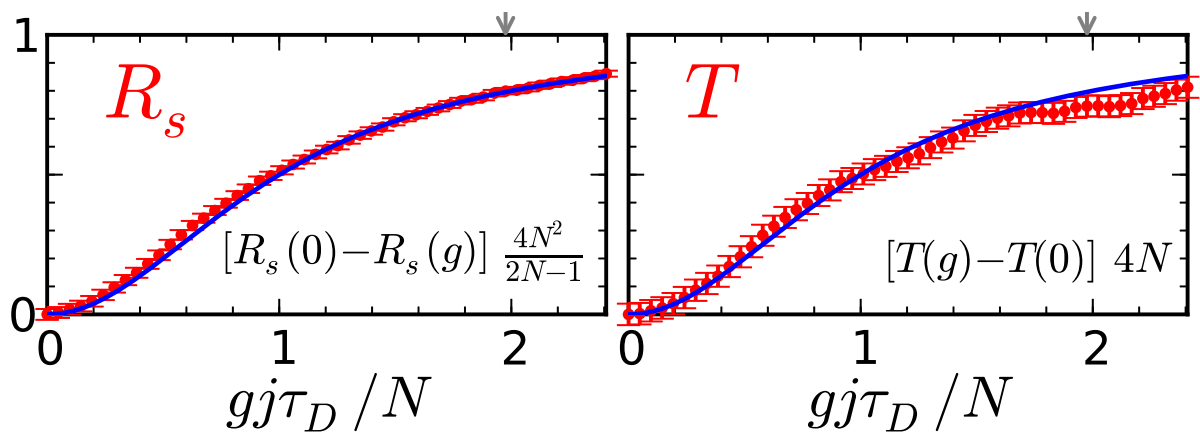


Figure 6.10: These figures show the reduction of the weak localization effect in the self-reflection R_s (left panel) and in the transmission T (right panel) as a function of the interaction strength g for zero magnetic field $B = 0$. The numerical results (red dots) agree very well with the semiclassical prediction Eq. (6.11) (blue line). The gray arrows mark the position $g = 0.04$.

cavity and the width of the leads severely restricts the possible range of wavelengths. Of course, the available computer power is a factor here, too, as shorter wavelengths imply more grid points.

- Diffraction effects [209] at the lead-openings are completely neglected in the semiclassical analysis. This is a factor here because of the quite large wavelength we are using.
- The discrepancies might be due to nonuniversal scattering effects that explicitly depend on the shape of the cavity. For example, as seen in Fig. 6.4 the path length distribution shows non-universal features for short paths, and something similar is true for the area distribution.

The influence of any of those effects on the transmission and reflection is very hard to estimate.

Let us now focus on the non-universal short trajectories, especially short self-retracing trajectories which are identical to their time-reversed counterpart. A simple scenario for this is a trajectory which leaves the left lead, hits the circular obstacle in the middle perpendicularly and is reflected back into the left lead. The directed area of such paths is zero and they therefore do not contribute to the amplitude of the Lorentzian in the diagonal approximation Eq. (6.5). This compromises the sum-rule based evaluation of this amplitude because such paths are overcounted.

On the other hand, as seen in Eq. (6.8) the influence of the magnetic field B on the difference¹⁰ $R_s(0) - R_s(g)$ is not based on just one path, but emerges from the combination of four or more trajectories which are connected by the non-linearity. The overcounting issue does not arise here and also diffraction effects should not influence this difference. Therefore non-universal short trajectories have much less influence on the difference $R_s(0) - R_s(g)$.

This argument is supported by the lower left panel in Fig. 6.8 which shows rather good agreement between the numerical data and the semiclassical prediction for this difference, i.e. the reduction of the weak localization peak with respect to the linear case $g = 0$. An even nicer agreement is shown in Fig. 6.10 where we focus on a vanishing magnetic field $B = 0$.

The transmission T , for which loop contributions are relevant, shows a similar behavior. As seen in Fig. 6.9 and Fig. 6.10, a nice agreement between numerics and semiclassical analysis is found after removing non-universal effects. One should also note here, that the averaged quantity T is an almost, but not perfect, symmetric function in the magnetic field B for non-vanishing values of the interaction strength g . This happens because the breaking of Onsager's relation (as described in Sec. 5.8.4) for a fixed parameter configuration is lifted by the averaging procedure. The reason is that paths in a classical chaotic cavity have (usually¹¹) no preferred sense of circulation or direction.

As discussed in Sec. 6.1.1, the magnitude of the weak localization effect is twice as big in R_s than in T . Also the magnetic field independent background for R_s is much smaller than for T . Therefore one can see the weak localization effect more clearly in R_s than in T .

Higher magnetic fields

The cyclotron radius r_{cyc} for a particle of mass m , velocity v and charge q in a magnetic field B is given by [50]

$$r_{\text{cyc}} = \frac{mv}{qB}.$$

¹⁰ For the sake of simplicity the function parameter B is dropped here from our notation.

¹¹ One has to note here that there exists chaotic cavities with unidirectional transport properties, for example the so-called "Monza" billiards [104, 205].

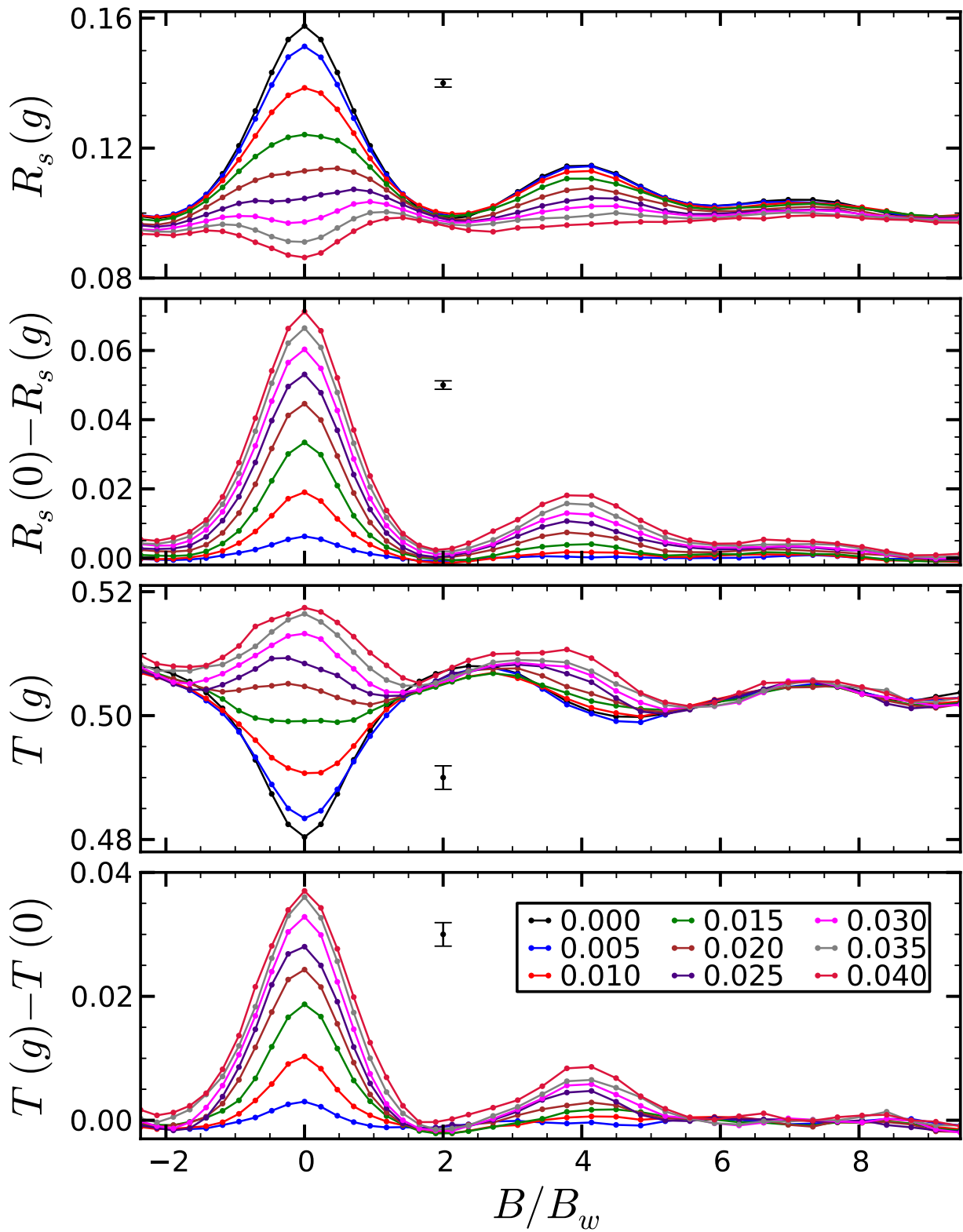


Figure 6.11: These figures show the numerical calculated self-reflection R_s and transmission T for higher magnetic fields. The corrections $R_s(0) - R_s(g)$ and $T(g) - T(0)$ induced by the nonlinearity are also shown. The single points at $B/B_w = 2$ show the size of the error bars.

For the magnetic field $B=B_w$ this gives with our choice of parameters $r_{\text{cyc}} = 58.3\sqrt{\Omega} = 1506\pi k_0^{-1}$. In other words, the cyclotron radius for $B=B_w$ is roughly 45 times the lateral dimension of the system B_5 . In the magnetic field range $B = -2.2B_w \dots 2.2B_w$ used in Fig. 6.8, classical trajectories inside the cavity therefore roughly follow straight lines. This fact justifies the perturbative treatment of the magnetic field in the semiclassical Green function Eq. (6.1).

One can safely use even larger values of the magnetic field; in Fig. 6.11 the range $B = -2.2B_w \dots 8.6B_w$ is explored¹². In the non-interacting case $g = 0$ we observe a weak signature of Aharonov-Bohm oscillations [50] caused by the obstacle in the middle (see also Sec. 5.9). This obstacle induces some kind of ring structure. But our “ring” is very broad, thus destroying the perfect symmetry of the normal Aharonov-Bohm oscillations. Therefore we can only observe one or two periods, and the periodicity is highly imperfect. The numerical results suggests an Aharonov-Bohm period of $B_{\text{AH}} = 4 B_w$. From¹³

$$B_{\text{AH}} = \frac{2\hbar}{q r_{\text{AH}}^2}$$

we can deduce an effective ring radius of $r_{\text{AH}} = 0.6\sqrt{\Omega} = 15.5\pi k_0^{-1}$. This corresponds to the outer boundary of the cavity and is a reasonable result.

For increasing values of the interaction strength g we observe that for $B \geq 2B_w$ the self-reflection R_s depends only weakly on B (the first repetition of the central peak gets essentially flattened). In contrast to R_s , the first repetition in the non-linearity induced correction $R_s(0) - R_s(g)$ shows a similar behaviour as the central peak albeit with smaller amplitude.

The situation for the transmission is slightly different. The correction $T(g) - T(0)$ of the first repetition resembles the central peak just like it was the case for $R_s(0) - R_s(g)$. But for large g and values of $B \geq 2$ the transmission still depends oscillatory on B .

As the periodicity (in B) should still be at least approximatively valid for non-vanishing interaction g , we can at least qualitatively understand the results. But no quantitative prediction is available. It seems that the oscillations are most cleanly realized in the correction $R_s(0) - R_s(g)$ and $T(g) - T(0)$ while the effect in R_s and T gets marred by non-universal path effects. This is similar to the discussion above.

6.1.5 Direct evaluation of the semiclassical sum

The sum-rule based semiclassical evaluation Eq. (6.7) is obviously not able to reproduce the Aharonov-Bohm oscillations shown in Fig. 6.11 as the effect is based on a non-universal path length/area distribution. In this section we therefore try to evaluate the (squared moduli of the) semiclassical scattering matrix (6.3) directly without using sum rules. To this end we note that the ray tracing method (see Sec. 6.1.3) is capable of evaluating all terms occurring in the semiclassical Green function Eq. (6.1) exactly: the stability amplitude A_γ (whose computation is described in App. G), the classical action S_γ and the directed area \mathcal{A}_γ (which are both trivial to evaluate) and the Maslov index (which is troublesome to evaluate but not needed for the diagonal approximation). The calculation is done only in the linear regime $g = 0$.

¹²For higher values of B the cyclotron radius approaches the system size, therefore we do not investigate this range.

¹³See [50]. Obviously this is based on the periodicity of $e^{i\phi_\gamma/\hbar}$ in Eq. (6.1).

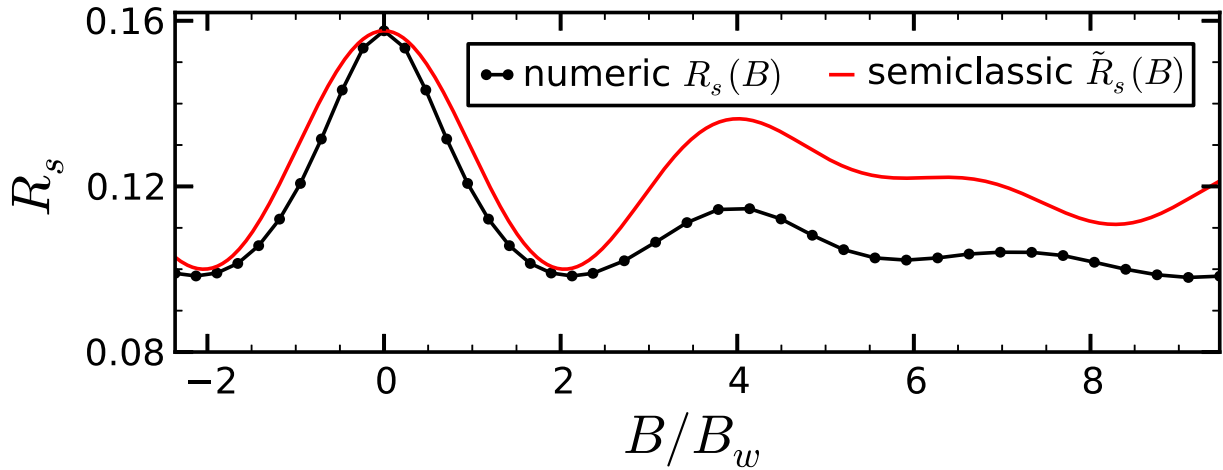


Figure 6.12: This figure compares the numerical value of the self reflection $R_s(B)$ (black) to the non-universal semiclassical prediction Eq. (6.19) $\tilde{R}_s(B)$ (red) in the linear regime $g = 0$. As Eq. (6.19) is missing an overall prefactor, the maximum of the semiclassical prediction is scaled to match the maximum of the numerical results.

There are several different approaches to numerically evaluate the complete semiclassical sum Eq. (6.3). We first discuss two approaches here which do not work and then present a successful approach using the diagonal approximation.

The first approach is to sum up Eq. (6.3) directly¹⁴. As previously discussed, the classical trajectories can only exit or enter the leads at certain discrete angles. Up to a given length there are only finitely many such paths (excluding degenerate ones). Combining raytracing with a non-linear equation solver one can try to find all such classical paths satisfying these boundary conditions. Sadly there are several obstacles in realizing this ambition:

- The number of paths fulfilling the boundary conditions grows exponentially with the path length.
- The path search algorithm might easily miss some paths, especially if the path length gets large.
- Even as the modulus of the A_γ drops fast with the path length the convergence of the whole sum Eq. (6.3) is highly problematic because of caustics and the exponential proliferation of paths.
- The Maslov indices u_γ are non-trivial to evaluate.

Some of these problems can be circumvented by using the cutoff length $L_0 = v\tau_d$ to artificially damp all contributions from longer paths. But even that does not give satisfactory results.

The second approach is to evaluate $G_{sc}(\mathbf{r}, \mathbf{r}')$ for a fixed energy and for fixed positions \mathbf{r} and \mathbf{r}' inside the leads. One does not use the fixed-angle boundary conditions (which arise through the stationary phase evaluation of the integral Eq. (6.2)); instead one approximates the integral Eq. (6.2) through Riemann sums. The fixed entry/exit angle boundary condition is replaced with a fixed entry/exit position condition; therefore this method is also computationally demanding. A

¹⁴ For the complete S matrix one additionally has to average over the energy μ .

major problem is now that the semiclassical Green function is additionally plagued by caustics in this approach. Also the results are not satisfactory.

The two previously discussed approaches to a direct evaluation of the semiclassical scattering matrix Eq. (6.3) did all not work very well, especially in relation with the effort involved. We now present a third approach based on direct paths which does work and gives satisfactory results.

The third approach starts similar to the second approach. One of the biggest obstacle are the boundary conditions fixing the both entry and exit angle (or both entry and exit position) of the trajectory, as it was done in the first and second approach. These boundary conditions can be avoided if one does not perform the stationary phase approximation for the integral over the lead modes. Therefore all classical paths from now on a priori do not need to satisfy any special boundary conditions.

But instead of evaluating the integral Eq. (6.2) directly we take an average over the channels and over the energy. Technically one evaluates the self reflection Eq. (6.6) using the Fisher-Lee relation Eq. (6.2) where we use the semiclassical Green function G_{sc} instead of the quantum mechanical one:

$$\tilde{R}_s = \frac{1}{N_1} \sum_{n=1}^{N_1} \langle |\mathcal{S}_{nn}|^2 \rangle \sim \sum_{n=1}^{N_1} \int \int \int \int dy_0 dy_1 dy'_0 dy'_1 \sin(ny_0) \sin(ny_1) \sin(ny'_0) \sin(ny'_1) \left\langle \sum_{\gamma, \gamma'} G_{sc, \gamma} G_{sc, \gamma'}^* \right\rangle_{\text{energy}} .$$

Here y_0, y_1, y'_0, y'_1 are suitable scaled transversal lead coordinates. The relation \sim means that we neglect all overall prefactors from now on. As before, the energy average reduces the double sum over all allowed paths to a single sum over correlated pairs. We are using the diagonal approximation here where a path $+\gamma$ is paired with itself and with its time reversed counterpath $-\gamma$. This involves that the (unordered) pair $\{y_0, y_1\}$ (the start/end point of γ) is identical to $\{y'_0, y'_1\}$ (the start/end point of γ'):

$$\tilde{R}_s \sim \sum_{n=1}^{N_1} \int \int dy_0 dy_1 [\sin(ny_0) \sin(ny_1)]^2 \sum_{\gamma} \left[G_{sc, +\gamma} G_{sc, +\gamma}^* + G_{sc, +\gamma} G_{sc, -\gamma}^* + G_{sc, -\gamma} G_{sc, +\gamma}^* + G_{sc, -\gamma} G_{sc, -\gamma}^* \right] .$$

Using $[\sin(ny_0) \sin(ny_1)]^2 = 1/4 + c_{\text{osci}}$ (where c_{osci} are oscillating terms which are neglected from now on as their effect averages out) and evaluating the integral as a sum in the sense of the Metropolis algorithm [172] we arrive at

$$\tilde{R}_s(B) \sim \sum_{\gamma} A_{\gamma}^2 [1 + \cos(2qA_{\gamma}B)] . \quad (6.19)$$

This is the final result representing the semi-classical evaluated self reflection using non-universal classical paths in the linear regime $g = 0$. Fig. 6.12 illustrates the performance of this expression. It is capable of reproducing the Aharonov-Bohm oscillations remarkably well. Of course the agreement is more qualitative and less quantitative; but given all the approximations resulting in Eq. (6.19) one cannot expect more. Especially loop contributions are missing in this formula. What Eq. (6.19) does not provide is an overall prefactor which we have neglected to take account of.

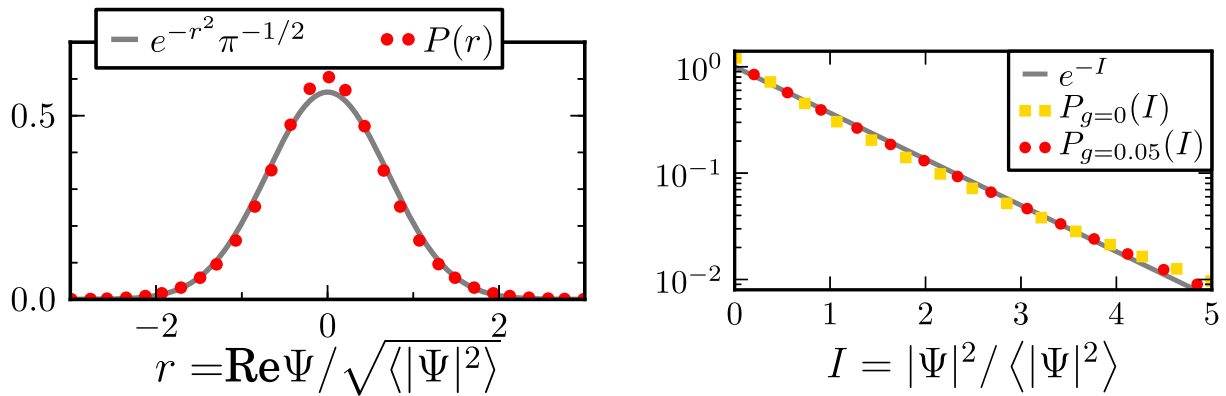


Figure 6.13: The left figure shows the numerical calculated distribution (red dots) of the real part of the wavefunction (for $B = 0$ and $g = 0$), which closely resembles a Gaussian distribution (solid line). The imaginary part shows the same behaviour. The right figure compares the numerical calculated intensity distributions for $g = 0$ and $g = 0.05$ ($B = 0$ in both cases) to the exponential distribution. One should note the tiny but noticeable deviation from the perfect exponential distribution which are shown in more detail in Fig. 6.14. The average $\langle \dots \rangle$ here is over position, energy and incoming channel.

Although Eq. (6.19) looks similar to the earlier result Eq. (6.4) (or Eq. (6.15)) the rationale behind the sum is different. While in Eq. (6.4) we use a sum over a discrete set of trajectories satisfying fixed entry/exit angle boundary conditions, the sum in Eq. (6.19) arises as an approximation of an integral (in the spirit of the Metropolis algorithm) without any boundary conditions. Eq. (6.19) can be thought to arise as one replaces the universal area/length distribution usually used to derive the weak localization effect (as it was done in Eq. (6.15)) by a system dependent one. Technically we evaluate Eq. (6.19) as it was done in Sec. 6.1.3. We take many randomly chosen trajectories that are starting in and exiting through the left lead. The transverse positions and momenta are chosen from a uniform distribution. The sum in Eq. (6.19) is taken over all those trajectories and the stability amplitude A_γ is calculated as explained in App. G.

At the very end it is worth noticing that there is also another approach going in the opposite direction[209]. Based on

$$G_{\text{sc}}(k, B) = \sum_{\gamma} A_{\gamma} \exp [ikL_{\gamma} + iqB\mathcal{A}_{\gamma}/\hbar - i\pi u_{\gamma}/2]$$

one can take the Fourier transform of the quantum mechanical scattering amplitude $\mathcal{S}_{nm}(k, B)$ with respect to k and B and obtain information about the classical length and area distribution. Obviously this does only make sense in the linear case $g = 0$. The programs are capable of performing this approach, but as I have done such calculations only for billiard systems not studied in this work, I do not go into details here.

6.2 Intensity distribution

6.2.1 Theoretical analysis

In the previous sections we have focused on the transport properties of matter waves through billiard geometries. Now we turn our attention to the intensity distribution of the stationary

scattering states inside the cavity. The stationary scattering states $\Psi(\mathbf{r})$ used here are the same as those in Sec. 6.1.4, especially we only investigate the system \mathcal{B}_5 here. The analysis of other systems is postponed to Sec. 6.3.

While in the previous section we used $\Psi(\mathbf{r})$ to calculate the transport properties we now use the hatched area in Fig. 5.35 to evaluate the distribution of the intensity $|\Psi(\mathbf{r})|^2$. The numerically obtained distribution is compared with a theoretical prediction. In this section I will only summarize the more thorough theoretical analysis presented in our work [97] which was developed by my coworkers while mine contribution were the numerical calculations.

Random Wave Model

In the non-interacting case $g = 0$ the highly successful standard approach to investigate the intensity distribution of wave functions inside cavities with classical chaotic dynamics is the Random Wave Model (RWM) [18, 195]. This approach makes the assumption that the wavefunction behaves like the superposition of random waves

$$\Psi(\mathbf{r}) \sim \sum_n a_n e^{i\mathbf{k}_n \cdot \mathbf{r}},$$

i.e. waves whose wavevector \mathbf{k} have all the same modulus $|\mathbf{k}| = \sqrt{2m\mu}/\hbar$ but random directions and random (complex) amplitudes a_n . Application of the central limit theorem gives a Gaussian distribution (see Eq. (6.20)) for the real and imaginary parts of the wavefunction Ψ from which an exponential distribution (see Eq. (6.21)) for the intensities can be derived [195]. In Fig. 6.13 we compare this theoretical predictions with numerical obtained intensity distributions. Overall the agreement is very good but one sees tiny but noticeable deviations from the theoretical predictions. The study of these deviations is the main topic of this section.

Our fundamental assumption is that the random wave model is also applicable for interacting systems, i.e. for $g \neq 0$.

The local Gaussian approach

In our numerical calculations of the intensity distribution we use the values of $|\Psi(\mathbf{r})|^2$ for many different energies, incoming channels and positions. Therefore both an energy and position average is applied. This double averaging procedure is now split apart based on the idea that for a fixed position \mathbf{r} the energy (and incoming channel) averaged intensity is itself a smooth function of \mathbf{r} .

One starts with a position dependent Gaussian distribution [202]

$$P_{\mathbf{r}}(\Psi_r, \Psi_i) = \frac{1}{\pi \langle |\Psi(\mathbf{r})|^2 \rangle_E} \exp \left[-\frac{\Psi_r^2 + \Psi_i^2}{\langle |\Psi(\mathbf{r})|^2 \rangle_E} \right] \quad (6.20)$$

for the real and imaginary part of $\Psi(\mathbf{r})$ at a fixed position \mathbf{r} . Here $\langle |\Psi(\mathbf{r})|^2 \rangle_E$ denotes the energy and incoming channel average of the intensity. The fact that $\langle |\Psi(\mathbf{r})|^2 \rangle_E$ is position dependent due to semiclassical scattering effects is responsible for the deviations between the numerical and the random wave model¹⁵ distribution visible in Fig. 6.13.

¹⁵This model is homogeneous, i.e. $\langle |\Psi(\mathbf{r})|^2 \rangle_E$ does not depend on \mathbf{r} .

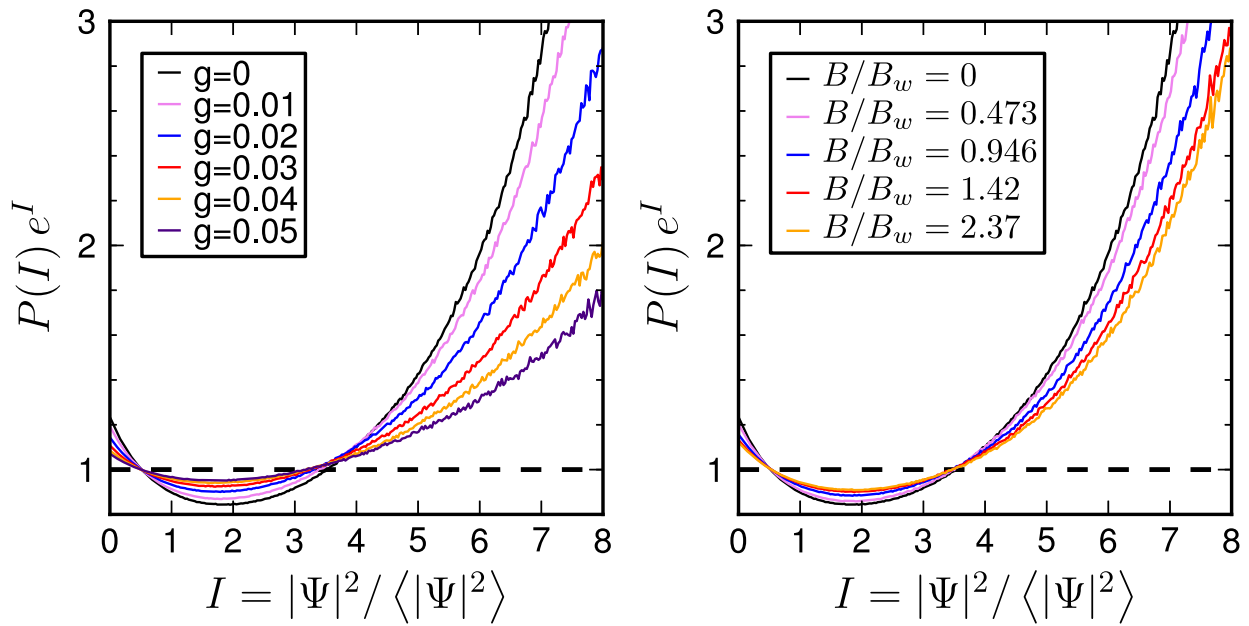


Figure 6.14: These figures show the deviations of the numerical obtained intensity distribution from the exponential distribution e^{-I} for several values of the interaction strength g (left panel, with $B = 0$) and the magnetic field B (right panel, with $g = 0$).

The subsequent analysis assumes that we restrict ourselves to the bulge and that we neglect any point close to the boundary from our analysis (see Fig. 5.35) as there the wavefunction $\Psi(\mathbf{r})$ vanishes which produces complicated boundary effects.

The intensity distribution can now be calculated as (here $\rho = |\Psi(\mathbf{r})|^2$):

$$\begin{aligned}
 P_r(\rho) &= \int_{-\infty}^{+\infty} \int_{-\infty}^{+\infty} P_r(\Psi_r, \Psi_i) \delta(\rho - \Psi_r^2 - \Psi_i^2) d\Psi_r d\Psi_i \\
 &= \frac{1}{\langle |\Psi(\mathbf{r})|^2 \rangle_E} \exp \left[-\frac{\rho}{\langle |\Psi(\mathbf{r})|^2 \rangle_E} \right], \tag{6.21}
 \end{aligned}$$

which is an exponential distribution known in this context as Porter-Thomas distribution¹⁶.

The next step is to split $\langle |\Psi(\mathbf{r})|^2 \rangle_E$ into a homogeneous and a fluctuating part $C(\mathbf{r})$

$$\langle |\Psi(\mathbf{r})|^2 \rangle_E = \frac{1}{A} [1 + C(\mathbf{r})]$$

by imposing the condition that the position average of $C(\mathbf{r})$ is zero: $\langle C(\mathbf{r}) \rangle_r = 0$. This also gives $A^{-1} = \langle \langle |\Psi(\mathbf{r})|^2 \rangle_E \rangle_r = \langle |\Psi(\mathbf{r})|^2 \rangle$ and allows us to write the distribution of the normalized

¹⁶The form of an exponential distribution depends crucially on the fact that we investigate scattering states where the real and imaginary part of the wavefunction satisfy independent Gaussian distributions. On the other side, for a closed cavity without magnetic field we can always choose the eigenstates completely real. In this case the corresponding distributions are $P_r(\Psi_r) = (2\pi \langle |\Psi(\mathbf{r})|^2 \rangle_E)^{-1/2} \exp(-\Psi_r^2 / (2 \langle |\Psi(\mathbf{r})|^2 \rangle_E))$ and $P_r(\rho) = (2\pi \langle |\Psi(\mathbf{r})|^2 \rangle_E \rho)^{-1/2} \exp(-\rho / (2 \langle |\Psi(\mathbf{r})|^2 \rangle_E))$; this is the usual form of the Porter-Thomas distribution encountered in the literature [42, 149].

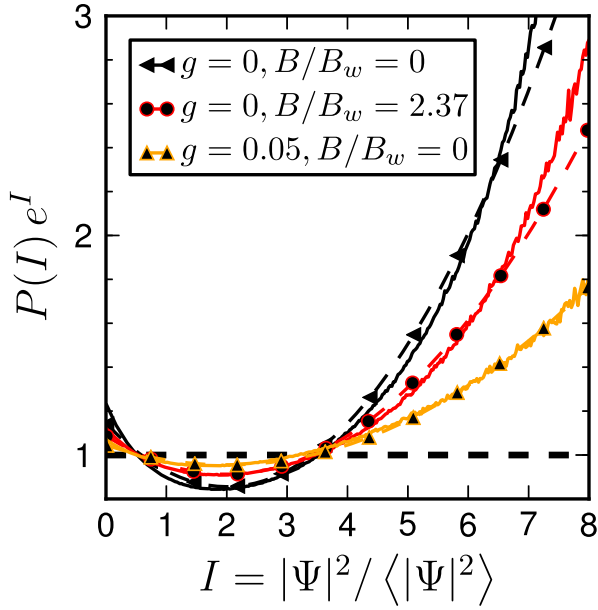


Figure 6.15: This figure compares Eq. (6.22) (dashed lines with marker symbols) with the numerical obtained intensity distribution (solid line). The a priori unknown parameter β is determined by fitting Eq. (6.22) to the numerical data in the range $1 \leq I \leq 7$.

intensity $I = |\Psi(\mathbf{r})|^2 / \langle |\Psi(\mathbf{r})|^2 \rangle$ as:

$$\begin{aligned} P_r(I) &= \frac{1}{1 + C(\mathbf{r})} \exp \left[-\frac{I}{1 + C(\mathbf{r})} \right] = \frac{e^{-I}}{1 - (-C(\mathbf{r}))} \exp \left[\frac{I(-C(\mathbf{r}))}{(-C(\mathbf{r})) - 1} \right] \\ &= e^{-I} \sum_{n=0}^{\infty} (-1)^n [C(\mathbf{r})]^n L_n(I) . \end{aligned}$$

Here L_n are the Laguerre polynomials [158]. Finally we apply a position average to obtain the position-independent intensity distribution up to second order in I :

$$\begin{aligned} P(I) &= \langle P_r(I) \rangle_r = e^{-I} \left[1 + \langle C(\mathbf{r})^2 \rangle_r L_2(I) \right] \\ &= e^{-I} \left[1 + \beta \left(1 - 2I + \frac{1}{2} I^2 \right) \right] . \end{aligned} \quad (6.22)$$

Here $\beta = \langle C(\mathbf{r})^2 \rangle_r$ is a single parameter which describes the deviation from the random wave model. As we see in Fig. 6.15 the numerical obtained intensity distribution can be very well described by Eq. (6.22).

Semiclassical evaluation of β

The next step is obviously to get a semiclassical description for β . While the semiclassical transport theory presented in [96] is very thorough, detailed and sound, the semiclassical theory for β presented in [97] is not so well developed and is mainly supported by analogies; in particular there is no diagrammatic perturbation theory. Here I present the main arguments leading to a semiclassical expression for β .

We firstly investigate the non-interacting case $g = 0$ and start with the linear retarded/advanced Green function (see also Eq. (3.6)):

$$G^\pm(\mathbf{r}, \mathbf{r}', E) = \sum_n \int dE' \lim_{\substack{\epsilon \rightarrow 0 \\ \epsilon > 0}} \frac{\Psi_{E',n}(\mathbf{r}) \Psi_{E',n}^*(\mathbf{r}')}{E - E' \pm i\epsilon} .$$

Here n labels the incoming channels and the $\Psi_{E,n}(\mathbf{r})$ are scattering states. The combination

$$G^+(\mathbf{r}, \mathbf{r}', E) - G^-(\mathbf{r}, \mathbf{r}', E) = -\frac{2}{\pi} \sum_n \int dE' \Psi_{E',n}(\mathbf{r}) \Psi_{E',n}^*(\mathbf{r}') \delta(E - E')$$

gives after averaging ($\langle \dots \rangle_E$ denotes an energy and incoming channel average)

$$\langle G^+(\mathbf{r}, \mathbf{r}', E) - G^-(\mathbf{r}, \mathbf{r}', E) \rangle_E \propto \langle \Psi_{E,n}(\mathbf{r}) \Psi_{E,n}^*(\mathbf{r}') \rangle_E. \quad (6.23)$$

Therefore $\langle |\Psi(\mathbf{r})|^2 \rangle_E$ can be calculated if we know $\langle G^+(\mathbf{r}, \mathbf{r}', E) - G^-(\mathbf{r}, \mathbf{r}', E) \rangle$ for $\mathbf{r} = \mathbf{r}'$. And for $\mathbf{r} = \mathbf{r}'$ we can apply a decomposition of following form using the semiclassical Green function G_{sc} (see Eq. (6.1))

$$G(\mathbf{r}, \mathbf{r}, E) \cong G_{\text{sc}}^{\text{zero}}(\mathbf{r}, \mathbf{r}, E) + G_{\text{sc}}^{\text{long}}(\mathbf{r}, \mathbf{r}, E)$$

where $G_{\text{sc}}^{\text{zero}}$ encompasses the zero length paths and $G_{\text{sc}}^{\text{long}}$ encompasses all longer paths which hit the boundaries one or more times. This expression maps to the decomposition $\langle |\Psi(\mathbf{r})|^2 \rangle_E = \frac{1}{A} [1 + C(\mathbf{r})]$ because zero length paths produce a position independent background and longer paths produce some fluctuation. This gives

$$C(\mathbf{r}) = \frac{\hbar^2}{mi} [G_{\text{sc}}^{\text{long}}(\mathbf{r}, \mathbf{r}, E) - G_{\text{sc}}^{\text{long}*}(\mathbf{r}, \mathbf{r}, E)]$$

and

$$\beta = \langle C(\mathbf{r})^2 \rangle_{\mathbf{r}} = -2 \left[\frac{\hbar^2}{mi} \right]^2 \langle G_{\text{sc}}^{\text{long}}(\mathbf{r}, \mathbf{r}) G_{\text{sc}}^{\text{long}*}(\mathbf{r}, \mathbf{r}) \rangle_{E, \mathbf{r}}.$$

Here we average over both energy and position. Only correlated pairs of paths therefore give a contribution to β . As in Sec. 6.1 the largest contributions comes from diagonal terms.

Up to now we have assumed the non-interacting case $g = 0$. The main assumption is now that all calculations carry over to the interacting case $g \neq 0$ and that the diagonal approximation for β resembles the diagonal approximation for the reflection into the incident channel Eq. (6.9). This gives us (see also Eq. (6.17))

$$\beta(B, g) = \frac{\tau_D}{\tau_H} + \frac{\tau_D}{\tau_H} \frac{[1 + (B/B_w)^2]}{[1 + (B/B_w)^2]^2 + (gj\tau_D/N)^2} \quad (6.24)$$

where τ_D is the classical dwell time and τ_H is the Heisenberg time (see Sec. 6.1.3).

6.2.2 Comparison with numerical results

In the semiclassical expressions for reflection and transmission Eq. (6.11) we used the universal prediction $(N_1 + N_2)^{-1} = \tau_{D,u}/\tau_H$ (see Eq. (6.17)) as prefactor instead of τ_D/τ_H . This is justified by comparison with random matrix theory which treats every outgoing channel the same way and by considering current conservation $R + T = 1$.

But the prefactor in the semiclassical prediction Eq. (6.24) for the parameter β is based on the numerical value of τ_D as obtained in Sec. 6.1.3. This gives better results and is justified by considering that β is not restricted by current conservation or symmetries.

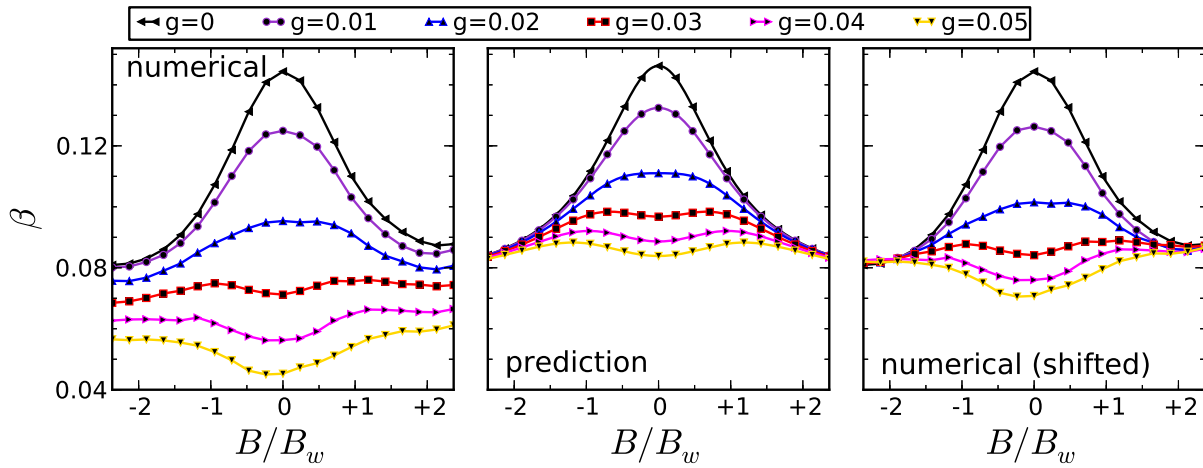


Figure 6.16: The middle panel shows the semiclassical prediction Eq. (6.24) for β while in the left panel the numerical values of β (see Fig. 6.15) are displayed. In the numerical values we observe a displacement which only depends on g but not on B . In the right panel this displacement is subtracted from the numerical data such that β for $g \neq 0$ and $B = \pm 2.2 B_w$ matches the equivalent numerical results for $g = 0$.

Numerically the parameter β is determined by fitting the parabola Eq. (6.22) to the numerical intensity distributions for all values of the magnetic field B and interaction strength g as shown in Fig. 6.15.

Fig. (6.16) compares the semiclassical prediction Eq. (6.24) of β (middle panel) to the numerical determined value (left panel). We observe that the parameter β behaves very much like the self-reflection R_s .

In the non-interaction case $g = 0$ the agreement is very good. For vanishing magnetic field $B = 0$ the parameter β is enhanced due to constructive interference between a path and its time reversed counterpath. For large values of B this symmetry is destroyed. The final form of β for $g = 0$ is a Lorentz peak.

For increasing values of the interaction strength g the height of the Lorentz peak is reduced. As the reduction is bigger for zero magnetic field than for large values of B a double peak structure with a dip in the middle emerges. Here the agreement between numerics and semiclassics is not so good. It seems that the numerical values of β for non-vanishing interaction are shifted downwards by a quantity which does only depend on the interaction g and not on the magnetic field B . If we remove this shift¹⁷ (right panel in Fig. (6.16)) the agreement between semiclassical prediction and numerical results is very nice.

There are many possible reasons for the observed discrepancy:

- As in Sec. 6.1.4 non-universal short paths may play a role. But this should only produce minor effects, like that the dip in the numerics for large values of g is deeper than predicted by the semiclassical theory. The global shift independent of B must have another explanation.
- As shown in Fig. 6.17, the value of $\langle |\Psi(\mathbf{r})|^2 \rangle$ shows a slight dependence on B and g . For increasing values of g , the value of $\langle |\Psi(\mathbf{r})|^2 \rangle$ gets reduced in a manner roughly independent of B . This tendency of the interaction to reduce the average intensity can be explained

¹⁷We match the numerical values of $\beta(g)$ for high magnetic fields with the corresponding numerical values of $\beta(0)$. This gives a value for the shift which is independent of the magnetic field.

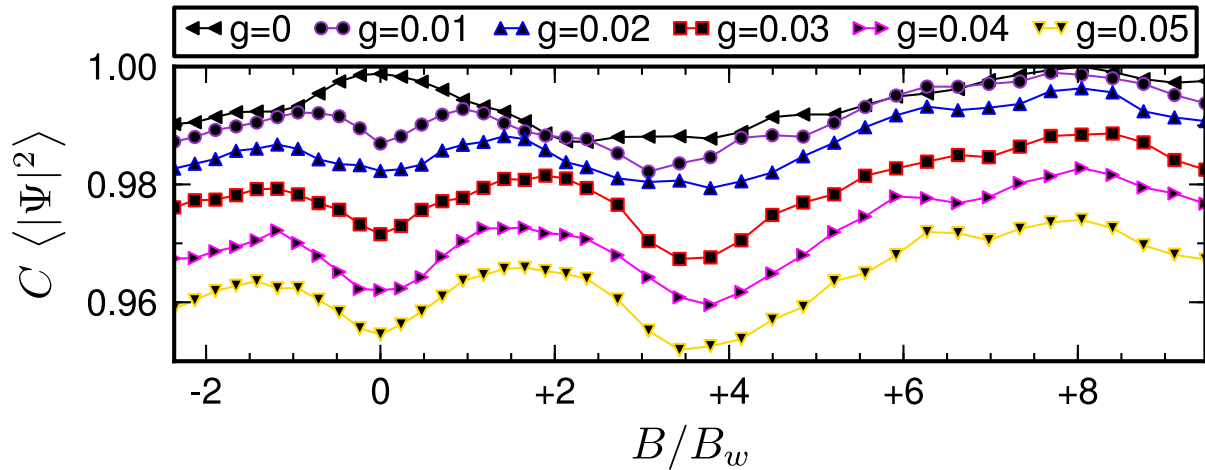


Figure 6.17: This figure shows the dependence of $\langle |\Psi(\mathbf{r})|^2 \rangle$ on the interaction strength g and the magnetic field B . The constant C is chosen to normalize the ordinate to one.

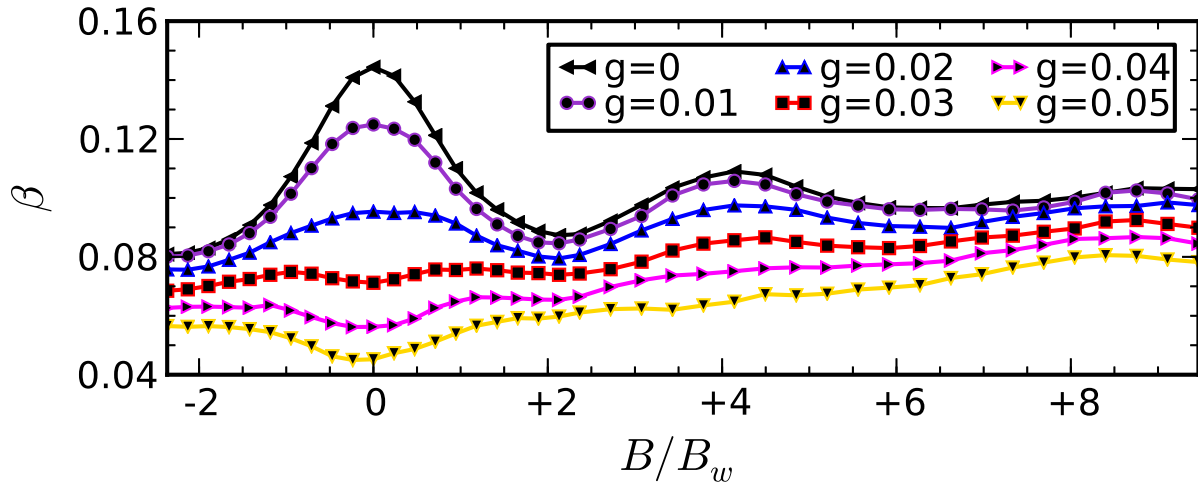


Figure 6.18: This figure shows how the parameter β behaves for larger magnetic fields.

by considering the non-linear interaction term $g(\mathbf{r})\hbar^2|\Psi(\mathbf{r})|^2/m$ as a repulsive static potential which repels particles. This effect might also influence the parameter β ; especially since the numerical data, on which the fitting procedure to determine β is applied, depends exponentially on $\langle |\Psi(\mathbf{r})|^2 \rangle$ (see Fig. 6.15).

- It is possible that a full diagrammatic theory for β , as it was developed in Sec. 6.1.2, is capable of explaining the downshift in both β and $\langle |\Psi(\mathbf{r})|^2 \rangle$. This theory would involve non-linear ladder-type diagrams for expectation values of higher moments of the local intensity. Similar to the analysis of universal conductance fluctuations, higher order loop contributions with two or more crossings would play a role here. But since such a theory is lacking, one can only speculate about this.

As shown in Fig. 6.18, in the linear case $g = 0$ the parameter β shows some weak Aharonov-Bohm oscillations for larger magnetic fields B . These oscillations are destroyed for large values of the interaction strength g . This is analogous to the discussion for the self-reflection R_s in Sec. 6.1.4 (see Fig. 6.11).

6.3 Other geometries

In this section we study the weak localization effect and intensity distribution for other billiard systems. All systems are wide open and have no kind of barrier inside the leads. The potential vanishes completely (except of course for the hard wall boundaries). While all investigated billiards have roughly the same size (which is limited by available computer power) they differ in shape. Of course, all shapes support chaotic classical dynamics. In some systems the lead width was varied, too.

The results for each system are summarized at two pages. The shape is illustrated by a scattering state and all system parameters are shown in a tabular. Each system has a geometric parameter which was varied in order to improve the statistical average. The number of different parameter values is denoted by “no. of geom. conf”. The details of the energy average vary with the lead width; “50 in $(0.93, 1.18)E_0$ ” denotes that the energy average is done over 50 equidistributed energies in the range $0.93E_0 \dots 1.18E_0$.

The plots for the transport properties (T , R_s) and intensity distribution (β) are built in the same way as in the previous sections. The gray arrows in the transmission plots for $B = 0$ mark the position at which the fraction of configurations with only unstable solutions reaches 0.02. This corresponds to the plot of the fraction of unstable parameter configurations.

6.3.1 B_9 : The clipped triangle

This cavity (Fig. 6.19 and Fig. 6.20) is a triangle which is clipped at one corner by a circle. The geometry is varied by changing the vertical position of the right lead. The fraction of unstable configurations grows faster than in B_5 , the fraction 0.02 is reached at $g = 0.03$. The numerical calculated transport properties are well described by the semiclassical prediction for zero magnetic field, but for large magnetic field there seems to be a small g -dependent shift. The transport T shows no clear peak structure for large interaction strengths g as it was the case for B_5 . The intensity distribution parameter for B_9 shows the same behaviour as for B_5 .

Overall one can say that for B_9 the agreement between numerical results and semiclassical prediction is quite good.

6.3.2 B_{10} : The stomach billiard

This cavity (Fig. 6.21 and Fig. 6.22) is a half-circle with two obstacles. For geometric variation we move the lower obstacle to the left and to the right. This lower obstacle prevents direct paths from the left to the right lead which would disturb the semiclassical analysis.

For historical reasons the intensity distribution is only done for 4 geometric configurations compared to the transport properties which use 11 configurations. This might explain the fact that the numerical obtained intensity distribution parameter β looks like it has a magnetic field dependent tilt. The numerical obtained absolute amplitude of β does also not fit the semiclassical prediction very well. It is possible that the agreement between numerics and semiclassics would improve with a more comprehensive geometrical average.

In the non-interacting case it looks like the amplitude of the Lorentz peak (dip) in reflection (transmission) is reduced in comparison to the semiclassical prediction. This is probably due to non-universal short paths. The corrections due to the non-linear interactions are well described by the semiclassical theory.

6.3.3 \mathcal{B}_{11} : The half circle (narrow leads)

This cavity (Fig. 6.23 and Fig. 6.24) consists of a half-circle with one obstacle. This obstacle is moved around for the geometrical average. Direct paths from the left to the right lead are prevented by shifting the right lead downwards. The lead openings are rounded to minimize diffraction effects.

The leads are quite narrow and have only $N = 4$ modes open. This explains why the fraction of unstable configurations raises very rapidly. The fraction 0.02 is reached at $g = 0.018$.

In the non-interacting case it looks like this system has a preference for reflection as the numerical reflection (transmission) is enhanced (reduced) in comparison with the semiclassical prediction. This is probably due to paths coming straight out of the left lead, hitting the right wall and going back to the left lead. The corrections due to the non-linear interactions seem to be well described by the semiclassical theory.

The intensity distribution parameter β is qualitatively well described by the semiclassical theory, except for the overall shift in g and a small magnetic field dependent tilt.

6.3.4 \mathcal{B}_{12} : The half circle (wide leads)

This cavity (Fig. 6.25 and Fig. 6.26) has the same shape as \mathcal{B}_{11} (Sec. 6.3.3) except that the leads are wider. There are $N = 6$ lead modes open and thus the fraction of unstable configurations raises much more slowly than in \mathcal{B}_{11} . The fraction 0.02 is reached at $g = 0.047$.

In the non-interacting case we see a preference for reflection as in \mathcal{B}_{11} . Qualitatively the semiclassical describes the numerics well, but quantitatively not. One also has to take the quite low number (i.e. 5) of geometric configurations used here into consideration. This leads to large statistical errors which might be in part responsible for the discrepancies.

6.3.5 \mathcal{B}_{13} : The limaçon (narrow leads)

This cavity (Fig. 6.27 and Fig. 6.28) is a wide open limaçon (see also Sec. 5.8.1) with two leads attached to the left. The vertical position of both leads can be varied for the geometrical average. Particles are injected into the upper lead.

The number of unstable configurations rises quite fast for a system with $N = 5$ open leads; the fraction 0.02 is reached at $g = 0.029$.

In the non-interacting case it looks like this system has a preference for transmission as the numerical transmission (reflection) is reduced (enhanced) in comparison with the semiclassical prediction. This is probably due to paths coming straight out of the upper left lead, hitting the right wall and going into the lower left lead. The corrections due to the non-linear interactions are qualitatively described by the semiclassical theory, albeit the statistical error is quite large because the geometric average is only performed over 4 configurations. The statistical error hampers also the numerical values for the intensity distribution parameter β .

6.3.6 \mathcal{B}_{14} : The limaçon (wide leads)

This cavity (Fig. 6.29 and Fig. 6.30) has the same shape as \mathcal{B}_{13} (Sec. 6.3.5) except that the leads are wider. There are $N = 6$ lead modes open and thus the fraction of unstable configurations raises more slowly than in \mathcal{B}_{13} . The fraction 0.02 is reached at $g = 0.047$.

In the non-interacting case again a preference for transmission is seen as in \mathcal{B}_{13} . The corrections induced by the non-linearity for R_s fit the semiclassical prediction better than the corresponding corrections for T . The reason might be that the statistical error of R_s is a priori smaller than the statistical error of T ; and therefore the discrepancies might be due to insufficient averaging.

The agreement between numerics and semiclassics for the intensity distribution parameter β is quite nice, apart from the g dependent shift.

par.	value	description
$\sqrt{\Omega}$	$27.0 \pi k_0^{-1}$	
N	5	no. of lead modes
W	$5.4 \pi k_0^{-1}$	lead width
Δx	$0.081 \pi k_0^{-1}$	lattice spacing
n	136569	lattice dimension
τ_D	$320.8 j_{\text{in}}^{-1} = 0.96 \tau_{D,u}$	classical dwell time
B_w	$0.463 B_0$	
	13	no. of geom. conf.
	50 in $(0.93, 1.18) E_0$	energy average

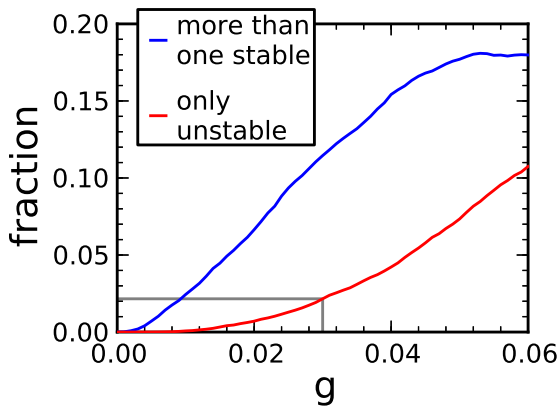
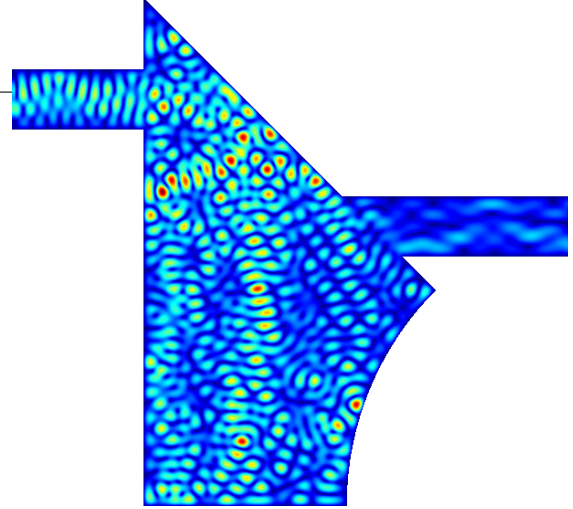
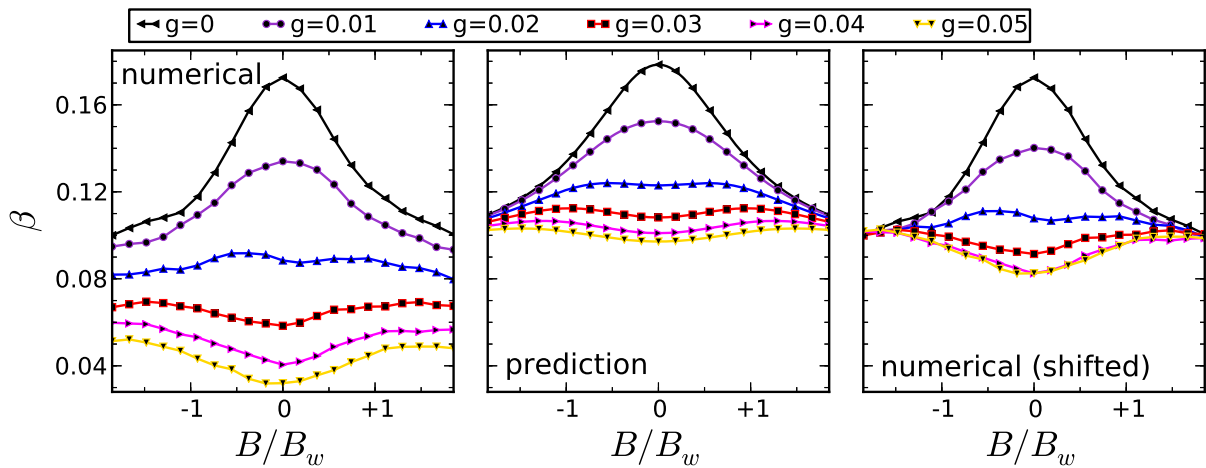
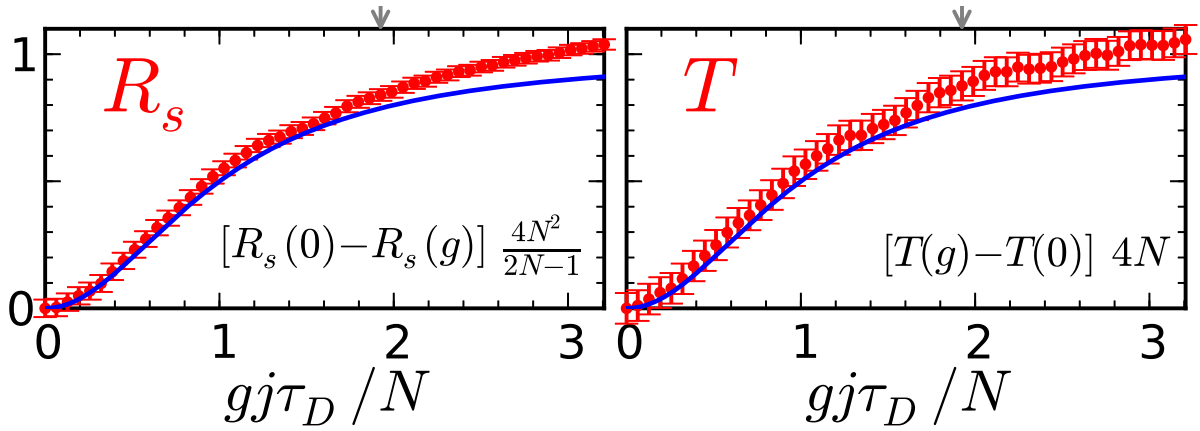


Figure 6.19: The upper part of this page shows the system \mathcal{B}_9 (see Sec. 6.3.1) and the corresponding parameters. The left figure shows the fraction of unstable configurations. The lower figure shows the transport properties for $B = 0$ while the lowest figure shows the intensity distribution parameter β .



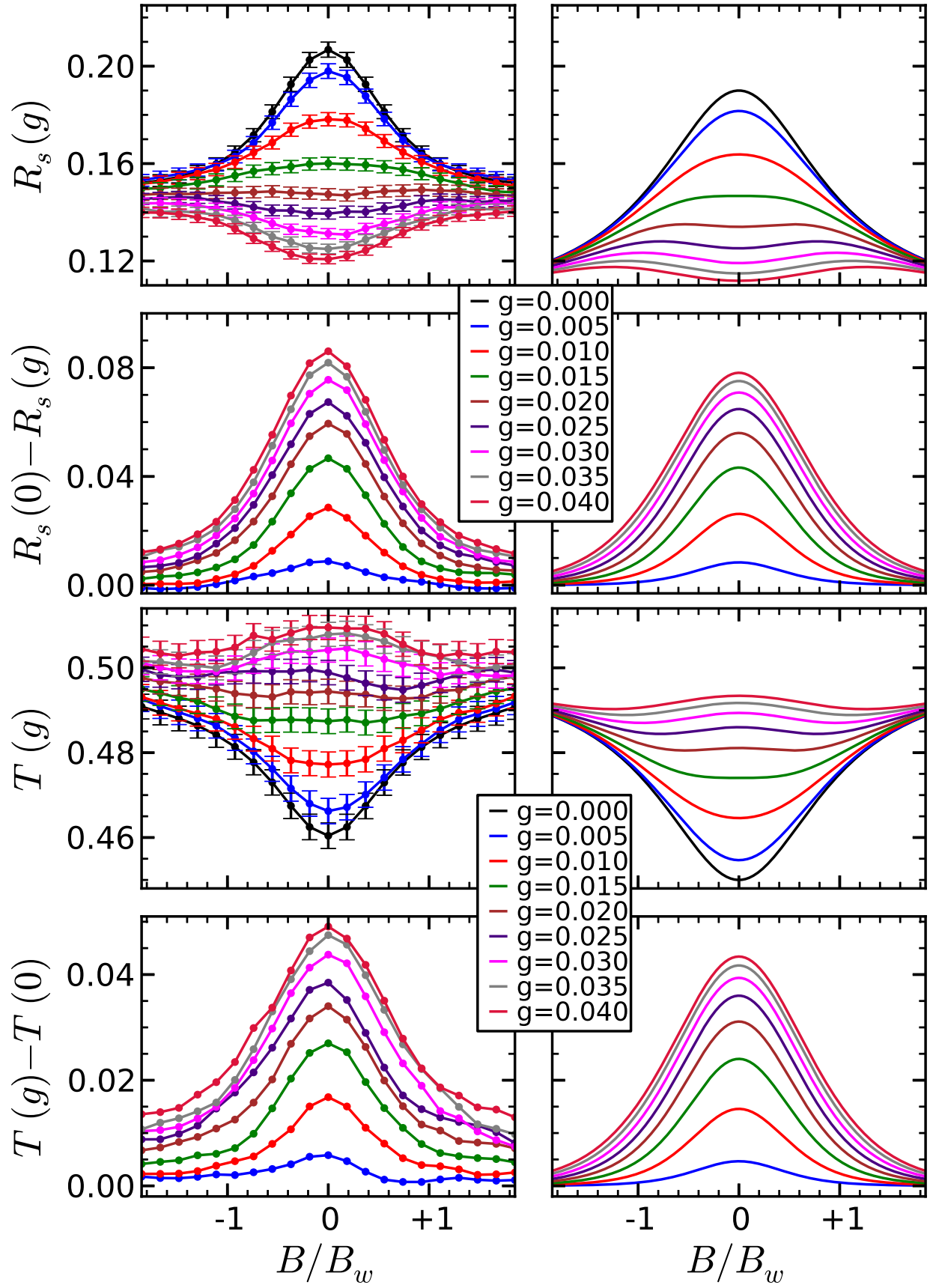


Figure 6.20: This figure shows the transport properties of \mathcal{B}_9 (see Sec. 6.3.1 and Fig. 6.19).

par.	value	description
$\sqrt{\Omega}$	$26.3 \pi k_0^{-1}$	
N	5	no. of lead modes
W	$5.4 \pi k_0^{-1}$	lead width
Δx	$0.081 \pi k_0^{-1}$	lattice spacing
n	114851	lattice dimension
τ_D	$266.7 j_{\text{in}}^{-1} = 0.84 \tau_{D,u}$	classical dwell time
B_w	$0.844 B_0$	
	11 (only 4 for β)	no. of geom. conf.
	50 in $(0.93, 1.18) E_0$	energy average

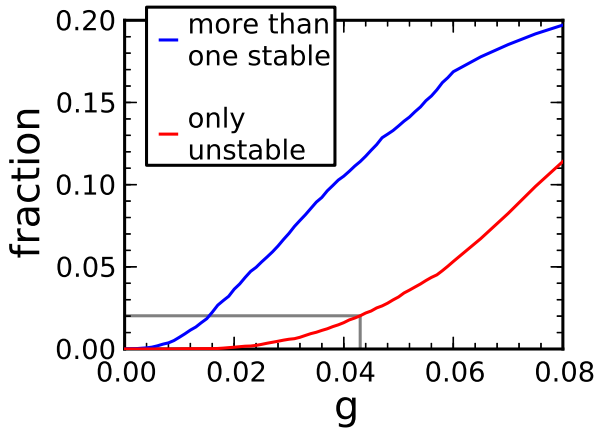
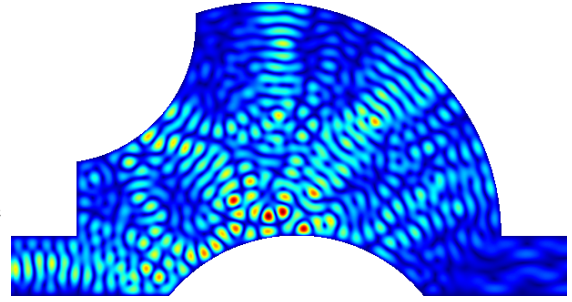
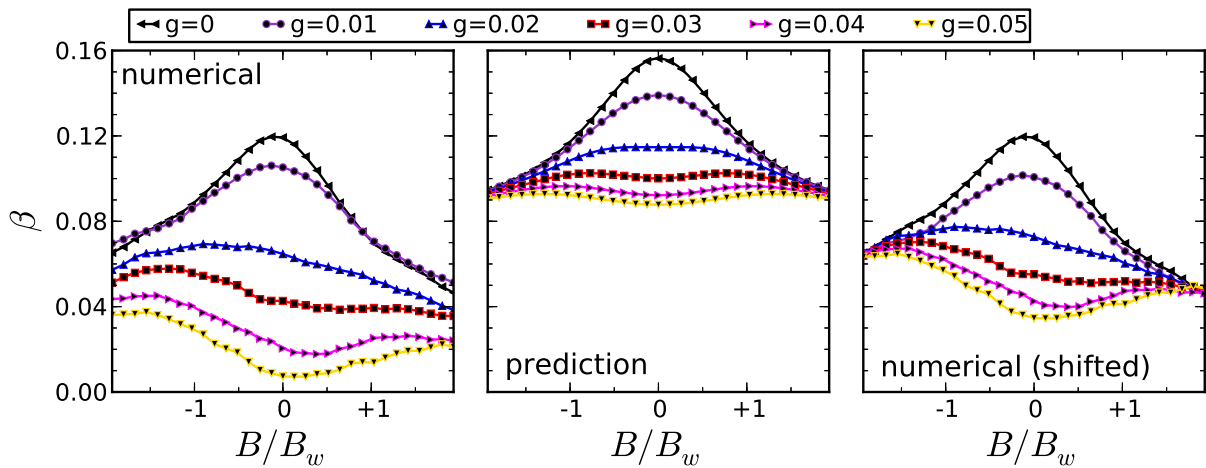
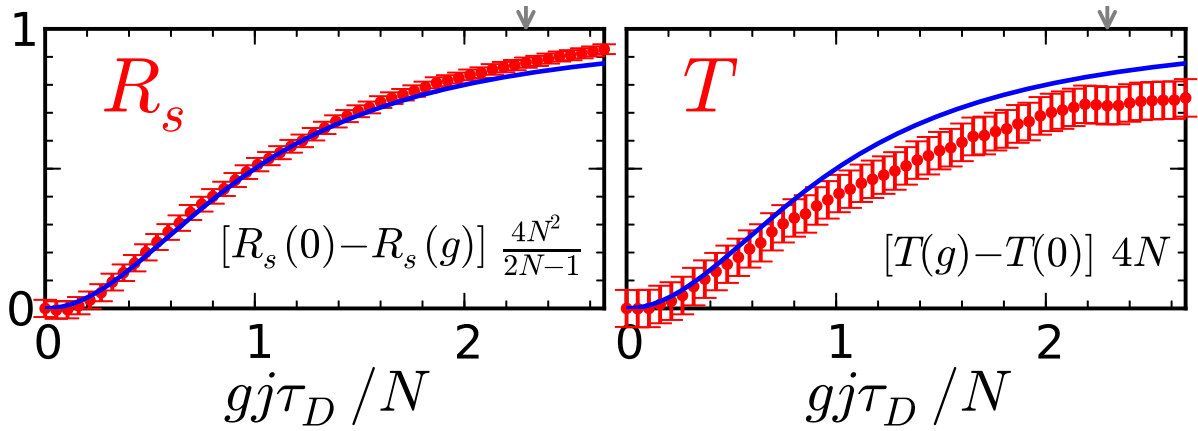


Figure 6.21: The upper part of this page shows the system \mathcal{B}_{10} (see Sec. 6.3.2) and the corresponding parameters. The left figure shows the fraction of unstable configurations. The lower figure shows the transport properties for $B = 0$ while the lowest figure shows the intensity distribution parameter β .



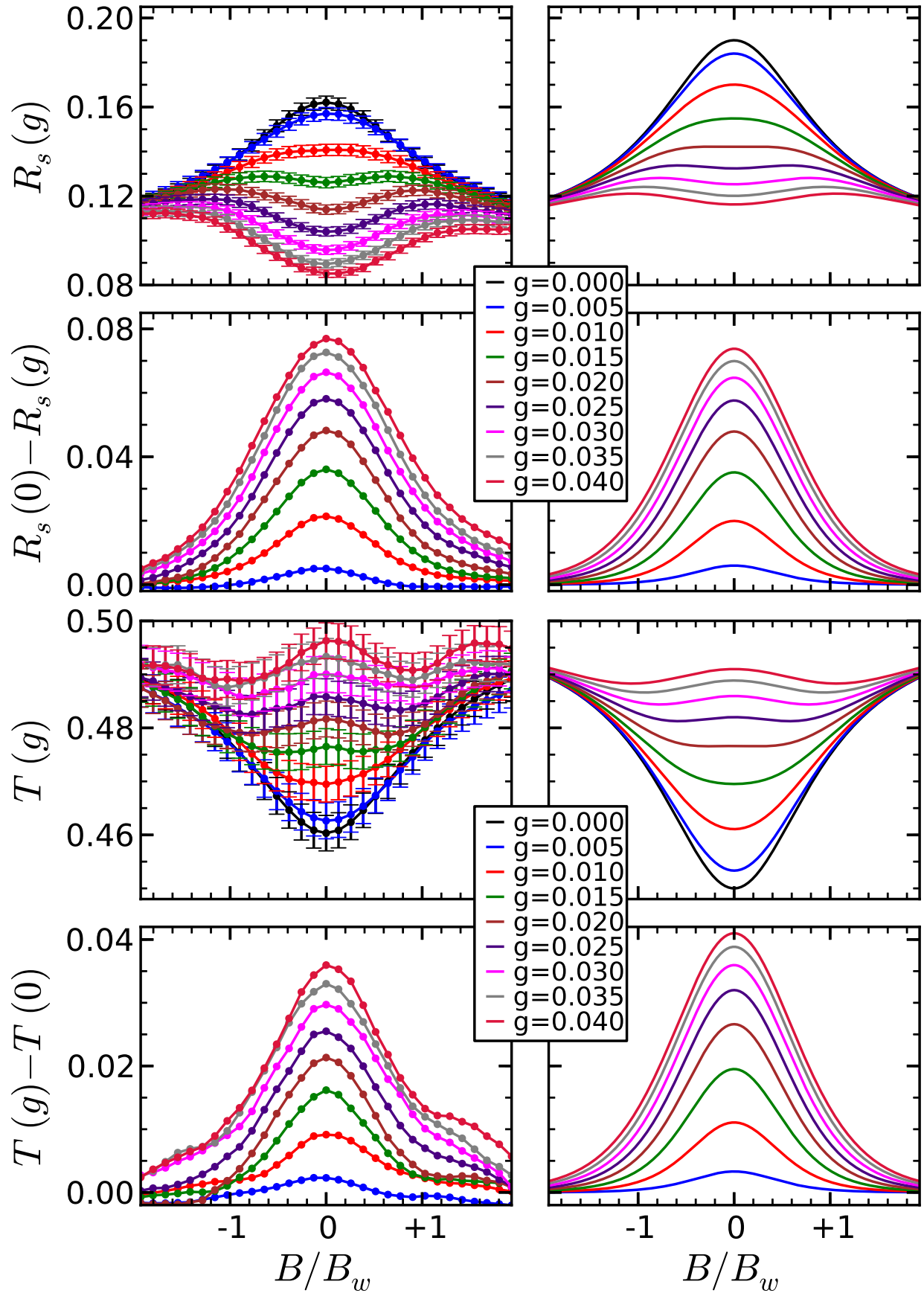


Figure 6.22: This figure shows the transport properties of B_{10} (see Sec. 6.3.2 and Fig. 6.21).

par.	value	description
$\sqrt{\Omega}$	$26.1 \pi k_0^{-1}$	
N	4	no. of lead modes
W	$4.5 \pi k_0^{-1}$	lead width
Δx	$0.081 \pi k_0^{-1}$	lattice spacing
n	113059	lattice dimension
τ_D	$352.4 j_{\text{in}}^{-1} = 0.94 \tau_{D,u}$	classical dwell time
B_w	$0.486 B_0$	
	21	no. of geom. conf.
	50 in $(0.9, 1.14) E_0$	energy average

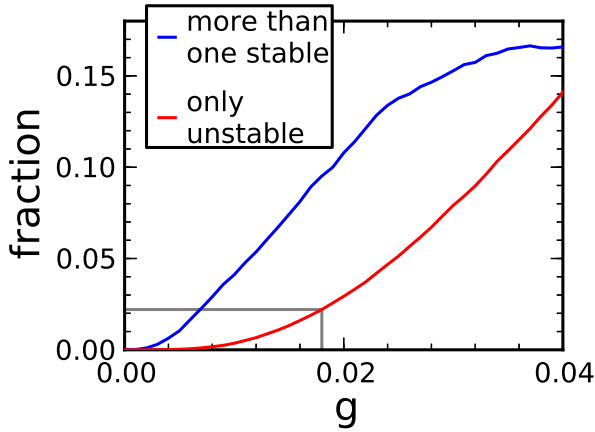
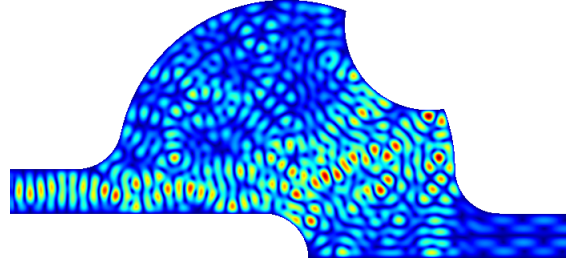
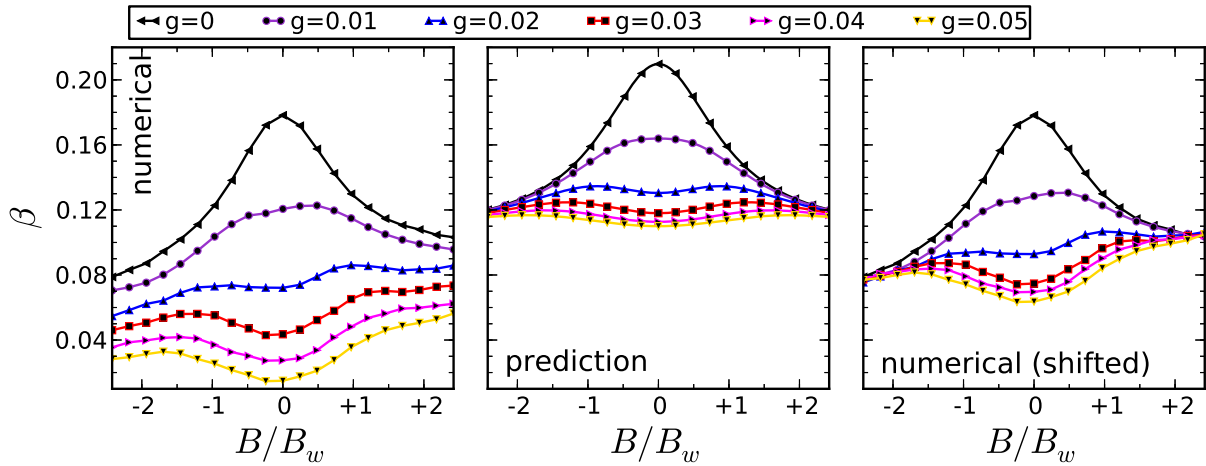
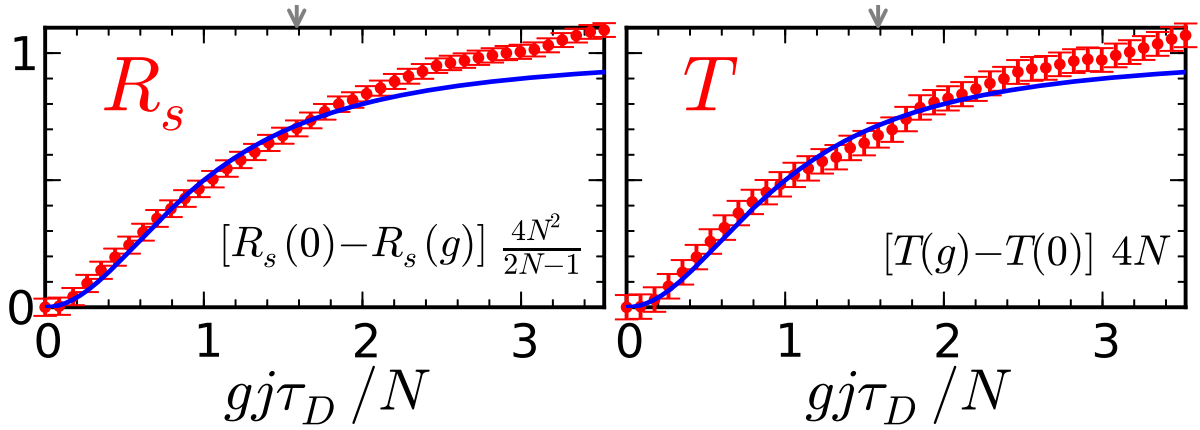


Figure 6.23: The upper part of this page shows the system \mathcal{B}_{11} (see Sec. 6.3.3) and the corresponding parameters. The left figure shows the fraction of unstable configurations. The lower figure shows the transport properties for $B = 0$ while the lowest figure shows the intensity distribution parameter β .



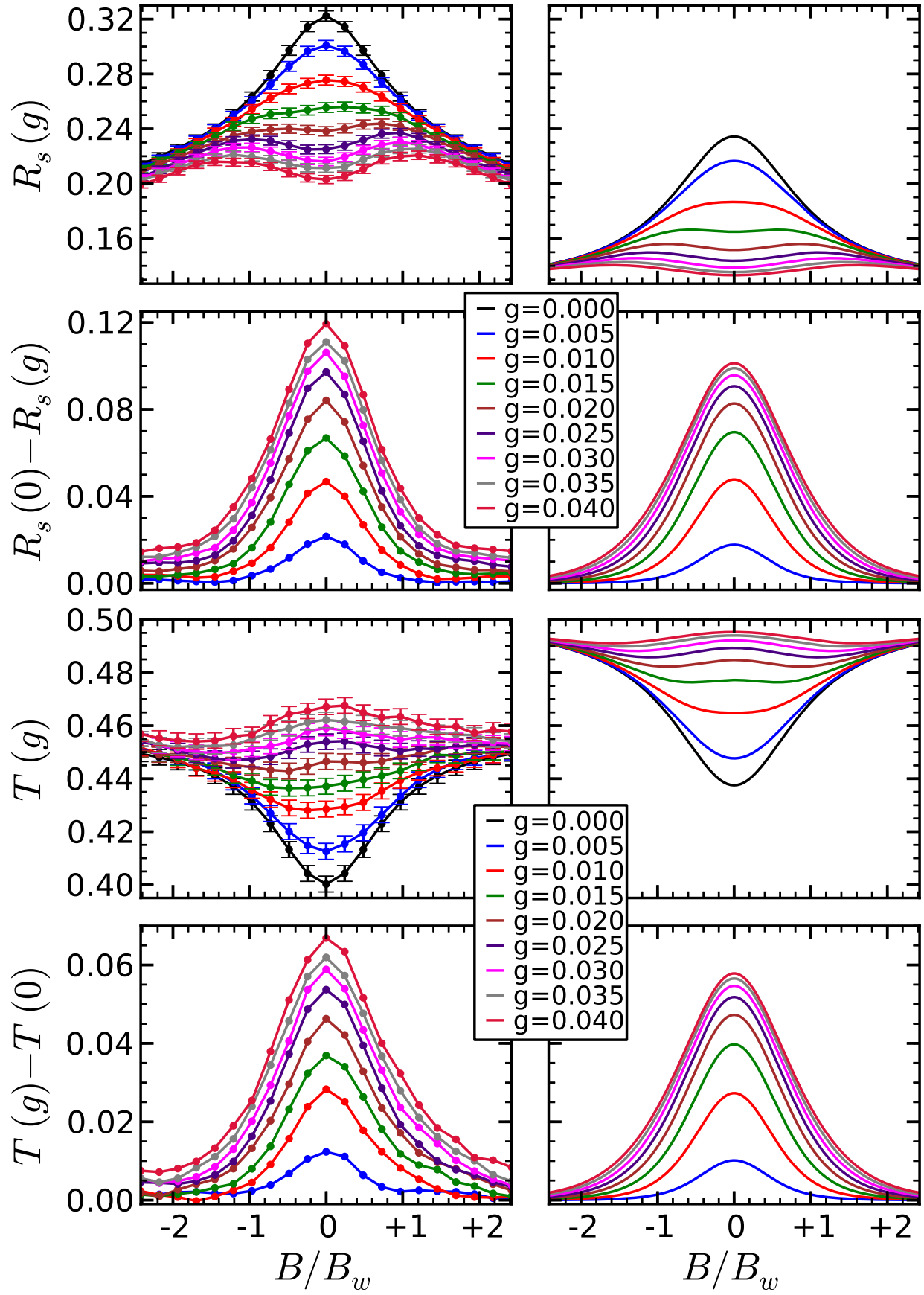


Figure 6.24: This figure shows the transport properties of \mathcal{B}_{11} (see Sec. 6.3.3 and Fig. 6.23).

par.	value	description
$\sqrt{\Omega}$	$28.4 \pi k_0^{-1}$	
N	6	no. of lead modes
W	$6.3 \pi k_0^{-1}$	lead width
Δx	$0.081 \pi k_0^{-1}$	lattice spacing
n	136326	lattice dimension
τ_D	$287.9 j_{\text{in}}^{-1} = 0.91 \tau_{D,u}$	classical dwell time
B_w	$0.497 B_0$	
	5	no. of geom. conf.
	50 in $(0.96, 1.17) E_0$	energy average

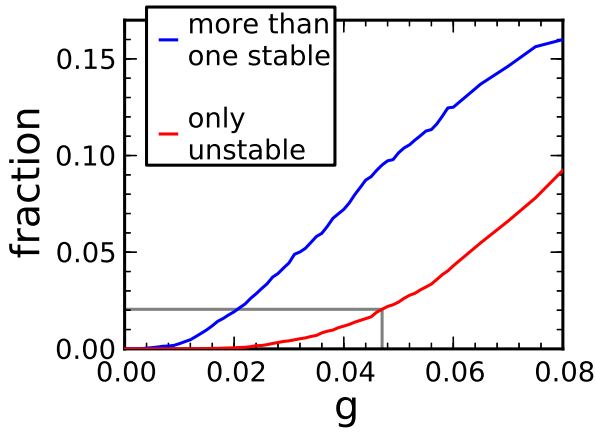
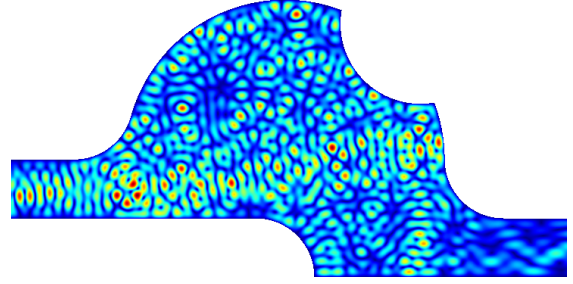
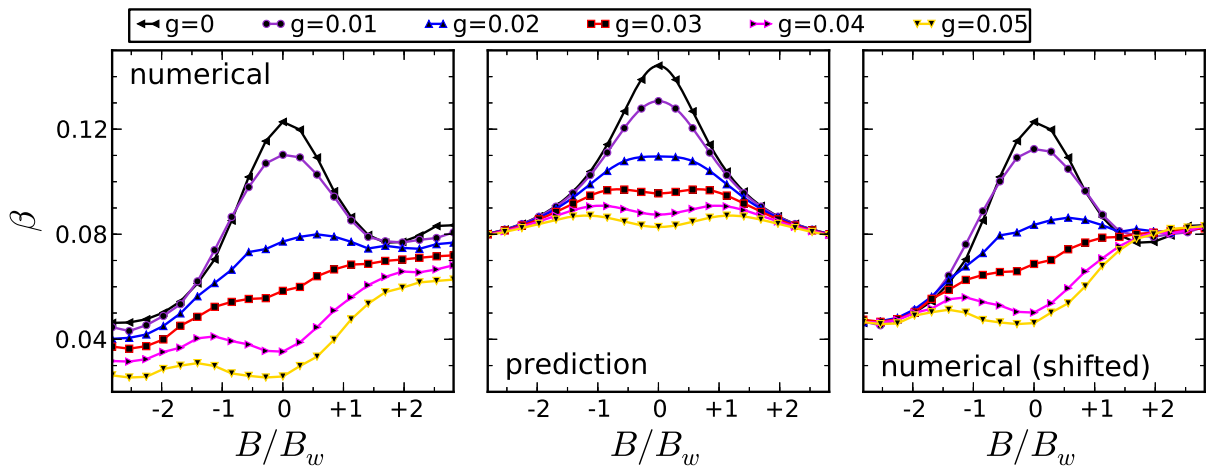
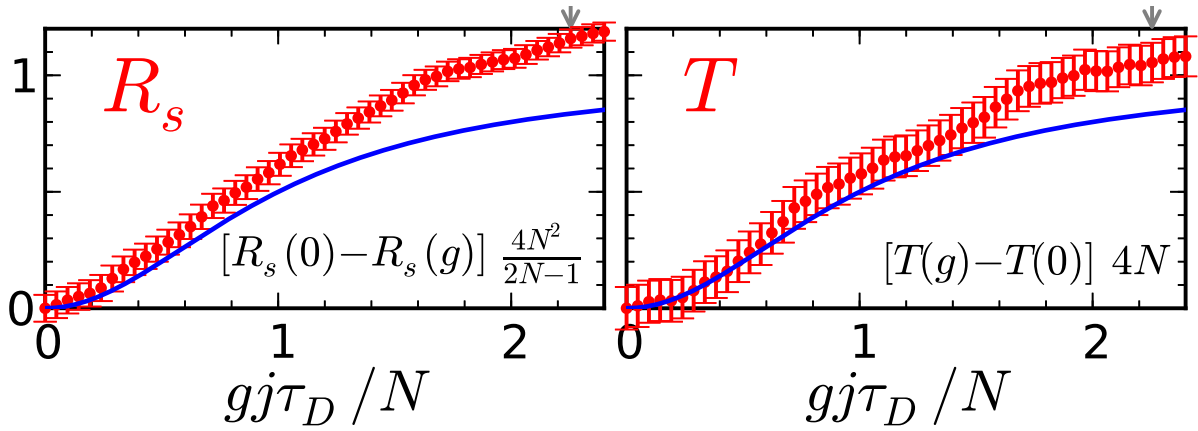


Figure 6.25: The upper part of this page shows the system \mathcal{B}_{12} (see Sec. 6.3.4) and the corresponding parameters. The left figure shows the fraction of unstable configurations. The lower figure shows the transport properties for $B = 0$ while the lowest figure shows the intensity distribution parameter β .



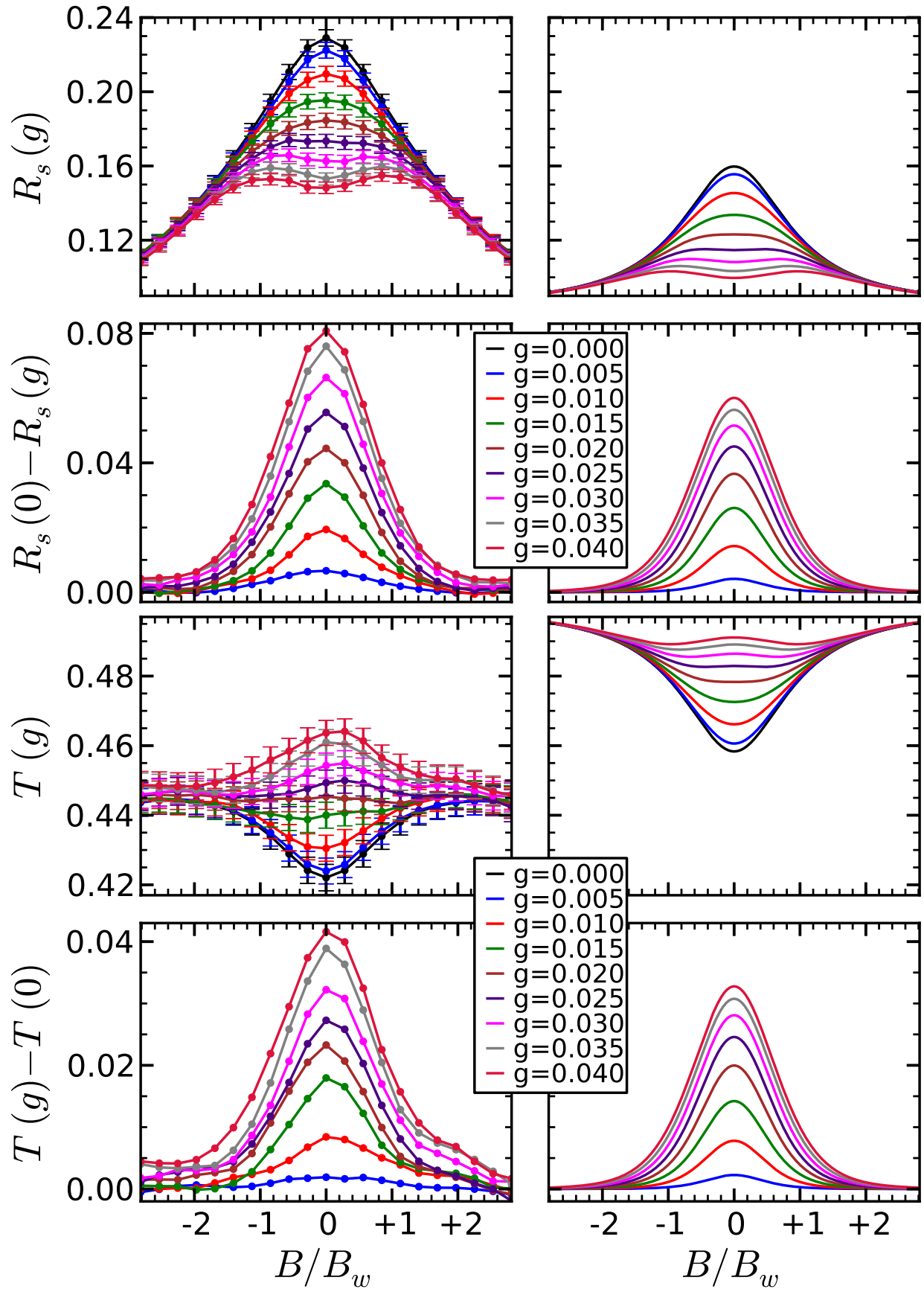


Figure 6.26: This figure shows the transport properties of B_{12} (see Sec. 6.3.4 and Fig. 6.25).

par.	value	description
$\sqrt{\Omega}$	$29.3 \pi k_0^{-1}$	
N	5	no. of lead modes
W	$5.4 \pi k_0^{-1}$	lead width
Δx	$0.081 \pi k_0^{-1}$	lattice spacing
n	152418	lattice dimension
τ_D	$351.4 j_{\text{in}}^{-1} = 0.9 \tau_{D,u}$	classical dwell time
B_w	$0.165 B_0$	
	4	no. of geom. conf.
	50 in $(0.93, 1.18) E_0$	energy average

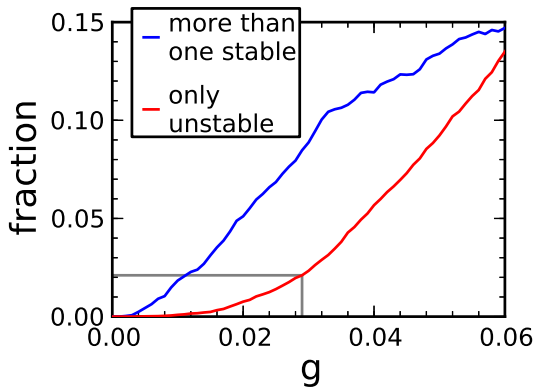
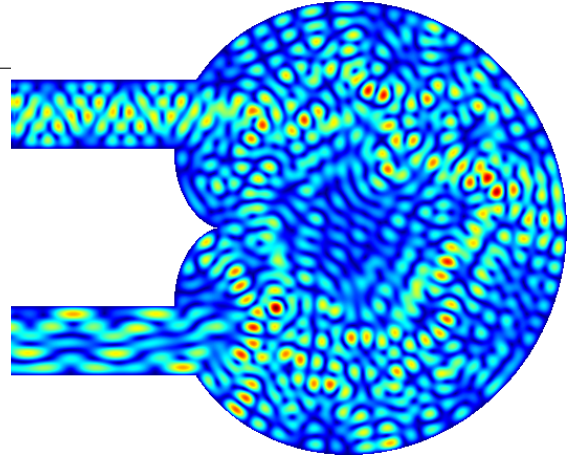
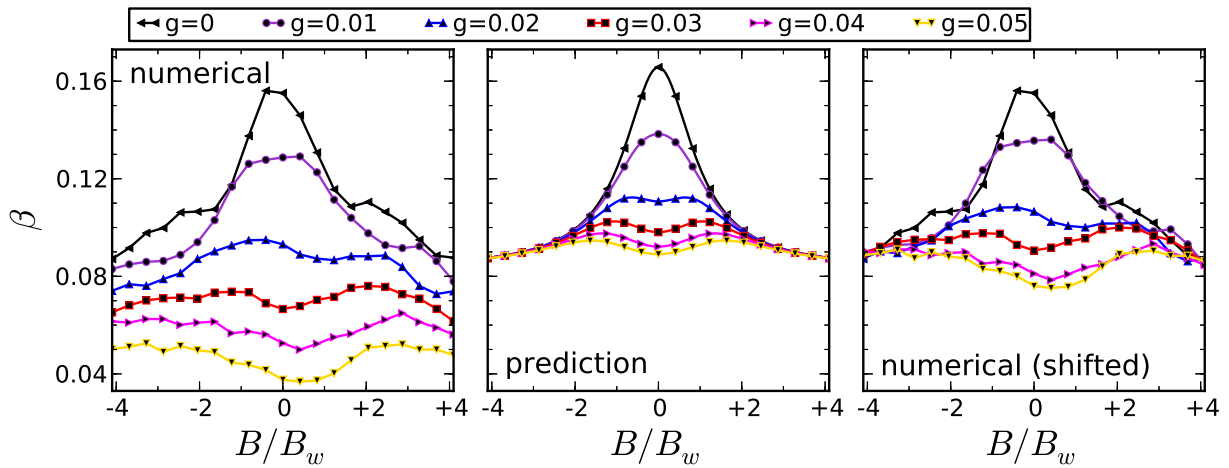
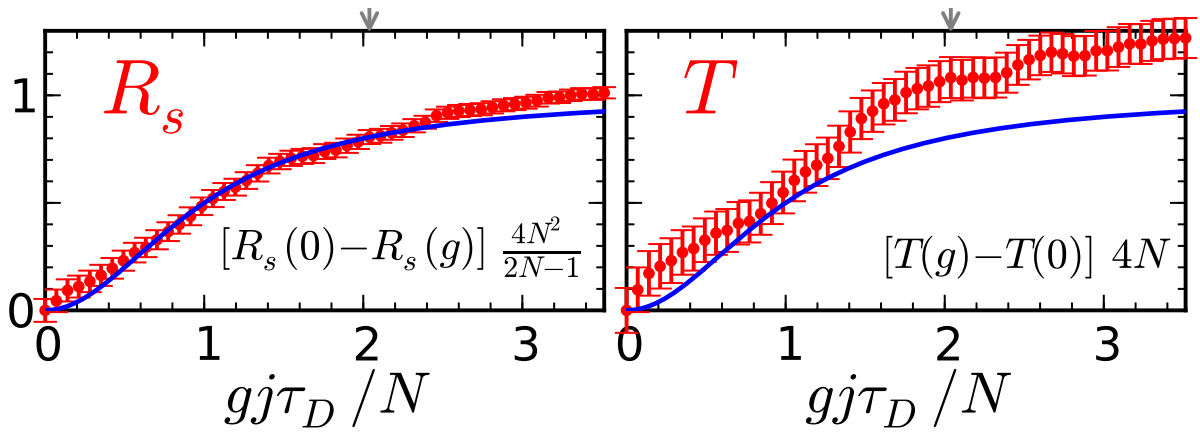


Figure 6.27: The upper part of this page shows the system \mathcal{B}_{13} (see Sec. 6.3.5) and the corresponding parameters. The left figure shows the fraction of unstable configurations. The lower figure shows the transport properties for $B = 0$ while the lowest figure shows the intensity distribution parameter β .



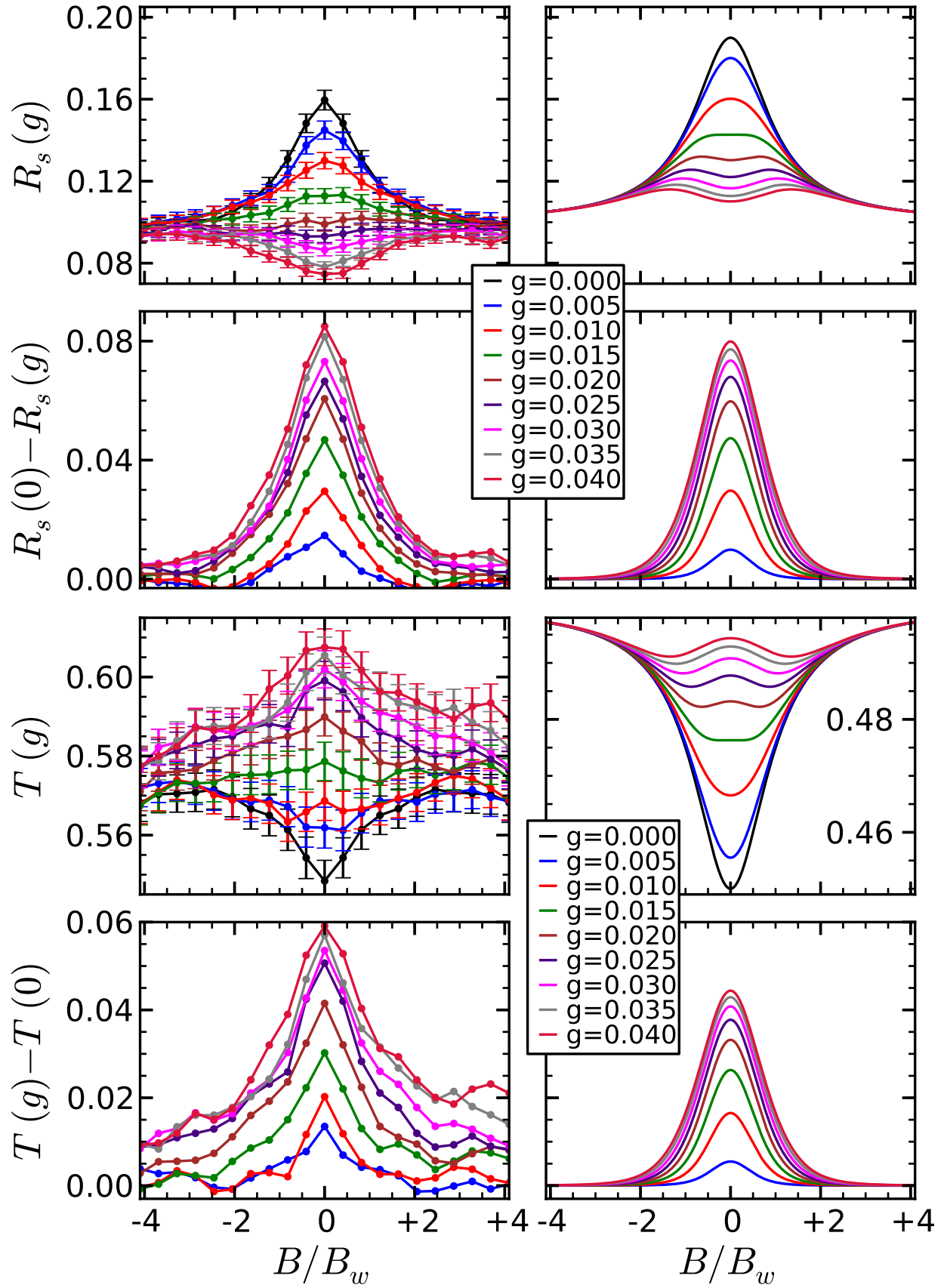


Figure 6.28: This figure shows the transport properties of B_{13} (see Sec. 6.3.5 and Fig. 6.27). Note the different ordinate ranges for T .

par.	value	description
$\sqrt{\Omega}$	$29.3 \pi k_0^{-1}$	
N	6	no. of lead modes
W	$6.3 \pi k_0^{-1}$	lead width
Δx	$0.081 \pi k_0^{-1}$	lattice spacing
n	156122	lattice dimension
τ_D	$296.4 j_{\text{in}}^{-1} = 0.88 \tau_{D,u}$	classical dwell time
B_w	$0.184 B_0$	
	17	no. of geom. conf.
	50 in $(0.99, 1.18) E_0$	energy average

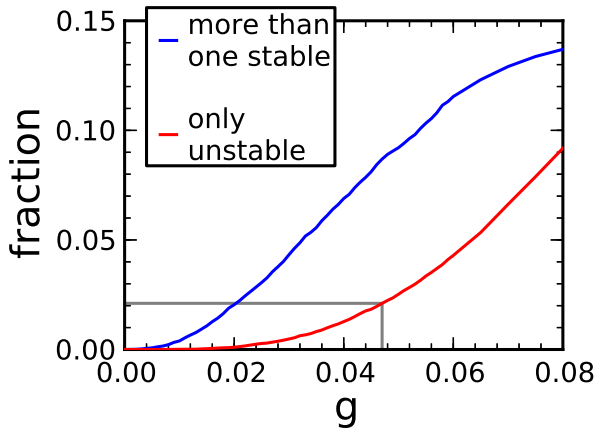
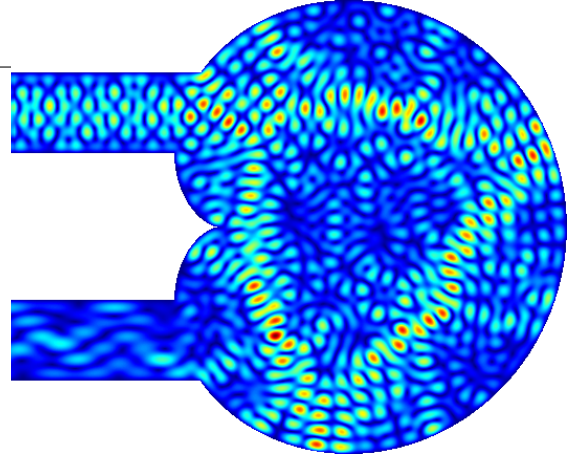
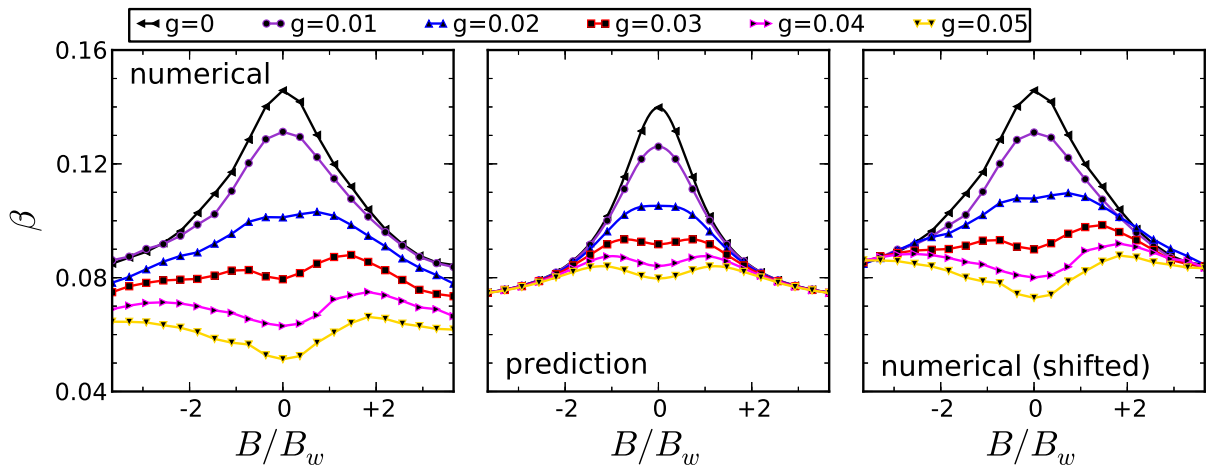
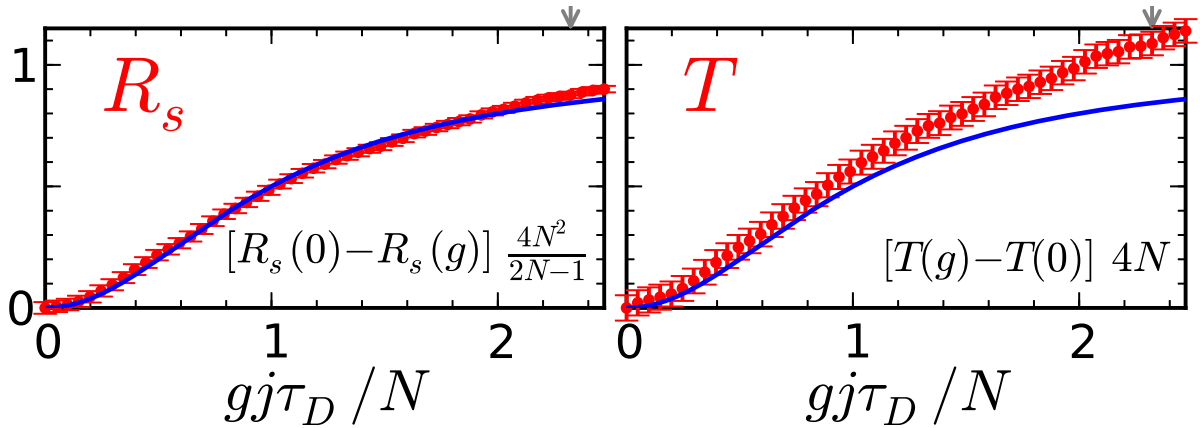


Figure 6.29: The upper part of this page shows the system \mathcal{B}_{14} (see Sec. 6.3.6) and the corresponding parameters. The left figure shows the fraction of unstable configurations. The lower figure shows the transport properties for $B = 0$ while the lowest figure shows the intensity distribution parameter β .



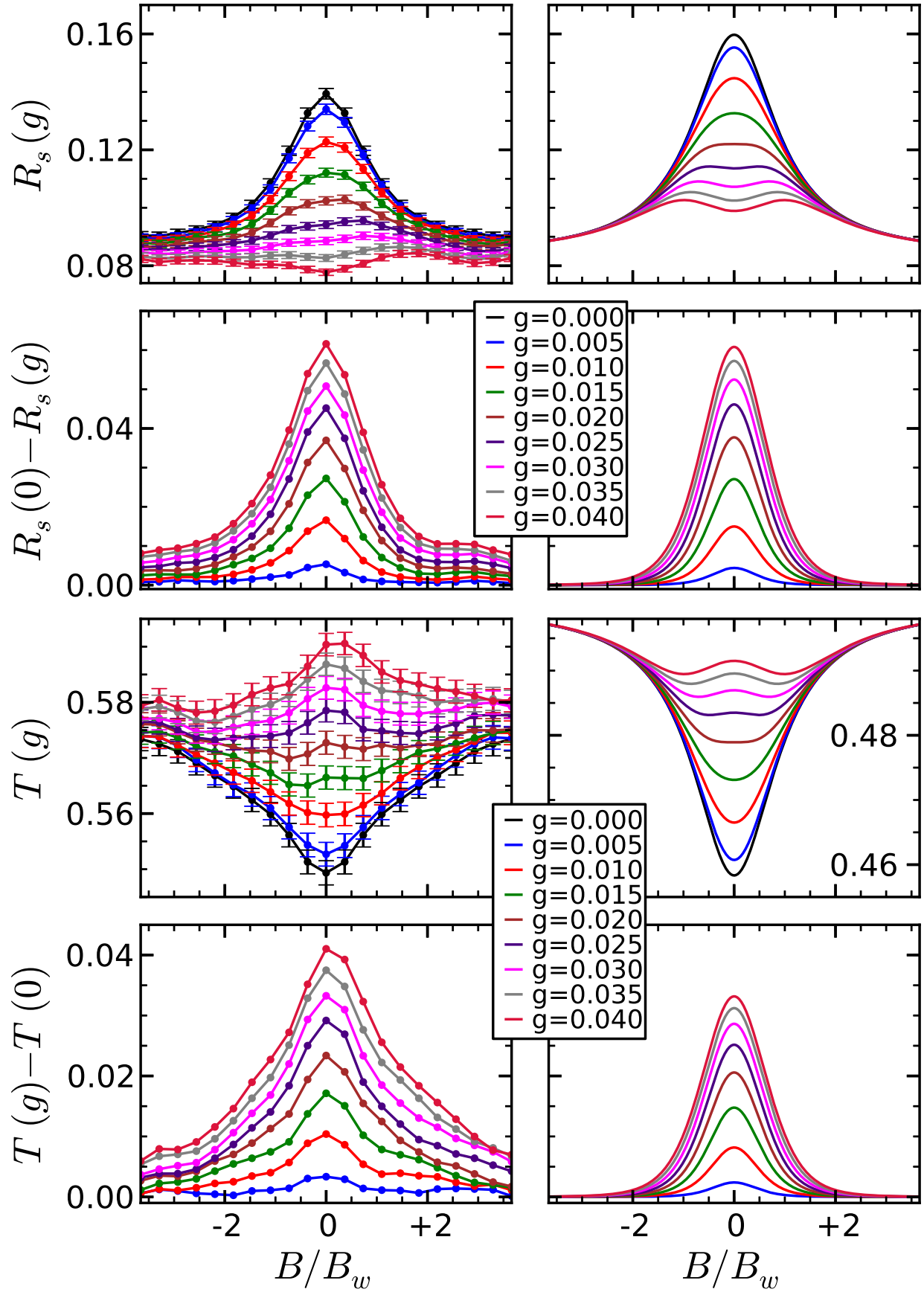


Figure 6.30: This figure shows the transport properties of B_{14} (see Sec. 6.3.6 and Fig. 6.29). Note the different ordinate ranges for T .

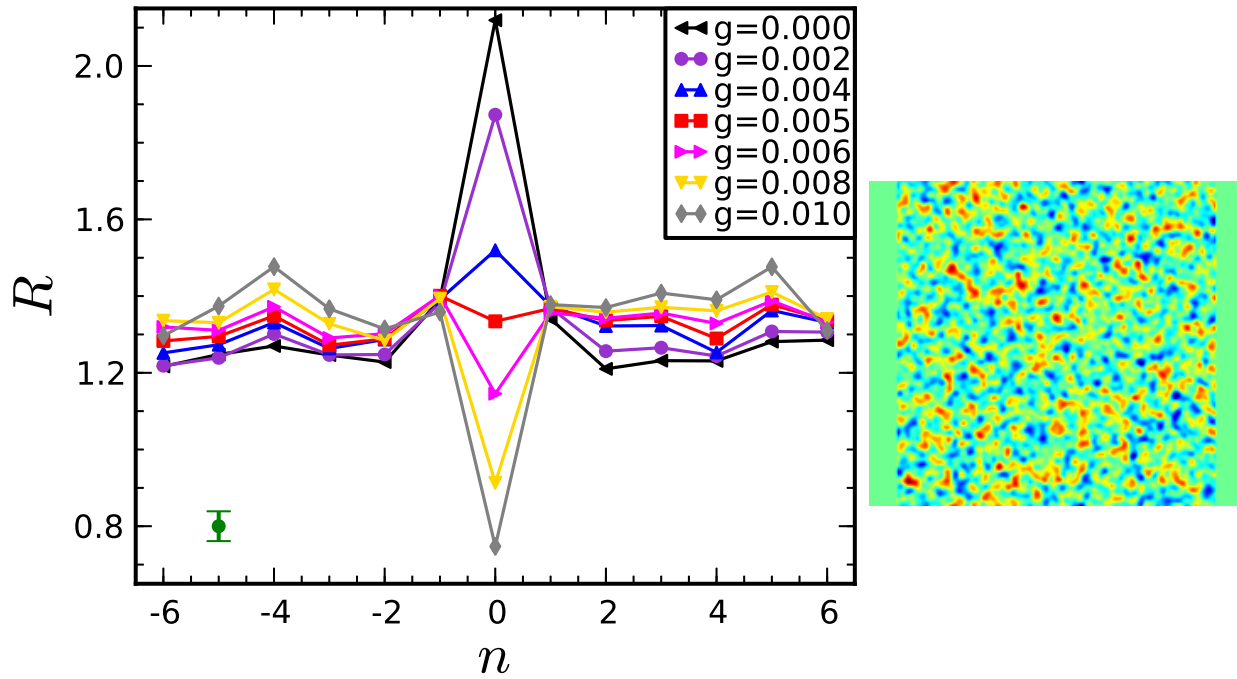


Figure 6.31: The left panel shows the mode resolved reflection for various values of g . The peak at $n = 0$ in the non-interacting case $g = 0$ is called the coherent backscattering effect. The normalization of R is chosen such that 1 corresponds to a scenario in which scattering into each mode both in transmission and reflection would be equal. The green point illustrates the size of the typical statistical error. The right panel shows a typical realization of the disordered potential.

6.4 Related effects in mesoscopic systems

6.4.1 Coherent backscattering in disordered potentials

In the previous sections we have studied the weak localization effect in classical chaotic cavities. These are *ballistic* systems, so called because the classical trajectories follow straight lines between bounces at the boundaries because of the flat potential $V = 0$.

But a related effect, also called weak localization, can be studied in *diffusive* systems [3, 190]. Instead of flat potentials (with hard walls) one uses disordered potentials $V(\mathbf{r})$

for these kind of systems. The energy (and geometric) average is replaced by an average over different realizations of $V(\mathbf{r})$. A manifestation of weak localization in diffusive systems is the coherent backscattering effect on which we will focus now.

While the works [98, 99]¹⁸ investigated coherent backscattering using time-dependent propagation methods, we now reproduce these results using non-linear stationary scattering states as explained in Chap. 5. This gives another confirmation that both methods give equivalent results. The numerical details are equivalent to those presented in Sec. 6.1.4.

We use a Gaussian correlated disordered potential

$$\begin{aligned} \langle V(\mathbf{r}) \rangle &= 0 \\ \langle V(\mathbf{r}) V(\mathbf{r}') \rangle &= V_0^2 \exp \left[-\frac{|\mathbf{r} - \mathbf{r}'|^2}{2\sigma^2} \right] \end{aligned} \quad (6.25)$$

¹⁸ The g used in these works is a factor of two larger than the g used here.

in a rectangular patch of dimension $W_x k_0 = W_y k_0 = 40$ (see Fig. 6.31). In the y -direction we are using periodic boundary conditions in order to simulate a disordered potential of infinite width but finite length. To the left and to the right of the disordered strip the potential is flat. The potential parameters are $V_0 = 0.614E_0$ and $\sigma k_0 = \frac{1}{2}$. This ensures that roughly half of the incident particles are transmitted and half are reflected and that the correlation length σ is smaller than the wave length. The average is taken over 1000 disorder realizations while the energy E_0 is kept constant.

We inject particles from the left. The source modes are the plane waves $\chi_n(y) = \exp[2\pi i n y / W_y]$. For our parameters the modes $n = -6 \cdots +6$ are open. In experiments n corresponds to an angle. The (total) incident current is chosen as $j_{\text{in}} = E_0 \hbar^{-1} W_y k_0$. This ensures that the current density is independent of W_y .

We only use the mode $n = 0$ to inject particles into the system. Then we measure the mode-resolved current in reflection. Fig. 6.31 shows the numerical results. In the linear case $g = 0$ the reflection into the incident mode $n = 0$ is enhanced by roughly a factor of two in comparison to all other modes $n \neq 0$ which all carry a similar current. This enhancement is called the coherent backscattering effect because it is caused by constructive interference between a scattering path and its time reversed counter-path inside the scattering region [3, 190]. This resembles the diagonal terms for the (self-)reflection in classical chaotic billiards (see Fig. 6.1).

For increasing interaction strength g the height of this peak at $n = 0$ gets reduced until it becomes a dip. Simultaneously the reflection in the other modes $n \neq 0$ is increased. For large g the dip is quite prominent in these diffusive systems while in ballistic billiards the dip vanishes in the background for $g \rightarrow \infty$.

6.4.2 Time-reversal mirrors in chaotic cavities

Chaotic billiard systems have the nice feature that one can implement a kind of time-reversal mirror with them [36, 74, 115]. Up to now this effect has only been investigated in the non-interacting case on which we will focus here. The study of the interacting case would be a nice extension of this work. This section reproduces the results of [36] using our numerical framework. The time propagation is done using the split-operator method introduced in Sec. 4.5.

The time-reversal mirror can be implemented by propagating a Gaussian wave packet inside a closed cavity. The value¹⁹ of the wave function $\Psi(\mathbf{r})$ is recorded at a single point $\mathbf{r} = \mathbf{r}_0$. After a certain time t_0 the cavity is emptied and we begin to inject particles using a source $S(\mathbf{r}) = S_0(t)\delta(\mathbf{r} - \mathbf{r}_0)$ centered at \mathbf{r}_0 into the system. The source amplitude $S_0(t)$ is modulated by the complex conjugated and time-reversed data we collected earlier. This information is enough to reconstruct the initial wavefunction after a time interval of length t_0 (see Fig. 6.32). This works only because the classical dynamics is chaotic. The semiclassical analysis of [36] gives a quantitative prediction of the revival. As we seen in Fig. 6.33 the agreement between numerics and semiclassics is quite good.

¹⁹ We need both amplitude and phase here. This is somewhat problematic for matter wave systems as experimentally the recording of the phase can only be accomplished by a measurement thus disrupting the time propagation. The experiment would have to be repeated from the start for each timestep. Better suited experimental systems use sound waves or microwaves. The time-reversal mirroring has already been experimentally realized using these systems. For microwaves non-linear media which are described by a non-linear Gross-Pitaevskii-like wave equation are available.

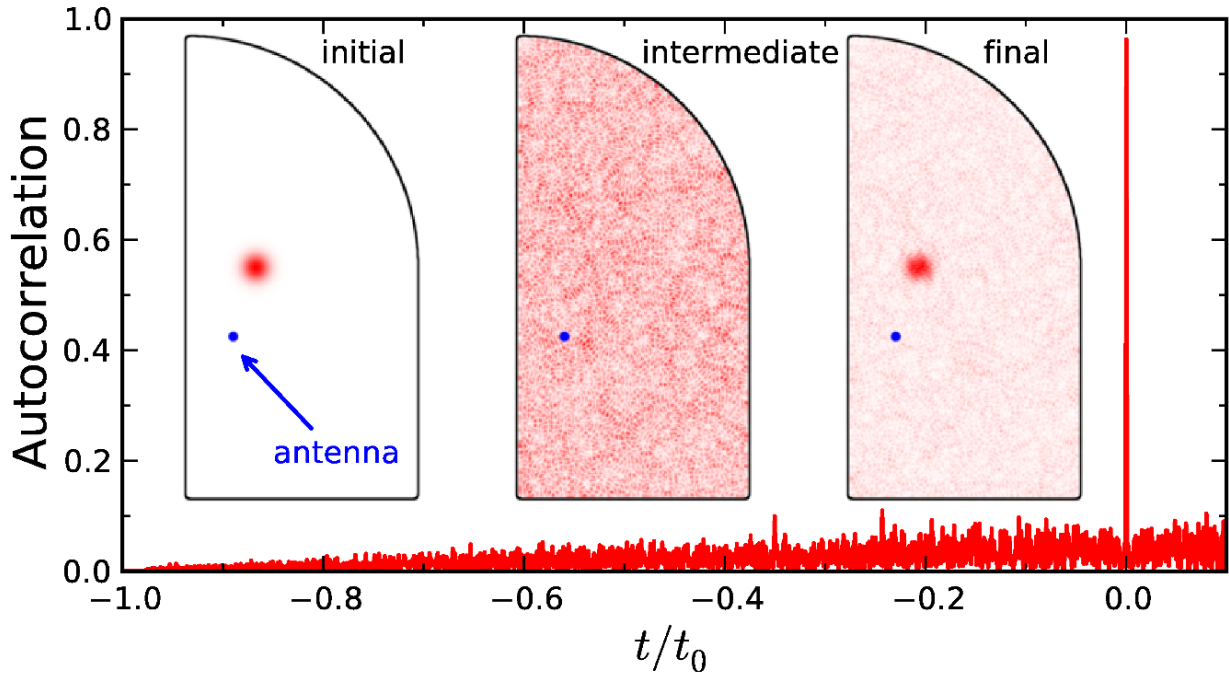


Figure 6.32: This figure illustrates the time-reversal mirroring. The *initial* wavepacket is propagated inside the cavity and the wavefunction is recorded using the *antenna* at \mathbf{r}_0 (blue point). Then the cavity is emptied and the time-reversed and complex-conjugated signal is fed into the system. At the *intermediate* time $t = -0.5t_0$ the wavefunction is completely spread out over the cavity. At the *final* time $t = 0$ the initial wavepacket is reconstructed. Also shown is the *autocorrelation* function.

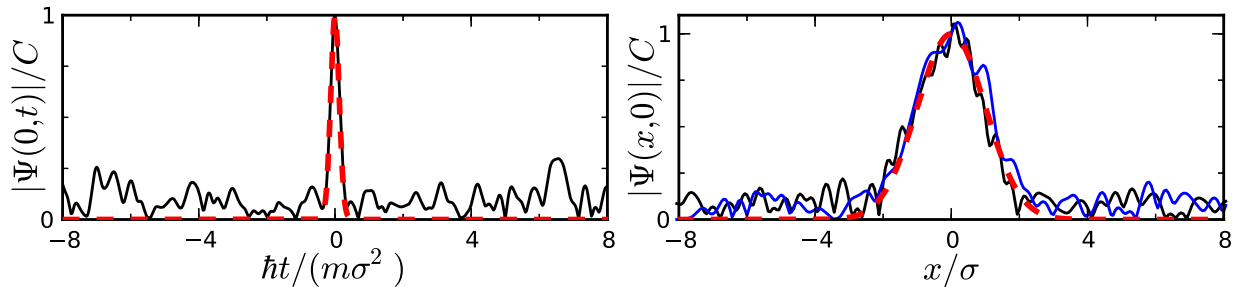


Figure 6.33: The left panel compares the numerical (black solid line) modulus of the wavefunction at the point $\mathbf{r}_0 = 0$ with the semiclassical prediction (red dashed line) in a small time interval around $t = 0$. The right panel compares for the fixed time $t = 0$ the modulus of the wavefunction along a section in horizontal (black solid line) and vertical (blue solid line) direction with the semiclassical prediction (red dashed line). The constant C is chosen so that the maximum value is one.

6.4.3 Half-period Aharonov-Bohm oscillations in disordered rings

An effect related to weak localization can be observed in one-dimensional ring systems with disorder potentials for vanishing interaction $g=0$ as investigated in Sec. 5.9. If we average the transmission over many disorder potentials, the period of the Aharonov-Bohm oscillations changes from 1 to $\frac{1}{2}$. This is a quantum interference effect²⁰ which can be explained using a diagrammatic

²⁰ In reflection a path circulating clockwise around the ring has to be paired with its time reversed counterpath circulating counterclockwise (because of the disorder average). This gives two times the phase due to a gauge field;

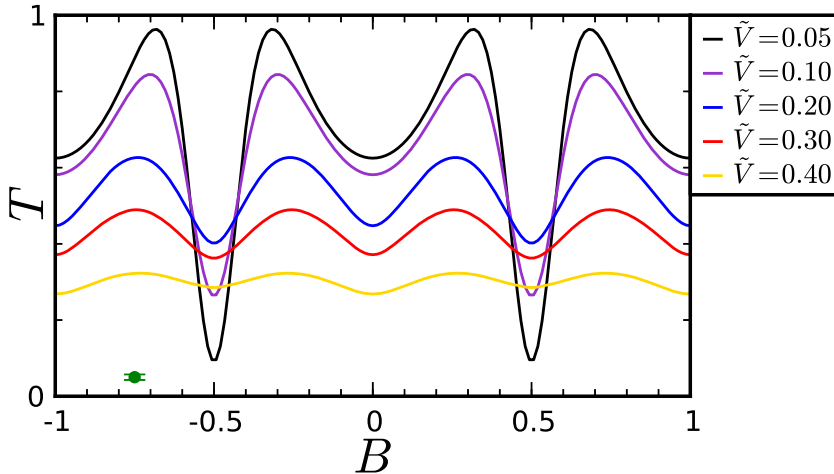


Figure 6.34: This figure shows how the frequency of the Aharonov-Bohm oscillations doubles with increasing strength \tilde{V} (measured in units of E_0) of the disorder potential. We assume a vanishing interaction $g=0$. The green point illustrates the statistical error bars. We use an arithmetic average here.

perturbation theory involving crossed diagrams [6, 59].

Fig. 6.34 illustrates this effect. We use a ring of circumference $L_0=45.02\pi k_0^{-1}$, lattice spacing $\Delta x=1/15\pi k_0^{-1}$, vanishing artificial confinement $\tilde{V}_c=0$ and a Gaussian correlated disorder potential with correlation length $\sigma=0.45\pi k_0^{-1}$ as described in Eq. (6.25). The statistical average is taken over 400 disorder realizations for one fixed chemical potential $\mu=E_0$.

For vanishing disorder $\tilde{V}=0$ the transmission is a periodic function of the magnetic field B with period 1. This is the normal Aharonov-Bohm effect. For increasing strength \tilde{V} of the disorder potential the transmission becomes a periodic function of the magnetic field B with period $\frac{1}{2}$. For very large values of \tilde{V} one has to use the geometrical average (not shown here) instead of arithmetical average (shown here) to study the effect.

The example presented here uses vanishing interaction $g=0$. I have also done numerical simulations for non-vanishing interaction strengths g . But no interesting effect was visible before the transmission became time-dependent for nearly every disorder realization. It would be a nice extension of this work to somehow stabilize the transmission through the rings for non-vanishing interaction g . Perhaps one has to switch the interaction g gradually off outside the ring or one has to use a finite width for the ring.

6.5 Summary and outlook

In this chapter we have studied the weak localization effect numerically and analytically for several different billiard systems with classical chaotic dynamics. The numerical investigation used stationary scattering states of the Gross-Pitaevskii equation as described in the previous chapters while the analytical study used semiclassical tools. The semiclassical analysis showed that the weak localization effect exhibits universal behaviour, i.e. the results do not depend at the specific details of potential and the shape of the cavity. For vanishing interaction strength $g=0$, the weak localization effect (in reflection) manifests itself as a Lorentzian peak structure as function of the magnetic field on top of a constant background. For finite values of the interaction strength g , the height of the peak gets reduced. This reduction is more effective in the middle than at the flanks such that a double peak structure with a dip in the middle emerges. The numerical results agree qualitatively very well with this semiclassical prediction, but quantitatively there are some devi-

hence period $\frac{1}{2}$. Without the disorder average the two paths do not need to form a time reversed pair; the length difference between the two paths may assume any integer multiple of the circumference; hence period 1.

ations. Especially the amplitudes of the background and the peak do not always agree with the universal semiclassical prediction. This is due to non-universal short path effects. If one removes this short path effects by studying the difference between reflection for $g = 0$ and finite values of g , the quantitative agreement becomes very good. For vanishing interaction strength $g = 0$, the non-universal Aharonov-Bohm oscillations effects in the annular billiard \mathcal{B}_5 (Sec. 5.8.4) can at least qualitatively be well described by a non-universal semiclassical analysis.

Similar results as for the reflection have been found for the transmission and the intensity distribution. Quantitatively the agreement is better for some billiards than for others. This is probably due to non-universal effects, most notably system specific short trajectories inside the billiards. Using more geometric configurations for the statistical average generally improves the quality of the numerical results. For large values of the interaction strength g , no dynamically stable stationary scattering states exists and the flow becomes time dependent. Narrow leads are responsible for a quick rise of unstable parameter configurations.

As outlook, there are several other robust interference effects in mesoscopic systems (time-reversal mirrors in chaotic cavities (Sec. 6.4.2), Aharonov-Bohm oscillations in disordered rings (Sec. 6.4.3)) for vanishing interaction strength $g = 0$ which are worth studying for finite values of g . Furthermore, weak localization in diffusive systems with non-vanishing gauge field and non-vanishing interaction has not yet been studied. The universal conductance fluctuations (see Sec. 6.1.3) could also be studied for non-vanishing magnetic field and interaction strength. Another feature of wave propagation due to the underlying classical dynamics is the formation of caustics in wave fronts [147]. The influence of a non-linearity on this effect is also worth studying. On the theoretical side, a full semiclassical diagrammatic perturbation theory for the intensity distribution (and for the conductance fluctuations) for finite values of g is desirable (albeit probably very difficult).

This whole thesis is based on the mean-field description of Bose-Einstein condensates. This is only an approximation of the true many-body dynamics. Of course the crucial question is now under which conditions this mean-field theory is valid and when does it break down. A beyond mean field approach based on cumulants can give at least partial answers to this question in one-dimensional systems [67, 87, 120]. An extension of these results to two-dimensional systems would be desirable albeit computational extremely expensive.

Another beyond-meanfield approach investigates the true many-body dynamics in very small systems using a Bose-Hubbard model. In this setting some kind of coherent backscattering in very tiny ring systems with disorder potential can be observed [63]. It would be desirable to obtain similar results for weak localization in chaotic cavities albeit the number of sites necessary to perform useful simulations of two-dimensional billiard cavities is well beyond any capabilities of even the fastest supercomputer. The work [63] also develops an alternative semiclassical theory of the true many-particle dynamics. While the semiclassical theory developed in Sec. 6.1 keeps the particle number N fixed and uses a stationary phase approach for $\hbar \rightarrow 0$ (allowing us to regard quantum effects as a perturbation around classical mechanics), [63] keeps \hbar fixed and uses the stationary phase method for $N \rightarrow \infty$. This allows one to regard the true many-body dynamics as perturbation around the mean-field equation of motion. Perhaps one could build on this and use the mean-field approach to study the true many-particle dynamics in chaotic cavities.

The most time consuming part of all calculations of stationary scattering states is the solution of linear systems of equations. This also limits the size of the system studied in this work. A reliable iterative method to solve these linear systems of equations would be desirable as discussed in Sec. 3.9.

Appendix A

The Newton method

We present here a short derivation of Newton's method as described in [157]. Let $F : \mathbb{R}^n \rightarrow \mathbb{R}^n$ be a two times continuously differentiable function. The goal is to find a solution $\tilde{\Psi}$ of the non-linear system of equations $F(\tilde{\Psi}) = 0$. Let Ψ_0 be an initial guess for the solution $\tilde{\Psi}$. We start by linearizing F around Ψ_0

$$F(\Psi_0 + \Delta\Psi) = F(\Psi_0) + \mathcal{D}F\Delta\Psi + \mathcal{O}(\|\Delta\Psi\|^2)$$

and using the linear part $F(\Psi_0) + \mathcal{D}F\Delta\Psi$ as an approximation to F . The zero of this linear part can be easily calculated

$$F(\Psi_0) + \mathcal{D}F\Delta\Psi = 0 \quad \implies \quad \Delta\Psi = -(\mathcal{D}F)^{-1} F(\Psi_0)$$

giving $\Psi_0 - (\mathcal{D}F)^{-1} F(\Psi_0)$ as a better approximation to $\tilde{\Psi}$. This process can be iterated

$$\Psi_{n+1} = \Psi_n - (\mathcal{D}F)^{-1} F(\Psi_n) \tag{A.1}$$

giving a sequence of successive better approximations to $\tilde{\Psi}$. This iteration is called the Newton method. The convergence behavior of this sequence can be analyzed using the function

$$G(\Psi) = \Psi - (\mathcal{D}F)^{-1} F(\Psi)$$

whose derivative is given by¹

$$\mathcal{D}G = \mathbb{1} - \left[\mathcal{D}(\mathcal{D}F)^{-1} \right] F - \underbrace{(\mathcal{D}F)^{-1} \mathcal{D}F}_{\mathbb{1}} = - \left[\mathcal{D}(\mathcal{D}F)^{-1} \right] F$$

We note that at the solution $\tilde{\Psi}$ of $F(\tilde{\Psi}) = 0$ following relations hold:

$$G(\tilde{\Psi}) = \tilde{\Psi} \quad \mathcal{D}G = 0 .$$

¹ As $(\mathcal{D}F)^{-1}$ is a matrix, i.e. a linear mapping $\mathbb{R}^n \rightarrow \mathbb{R}^n$, the object $\mathcal{D}(\mathcal{D}F)^{-1}$ is a tensor, i.e. a bilinear mapping $\mathbb{R}^n \times \mathbb{R}^n \rightarrow \mathbb{R}^n$.

The Newton iteration (A.1) can be written as $\Psi_{n+1} = G(\Psi_n)$. We now use the linearization of the Newton iteration around $\tilde{\Psi}$:

$$\underbrace{G(\Psi_n)}_{\Psi_{n+1}} = G(\tilde{\Psi} + \Psi_n - \tilde{\Psi}) = \underbrace{G(\tilde{\Psi})}_{\tilde{\Psi}} + \underbrace{\mathcal{D}G}_0(\Psi_n - \tilde{\Psi}) + \mathcal{O}(\|\Psi_n - \tilde{\Psi}\|^2)$$

giving us the relation

$$\|\Psi_{n+1} - \tilde{\Psi}\| = \mathcal{O}(\|\Psi_n - \tilde{\Psi}\|^2)$$

which implies local quadratic convergence. This means once we get into the vicinity of $\tilde{\Psi}$ where the error term $\|\Psi_n - \tilde{\Psi}\|$ is sufficient small each successive iteration will double the number of correct digits of the approximations Ψ_n . Of course this only works if $\mathcal{D}F$ is not singular at $\tilde{\Psi}$ and if F is two times continuous differentiable.

In practical applications quadratic convergence is quite fast and the best one could hope for. There are higher order iterative methods but they are much more complicated so that they are impractical, especially for multi-dimensional systems of equations [201].

If the start vector Ψ_0 is not sufficient close to a solution $\tilde{\Psi}$ of $F(\tilde{\Psi}) = 0$, the Newton iteration (A.1) becomes quite erratic. The vectors Ψ_n can wander wildly through \mathbb{R}^n without ever converging. The correction term $-(\mathcal{D}F)^{-1}F(\Psi_n)$ may become unreasonable big if the iteration hits the vicinity of a non-zero local minima of $\|F(\Psi)\|^2$ where $\mathcal{D}F$ becomes singular. Or the iteration can hit a basin of attraction of a solution $\tilde{\Psi}$ by chance. But if there multiple solutions $\tilde{\Psi}$ the solution it converges to is quite randomly chosen.

Consider for example the equation $z^3 - 1 = 0$. Here Newton's method has following form:

$$z_{n+1} = z_n - \frac{z_n^3 - 1}{3z_n^2} \quad (\text{A.2})$$

Depending on the starting value z_0 this iteration eventually converges to one of the three solutions $\{1, e^{+i2\pi/3}, e^{-i2\pi/3}\}$. But given z_0 one cannot tell which solution the Newton iteration converges

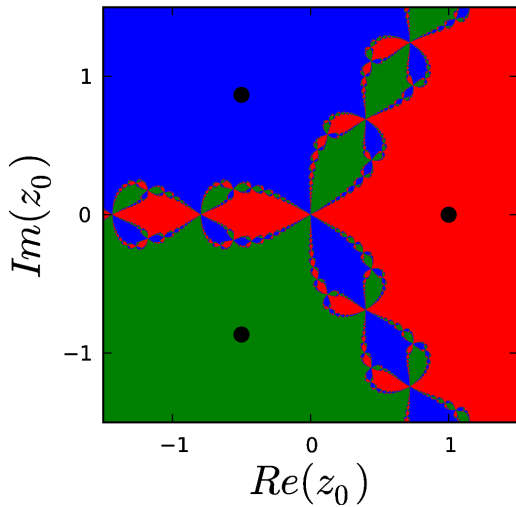


Figure A.1: The figure shows the basins of attraction of the Newton iteration (A.2). Points colored in red converge to the solution 1, points colored in blue converge to $e^{+i2\pi/3}$ and points colored in green converge to $e^{-i2\pi/3}$. The solutions themselves are shown as black dots. The border between the basins has a complicated fractal structure.

to because the basins of attraction for the three solutions are fractals [164, 172] as depicted in Fig. A.1.

This erratic behavior of the Newton iteration is sometimes unwanted. In this cases one can tame the Newton method by a region of trust approach. A popular choice is Powell's dog leg method [140, 157, 170]. At the very heart this method uses a Newton iteration. But if it becomes apparent that the Newton method is about to fail it uses different iteration steps based on a steepest descent approach. Therefore this method can sometimes find solutions where the Newton method fails. Also the iteration does not wander wildly around. Instead it might get stuck at non-zero local minima of $\|F(\Psi)\|^2$ and so Powell's dog leg method cannot guarantee to find a solution of $F(\Psi) = 0$. This is a grave disadvantage but on the other side this characteristic makes Powell's dog leg method very useful in the related topic of multi-dimensional function optimization where one is especially interested in such minima of $\|F(\Psi)\|^2$. Indeed, the optimization problem and the root finding problem are inherently related because the zeros of the function $\mathbb{R}^n \rightarrow \mathbb{R}^n$ defined as $\Psi \mapsto F(\Psi)^T \mathcal{D}F$ are the extremal points of the function $\mathbb{R}^n \rightarrow \mathbb{R}$ defined as $\Psi \mapsto \|F(\Psi)\|^2$ where in this context F is allowed to be a function $\mathbb{R}^n \rightarrow \mathbb{R}^m$.

Conclusion

The Newton method is a purely local algorithm to calculate solutions of $F(\Psi) = 0$. The convergence properties depend strongly on the start vector Ψ_0 . Global convergence cannot be guaranteed. If one wants to ensure to find a solution of $F(\Psi) = 0$ one therefore has to use some other method, for example the continuation method described in Sec. 5.3. But if the Newton method converges, the convergence speed is quadratic which is quite rapid.

Appendix B

The Onsager relations

In this appendix we will derive the Onsager relations which predict that for two terminal devices (i.e. systems with two attached leads) the total transmission is a symmetric function of the magnetic field B (see Eq. (B.16)). During the derivation it will become obvious that such a strict symmetry can only hold in the non-interacting case $g = 0$. The scattering matrix related part of this appendix follows [50]. For some additional information see Sec. 5.8.4 where the breakdown of the Onsager relations is discussed for a specific example billiard.

In this appendix we work with the continuous (i.e. undiscretized) system which implies that the Hilbert space we work with is $L^2(\mathbb{R}^2)$. The Hamilton operator we use here is the usual two dimensional one with a magnetic gauge field (Eq. (2.17) without interaction):

$$H = \frac{1}{2m} [-i\hbar\nabla - q\mathbf{A}(\mathbf{r})]^2 + V(\mathbf{r}) .$$

We assume that the scattering system has two attached leads. A prototype of such a system is shown in Fig. 3.11 but nearly all other systems studied in this work are also of this type. For the sake of simplicity¹ we assume that the magnetic field (and also the gauge field) is adiabatically switched off inside the leads as explained in Sec. 3.6.4. In Sec. B.1 and Sec. B.2 we assume the non-interacting case $g = 0$ while in Sec. B.3 and Sec. B.4 we investigate the effect of a non-vanishing interaction.

In order to avoid confusion we here list the notation for matrix operations used in this appendix:

A^*	complex conjugation without transposition
A^T	transposition without complex conjugation
A^\dagger	the hermitian adjoint, i.e. transposition and complex conjugation

B.1 Symmetries of the scattering matrix

Lead no. 1 and no. 2 are assumed to have N_1 and N_2 open channels respectively. The first step is now to introduce a current amplitude vector (i.e. the squared modulus is the current) of following

¹ The derivation presented in this section is still valid for a constant non-vanishing magnetic field inside the leads. But the details are more involved as the lead-eigenmodes are then determined by a quadratic eigenvalue problem [84, 199, 208]. Especially the operators P and Q have to be adjusted.

form:

$$x = [x_{1,1}, x_{1,2}, \dots, x_{1,N_1}, x_{2,1}, x_{2,2}, \dots, x_{2,N_2}]^T \in \mathbb{C}^{N_1+N_2}.$$

The next step is to introduce a linear operator

$$P : \mathbb{C}^{N_1+N_2} \rightarrow L^2(\mathbb{R}^2)$$

$$x = [x_{l,n}]_{l,n} \mapsto \sum_{l,n} x_{l,n} i\hbar \sqrt{\hbar k_{l,n}/m} \chi_{l,n}((\mathbf{r} - \mathbf{r}_{l,n}) \cdot \mathbf{n}_{l,n}^\perp) \delta((\mathbf{r} - \mathbf{r}_{l,n}) \cdot \mathbf{n}_{l,n})$$

which creates a source term S at position $\mathbf{r}_{l,n}$ with normal $\mathbf{n}_{l,n}$ when applied to the channel amplitude vector x . This source term S is assumed to excite a incoming plane wave with amplitude proportional to $x_{l,n}$ and current equal to $|x_{l,n}|^2$ in lead l and channel n (lead eigenmode $\chi_{l,n}(y)$, wave vector $k_{l,n}$ corresponding to energy μ) when subjected to the retarded Green function. This is the multi-channel continuum equivalent of Eq. (3.47) (see also Eq. (3.23)).

Likewise we introduce the linear operator

$$Q : L^2(\mathbb{R}^2) \rightarrow \mathbb{C}^{N_1+N_2}$$

$$\Psi \mapsto \left[\sqrt{\hbar k_{l,n}/m} \int \Psi(\mathbf{r}) \chi_{l,n}((\mathbf{r} - \mathbf{r}_{l,n}) \cdot \mathbf{n}_{l,n}^\perp) \delta((\mathbf{r} - \mathbf{r}_{l,n}) \cdot \mathbf{n}_{l,n}) d\mathbf{r} \right]_{l,n}$$

which measures the current amplitudes of the plane waves corresponding to each channel inside the leads. At a wavefunction which is excited by the source term S the operator Q measures the sum of the amplitudes of the ingoing and outgoing plane waves. In order to measure only the outgoing component we have to remove the incoming part which is excited by the source. The removal of the incoming part can be either done by a projection method as explained in Eq. (3.26) or we can use the fact that the amplitude of the excited incoming plane wave at the position of the source is equal to $x_{l,n} \sqrt{m/(\hbar k_{l,n})}$ and thus can be simply subtracted. The latter option is implemented now.

We are now ready to define the scattering matrix $\mathcal{S} \in \text{Mat}((N_1 + N_2) \times (N_1 + N_2), \mathbb{C})$ as follows:

$$\mathcal{S} = Q \lim_{\substack{\epsilon \rightarrow 0 \\ \epsilon > 0}} [\mu + i\epsilon - H]^{-1} P - \mathbb{1}. \quad (\text{B.1})$$

This is nothing more than a reformulation of the Fischer-Lee relation Eq. (3.48) [50, 127] in a more abstract way better suited for the purposes of this appendix.

This scattering matrix \mathcal{S} relates the incoming current amplitudes x with the corresponding outgoing current amplitudes y as follows:

$$y = \mathcal{S}x. \quad (\text{B.2})$$

Current conservation is automatically included as follows (see Sec. B.4):

$$\|x\|^2 = \|y\|^2 \quad \text{or equivalently} \quad x^\dagger x = y^\dagger y. \quad (\text{B.3})$$

The most important observation is now that as P, Q and H (and therefore $[\mu + i\epsilon - H]^{-1}$) are linear operators, the scattering matrix \mathcal{S} is also a linear operator, i.e. it satisfies the superposition principle:

$$\begin{aligned} y &= \mathcal{S}x & \text{and} & \quad \eta \in \mathbb{C} & \text{leads to} & \quad \eta y = \eta \mathcal{S}x = \mathcal{S} \eta x \\ y_0 &= \mathcal{S}x_0 & \text{and} & \quad y_1 = \mathcal{S}x_1 & \text{leads to} & \quad y_0 + y_1 = \mathcal{S}x_0 + \mathcal{S}x_1 = \mathcal{S}(x_0 + x_1). \end{aligned} \quad (\text{B.4})$$

The current conservation Eq. (B.3) and the superposition principle Eq. (B.4) allow us now to establish the unitarity of the scattering matrix \mathcal{S} .

Eq. (B.3) is the statement that for every vector $x \in \mathbb{C}^{N_1+N_2}$ we have following relation:

$$x^\dagger x = x^\dagger \mathcal{S}^\dagger \mathcal{S} x . \quad (\text{B.5})$$

Let $u, v \in \mathbb{C}^{N_1+N_2}$ we now two arbitrary vectors. We can now use the linearity of \mathcal{S} and Eq. (B.5) to conclude:

$$\begin{aligned} u^\dagger v &= \frac{1}{4}(u+v)^\dagger(u+v) - \frac{1}{4}(u-v)^\dagger(u-v) \\ &= \frac{1}{4}(u+v)^\dagger \mathcal{S}^\dagger \mathcal{S}(u+v) - \frac{1}{4}(u-v)^\dagger \mathcal{S}^\dagger \mathcal{S}(u-v) = u^\dagger \mathcal{S}^\dagger \mathcal{S} v . \end{aligned} \quad (\text{B.6})$$

As u and v are arbitrary (finite-dimensional) vectors it follows automatically that the scattering matrix \mathcal{S} is unitary:

$$\mathcal{S}^\dagger \mathcal{S} = \mathcal{S} \mathcal{S}^\dagger = \mathbb{1} . \quad (\text{B.7})$$

This is the first important symmetry of the scattering matrix \mathcal{S} .

The second important symmetry of \mathcal{S} involves the magnetic field B corresponding to the gauge field \mathbf{A} . We start with Eq. (B.2)

$$y = \mathcal{S}(+B) x$$

and taking the complex conjugate of this equation:

$$y^* = \mathcal{S}(+B)^* x^* . \quad (\text{B.8})$$

In order to understand what effect the complex conjugation has we look at the wave function $\Psi = [\mu + i\epsilon - H]^{-1} Px$ inside the cavity where the source term $S = Px$ vanishes:

$$\frac{1}{2m} [-i\hbar \nabla - q\mathbf{A}]^2 \Psi + V\Psi = \mu\Psi .$$

The complex conjugation transforms this equation into:

$$\frac{1}{2m} [-i\hbar \nabla + q\mathbf{A}]^2 \Psi^* + V\Psi^* = \mu\Psi^* . \quad (\text{B.9})$$

From this equation we see that the complex conjugation has two effects: The magnetic field is reversed and the incoming/outgoing plane waves are interchanged. Therefore we can interpret Eq. (B.9) as follows:

$$x^* = \mathcal{S}(-B) y^* \quad \text{or equivalently} \quad y^* = \mathcal{S}(-B)^\dagger x^* . \quad (\text{B.10})$$

In the last step we have used the unitarity of the scattering matrix Eq. (B.7) and thus implicitly assumed that the superposition principle holds.

Combining Eq. (B.8) and Eq. (B.10) we can establish the second important symmetry of the scattering matrix \mathcal{S} :

$$\mathcal{S}(-B) = \mathcal{S}(+B)^T . \quad (\text{B.11})$$

In summary we have derived here following symmetries of the scattering matrix \mathcal{S} :

$$\begin{aligned} \mathcal{S}^{-1} &= \mathcal{S}^\dagger && \text{unitarity, Eq. (B.7)} \\ \mathcal{S}(-B) &= \mathcal{S}(+B)^T && \text{magnetic field, Eq.(B.11)} . \end{aligned}$$

B.2 The Onsager relations

In order to derive the Onsager relations we start by splitting the scattering matrix into four blocks corresponding to the two leads:

$$\mathcal{S} = \begin{bmatrix} \mathcal{R}_{1 \leftarrow 1} & \mathcal{T}_{1 \leftarrow 2} \\ \mathcal{T}_{2 \leftarrow 1} & \mathcal{R}_{2 \leftarrow 2} \end{bmatrix}.$$

Here $\mathcal{T}_{2 \leftarrow 1}$ is the transmission matrix from lead 1 to lead 2, $\mathcal{R}_{1 \leftarrow 1}$ is the reflection matrix from lead 1 into itself. $\mathcal{T}_{1 \leftarrow 2}$ and $\mathcal{R}_{2 \leftarrow 2}$ are the corresponding matrices with the other lead as source.

The first step is to use following relation which is a consequence of the unitarity of the scattering matrix (B.7) and of the fact that \mathcal{S} is finite-dimensional:

$$\mathcal{S}^\dagger \mathcal{S} = \mathcal{S} \mathcal{S}^\dagger.$$

This gives us four matrix relations between $\mathcal{T}_{2 \leftarrow 1}, \mathcal{R}_{1 \leftarrow 1}, \mathcal{T}_{1 \leftarrow 2}$ and $\mathcal{R}_{2 \leftarrow 2}$. The most useful relation is

$$\mathcal{R}_{1 \leftarrow 1}^\dagger \mathcal{R}_{1 \leftarrow 1} + \mathcal{T}_{2 \leftarrow 1}^\dagger \mathcal{T}_{2 \leftarrow 1} = \mathcal{R}_{1 \leftarrow 1} \mathcal{R}_{1 \leftarrow 1}^\dagger + \mathcal{T}_{1 \leftarrow 2} \mathcal{T}_{1 \leftarrow 2}^\dagger.$$

We proceed by taking the trace of this matrix equation and using the cyclic invariance of the trace to get

$$\begin{aligned} \text{tr} [\mathcal{T}_{1 \leftarrow 2} \mathcal{T}_{1 \leftarrow 2}^\dagger] &= \text{tr} [\mathcal{T}_{2 \leftarrow 1} \mathcal{T}_{2 \leftarrow 1}^\dagger] \\ \sum_{m,n} |\mathcal{T}_{1 \leftarrow 2, (m,n)}|^2 &= \sum_{m,n} |\mathcal{T}_{2 \leftarrow 1, (m,n)}|^2. \end{aligned} \quad (\text{B.12})$$

Defining the total transmission T , i.e. the transmission summed over all incoming modes, as

$$T_{1 \leftarrow 2} = \sum_{m,n} |\mathcal{T}_{1 \leftarrow 2, (m,n)}|^2 \quad \text{and} \quad T_{2 \leftarrow 1} = \sum_{m,n} |\mathcal{T}_{2 \leftarrow 1, (m,n)}|^2 \quad (\text{B.13})$$

we can rewrite Eq. (B.12) as

$$T_{1 \leftarrow 2} = T_{2 \leftarrow 1} \quad (\text{B.14})$$

which implies that the total transmission is the same for both directions from lead 1 to lead 2 and from lead 2 to lead 1.

The second step is to use the symmetry (B.11) with regard to the magnetic field B . This gives us

$$\mathcal{T}_{1 \leftarrow 2}(+B) = \mathcal{T}_{2 \leftarrow 1}(-B)^T$$

or equivalently using the fact that the trace is invariant with respect to transposition:

$$\begin{aligned} \text{tr} [\mathcal{T}_{1 \leftarrow 2}(+B) \mathcal{T}_{1 \leftarrow 2}(+B)^\dagger] &= \text{tr} [\mathcal{T}_{2 \leftarrow 1}(-B) \mathcal{T}_{2 \leftarrow 1}(-B)^\dagger] \\ \sum_{m,n} |\mathcal{T}_{1 \leftarrow 2, (m,n)}(+B)|^2 &= \sum_{m,n} |\mathcal{T}_{2 \leftarrow 1, (m,n)}(-B)|^2. \end{aligned}$$

Using the total transmission T this can be rewritten as

$$T_{1 \leftarrow 2}(+B) = T_{2 \leftarrow 1}(-B). \quad (\text{B.15})$$

Combining Eq. (B.14) and Eq. (B.14) we finally get the Onsager relation

$$T_{2\leftarrow 1}(+B) = T_{2\leftarrow 1}(-B) \quad (\text{B.16})$$

which implies that the total transmission is a symmetric function of the magnetic field.

Analogously to the previous discussion one can define a total self reflection

$$R_{s,1\leftarrow 1} = \sum_n |\mathcal{R}_{1\leftarrow 1,(n,n)}|^2$$

and directly deduce from Eq. (B.11) following symmetry:

$$R_{s,1\leftarrow 1}(+B) = R_{s,1\leftarrow 1}(-B) .$$

Especially each self reflection term $|\mathcal{R}_{1\leftarrow 1,(n,n)}|^2$ is a symmetric function of the magnetic field B .

B.3 The breakdown of the Onsager relations in the interacting case

The most important ingredient in the derivation of the Onsager relation (B.16) is the unitarity of the scattering matrix \mathcal{S} , i.e. Eq. (B.7), which itself depends on the superposition principle, i.e. the linearity of H . In the interacting case $g \neq 0$ this linearity is broken and so the superposition principle fails and with it the unitarity of \mathcal{S} . So we cannot expect that the strict symmetry of the Onsager relation (B.16) to hold for $g \neq 0$.

We now describe explicitly what we understand as the scattering “matrix” \mathcal{S} in the interacting case $g \neq 0$. To this end we introduce the auxiliary function

$$F : \Psi(\mathbf{r}) \mapsto [\mu - H] \Psi(\mathbf{r}) - g(\mathbf{r}) \frac{\hbar^2}{m} |\Psi(\mathbf{r})|^2 \Psi(\mathbf{r})$$

and define the scattering “matrix” as

$$\mathcal{S} = QF^{-1}P - \mathbb{1} .$$

For $g \neq 0$ the function F is non-linear and so is F^{-1} . Thus the scattering “matrix” \mathcal{S} is a non-linear mapping $\mathbb{C}^{N_1+N_2} \rightarrow \mathbb{C}^{N_1+N_2}$ and the name “matrix” is not justified anymore for $g \neq 0$. Especially the inverse mapping \mathcal{S}^{-1} cannot be simply calculated by taking the hermitian adjoint.

But we can conveniently define a matrix-like object $\tilde{\mathcal{S}}$ which reduces to the ordinary scattering matrix in the linear case $g = 0$. To this end we use the unit-vectors $e_n \in \mathbb{C}^{N_1+N_2}$ defined by $[e_n]_m = \delta_{n,m}$ using the Kronecker- δ -symbol:

$$\tilde{\mathcal{S}} = [\mathcal{S} e_1 | \mathcal{S} e_2 | \dots | \mathcal{S} e_{N_1+N_2}] .$$

This matrix $\tilde{\mathcal{S}}$ gives the transmission and reflection if we inject the particles through a single mode in one of the leads. This exactly what we are doing in this work as we are using pure modes and not any superposition of modes to inject particles.

B.4 The generalized continuity equation

As we have seen in Sec. B.1 current conservation is the precursor to the unitarity of the scattering matrix. While in the non-linear case $g \neq 0$ current conservation still holds (see Eq. (B.3)), i.e.

$$\|\mathcal{S}x\|^2 = \|x\|^2 \quad \text{for all } x \in \mathbb{C}^{N_1+N_2}, \quad (\text{B.17})$$

we will now show where exactly the breaking of the unitarity happens.

Let ψ and χ be two solutions of the Schrödinger equation

$$i\hbar \frac{\partial}{\partial t} \Psi = H\Psi.$$

A short calculation gives us

$$\begin{aligned} \frac{\partial}{\partial t} [\psi^* \phi] &= \frac{i}{\hbar} \phi \left[\frac{1}{2m} [+i\hbar \nabla - q\mathbf{A}]^2 \psi^* + V\psi^* \right] - \frac{i}{\hbar} \psi^* \left[\frac{1}{2m} [-i\hbar \nabla - q\mathbf{A}]^2 \phi + V\phi \right] \\ &= + \frac{i}{2m\hbar} \left[-\hbar^2 \phi \Delta \psi^* - 2iq\hbar \phi (\mathbf{A} \cdot \nabla \psi^*) - iq\hbar \phi \psi^* (\nabla \cdot \mathbf{A}) + q\mathbf{A}^2 \phi \psi^* \right] \\ &\quad + \frac{i}{2m\hbar} \left[+\hbar^2 \psi^* \Delta \phi - 2iq\hbar \psi^* (\mathbf{A} \cdot \nabla \phi) - iq\hbar \phi \psi^* (\nabla \cdot \mathbf{A}) - q\mathbf{A}^2 \phi \psi^* \right] \\ &= \nabla \cdot \left[-i \frac{\hbar}{2m} [\phi \nabla \psi^* - \psi^* \nabla \phi] + \frac{q}{m} \mathbf{A} \psi^* \phi \right]. \end{aligned} \quad (\text{B.18})$$

This is the generalized continuity equation

$$\frac{\partial}{\partial t} [\psi^* \phi] = \nabla \cdot \left[-i \frac{\hbar}{2m} [\phi \nabla \psi^* - \psi^* \nabla \phi] + \frac{q}{m} \mathbf{A} \psi^* \phi \right]. \quad (\text{B.19})$$

If ϕ is equal to ψ this gives us the continuity equation in the usual form [50]

$$\frac{\partial}{\partial t} [\psi^* \psi] + \nabla \cdot \mathbf{j} = 0 \quad (\text{B.20})$$

where we have introduced the probability current density (see also Eq. (3.51))

$$\mathbf{j} = \frac{\hbar}{m} \text{Im} [\psi^* \nabla \psi] - \frac{q}{m} \mathbf{A} \psi^* \psi. \quad (\text{B.21})$$

The generalized continuity equation (B.19) is an alternative route to derive the unitarity of the scattering matrix Eq. (B.7). Let ψ and ϕ be two stationary solutions of the Schrödinger equation corresponding to the energy μ :

$$H\psi = \mu\psi \quad \text{and} \quad H\phi = \mu\phi.$$

Then Eq. (B.19) reduces to

$$\nabla \cdot \left[-i \frac{\hbar}{2m} [\phi \nabla \psi^* - \psi^* \nabla \phi] + \frac{q}{m} \mathbf{A} \psi^* \phi \right] = 0.$$

We now apply Gauss theorem [33] to get²

$$\int_{\text{lead no. 1}} \left[\phi(x, y) \frac{\partial}{\partial x} \psi(x, y)^* - \psi(x, y)^* \frac{\partial}{\partial x} \phi(x, y) \right] dy = \int_{\text{lead no. 2}} \left[\phi(x, y) \frac{\partial}{\partial x} \psi(x, y)^* - \psi(x, y)^* \frac{\partial}{\partial x} \phi(x, y) \right] dy . \quad (\text{B.22})$$

Here without losing generality we assumed that lead no. 1 stretches $-x$ direction, the lead no. 2 in $+x$ direction and that the transversal direction is y .

In lead no. l the wavefunction ϕ can be decomposed into the lead eigenmodes

$$\phi(x, y) = \sum_n \left[a_{\phi, l, n} e^{+ik_{l, n} x} + b_{\phi, l, n} e^{-ik_{l, n} x} \right] \sqrt{\frac{m}{\hbar k_{l, n}}} \chi_{l, n}(y)$$

and a similar decomposition holds for ψ . Inserting this decomposition into Eq. (B.22) and using the orthogonality of the lead eigenmodes gives us

$$\sum_n \left[a_{\phi, 1, n}^* a_{\psi, 1, n}^* - b_{\phi, 1, n}^* b_{\psi, 1, n}^* \right] = \sum_n \left[a_{\phi, 2, n}^* a_{\psi, 2, n}^* - b_{\phi, 2, n}^* b_{\psi, 2, n}^* \right] .$$

Keeping track of incoming and outgoing modes we see that this is equivalent to the unitarity of the scattering matrix \mathcal{S} in form of Eq. (B.6). For ϕ equal to ψ this gives us the current conservation in form of Eq. (B.17).

The continuity equation (B.20) holds also for the non-linear Gross-Pitaevskii equation

$$i\hbar \frac{\partial}{\partial t} \Psi(\mathbf{r}, t) = H\Psi(\mathbf{r}, t) + g(\mathbf{r}) \frac{\hbar^2}{m} |\Psi(\mathbf{r}, t)|^2 \Psi(\mathbf{r}, t)$$

as the non-linear scattering potential $g(\mathbf{r}) \frac{\hbar^2}{m} |\Psi(\mathbf{r}, t)|^2$ drops out similar to the scattering potential $V(\mathbf{r})$ in the derivation carried out in Eq. (B.18). But the generalized continuity equation (B.19) fails to hold in the non-linear case for ϕ not equal to ψ as now the non-linear potential does not drop out. So the current conservation in form of Eq. (B.17) still holds in the interacting case while the unitarity fails.

² As the magnetic field is assumed to vanish inside the leads we can always choose a gauge field $A(\mathbf{r})$ which also vanishes inside the leads [50].

Appendix C

Transparent boundary conditions

In this section we will derive transparent boundary conditions (abbr. “*TBC*” henceforth) as described in [10, 11] for the Crank-Nicolson time propagation method (4.5) applied to the (one dimensional) tight binding Hamiltonian (3.11). These *TBC* will allow us to handle the leads for time dependent simulations in an appropriate way just like the self energy boundary conditions (3.36) allowed us to handle the leads for Green function calculations. That way we can restrict the simulation to the scattering region without (almost) introducing any error.

The wavefunction $\Psi(x, t)$ is discretized both in space and time on a regular lattice with spacing Δx and Δt respectively. As an abbreviation we therefore introduce

$$\Psi_j^n = \Psi(j \Delta x, n \Delta t) .$$

Using that notation the Crank-Nicolson method (4.5) can be written as

$$i\hbar \frac{\Psi_j^{n+1} - \Psi_j^n}{\Delta t} = H \frac{\Psi_j^{n+1} + \Psi_j^n}{2}$$

where H is the one dimensional tight binding Hamiltonian (3.11) which is now applied explicitly. Introducing

$$r = -i \frac{2\hbar}{\alpha \Delta t} = -i \frac{4m(\Delta x)^2}{\hbar \Delta t} \quad w = -\frac{1}{\alpha} = -\frac{2m(\Delta x)^2}{\hbar^2}$$

this results in

$$\begin{aligned} r [\Psi_j^{n+1} - \Psi_j^n] &= \Psi_{j+1}^{n+1} + \Psi_{j-1}^{n+1} - 2\Psi_j^{n+1} \\ &+ \Psi_{j+1}^n + \Psi_{j-1}^n - 2\Psi_j^n + wV_j [\Psi_j^{n+1} + \Psi_j^n] . \end{aligned} \quad (\text{C.1})$$

We now split the system into a scattering region $j > 0$ and a lead $j \leq 0$. Inside the lead the potential is assumed to be constant, so $V_j = V$ for $j \leq 0$. The goal is to eliminate the values of the wavefunction inside the lead (i.e. Ψ_j^n for $j \leq 0$) from the equation of motion (C.1). To this end we apply a \mathcal{Z} -transformation [58] (which is a discrete form of the Laplace transformation) inside the lead:

$$\mathcal{Z} : \Psi_j^n \mapsto \hat{\Psi}_j(z) = \sum_{n=0}^{\infty} \Psi_j^n z^{-n} \quad \text{for } j \leq 0 .$$

We assume that $\Psi_j^n = 0$ for $n \leq 0$, i.e. we start with a vanishing wavefunction. As then the relation

$$\mathcal{Z} \left\{ \Psi_j^{n+1} \pm \Psi_j^n \right\} = (z \pm 1) \hat{\Psi}_j(z)$$

holds, Eq. (C.1) is transformed into

$$\hat{\Psi}_{j+1}(z) - 2a(z)\hat{\Psi}_j(z) + \hat{\Psi}_{j-1}(z) = 0 \quad (\text{C.2})$$

with

$$a(z) = 1 + \frac{r}{2} \frac{z-1}{z+1} - \frac{wV}{2}.$$

Eq. (C.2) is a linear three term recursion formula in j with constant coefficients which has two independent solutions. This recursion can be solved by the ansatz $\Psi_j(z) = C [b(z)]^j$. which inserted into Eq. (C.2) gives an equation for $b(z)$:

$$[b(z)]^2 - 2a(z)b(z) + 1 = 0.$$

From this we get two solutions for $b(z)$:

$$b_{\pm}(z) = a(z) \pm \sqrt{[a(z)]^2 - 1}. \quad (\text{C.3})$$

As the relation $b_+(z)b_-(z) = 1$ holds, one solution has a modulus bigger than one while the other solution has a modulus smaller than one. In the lead the wave function Ψ_j^n should vanish for $j \rightarrow -\infty$ (i.e. $x \rightarrow -\infty$) therefore we have to select the solution with modulus bigger than one as the only admissible solution of the recursion (C.2) which is henceforth called simply $b(z)$. The actual sign used in Eq. (C.3) can be left ambiguous for the moment.

We have therefore the relation

$$\hat{\Psi}_0(z) = b(z)\hat{\Psi}_{-1}(z) \quad (\text{C.4})$$

between the first and the second point inside the lead. Introducing the Laurent expansion of $b(z)$ around $z = 0$

$$b(z) = \sum_{n=0}^{\infty} b_n z^{-n}$$

we can rewrite Eq. (C.4) as

$$\Psi_0^{n+1} = \sum_{k=0}^{n+1} b_{n+1-k} \Psi_{-1}^k. \quad (\text{C.5})$$

For actual computations it is more convenient to rewrite this equation in a different way. To this end we introduce

$$\begin{aligned} s(z) &= (1+z)b(z) = \sum_{n=-1}^{\infty} s_n z^{-n} \\ &= A + Bz \pm \sqrt{z^2(B^2 - 1) + 2z(AB - 1) + A^2 - 1} \end{aligned} \quad (\text{C.6})$$

where we have defined

$$\begin{aligned} A &= 1 - \frac{w}{2}V - \frac{r}{2} \\ B &= 1 - \frac{w}{2}V + \frac{r}{2}. \end{aligned}$$

This allows us to write Eq. (C.5) as

$$\Psi_0^{n+1} - s_{-1}\Psi_{-1}^{n+1} = s_0\Psi_{-1}^n - \Psi_0^n + \sum_{k=1}^n s_k\Psi_{-1}^{n-k}. \quad (\text{C.7})$$

This is the defining equation of the transparent boundary conditions. The simulated region includes the points $j \geq -1$. At the point $j = -1$ we use Eq. (C.7) for performing the propagation while for $j \geq 0$ we use Eq. (C.1). It is important to stress the fact that the *TBC* (C.7) are non-local in time. To compute Ψ_{-1}^{n+1} we have to know Ψ_{-1}^k at all earlier times $0 \leq k \leq n$. This means we have to store Ψ_{-1}^n at all time steps which makes the *TBC* somewhat inconvenient to use.

In order to calculate the coefficients $\{s_n\}_{n=-1}^\infty$ we deduce from Eq. (C.6) the differential equation $s(z)$ fulfills:

$$s'(z) \left[z^2(B^2 - 1) + 2z(AB - 1) + A^2 - 1 \right] = s(z) \left[z(B^2 - 1) + AB - 1 \right] + (1 + z)(A - B).$$

Inserting the Laurent expansion of $s(z)$ into this differential equation gives us recursion relations for the coefficients s_n :

$$\begin{aligned} n = -1 & : (B^2 - 1)s_0 - (AB - 1)s_{-1} = B - A \\ n = 0 & : 2(B^2 - 1)s_1 + (AB - 1)s_0 - (A^2 - 1)s_{-1} = B - A \\ n \geq 1 & : (B^2 - 1)(n + 2)s_{n+1} + (AB - 1)(2n + 1)s_n + (A^2 - 1)(n - 1)s_{n-1} = 0. \end{aligned}$$

Knowing s_{-1} we can calculate all $\{s_n\}_{n \geq 0}$ using this relations. The missing coefficient s_{-1} can be calculated from $s_{-1} = b_0 = \lim_{z \rightarrow \infty} b(z)$ and $\lim_{z \rightarrow \infty} a(z) = B$ as

$$s_{-1} = B \pm \sqrt{B^2 - 1}.$$

Again the sign of the square root has to be chosen such that $|s_{-1}| > 1$.

The sum $\sum_{k=1}^n s_k \Psi_{-1}^{n-k}$ in Eq. (C.7) is inconvenient to carry out because the computational complexity to evaluate it grows linear in time. Therefore we now introduce an approximation to this sum. The main idea is to use the exact values $\{s_n\}_{n=1}^{2L}$ and only approximative values for $\{s_n\}_{n > 2L}$. Here L is some number determining the quality of the approximation. In actual computations an empirical guideline is that $L\Delta t$ should be of the same magnitude as the typical time scales involved in the simulation.

To develop the approximation to s_n we introduce the (formal) power series $f(x) = \sum_{n=0}^\infty s_{n+1}x^n$ and apply a $(L - 1, L)$ -Padé approximation [47, 102] onto it:

$$f(x) = \sum_{n=0}^\infty s_{n+1}x^n = \frac{P_{L-1}(x)}{Q_L(x)} + \mathcal{O}(x^{2L}).$$

Here $P_{L-1}(x)$ is a polynomial of degree $L - 1$ and $Q_L(x)$ is a polynomial of degree L with $Q_L(0) = 1$. Provided that $Q_L(x)$ has only simple zeros we can now calculate a partial fraction expansion of the Padé approximation:

$$\frac{P_{L-1}(x)}{Q_L(x)} = \sum_{l=1}^L \frac{p_l}{q_l - x}.$$

By taking the derivatives of this partial fraction expansion we obtain approximations to the s_n :

$$s_n \cong \sum_{l=1}^L p_l q_l^{-n} . \quad (\text{C.8})$$

These relations holds by construction exactly for $n = 1 \dots 2L$ but only approximatively for $n > 2L$. The conjecture (supported by empirical evidence) is that the approximation converges towards the exact values of s_n for increasing L but one cannot prove this because the knowledge of the mathematical properties of the Padé approximation is still limited.

Using this approximation (C.8) one can rewrite the sum in Eq. (C.7) as

$$\sum_{k=1}^n s_k \Psi_{-1}^{n-k} \cong \sum_{l=1}^L \sigma_l^n$$

where we have introduced L auxiliary quantities σ_l^n which obey the recursion relations

$$\sigma_l^{n+1} = \frac{p_l \Psi_{-1}^n + \sigma_l^n}{q_l} .$$

Using these recursion relations we do not have to store the σ_l^n and Ψ_{-1}^n at all previous times and the computational complexity to evaluate the sum this way remains constant with time. The actual state of the propagation at time step n is determined by $\{\Psi_j^n\}_{j \geq -1}$ and by the $\{\sigma_l^n\}_{l=1}^L$. This is the preferred way to apply the *TBC* (C.7).

For the simulation of two dimensional systems one can separate the leads into eigenmodes. Each eigenmode can be treated as an one dimensional system onto which the *TBC* can be applied separately.

The calculation of the Padé approximation and of the partial fraction expansion is numerically quite delicate and requires eventually that the calculations are done with arbitrary precision floating point numbers. We use the software libraries *MPFR* and *MPC* [62, 76] for such calculations. Luckily the coefficients p_l and q_l do only depend on $\hbar, m, \Delta x, \Delta t$ and V and therefore can be reused by subsequent simulations.

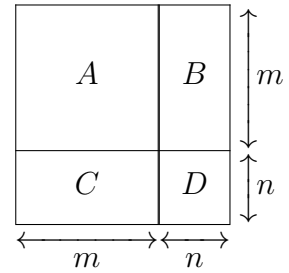
Appendix D

Block Gauß matrix inversion

In this Appendix want to invert a matrix $M \in \text{Mat}((m+n) \times (m+n), \mathbb{C})$ which consists of four submatrices $A \in \text{Mat}(m \times m, \mathbb{C})$, $B \in \text{Mat}(m \times n, \mathbb{C})$, $C \in \text{Mat}(n \times m, \mathbb{C})$ and $D \in \text{Mat}(n \times n, \mathbb{C})$ in following way:

$$M = \begin{bmatrix} A & B \\ C & D \end{bmatrix}.$$

The figure on the right illustrates the dimension of the involved matrices more clearly:



The inversion process is now done using a blockwise Gauß algorithm (see for example [179]):

$$\begin{aligned} \left[\begin{array}{cc|cc} A & B & 1 & 0 \\ C & D & 0 & 1 \end{array} \right] &\Rightarrow \left[\begin{array}{cc|cc} 1 & A^{-1}B & A^{-1} & 0 \\ C & D & 0 & 1 \end{array} \right] \Rightarrow \left[\begin{array}{cc|cc} 1 & A^{-1}B & A^{-1} & 0 \\ 0 & D - CA^{-1}B & -CA^{-1} & 1 \end{array} \right] \\ \Rightarrow \left[\begin{array}{cc|cc} 1 & A^{-1}B & A^{-1} & 0 \\ 0 & 1 & -S^{-1}CA^{-1} & S^{-1} \end{array} \right] &\Rightarrow \left[\begin{array}{cc|cc} 1 & 0 & A^{-1} + A^{-1}BS^{-1}CA^{-1} & -A^{-1}BS^{-1} \\ 0 & 1 & -S^{-1}CA^{-1} & S^{-1} \end{array} \right]. \end{aligned}$$

Here we used the abbreviation

$$S = D - CA^{-1}B.$$

This matrix is called Schur's complement [85, 179].

Finally get for the inverse of M :

$$M^{-1} = \left[\begin{array}{cc|cc} A^{-1} + A^{-1}BS^{-1}CA^{-1} & -A^{-1}BS^{-1} \\ -S^{-1}CA^{-1} & S^{-1} \end{array} \right].$$

Of course the whole process assumes that A and S are invertible matrices.

Appendix E

The Dyson equation

Some readers might be uneasy with the matrix approach used in Sec. 3.5.1 because the matrices therein are of possible infinite size. But we can justify Eq. (3.36) in a similar way using the following Dyson equation approach.

Using the notations introduced in Sec. 3.5.1 we define

$$\begin{aligned} H_0 &= P_I H P_I + P_{II} H P_{II} \\ \tilde{V} &= P_I H P_{II} + P_{II} H P_I = V + V^\dagger \end{aligned}$$

giving us $H = H_0 + \tilde{V}$. We now use the general relation

$$A^{-1} - B^{-1} = B^{-1}(B - A)A^{-1}$$

for the specific case $A = \mu - H$ and $B = \mu - H_0$:

$$(\mu - H)^{-1} - (\mu - H_0)^{-1} = (\mu - H_0)^{-1}(H - H_0)(\mu - H)^{-1}$$

Setting $G = (\mu - H)^{-1}$ and $G_0 = (\mu - H_0)^{-1}$ and considering $H - H_0 = \tilde{V}$ we arrive at the Dyson equation [70, 146]

$$G = G_0 + G_0 \tilde{V} G \tag{E.1}$$

which is an implicit equation for G . Solving for G one obtains

$$G = \left(\mathbb{1} - G_0 \tilde{V} \right)^{-1} G_0 .$$

We are not interested in G but only onto the restriction of G on region II. So using the projection operators P_I and P_{II} (defined in Eq. (3.34)) we now split the Dyson equation (E.1) into two parts:

$$P_{II} G P_{II} = P_{II} G_0 P_{II} + P_{II} G_0 \tilde{V} G P_{II} = P_{II} G_0 P_{II} + P_{II} G_0 P_{II} V^\dagger P_I G P_{II} \tag{E.2}$$

$$P_I G P_{II} = P_I G_0 P_{II} + P_I G_0 \tilde{V} G P_{II} = P_I G_0 P_I V P_{II} G P_{II} \tag{E.3}$$

Here we have used following relations which follow from the properties of the projection operators and the definitions:

$$\begin{aligned} P_{II} \tilde{V} &= P_{II} V^\dagger P_I & G_0 P_I &= P_I G_0 & P_I G_0 P_{II} &= 0 \\ P_I \tilde{V} &= P_I V P_{II} & G_0 P_{II} &= P_{II} G_0 . \end{aligned}$$

Inserting Eq. (E.3) into Eq. (E.2) we arrive at

$$G_{\text{II}} = P_{\text{II}} G P_{\text{II}} = \underbrace{P_{\text{II}} G_0 P_{\text{II}}}_{(\mu - H_{\text{II}})^{-1}} + \underbrace{P_{\text{II}} G_0 P_{\text{II}}}_{(\mu - H_{\text{II}})^{-1}} V^\dagger \underbrace{P_{\text{I}} G_0 P_{\text{I}}}_{(\mu - H_{\text{I}})^{-1}} V P_{\text{II}} G P_{\text{II}}$$

giving us the Dyson equation¹ for G_{II} :

$$G_{\text{II}} = (\mu - H_{\text{II}})^{-1} + (\mu - H_{\text{II}})^{-1} V^\dagger (\mu - H_{\text{I}})^{-1} V G_{\text{II}} .$$

Solving this Dyson equation for G_{II} we get:

$$\begin{aligned} G_{\text{II}} &= \left[\mathbb{1} - (\mu - H_{\text{II}})^{-1} V^\dagger (\mu - H_{\text{I}})^{-1} V \right]^{-1} (\mu - H_{\text{II}})^{-1} \\ &= \left[\mu - H_{\text{II}} - V^\dagger (\mu - H_{\text{I}})^{-1} V \right]^{-1} \\ &= [\mu - H_{\text{II}} - \Sigma_{\text{I}}]^{-1} . \end{aligned} \tag{E.4}$$

Here Σ_{I} is the self energy (3.37). So we arrived at the same result as given in Eq. (3.36).

¹ Strictly speaking we omitted a projection operator P_{II} on the right hand side. Since we only want to apply G_{II} onto vectors from $\text{range}(P_{\text{II}})$ this projection operator is not necessary and only obscures the derivation.

Appendix F

Derivation of the Peierls phase

In this appendix we want to give a more detailed derivation of the Peierls phase occurring in the tight binding Hamiltonian (3.50) describing a magnetic gauge field.

We start from the two dimensional continuous Schrödinger equation with a magnetic gauge field:

$$\begin{aligned} H &= \frac{1}{2m} [-i\hbar\nabla - q\mathbf{A}]^2 + V \\ &= -\frac{\hbar^2}{2m}\Delta + \frac{q^2}{2m}\mathbf{A}^2 + i\frac{\hbar q}{2m}[\nabla\cdot\mathbf{A}] + i\frac{\hbar q}{m}\mathbf{A}\cdot\nabla + V. \end{aligned} \quad (\text{F.1})$$

In the following considerations we focus on the x direction and only consider the special case $\mathbf{A}(x, y) = \begin{bmatrix} A(x) \\ 0 \end{bmatrix}$ (the y dependence of A is at the moment of no concern). The general case can be recovered by applying the same considerations to the y direction.

As a first step we discretize the operator (F.1) using the finite difference approximations (3.9):

$$\begin{aligned} (H\Psi)_j &= -\frac{\hbar^2}{2m(\Delta x)^2} [\Psi_{j+1} + \Psi_{j-1} - 2\Psi_j] + i\frac{\hbar q}{2m\Delta x} A_j [\Psi_{j+1} - \Psi_{j-1}] \\ &\quad + \left[\frac{q^2}{2m} A_j^2 + i\frac{\hbar q}{2m} \frac{\partial A_j}{\partial x} \right] \Psi_j + V_j \Psi_j + \mathcal{O}((\Delta x)^2) \\ &= -\alpha \Psi_{j+1} \left[1 - i\frac{q}{\hbar} A_j \Delta x \right] - \alpha \Psi_{j-1} \left[1 + i\frac{q}{\hbar} A_j \Delta x \right] \\ &\quad + (2\alpha + V_j) \Psi_j + \left[\frac{q^2}{2m} A_j^2 + i\frac{\hbar q}{2m} \frac{\partial A_j}{\partial x} \right] \Psi_j + \mathcal{O}((\Delta x)^2). \end{aligned} \quad (\text{F.2})$$

Here we have used the lattice parameter $\alpha = \frac{\hbar^2}{2m(\Delta x)^2}$ introduced in Eq. (3.10). The goal is now to transform Eq. (F.2) into a more convenient form while retaining the same order $\mathcal{O}((\Delta x)^2)$ of the error term.

We first use the relations

$$\begin{aligned} -A_j \Delta x &= -\int_{x_j}^{x_{j+1}} A(s) ds + \frac{1}{2} \frac{\partial A_j}{\partial x} (\Delta x)^2 + \frac{1}{6} \frac{\partial^2 A_j}{\partial x^2} (\Delta x)^3 + \mathcal{O}((\Delta x)^4) \\ +A_j \Delta x &= -\int_{x_j}^{x_{j-1}} A(s) ds + \frac{1}{2} \frac{\partial A_j}{\partial x} (\Delta x)^2 - \frac{1}{6} \frac{\partial^2 A_j}{\partial x^2} (\Delta x)^3 + \mathcal{O}((\Delta x)^4) \end{aligned} \quad (\text{F.3})$$

$$\frac{1}{2} [\Psi_{j+1} + \Psi_{j-1}] = \Psi_j + \mathcal{O}((\Delta x)^2) \quad \Psi_{j+1} - \Psi_{j-1} = \mathcal{O}(\Delta x) \quad (\text{F.4})$$

derived from Taylor series of $A(x)$ and $\Psi(x)$ around the point x_j to eliminate the term $i \frac{\hbar q}{2m} \frac{\partial A_j}{\partial x} \Psi_j$ from Eq. (F.2):

$$\begin{aligned} & -\alpha \Psi_{j+1} \left[1 - i \frac{q}{\hbar} A_j \Delta x \right] - \alpha \Psi_{j-1} \left[1 + i \frac{q}{\hbar} A_j \Delta x \right] + i \frac{\hbar q}{2m} \frac{\partial A_j}{\partial x} \Psi_j \\ &= -\alpha \Psi_{j+1} \left[1 - i \frac{q}{\hbar} \int_{x_j}^{x_{j+1}} A(s) ds \right] - \alpha \Psi_{j-1} \left[1 - i \frac{q}{\hbar} \int_{x_j}^{x_{j-1}} A(s) ds \right] + i \frac{\hbar q}{2m} \frac{\partial A_j}{\partial x} \Psi_j \\ & \quad - i \frac{\hbar q}{2m} \frac{\partial A_j}{\partial x} \frac{1}{2} [\Psi_{j+1} + \Psi_{j-1}] + i \frac{\hbar q}{2m} \frac{\partial^2 A_j}{\partial x^2} \Delta x \frac{1}{6} [\Psi_{j-1} - \Psi_{j+1}] + \mathcal{O}((\Delta x)^2) \\ &= -\alpha \Psi_{j+1} \left[1 - i \frac{q}{\hbar} \int_{x_j}^{x_{j+1}} A(s) ds \right] - \alpha \Psi_{j-1} \left[1 - i \frac{q}{\hbar} \int_{x_j}^{x_{j-1}} A(s) ds \right] + \mathcal{O}((\Delta x)^2). \end{aligned}$$

We now use the exponential transformation

$$\begin{aligned} 1 - i \frac{q}{\hbar} \int_{x_j}^{x_{j+1}} A(s) ds &= \exp \left[-i \frac{q}{\hbar} \int_{x_j}^{x_{j+1}} A(s) ds \right] + \frac{q^2}{2\hbar^2} \left[\int_{x_j}^{x_{j+1}} A(s) ds \right]^2 \\ & \quad - \frac{i q^3}{6 \hbar^3} \left[\int_{x_j}^{x_{j+1}} A(s) ds \right]^3 + \mathcal{O}((\Delta x)^4) \\ &= \exp \left[-i \frac{q}{\hbar} \int_{x_j}^{x_{j+1}} A(s) ds \right] + \frac{q^2}{2\hbar^2} A_j^2 (\Delta x)^2 \\ & \quad + \left[\frac{q^2}{2\hbar^2} A_j \frac{\partial A_j}{\partial x} - \frac{i q^3}{6 \hbar^3} A_j^3 \right] (\Delta x)^3 + \mathcal{O}((\Delta x)^4) \end{aligned}$$

and the equivalent transformation for $1 - i \frac{q}{\hbar} \int_{x_j}^{x_{j-1}} A(s) ds$ to further eliminate the term $\frac{q^2}{2m} A_j^2 \Psi_j$ from Eq. (F.2):

$$\begin{aligned} & -\alpha \Psi_{j+1} \left[1 - i \frac{q}{\hbar} \int_{x_j}^{x_{j+1}} A(s) ds \right] - \alpha \Psi_{j-1} \left[1 - i \frac{q}{\hbar} \int_{x_j}^{x_{j-1}} A(s) ds \right] + \frac{q^2}{2m} A_j^2 \Psi_j \\ &= -\alpha \Psi_{j+1} \exp \left[-i \frac{q}{\hbar} \int_{x_j}^{x_{j+1}} A(s) ds \right] - \alpha \Psi_{j-1} \exp \left[-i \frac{q}{\hbar} \int_{x_j}^{x_{j-1}} A(s) ds \right] \\ & \quad - \frac{q^2}{2m} A_j^2 \frac{1}{2} [\Psi_{j+1} + \Psi_{j-1}] + \frac{q^2}{2m} A_j^2 \Psi_j + [\Psi_{j+1} - \Psi_{j-1}] \mathcal{O}(\Delta x) + \mathcal{O}((\Delta x)^2) \\ &= -\alpha \Psi_{j+1} \exp \left[-i \frac{q}{\hbar} \int_{x_j}^{x_{j+1}} A(s) ds \right] - \alpha \Psi_{j-1} \exp \left[-i \frac{q}{\hbar} \int_{x_j}^{x_{j-1}} A(s) ds \right] + \mathcal{O}((\Delta x)^2). \end{aligned}$$

Again we here used the relations (F.4).

So we finally transformed Eq. (F.2) into the form:

$$\begin{aligned} (H\Psi)_j &= -\alpha \Psi_{j+1} \exp \left[-i \frac{q}{\hbar} \int_{x_j}^{x_{j+1}} A(s) ds \right] - \alpha \Psi_{j-1} \exp \left[-i \frac{q}{\hbar} \int_{x_j}^{x_{j-1}} A(s) ds \right] \\ & \quad + (2\alpha + V_j) \Psi_j + \mathcal{O}((\Delta x)^2). \end{aligned} \quad (\text{F.5})$$

This form (F.5) is superior to the original form (F.2) because of following three reasons:

- The modulus of the coupling matrix elements is left unchanged in Eq. (F.5). Only the phase of the coupling matrix elements gets alternated by the magnetic gauge field. This phase factor $\exp \left[-i \frac{q}{\hbar} \int_{x_j}^{x_{j \pm 1}} A(s) ds \right]$ is called a Peierls phase [163].
- The tight binding Hamiltonian (F.5) is automatically selfadjoint in contrast to Eq. (F.2).
- If one assumes for a moment that A does not depend on x one can calculate the eigenenergies of Eq. (F.5) as it was done in Sec. 3.4.1. This gives as a generalization of Eq. (3.15) the dispersion relation

$$\mu = V + 2\alpha \left(1 - \cos \left[\left(k - \frac{q}{\hbar} A \right) \Delta x \right] \right) . \quad (\text{F.6})$$

Because of the relation $p = \hbar k$ this is a realization of the minimal coupling scheme [186] $\mathbf{p} \rightarrow \mathbf{p} - q\mathbf{A}$ to include magnetic gauge fields in the framework of the tight binding model. The same argument is also used in the alternative derivation given in Sec. 3.6.3.

Repeating the derivation of Eq. (F.5) for the the y direction we get the most general discretization of the continuous two dimensional Schrödinger equation (F.1) with a magnetic gauge field:

$$\begin{aligned} (H\Psi)_{(x,y)} &= \left(4\alpha + V_{(x,y)} \right) \Psi_{(x,y)} \\ &- \alpha \exp \left(i \frac{q}{\hbar} \int_{(x+1,y)}^{(x,y)} \mathbf{A}(\mathbf{r}) d\mathbf{r} \right) \Psi_{(x+1,y)} - \alpha \exp \left(i \frac{q}{\hbar} \int_{(x-1,y)}^{(x,y)} \mathbf{A}(\mathbf{r}) d\mathbf{r} \right) \Psi_{(x-1,y)} \\ &- \alpha \exp \left(i \frac{q}{\hbar} \int_{(x,y+1)}^{(x,y)} \mathbf{A}(\mathbf{r}) d\mathbf{r} \right) \Psi_{(x,y+1)} - \alpha \exp \left(i \frac{q}{\hbar} \int_{(x,y-1)}^{(x,y)} \mathbf{A}(\mathbf{r}) d\mathbf{r} \right) \Psi_{(x,y-1)} . \end{aligned} \quad (\text{F.7})$$

This is the most natural generalization of the tight binding Hamiltonian (3.41) to include a magnetic gauge field. Here (x, y) is a integer pair describing the point on the lattice. The integral $\int_a^b \mathbf{A}(\mathbf{r}) d\mathbf{r}$ is taken along the edge connecting the two neighboring lattice points a and b .

Another rigorous derivation of the Peierls phase used in the tight binding Hamiltonian (F.7) is given in [29].

Appendix G

The stability amplitude in Birkhoff coordinates

The topic of this appendix is to calculate the stability amplitude A_γ which appears in the semi-classical Green function Eq. (6.1). We restrict ourselves to two dimensional billiard systems where one can use local Birkhoff coordinates [123] to characterize trajectories inside the cavity. At boundary points \mathbf{r}_n we use the arclength along the boundary as position s_n and the variable $p_n = \cos \alpha_n$ (here α_n is the angle between the trajectory and the tangent) as (dimensionless) momentum (see Fig. G.1). The derivative of the (discrete) time evolution in the variables (s_n, p_n) is calculated as follows¹ (here $q_n = \sin \alpha_n$ and κ_n is the curvature of the boundary at point \mathbf{r}_n) [19, 123]

$$\begin{bmatrix} \frac{\partial s_{n+1}}{\partial s_n} & \frac{\partial s_{n+1}}{\partial p_n} \\ \frac{\partial p_{n+1}}{\partial s_n} & \frac{\partial p_{n+1}}{\partial p_n} \end{bmatrix} = \begin{bmatrix} -\frac{q_n}{q_{n+1}} - \frac{L_n \kappa_n}{q_{n+1}} & -\frac{L_n}{q_n q_{n+1}} \\ -\kappa_n q_{n+1} - \kappa_{n+1} q_n - L_n \kappa_n \kappa_{n+1} & -\frac{q_{n+1}}{q_n} - \frac{L_n \kappa_{n+1}}{q_n} \end{bmatrix}. \quad (\text{G.1})$$

The derivative for a trajectory involving bounces at multiple boundary points can be calculated using the chain rule which amounts to matrix multiplication of Eq. (G.1).

The stability amplitude A_γ used in the semiclassical Green function Eq. (6.1) can be calculated as follows:

$$A_\gamma = \frac{2\pi}{(2\pi i \hbar)^{3/2}} |\det a_\gamma|^{-1/2} \quad \text{with} \quad a_\gamma = \frac{\partial(\mathbf{r}, \mathbf{r}', E)}{\partial(\mathbf{p}', \mathbf{r}', T)}.$$

¹ The signs in this formula depend on the convention used for the local coordinate system, especially for the curvature. Therefore other authors might use different signs.

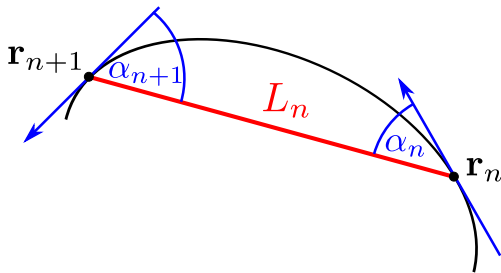


Figure G.1: For a trajectory between point \mathbf{r}_n and \mathbf{r}_{n+1} we use the cosines of the angles α_n and α_{n+1} between the trajectory and the tangents as (dimensionless) momenta. The length L_n is the distance between \mathbf{r}_n and \mathbf{r}_{n+1} .

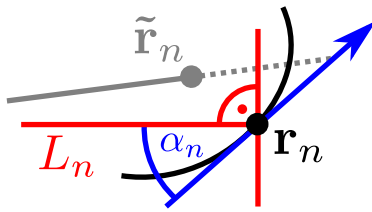


Figure G.2: This figure illustrates how to calculate $\frac{\partial \mathbf{r}_n}{\partial p_0}$ for a fixed total travelling time T . If we change p_0 , the endpoint moves from \mathbf{r}_n to $\tilde{\mathbf{r}}_n$. Noting that the modified trajectory remains approximately parallel to the old one (allowing us to discard second order effects) we arrive at $\frac{\partial \mathbf{r}_n}{\partial p_0} = q_n \frac{\partial s_n}{\partial p_0} \hat{v}_\perp + \hat{v}_\parallel c_\parallel$ where c_\parallel is some constant which is not interesting to us.

Here \mathbf{r}' and \mathbf{r} (with $\mathbf{r}' \equiv \mathbf{r}_0$ and $\mathbf{r} \equiv \mathbf{r}_n$) denote respectively the start and endpoint of the trajectory; T is the time coordinate and $E = mv^2/2 = \hbar^2 k^2/(2m)$ is the energy. Developing the determinant after \mathbf{r}' gives

$$|\det a_\gamma| = \left| \det \frac{\partial(\mathbf{r}, E)}{\partial(\mathbf{p}', T)} \right| \quad \text{for } \mathbf{r}' \text{ fixed.}$$

Instead of \mathbf{p}' we now use the dimensionless Birkhoff coordinate p' (with $p' \equiv p_0$ and $p \equiv p_n$) and the wavevector k (which does not influence the shape of the trajectory)

$$\mathbf{p}' = \hbar k \begin{pmatrix} \sqrt{1 - p'^2} \\ p' \end{pmatrix}$$

which allows us to write

$$|\det a_\gamma| = \left| \det \frac{\partial(\mathbf{r}, E)}{\partial(\mathbf{p}', T)} \right| = \left| \det \frac{\partial(\mathbf{r}, E)}{\partial(p', k, T)} \right| \left| \det \frac{\partial(\mathbf{p}', T)}{\partial(p', k, T)} \right|^{-1}.$$

The determinant of the two matrices can now be calculated separately. $\frac{\partial(\mathbf{p}', T)}{\partial(p', k, T)}$ is easy to handle:

$$\left| \det \frac{\partial(\mathbf{p}', T)}{\partial(p', k, T)} \right| = \left| \det \begin{pmatrix} -\hbar k p' (1 - p'^2)^{-1/2} & \sqrt{1 - p'^2} \hbar \\ \hbar k & p' \hbar \end{pmatrix} \right| = \frac{\hbar^2 k}{q'}.$$

$\frac{\partial(\mathbf{r}, E)}{\partial(p', k, T)}$ requires some tricks:

$$\begin{aligned} \left| \det \frac{\partial(\mathbf{r}, E)}{\partial(p', k, T)} \right| &= \left| \det \begin{array}{c|cc} & \mathbf{p}' & \mathbf{k} & \mathbf{T} \\ \hline \mathbf{r} & * & * & * \\ \hline E & 0 & \hbar^2 k/m & 0 \end{array} \right| = \frac{\hbar^2 k}{m} \left| \det \left[\frac{\partial \mathbf{r}}{\partial p'} \mid \frac{\partial \mathbf{r}}{\partial T} \right] \right| \\ &= \frac{\hbar^3 k^2}{m^2} q \frac{\partial s}{\partial p'} \left| \det \left[\hat{v}_\perp \mid \hat{v}_\parallel \right] \right| = \frac{\hbar^3 k^2}{m^2} q \frac{\partial s}{\partial p'}. \end{aligned}$$

Firstly we develop the determinant after the last row. Then we use $\frac{\partial \mathbf{r}}{\partial T} = \hat{v}_\parallel \hbar k/m$ where \hat{v}_\parallel is the unit vector giving the trajectory direction at the endpoint. For the other column we use the relation $\frac{\partial \mathbf{r}}{\partial p'} = q \frac{\partial s}{\partial p'} \hat{v}_\perp + \hat{v}_\parallel c_\parallel$ (see Fig. G.2) where \hat{v}_\perp is the unit vector perpendicular to \hat{v}_\parallel . The rest follows from the column-linearity of the determinant, $\left| \det \left[\hat{v}_\perp \mid \hat{v}_\parallel \right] \right| = 1$ and $\left| \det \left[\hat{v}_\parallel \mid \hat{v}_\parallel \right] \right| = 0$.

The final result is thus

$$A_\gamma = \frac{2\pi}{(2\pi i \hbar)^{3/2}} |\det a_\gamma|^{-1/2} \quad \text{with} \quad |\det a_\gamma| = q q' \frac{\hbar k}{m^2} \frac{\partial s}{\partial p'}.$$

Appendix H

A smooth switching function

Let $I \subset \mathbb{R}$ be an interval and $\mathbb{R} \ni d > 0$ a positive number. We seek now a function $F : \mathbb{R} \rightarrow \mathbb{R}$ which is exactly one inside I and is exactly zero on any point which has at least a distance d from I . In between the function should vary smoothly between zero and one. See Fig. H.1 for an illustration. More exactly we require that $F \in C^\infty(\mathbb{R})$ which means that F is infinitely often continuously differentiable. (Of course F cannot be analytic.)

In the following sections a and b denote two constants which will be fixed later. These two constants are subject to following constraints:

$$\begin{aligned} a &\in \mathbb{R} \\ b &\in \mathbb{R} \quad \text{with} \quad b > 0. \end{aligned} \tag{H.1}$$

In the end any allowed values of a and b will give us a function F with the desired characteristics, but we use a and b to optimize the properties of F .

The material in this section is not new. A similar construction is the “partition of unity” which is used in vector analysis (see for example [141]).

An auxiliary function

We now define an auxiliary function $g : [-1, 1] \rightarrow \mathbb{R}$ as follows:

$$g(x) = \begin{cases} e^{-b\left(ax^2 + \frac{1}{1-x^2}\right)} & \text{for } |x| < 1 \\ 0 & \text{for } |x| = 1. \end{cases}$$

We have

- $g(x) = g(-x)$
- $g^{(n)}(+1) = g^{(n)}(-1) = 0$ for all $n \in \mathbb{N}_0$.

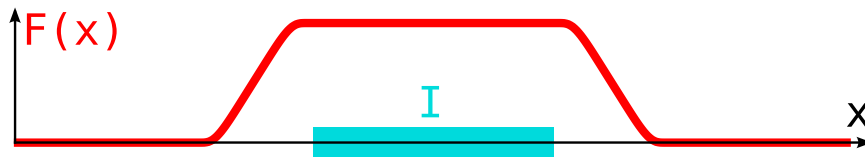


Figure H.1: The function $F(x)$. It is one inside the interval I and is zero on points which are at least a given distance $d > 0$ away from I .

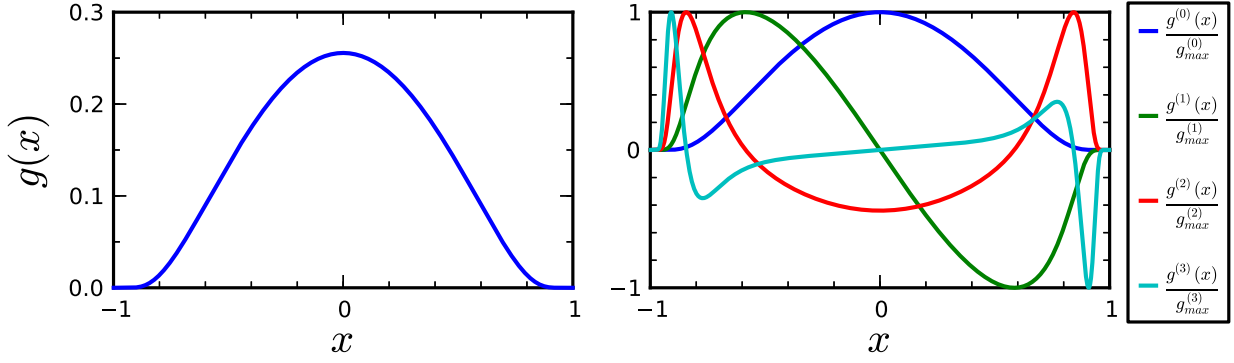


Figure H.2: The left panel shows a plot of $g(x)$. The right panel shows a plot of the normalized derivatives of $g(x)$. The parameter set (H.7) is used here.

Only the last item needs clarification. We first note that we understand the derivatives of $g(x)$ at $x = 1$ as limit in the following way:

$$g^{(n)}(+1) = \lim_{\substack{x \rightarrow 1 \\ x < 1}} g^{(n)}(x) .$$

Every derivative of $g(x)$ has the form

$$g^{(n)}(x) = R(x)e^{-b\left(ax^2 + \frac{1}{1-x^2}\right)}$$

where $R(x)$ denotes a rational function. Because of

$$\frac{1}{1-x^2} = \frac{1}{2} \left(\frac{1}{1+x} + \frac{1}{1-x} \right)$$

we have:

$$\lim_{\substack{x \rightarrow 1 \\ x < 1}} g^{(n)}(x) = e^{-b(a+\frac{1}{4})} \lim_{\substack{x \rightarrow 1 \\ x < 1}} R(x)e^{-\frac{b}{2} \frac{1}{1-x}} .$$

We now make the variable substitution

$$\tilde{x} = \frac{b}{2} \frac{1}{1-x} .$$

This results in

$$\lim_{\substack{x \rightarrow 1 \\ x < 1}} g^{(n)}(x) = \lim_{\tilde{x} \rightarrow \infty} \frac{\tilde{R}(\tilde{x})}{e^{\tilde{x}}}$$

where $\tilde{R}(\tilde{x})$ is another rational function. Therefore it is at most of polynomial growth as $\tilde{x} \rightarrow \infty$. Because $e^{\tilde{x}}$ grows faster than any power of \tilde{x} as $\tilde{x} \rightarrow \infty$ we get

$$\lim_{\substack{x \rightarrow 1 \\ x < 1}} g^{(n)}(x) = 0 .$$

This establish simultaneously the continuity of $g(x)$ at $x = 1$.

We can continue $g(x)$ to a function $\mathbb{R} \rightarrow \mathbb{R}$ if we set $g(x) = 0$ for $|x| \geq 1$. Then g belongs to the class $\mathcal{C}^\infty(\mathbb{R})$. This extended g is then called a “bump” function.

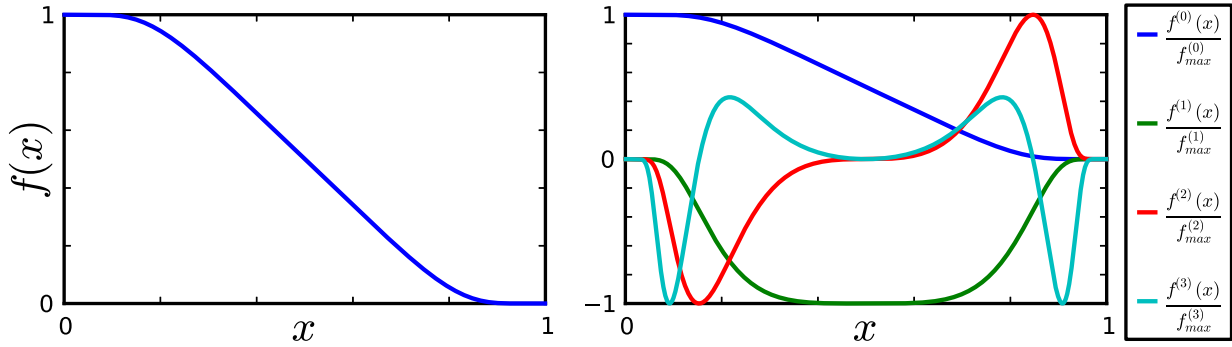


Figure H.3: The left panel shows a plot of $f(x)$. The right panel shows a plot of the normalized derivatives of $f(x)$. The parameter set (H.7) is used here.

The switching function

We now define a function $f : [0, 1] \rightarrow \mathbb{R}$ which varies smoothly from zero to one:

$$f(x) = \frac{g(x)}{g(x-1) + g(x)}.$$

We have following properties:

$$f(0) = 1 \quad \text{and} \quad f(1) = 0 \tag{H.2}$$

$$f^{(n)}(0) = f^{(n)}(1) = 0 \quad \text{for all } n \in \mathbb{N} \tag{H.3}$$

$$f(x) = 1 - f(1-x) \tag{H.4}$$

$$f^{(2n)}(\tfrac{1}{2}) = 0 \quad \text{for all } n \in \mathbb{N}. \tag{H.5}$$

(H.2) and (H.3) follow directly from the properties of $g(x)$. (H.4) follows from the symmetry relation of $g(x)$ and from the definition. (H.5) is a direct consequence of (H.4).

We are now ready to build the desired function $F(x)$. Let x_0, x_1, x_2 and x_3 be four points in \mathbb{R} with $x_0 < x_1 < x_2 < x_3$. The interval I is in this case equivalent to $[x_1, x_2]$. Define $F : \mathbb{R} \rightarrow \mathbb{R}$ as:

$$F(x) = \begin{cases} 0 & \text{for } x \leq x_0 \\ f\left(\frac{x-x_1}{x_0-x_1}\right) & \text{for } x_0 \leq x \leq x_1 \\ 1 & \text{for } x_1 \leq x \leq x_2 \\ f\left(\frac{x-x_2}{x_3-x_2}\right) & \text{for } x_2 \leq x \leq x_3 \\ 0 & \text{for } x_3 \leq x. \end{cases}$$

This F has all desired properties mentioned at the beginning of this appendix. One has to stress that F is an element of $\mathcal{C}^\infty(\mathbb{R})$, which means that F is infinitely often continuously differentiable (albeit it is not analytic). This follows from (H.2) and (H.3). See Fig. H.1 for a plot of F .

These considerations are valid for all allowed parameters a and b . We will now select the parameters so that the function $F(x)$ is optimal in a later specified way.

Selection of the parameter b

The first criterion is that $f(x)$ should resemble a straight line as much as possible at the position $x = \frac{1}{2}$. We already have $f^{(2n)}(\frac{1}{2}) = 0$ for all $n \in \mathbb{N}$. Therefore it is natural to postulate:

$$f^{(3)}(\tfrac{1}{2}) = 0.$$

This will give us a quadratic equation which a and b must satisfy.

We rewrite $f(x)$ as

$$f(x) = \frac{1}{\frac{g(x-1)}{g(x)} + 1} = \frac{1}{e^{R(x)} + 1}$$

where $R(x)$ is following rational function:

$$\begin{aligned} R(x) &= -b \left[a(1-2x) + \frac{1}{x(2-x)} - \frac{1}{1-x^2} \right] \\ &= -ba(1-2x) - \frac{b}{2} \left[\frac{1}{x} + \frac{1}{2-x} - \frac{1}{1+x} - \frac{1}{1-x} \right]. \end{aligned}$$

The relation $R(\frac{1}{2}) = R^{(2)}(\frac{1}{2}) = 0$ (note the symmetry of the bracket under the replacement $x \mapsto 1-x$) enable us to calculate $f^{(3)}(\frac{1}{2})$ in following way

$$f^{(3)}(\frac{1}{2}) = \frac{1}{8} \left(R^{(1)}(\frac{1}{2}) \right)^3 - \frac{1}{4} R^{(3)}(\frac{1}{2})$$

which leads to

$$b^3 \left(2a + \frac{32}{9} \right)^3 - \frac{5120}{27} b = 0.$$

The only interesting solution of this is

$$b = \frac{720}{\sqrt{30}(9a+16)^{3/2}} = \frac{720}{(9a+16)\sqrt{270a+480}}. \quad (\text{H.6})$$

We now have b as a function of a . It remains to fix a .

Selection of the parameter a

The second criterion is that the slope of $f(x)$ should vary as smooth as possible. We therefore have to minimize $f^{(2)}(x)$ in some suitable way. In order to quantize this we therefore postulate that the maximum of $f^{(2)}(x)$ should be as small as possible as a function of a . This criterion gives the non-linear system of equations

$$\frac{\partial^3 f(a, x)}{\partial x^3} = 0 \qquad \frac{\partial^3 f(a, x)}{\partial x^2 \partial a} = 0.$$

Of course b is here fixed as in Eq. (H.6). This system of equation can be solved numerically with the Newton method described as in App. A. This gives the solution set (with $x = 0.847058295857\dots$)

$$a = 0.55774661228311051916\dots \qquad b = 1.36405378305679796381\dots \quad (\text{H.7})$$

Rational approximation of the parameters

The exact values of (H.7) are quite unhandy. In practice one can use a rational approximation to a . We here use continued fractions which in some sense are the best rational approximations to elements of \mathbb{R} (see [131]).

$$a = \text{contfrac}(0, 1, 1, 3, 1, 4, 1, 5, 1, 58, 1, \dots) = (1 + (1 + (3 + (1 + (4 + \dots)^{-1})^{-1})^{-1})^{-1})^{-1}$$

We therefore have following series of rational approximations to a :

$$1, \frac{1}{2}, \frac{4}{7}, \frac{5}{9}, \frac{24}{43}, \frac{29}{52}, \frac{169}{303}, \frac{198}{355}, \dots$$

A good choice is following parameter set where b is fixed as in Eq. (H.6):

$$a = \frac{5}{9} \qquad b = \frac{8}{7} \sqrt{\frac{10}{7}}. \quad (\text{H.8})$$

The difference between $f(x)$ with the parameters (H.7) and $f(x)$ with the parameters (H.8) is minimal:

$$\max_{x \in [0,1]} |f_{a=\frac{5}{9}}(x) - f_{a=0.557746612283\dots}(x)| < 1.44 \cdot 10^{-4}.$$

Miscellaneous

Sometimes it is necessary to differentiate or to integrate $F(x)$. Differentiation is straightforward, but integration is not. The best method to calculate the antiderivative of $F(x)$ is to use an Chebyshev approximation of $f(x)$ and use the Chebyshev coefficients to numerically evaluate the antiderivative. For details on how to do that see [172].

The Chebyshev coefficients do not change once a and b is fixed, so one can calculate them once and for all and put them into a programming library. In comparison to this the awkwardness of (H.7) is negligible and so I use this parameter set.

In principle one could have avoided the complicated construction of $F(x)$ and use a function like

$$\tilde{F}(x) = \frac{1}{2} \left[1 + \tanh \left(\frac{x - x_0}{\alpha} \right) \right] \frac{1}{2} \left[1 + \tanh \left(\frac{x_1 - x}{\alpha} \right) \right].$$

$\tilde{F}(x)$ is also useful as a switching function. But it has the disadvantage that it is never exactly zero and never exactly one. Instead these values are only taken approximately over certain intervals. So the length of the region where $\tilde{F}(x)$ goes from zero to one is not well defined. The length depends on the parameter α and one has to do some ad hoc decision on how to choose α .

Once one has encapsulated $F(x)$ into a library it is as easy to use as the tanh-approach $\tilde{F}(x)$. Therefore I prefer to use $F(x)$.

The analysis of the optimal parameters a and b is not new. I found the parameter set (H.8) in an old wikipedia article albeit without any reference or any explanation why this particular values are chosen. I was not able to find any “real” reference of (H.7) or (H.8) in the literature. Only the obvious choice $a = 0$ and $b = 1$ can be easily found ([141]).

References

- [1] M. Abramowitz and I. A. Stegun (editors). *Handbook of Mathematical Functions* (National Bureau of Standards, 1970)
- [2] J. Aguilar and J. M. Combes. *A Class of Analytic Perturbations for One-body Schrödinger Hamiltonians*. Commun. math. Phys. **22** (1971), p. 269
- [3] E. Akkermans and G. Montambaux. *Mesoscopic Physics of Electrons and Photons* (2007)
- [4] E. Akkermans, P. E. Wolf and R. Maynard. *Coherent Backscattering of Light by Disordered Media: Analysis of the Peak Line Shape*. Phys. Rev. Lett. **56** (1986), p. 1471
- [5] M. P. V. Albada and A. Lagendijk. *Observation of Weak Localization of Light in a Random Medium*. Phys. Rev. Lett. **55** (1985), p. 2692
- [6] B. Al'tshuler, A. Aronov and B. Spivak. *The Aaranov-Bohm effect in disordered conductors*. JETP Letters **33** (1981), p. 94
- [7] M. H. Anderson, J. R. Ensher, M. R. Matthews, C. E. Wieman and E. A. Cornell. *Observation of Bose-Einstein Condensation in a Dilute Atomic Vapor*. Science **269** (1995), p. 198
- [8] P. W. Anderson. *Absence of Diffusion in Certain Random Lattices*. Phys. Rev. **109** (1958), p. 1492
- [9] J. F. Annett. *Superconductivity, Superfluids and Condensates* (Oxford University Press, 2003)
- [10] X. Antoine, A. Arnold, C. Besse, M. Ehrhardt and A. Schädle. *A Review of Transparent and Artificial Boundary Conditions Techniques for Linear and Nonlinear Schrödinger Equations*. Communications in Computational Physics **4** (2008), p. 729
- [11] A. Arnold, M. Ehrhardt and I. Sofronov. *Discrete transparent boundary conditions for the Schrödinger equation: Fast calculation, approximation and stability*. Comm. Math. Sci. **1** (2003), p. 501

- [12] G. Ashkenazi, R. Kosloff, S. Ruhman and H. Tal-Ezer. *Newtonian propagation methods applied to the photodissociation dynamics of I_3^-* . Journal of Chemical Physics **103** (1995), p. 10005
- [13] M. Y. Azbel'. *Quantum turbulence and resonant tunneling*. Phys. Rev. B **59** (1999), p. 8049
- [14] E. Balslev and J. M. Combes. *Spectral Properties of Many-body Schrödinger Operators with Dilatation-analytic Interactions*. Commun. math. Phys. **22** (1971), p. 280
- [15] H. Baranger, R. Jalabert and A. D. Stone. *Quantum-chaotic scattering effects in semiconductor microstructures*. Chaos **3** (1993), p. 665
- [16] S. M. Barnett. *Why a Condensate Can Be Thought of as Having a Definite Phase*. Journal of Research of the National Institute of Standards and Technology **101** (1996), p. 593
- [17] K. Bergmann, H. Theuer and B. W. Shore. *Coherent population transfer among quantum states of atoms and molecules*. Rev. Mod. Phys. **70** (1998), p. 1003
- [18] M. V. Berry. *Regular and irregular semiclassical wavefunctions*. Journal of Physics A: Mathematical and General **10** (1977), p. 2083
- [19] M. V. Berry. *Regularity and chaos in classical mechanics, illustrated by three deformations of a circular 'billiard'*. European Journal of Physics **2** (1981), p. 91
- [20] J. Billy, V. Josse, Z. Zuo, A. Bernard, B. Hambrecht, P. Lugan, D. Clément, L. Sanchez-Palencia, P. Bouyer and A. Aspect. *Direct observation of Anderson localization of matter waves in a controlled disorder*. Nature **453** (2008), p. 891
- [21] G. Birkel and J. Fortágh. *Micro traps for quantum information processing and precision force sensing*. Laser & Photon **1** (2007), p. 12
- [22] F. Bloch. *Über die Quantenmechanik der Elektronen in Kristallgittern*. Zeitschrift für Physik **52** (1929), p. 555
- [23] Blümel and U. Smilansky. *Classical Irregular Scattering and Its Quantum-Mechanical Implications*. Physical Review Letters **60** (1988), p. 477
- [24] J. D. Bodyfelt, T. Kottos and B. Shapiro. *One-Parameter Scaling Theory for Stationary States of Disordered Nonlinear Systems*. Phys. Rev. Lett. **104** (2010), p. 164102
- [25] S. Bose. *Plancks Gesetz und Lichtquantenhypothese*. Zeitschrift für Physik **26** (1924), p. 178
- [26] W. E. Boyce and R. C. DiPrima. *Elementary Differential Equations and Boundary Value Problems* (John Wiley & Sons, Inc., 2001)
- [27] R. Boyd. *Nonlinear Optics* (2007), third edition
- [28] V. Boyer, R. Godun, G. Smirne, D. Cassettari, C. Chandrashekar, A. Deb, Z. Laczik and C. Foot. *Dynamic manipulation of Bose-Einstein condensates with a spatial light modulator*. Physical Review A **73** (2006), p. 031402

- [29] T. Boykin, R. C. Bowen and G. Klimeck. *Electromagnetic coupling and gauge invariance in the empirical tight-binding method*. Physical Review B **63** (2001), p. 245314
- [30] M. Brack and R. K. Bhaduri. *Semiclassical Physics* (Addison-Wesley, 1997)
- [31] C. C. Bradley, C. A. Sackett, J. J. Tollett and R. G. Hulet. *Evidence of Bose-Einstein Condensation in an Atomic Gas with Attractive Interactions*. Phys. Rev. Lett. **75** (1995), p. 1687
- [32] G. Breit and E. Wigner. *Capture of Slow Neutrons*. Phys. Rev. **49** (1936), p. 519
- [33] I. Bronstein, K. A. Semendjajew, G. Musiol and H. Mühlig. *Taschenbuch der Mathematik* (1999), forth edition
- [34] P. Brouwer and S. Rahav. *A semiclassical theory of the Ehrenfest-time dependence of quantum transport in ballistic quantum dots*. Physical Review B **74** (2006), p. 075322
- [35] P. Böhi, M. Riedel, J. Hoffrogge, J. Reichel, T. Hänsch and P. Treutlein. *Coherent manipulation of Bose-Einstein condensates with state-dependent microwave potentials on an atom chip*. Nature Physics **5** (2009), p. 592
- [36] H. L. Calvo, R. A. Jalabert and H. M. Pastawski. *Semiclassical Theory of Time-Reversal Focusing*. Physical Review Letters **101** (2008), p. 240403
- [37] B. Canuel, F. Leduc, D. Holleville, A. Gauguet, J. Fils, A. Virdis, A. Clairon, N. Dimarcq, C. J. Bordé, A. Landragin and P. Bouyer. *Six-Axis Inertial Sensor Using Cold-Atom Interferometry*. Phys. Rev. Lett. **97** (2006), p. 010402
- [38] I. Carusotto and G. C. La Rocca. *Modulated Optical Lattice as an Atomic Fabry-Perot Interferometer*. Phys. Rev. Lett. **84** (2000), p. 399
- [39] Y. Castin and R. Dum. *Low-temperature Bose-Einstein condensates in time-dependent traps: Beyond the $U(1)$ symmetry-breaking approach*. Physical Review A **57** (1998), p. 3008
- [40] E. Cerboneschi, R. Mannella, E. Arimondo and L. Salasnich. *Oscillation frequencies for a Bose condensate in a triaxial magnetic trap*. Physics Letters A **249** (1998), p. 495
- [41] R. Charrière, M. Cadoret, N. Zahzam, Y. Bidel and A. Bresson. *Local gravity measurement with the combination of atom interferometry and Bloch oscillations*. Phys. Rev. A **85** (2012), p. 013639
- [42] C. Chen, C. Liu, K. Su, T. Lu, Y. Chen and K. Huang. *Statistical properties of experimental coherent waves in microcavity lasers: Analogous study of quantum billiard wave functions*. Physical Review E **75** (2007), p. 046202
- [43] V. Chernyak, S. Choi and S. Mukamel. *Generalized coherent state representation of Bose-Einstein condensates*. Physical Review A **67** (2003), p. 053604
- [44] C. Chin and R. Grimm. *Feshbach resonances in ultracold gases*. Reviews of Modern Physics **82** (2010), p. 1225

- [45] A. Couvert, M. Jeppesen, T. Kawalec, G. Reinaudi, R. Mathevet and D. Guéry-Odelin. *A quasi-monomode guided atom laser from an all-optical Bose-Einstein condensate*. EPL **83** (2008), p. 50001
- [46] J. K. Cullum and R. A. Willoughby. *Lanczos Algorithms for Large Symmetric Eigenvalue Computations* (Birkhäuser, 1985)
- [47] A. Cuyt and L. Wuytack. *Nonlinear Methods in Numerical Analysis* (Elsevier Science Publishers B.V., 1987)
- [48] F. Dalfovo, S. Giorgini and L. P. Pitaevskii. *Theory of Bose-Einstein condensation in trapped gases*. Reviews of Modern Physics **71** (1999), p. 463
- [49] J. Dalibard, F. Gerbier, G. Juzeliūnas and P. Öhberg. *Colloquium : Artificial gauge potentials for neutral atoms*. Rev. Mod. Phys. **83** (2011), p. 1523
- [50] S. Datta. *Electronic Transport in Mesoscopic Systems* (Cambridge University Press, Cambridge, 2007)
- [51] K. B. Davis, M. O. Mewes, M. R. Andrews, N. J. van Druten, D. S. Durfee, D. M. Kurn and W. Ketterle. *Bose-Einstein Condensation in a Gas of Sodium Atoms*. Phys. Rev. Lett. **75** (1995), p. 3969
- [52] T. A. Davis. *Algorithm 832: UMFPACK V4.3—an unsymmetric-pattern multifrontal method*. ACM Transactions On Mathematical Software **30** (2004), p. 196
- [53] T. A. Davis. *User's Guide for SuiteSparseQR, a multifrontal multithreaded sparse QR factorization package*, 2010. <http://www.cise.ufl.edu/research/sparse/SPQR/>
- [54] H. De Raedt and B. De Raedt. *Applications of the generalized Trotter formula*. Physical Review A **28** (1983), p. 3575
- [55] J. E. Debs. *The Application of Bose-Einstein Condensates to Inertial Sensing*. Ph.D. thesis, The Australian National University, 2012
- [56] J. E. Debs, P. A. Altin, T. H. Barter, D. Döring, G. R. Dennis, G. McDonald, R. P. Anderson, J. D. Close and N. P. Robins. *Cold-atom gravimetry with a Bose-Einstein condensate*. Phys. Rev. A **84** (2011), p. 033610
- [57] S. M. Dickerson, J. M. Hogan, A. Sugarbaker, D. M. S. Johnson and M. A. Kasevich. *Multiaxis Inertial Sensing with Long-Time Point Source Atom Interferometry*. Phys. Rev. Lett. **111** (2013), p. 083001
- [58] G. Doetsch. *Anleitung zum praktischen Gebrauch der Laplace-Transformation und der Z-Transformation* (R. Oldenburg Verlag, 1967), third edition
- [59] B. Douçot and R. Rammal. *Quantum Oscillations in Normal-Metal Networks*. Physical Review Letters **55** (1985), p. 1148

- [60] A. Einstein. *Quantentheorie des einatomigen idealen Gases*. Sitzungsberichte der Preussischen Akademie der Wissenschaften, Physikalisch-mathematische Klasse (1924), p. 261
- [61] A. Einstein. *Quantentheorie des einatomigen idealen Gases, 2. Abhandlung*. Sitzungsberichte der Preussischen Akademie der Wissenschaften, Physikalisch-mathematische Klasse (1925), p. 3
- [62] A. Enge, P. Théveny and P. Zimmermann. *mpc — A library for multiprecision complex arithmetic with exact rounding*. INRIA, 0.8.2 edition, 2010. <http://mpc.multiprecision.org/>
- [63] T. Engl, J. Dujardin, A. Argüelles, P. Schlagheck, K. Richter and J. D. Urbina. *Coherent Backscattering in Fock Space: A Signature of Quantum Many-Body Interference in Interacting Bosonic Systems*. Phys. Rev. Lett. **112** (2014), p. 140403
- [64] L. Erdős, B. Schlein and H.-T. Yau. *Rigorous Derivation of the Gross-Pitaevskii Equation*. Physical Review Letters **98** (2007), p. 040404
- [65] T. Ericson. *Fluctuations of Nuclear Cross Sections in the “Continuum” Region*. Physical Review Letters **5** (1960), p. 430
- [66] O. G. Ernst and M. J. Gander. *Why it is Difficult to Solve Helmholtz Problems with Classical Iterative Methods*. In I. Graham, T. Hou, O. Lakkis and R. Scheichl (editors), *Numerical Analysis of Multiscale Problems*, volume 83, p. 325–361 (Springer, 2011)
- [67] T. Ernst, T. Paul and P. Schlagheck. *Transport of ultracold Bose gases beyond the Gross-Pitaevskii description*. Phys. Rev. A **81** (2010), p. 013631
- [68] M. Fattori, C. D’Errico, G. Roati, M. Zaccanti, M. Jona-Lasinio, M. Modugno, M. Inguscio and G. Modugno. *Atom Interferometry with a Weakly Interacting Bose-Einstein Condensate*. Phys. Rev. Lett. **100** (2008), p. 080405
- [69] M. D. Feit, J. A. Fleck and A. Steigner. *Solution of the Schrödinger Equation by a Spectral Method*. Journal of Computational Physics **47** (1982), p. 412
- [70] D. K. Ferry and S. M. Goodnick. *Transport in Nanostructures* (Cambridge University Press, Cambridge, 2001), first edition
- [71] A. L. Fetter. *Nonuniform States of an Imperfect Bose Gas*. Annals of Physics **70** (1972), p. 67
- [72] A. L. Fetter and J. D. Walecka. *Quantum Theory of Many-Particle Systems* (Dover Publications, 2003)
- [73] M. Fierz. *Über die relativistische Theorie kräftefreier Teilchen mit beliebigem Spin*. Helv. Phys. Acta **12** (1939), p. 3
- [74] M. Fink and C. Draeger. *One-Channel Time Reversal of Elastic Waves in a Chaotic 2D-Silicon Cavity*. Physical Review Letters **79** (1997), p. 407

- [75] O. Forster. *Analysis 2* (Vieweg + Teubner, 2008)
- [76] L. Fousse, G. Hanrot, V. Lefèvre, P. Pélissier and P. Zimmermann. *MPFR: A Multiple-Precision Binary Floating-Point Library with Correct Rounding*. ACM Transactions on Mathematical Software **33** (2007), p. 13:1. <http://www.mpfr.org/>
- [77] E. Freitag and R. Busam. *Funktionentheorie 1* (Springer, 2006), fourth. edition
- [78] N. Friedman, A. Kaplan, D. Carasso and N. Davidson. *Observation of Chaotic and Regular Dynamics in Atom-Optics Billiards*. Phys. Rev. Lett. **86** (2001), p. 1518
- [79] M. Frigo and S. G. Johnson. *The Design and Implementation of FFTW3*. Proceedings of the IEEE **93** (2005), p. 216. Special issue on “Program Generation, Optimization, and Platform Adaptation”
- [80] R. Geiger, V. Menoret, G. Stern, N. Zahzam, P. Cheinet, B. Battelier, A. Villing, F. Moron, M. Lours, Y. Bidel, A. Bresson, A. Landragin and P. Bouyer. *Detecting inertial effects with airborne matter-wave interferometry*. Nat Commun **2** (2011), p. 474
- [81] J. Ginibre. *On the Asymptotic Exactness of the Bogoliubov Approximation for Many Boson Systems*. Communications mathematical Physics **8** (1968), p. 26
- [82] N. J. Giordano. *Computational Physics* (Prentice-Hall, Inc., 1997)
- [83] Gligorić, G., Bodyfelt, J. D. and Flach, S. *Interactions destroy dynamical localization with strong and weak chaos*. EPL **96** (2011), p. 30004
- [84] I. Gohberg, P. Lancaster and L. Rodman. *Matrix Polynomials* (Academic Press, New York, 1982)
- [85] G. H. Golub and C. F. van Loan. *Matrix computations* (The Johns Hopkins University Press, 1996), third edition
- [86] M. Greiner, O. Mandel, T. Esslinger, T. W. Hansch and I. Bloch. *Quantum phase transition from a superfluid to a Mott insulator in a gas of ultracold atoms*. Nature **415** (2002), p. 39
- [87] A. Griffin, T. Nikuni and E. Zaremba. *Bose-Condensed Gases at finite Temperatures* (Cambridge University Press, 2009)
- [88] W. Guerin, J.-F. Riou, J. P. Gaebler, V. Josse, P. Bouyer and A. Aspect. *Guided Quasicon- tinuous Atom Laser*. Phys. Rev. Lett. **97** (2006), p. 200402
- [89] G. M. Gusev, Z. D. Kvon, E. B. Olshanetsky and A. Y. Plotnikov. *Magnetic-field asymme- try of nonlinear transport in a small ring*. EPL **88** (2009), p. 47007
- [90] T. L. Gustavson, P. Bouyer and M. A. Kasevich. *Precision Rotation Measurements with an Atom Interferometer Gyroscope*. Phys. Rev. Lett. **78** (1997), p. 2046
- [91] M. C. Gutzwiller. *Chaos in Classical and Quantum Mechanics* (Springer, 1990)
- [92] F. Haake. *Quantum Signatures of Chaos* (Springer, 2001), second edition

- [93] H. Haken and H. Wolf. *Atom- und Quantenphysik* (Springer, 2000), seventh edition
- [94] J. H. Hannay and A. M. Ozorio De Almeida. *Periodic orbits and a correlation function for the semiclassical density of states*. J. Phys. A: Math. Gen. **17** (1984), p. 3429
- [95] T. Hartmann, F. Keck, H. J. Korsch and S. Mossmann. *Dynamics of Bloch oscillations*. New Journal of Physics **6** (2004), p. 2
- [96] T. Hartmann, J. Michl, C. Petitjean, T. Wellens, J.-D. Urbina, K. Richter and P. Schlagheck. *Weak localization with nonlinear bosonic matter waves*. Annals of Physics **327** (2012), p. 1998
- [97] T. Hartmann, J.-D. Urbina, K. Richter and P. Schlagheck. *Intensity distribution of non-linear scattering states*. In M. Robnik (editor), *AIP Conference Proceedings, Volume 1468 - "Let's Face Chaos through Nonlinear Dynamics" 8th International Summer School/Conference*, p. 193 (American Institute of Physics, 2012)
- [98] M. Hartung. *Transport and Coherent Backscattering of Bose-Einstein Condensates in Mesoscopic Systems*. Ph.D. thesis, Universität Regensburg, 2009
- [99] M. Hartung, T. Wellens, C. A. Müller, K. Richter and P. Schlagheck. *Coherent Backscattering of Bose-Einstein Condensates in Two-Dimensional Disorder Potentials*. Physical Review Letters **101** (2008), p. 020603
- [100] F. He, C. Ruiz and A. Becker. *Absorbing boundaries in numerical solutions of the time-dependent Schrödinger equation on a grid using exterior complex scaling*. Phys. Rev. A **75** (2007), p. 053407
- [101] K. Henderson, C. Ryu, C. MacCormick and M. G. Boshier. *Experimental demonstration of painting arbitrary and dynamic potentials for Bose-Einstein condensates*. New Journal of Physics **11** (2009), p. 043030
- [102] P. Henrici. *Computational Complex Analysis, Volume 2* (John Wiley & Sons, Inc., 1977)
- [103] P. Henrici. *Computational Complex Analysis, Volume 3* (John Wiley & Sons, Inc., 1986)
- [104] M. Horvat and T. Prosen. *Uni-directional transport properties of a serpent billiard*. Journal of Physics A: Mathematical and General **37** (2004), p. 3133
- [105] N. Houston, E. Riss and A. Arnold. *Reproducible dynamic dark ring lattices for ultracold atoms*. Journal of Physics B: Atomic, Molecular and Optical Physics **41** (2008), p. 211001
- [106] T. J. Hughes. *The Finite Element Method* (Prentice-Hall, Inc., 1987)
- [107] W. Huisinga, L. Pesce, R. Kosloff and P. Saalfrank. *Faber and Newton polynomial integrators for open-system density matrix propagation*. Journal of Chemical Physics **110** (1999), p. 5538
- [108] W. Hänsel, P. Hommelhoff, T. Hänsch and J. Reichel. *Bose-Einstein condensation on a microelectronic chip*. Nature **413** (2001), p. 498

- [109] P. Šeba, I. Rotter, M. Müller, E. Persson and K. Pichugin. *Collective modes in an open microwave billiard*. Phys. Rev. E **61** (2000), p. 66
- [110] R. A. Jalabert. *The semiclassical tool in mesoscopic physics*. In G. Casati, I. Guarneri and U. Smilansky (editors), *Proceedings of the International School of Physics “Enrico Fermi” Course CXLIII “New Directions in Quantum Chaos”*, p. 145 (IOS Press, Amsterdam, 2000)
- [111] F. Jendrzejewski, A. Bernard, K. Müller, P. Cheinet, V. Josse, M. Piraud, L. Pezze, L. Sanchez-Palencia, A. Aspect and P. Bouyer. *Three-dimensional localization of ultracold atoms in an optical disordered potential*. Nat Phys **8** (2012), p. 398
- [112] F. Jendrzejewski, K. Müller, J. Richard, A. Date, T. Plisson, P. Bouyer, A. Aspect and V. Josse. *Coherent Backscattering of Ultracold Atoms*. Phys. Rev. Lett. **109** (2012), p. 195302
- [113] R. V. Jensen. *Chaotic scattering, unstable periodic orbits, and fluctuations in quantum transport*. Chaos **1** (1991), p. 101
- [114] G. Juzeliūnas, P. Öhberg, J. Ruseckas and A. Klein. *Effective magnetic fields in degenerate atomic gases induced by light beams with orbital angular momenta*. Phys. Rev. A **71** (2005), p. 053614
- [115] R. Kaiser and D. Wiersma (editors). *Proceedings of the International School of Physics “Enrico Fermi” Course CLXXIII “Nano Optics and Atomics: Transport of Light and Matter Waves”* (IOS Press, 2011)
- [116] A. Kaplan, M. Andersen, N. Friedman and N. Davidson. *Atom optics billiards*. In P. Collet, M. Courbage, S. Metens, A. Neishtadt and G. Zaslavsky (editors), *NATO Science Series Volume 182: Chaotic Dynamics and Transport in Classical and Quantum Systems* (Springer, 2005)
- [117] J. Kasprzak, M. Richard, S. Kundermann, A. Baas, P. Jeambrun, J. M. J. Keeling, F. M. Marchetti, M. H. Szymanska, R. Andre, J. L. Staehli, V. Savona, P. B. Littlewood, B. Deveaud and L. S. Dang. *Bose-Einstein condensation of exciton polaritons*. Nature **443** (2006), p. 409
- [118] K. Kato. *Resonances and continuum states in the complex scaling method*. Journal of Physics: Conference Series **49** (2006), p. 73
- [119] J. Klaers, J. Schmitt, F. Vewinger and M. Weitz. *Bose-Einstein condensation of photons in an optical microcavity*. Nature **468** (2010), p. 545
- [120] T. Köhler and K. Burnett. *Microscopic quantum dynamics approach to the dilute condensed Bose gas*. Physical Review A **65** (2002), p. 033601
- [121] T. Köhler and G. Krzysztow. *Production of cold molecules via magnetically tunable Feshbach resonances*. Reviews of Modern Physics **78** (2006), p. 1311
- [122] S. S. Kondov, W. R. McGehee, J. J. Zirbel and B. DeMarco. *Three-Dimensional Anderson Localization of Ultracold Matter*. Science **334** (2011), p. 66

- [123] H. J. Korsch, H.-J. Jodl and T. Hartmann. *Chaos - A Program Collection for the PC* (Springer, 2008), third edition
- [124] V. Lakshmikantham and D. Trigiante. *Theory of Difference Equations* (Academic Press, Inc., 1988)
- [125] R. H. Landau, M. J. Páez and C. C. Bordeianu. *A Survey of Computational Physics* (Princeton University Press, 2008)
- [126] P. Lee and D. Fisher. *Anderson localization in two dimensions*. Physical Review Letters **47** (1981), p. 882
- [127] P. Lee and D. Fisher. *Relation between conductivity and transmission matrix*. Physical Review B **23** (1981), p. 6851
- [128] A. Leggett. *Quantum Liquids* (Oxford University Press, 2006)
- [129] A. J. Leggett. *Bose-Einstein condensation in the alkali gases: Some fundamental concepts*. Reviews of Modern Physics **73** (2001), p. 307
- [130] R. B. Lehoucq, D. C. Sorensen and C. Yang. *ARPACK Users' Guide: Solution of Large Scale Eigenvalue Problems with Implicitly Restarted Arnoldi Methods.*, 1997
- [131] A. Leutbecher. *Zahlentheorie-Eine Einführung in die Algebra* (Springer, 1996)
- [132] E. H. Lieb and R. Seiringer. *Proof of Bose-Einstein Condensation for Dilute Trapped Gases*. Physical Review Letters **88** (2002), p. 170409
- [133] E. H. Lieb, R. Seiringer, J. P. Solovej and J. Yngvason. *The Mathematics of the Bose Gas and its Condensation* (Birkhäuser Verlag, 2000)
- [134] E. H. Lieb, R. Seiringer and J. Yngvason. *Bosons in a trap: A rigorous derivation of the Gross-Pitaevskii energy functional*. Physical Review A **61** (2000), p. 043602
- [135] Y.-J. Lin, R. L. Compton, K. Jiménez-Grací, W. D. Phillips, J. V. Porto and I. B. Spielman. *Bose-Einstein Condensate in a Uniform Light-Induced Vector Potential*. Nature Physics **7** (2011), p. 531
- [136] Y.-J. Lin, R. L. Compton, A. R. Perry, W. D. Phillips, J. V. Porto and I. B. Spielman. *Bose-Einstein Condensate in a Uniform Light-Induced Vector Potential*. Phys. Rev. Lett. **102** (2009), p. 130401
- [137] F. London. *On the Bose-Einstein Condensation*. Phys. Rev. **54** (1938), p. 947
- [138] A. MacKinnon. *The conductivity of the one-dimensional disordered Anderson model: a new numerical method*. Journal of Physics C.: Solid State Physics **13** (1980), p. 1031
- [139] A. MacKinnon. *The Calculation of Transport Properties and Density of States of Disordered Solids*. Zeitschrift für Physik B **59** (1985), p. 385
- [140] K. Madsen, H. Bruun and O. Tingleff. *Methods for non-linear least squares problems*, 2004

- [141] J. E. Marsden, T. Ratiu and R. Abraham. *Manifolds, Tensor Analysis and Applications* (Springer, 2002), third edition
- [142] C. W. McCurdy, D. A. Horner and T. N. Rescigno. *Time-dependent approach to collisional ionization using exterior complex scaling*. Phys. Rev. A **65** (2002), p. 042714
- [143] C. W. McCurdy and C. K. Stroud. *Eliminating wavepacket reflection from grid boundaries using complex coordinate contours*. Computer Physics Communications **63** (1991), p. 323
- [144] C. W. McCurdy, C. K. Stroud and M. K. Wisinski. *Solving the time-dependent Schrödinger equation using complex-coordinate contours*. Phys. Rev. A **43** (1991), p. 5980
- [145] A. Meister. *Numerik linearer Gleichungssysteme* (Vieweg, 2008), third edition
- [146] P. A. Mello and N. Kumar. *Quantum Transport in Mesoscopic Systems* (Oxford University Press, 2004)
- [147] J. J. Metzger, R. Fleischmann and T. Geisel. *Universal Statistics of Branched Flows*. Phys. Rev. Lett. **105** (2010), p. 020601
- [148] V. Milner, J. L. Hanssen, W. C. Campbell and M. G. Raizen. *Optical Billiards for Atoms*. Phys. Rev. Lett. **86** (2001), p. 1514
- [149] A. D. Mirlin. *Statistics of Energy Levels and Eigenfunctions in Disordered Systems*. Physics Reports **326** (2000), p. 259
- [150] N. Moiseyev. *Quantum theory of resonances: calculating energies, widths and cross-sections by complex scaling*. Physics Reports **302** (1998), p. 211
- [151] J. J. Moré, D. C. Sorensen, K. E. Hillstom and B. S. Garbow. *The MINPACK Project*. In W. J. Cowell (editor), *Sources and Development of Mathematical Software*, p. 88–111 (Prentice-Hall, 1984)
- [152] A. P. Morgan. *A Homotopy for Solving Polynimial Systems*. Applied Mathematics and Computation **18** (1986), p. 87
- [153] S. Müller, S. Heusler, P. Braun and F. Haake. *Semiclassical approach to chaotic quantum transport*. New J. Phys. **9** (2007), p. 12
- [154] V. F. Müller. *Quantenmechanik* (Oldenburg Wissenschaftsverlag, 2000)
- [155] Müntinga, H. and Ahlers, H. and Krutzik, M. and Wenzlawski, A. and Arnold, S. and Becker, D. and Bongs, K. and Dittus, H. and Duncker, H. and Gaaloul, N. and Gherasim, C. and Giese, E. and Grzeschik, C. and Hänsch, T. W. and Hellmig, O. and Herr, W. and Herrmann, S. and Kajari, E. and Kleinert, S. and Lämmerzahl, C. and Lewoczko-Adamczyk, W. and Malcolm, J. and Meyer, N. and Nolte, R. and Peters, A. and Popp, M. and Reichel, J. and Roura, A. and Rudolph, J. and Schiemangk, M. and Schneider, M. and Seidel, S. T. and Sengstock, K. and Tamma, V. and Valenzuela, T. and Vogel, A. and Walser, R. and Wendrich, T. and Windpassinger, P. and Zeller, W. and van Zoest, T. and Ertmer, W. and Schleich, W. P. and Rasel, E. M. *Interferometry with Bose-Einstein Condensates in Microgravity*. Phys. Rev. Lett. **110** (2013), p. 093602
- [156] J. W. Negele and H. Orland. *Quantum Many-Particle Systems* (Westview Press, 1998)

- [157] J. Nocedal and S. J. Wright. *Numerical Optimization* (Springer, Berlin, 2006), second edition
- [158] F. W. J. Olver, D. W. Lozier, R. F. Boisvert and C. W. Clark (editors). *NIST Handbook of Mathematical Functions* (NIST and Cambridge University Press, New York, 2010)
- [159] T. Paul. *Transport von Bose-Einstein Kondensaten in mesoskopischen Strukturen*. Ph.D. thesis, Universität Regensburg, 2006
- [160] T. Paul, M. Hartung, K. Richter and P. Schlagheck. *Nonlinear transport of Bose-Einstein condensates through mesoscopic waveguides*. *Physical Review A* **76** (2007), p. 063605
- [161] T. Paul, K. Richter and P. Schlagheck. *Nonlinear Resonant Transport of Bose-Einstein Condensates*. *Physical Review Letters* **94** (2005), p. 020404
- [162] W. Pauli. *The Connection Between Spin and Statistics*. *Phys. Rev.* **58** (1940), p. 716
- [163] R. Peierls. *Zur Theorie des Diamagnetismus von Leitungselektronen*. *Z. f. Phys. A* **80** (1933), p. 763
- [164] H.-O. Peitgen, H. Jürgens and D. Saupe. *Chaos and Fractals* (Springer, 2004), second edition
- [165] E. Persson, K. Pichugin, I. Rotter and P. Šeba. *Interfering resonances in a quantum billiard*. *Phys. Rev. E* **58** (1998), p. 8001
- [166] M. Peskin and D. Schroeder. *An Introduction to Quantum Field Theory* (Addison-Wesley, 1995)
- [167] C. Pethick and H. Smith. *Bose-Einstein Condensation in Dilute Gases* (Cambridge University Press, 2008), second edition
- [168] P. Pickl. *Derivation of the Time Dependent Gross-Pitaevskii Equation Without Positivity Condition on the Interaction*. *Journal of Statistical Physics* **140** (2010), p. 76
- [169] L. Pitaevskii and S. Stringari. *Bose-Einstein Condensation* (Oxford University Press, 2003)
- [170] M. J. D. Powell. *A Hybrid Method for Non-Linear Equations*. In P. Rabinowitz (editor), *Numerical Methods for Non-Linear Algebraic Equations*, p. 87 ff (Gordon and Breach, 1970)
- [171] C. Presilla, G. Jona-Lasinio and F. Capasso. *Nonlinear feedback oscillations in resonant tunneling through double barriers*. *Phys. Rev. B* **43** (1991), p. 5200
- [172] W. H. Press, S. A. Teukolsky, W. T. Vetterling and B. P. Flannery. *Numerical Recipes in C: The Art of Scientific Computing* (Cambridge University Press, 1992), second edition
- [173] M. Reed and B. Simon. *Methods of modern Mathematical Physics IV: Analysis of Operators* (Academic Press, Inc., 1978)
- [174] R. Reinisch, E. Popov and M. Nevière. *Second-harmonic-generation-induced optical bistability in prism or grating couplers*. *Optics Letters* **20** (1995), p. 854

- [175] R. Reinisch and G. Vitrant. *Coupled-mode theory of diffraction-induced transverse effects in nonlinear optical resonators*. Physical Review B **44** (1991), p. 7870
- [176] K. Richter. *Semiclassical Theory of Mesoscopic Quantum Systems* (Springer, Heidelberg, 2000)
- [177] K. Richter and M. Sieber. *Semiclassical Theory of Chaotic Quantum Transport*. Physical Review Letters **89** (2002), p. 206801
- [178] G. Roati, C. D'Errico, L. Fallani, M. Fattori, C. Fort, M. Zaccanti, G. Modugno, M. Modugno and M. Inguscio. *Anderson localization of a non-interacting Bose-Einstein condensate*. Nature **453** (2008), p. 895
- [179] Y. Saad. *Iterative Methods for Sparse Linear Systems* (Society for Industrial and Applied Mathematics, 2000)
- [180] D. Sánchez and M. Büttiker. *Magnetic-Field Asymmetry of Nonlinear Mesoscopic Transport*. Physical Review Letters **93** (2004), p. 106802
- [181] D. Sánchez and M. Büttiker. *Interaction-Induced Magnetic Field Asymmetry of Nonlinear Mesoscopic Electrical Transport*. International Journal of Quantum Chemistry **105** (2005), p. 906
- [182] L. Sanchez-Palencia and M. Lewenstein. *Disordered quantum gases under control*. Nature Physics **6** (2010), p. 87
- [183] P. Schlagheck and T. Paul. *Complex-scaling approach to the decay of Bose-Einstein condensates*. Physical Review A **73** (2006), p. 023619
- [184] P. Schlagheck and S. Wimberger. *Nonexponential decay of Bose-Einstein condensates: a numerical study based on the complex scaling method*. Applied Physics B **86** (2007), p. 385
- [185] O. Schubert, M. Hohenleutner, F. Langer, B. Urbanek, C. Lange, U. Huttner, D. Golde, T. Meier, M. Kira, S. Koch and R. Huber. *Sub-cycle control of terahertz high-harmonic generation by dynamical Bloch oscillations*. Nature Photonics **8** (2014), p. 119
- [186] F. Schwabl. *Advanced Quantum Mechanics* (Springer, 2005), third edition
- [187] F. Schwabl. *Quantum Mechanics* (Springer, 2007), fourth edition
- [188] R. Schwartz, N. Naka, F. Kieseling and H. Stolz. *Dynamics of excitons in a potential trap at ultra-low temperatures: paraexcitons in Cu₂O*. New Journal of Physics **14** (2012), p. 023054
- [189] R. Seydel. *From Equilibrium to Chaos - Practical Bifurcation and Stability Analysis* (Elsevier, Amsterdam, 1988)
- [190] P. Sheng. *Introduction to Wave Scattering, Localization and Mesoscopic Phenomena* (2006), second edition

- [191] M. Sieber and K. Richter. *Correlations between periodic orbits and their Rôle in Spectral Statistics*. Phys. Scr. **T90** (2001), p. 128
- [192] A. Siegert. *On the Derivation of the Dispersion Formula for Nuclear Reactions*. Physical Review **56** (1939), p. 750
- [193] D. C. Sorensen. *Implicit application of polynomial filters in a k-step Arnoldi method*. SIAM Journal on Matrix Analysis and Applications **13** (1992), p. 357
- [194] D. C. Sorensen. *Implicitly restarted Arnoldi/Lanczos Methods for Large Scale Eigenvalue Calculations*. In D. Keyes, A. Sameh and V. Venkatakrishnan (editors), *Parallel Numerical Algorithms: Proceedings of an ICASE/LaRC Workshop* (Kluwer, 1994)
- [195] H.-J. Stöckmann. *QUANTUM CHAOS - An Introduction* (Cambridge University Press, Cambridge, 1999), first edition
- [196] M. Suzuki. *Decomposition formulas of exponential operators and Lie exponentials with some applications to quantum mechanics and statistical physics*. Journal of Mathematical Physics **26** (1985), p. 601
- [197] H. Tal-Ezer and R. Kosloff. *An accurate and efficient scheme for propagating the time dependent Schrödinger equation*. Journal of Chemical Physics **81** (1984), p. 3967
- [198] J. R. Taylor. *Scattering Theory* (John Wiley & Sons, Inc., 1972)
- [199] F. Tisseur and K. Meerbergen. *The Quadratic Eigenvalue Problem*. SIAM Rev. **43** (2001), p. 235
- [200] A. Tourin, A. Derode, P. Roux, B. A. van Tiggelen and M. Fink. *Time-Dependent Coherent Backscattering of Acoustic Waves*. Phys. Rev. Lett. **79** (1997), p. 3637
- [201] J. F. Traub. *Iterative Methods for the Solution of Equations* (Prentice-Hall, Inc., 1964)
- [202] J. D. Urbina and K. Richter. *Statistical Description of Eigenfunctions in Chaotic and Weakly Disordered Systems beyond Universality*. Phys. Rev. Lett. **97** (2006), p. 214101
- [203] R. Vallejos and C. H. Lewenkopf. *On the semiclassical theory for universal transmission fluctuations in chaotic systems: the importance of unitarity*. Journal of Physics A: Mathematical and General **34** (2001), p. 2713
- [204] van Zoest, T. and Gaaloul, N. and Singh, Y. and Ahlers, H. and Herr, W. and Seidel, S. T. and Ertmer, W. and Rasel, E. and Eckart, M. and Kajari, E. and Arnold, S. and Nandi, G. and Schleich, W. P. and Walser, R. and Vogel, A. and Sengstock, K. and Bongs, K. and Lewoczko-Adamczyk, W. and Schiemangk, M. and Schuldt, T. and Peters, A. and Könnemann, T. and Müntinga, H. and Lämmerzahl, C. and Dittus, H. and Steinmetz, T. Hänsch, T. W. and Reichel, J. *Bose-Einstein Condensation in Microgravity*. Science **328** (2010), p. 1540
- [205] G. Veble, T. Prosen and M. Robnik. *Expanded boundary integral method and chaotic time-reversal doublets in quantum billiards*. New Journal of Physics **9** (2007), p. 15
- [206] M. Weidemüller and C. Zimmermann. *Interactions in Ultracold Gases* (Wiley-VCH, 2003)

- [207] S. Wimberger, P. Schlagheck and R. Mannella. *Tunnelling rates for the nonlinear Wannier-Stark problem*. Journal of Physics B.: Atomic, Molecular and Optical Physics **39** (2006), p. 729
- [208] M. Wimmer. *Quantum transport in nanostructures: From computational concepts to spintronics in graphene and magnetic tunnel junctions*. Ph.D. thesis, Universität Regensburg, 2008
- [209] L. Wirtz, J.-Z. Tang and J. Burgdörfer. *Gauge-invariant theory for semiclassical magneto-transport through ballistic microstructures*. Physical Review B **59** (1999), p. 2956
- [210] V. I. Yukalov. *Nonequivalent operator representations for Bose-condensed systems*. Laser Physics **16** (2006), p. 511
- [211] V. I. Yukalov. *Bose-Einstein condensation and gauge symmetry breaking*. Laser Physics Letters **4** (2007), p. 632
- [212] V. Zakharov. *Stability of periodic waves of finite amplitude on the surface of a deep fluid*. Journal of Applied Mechanics and Technical Physics **9** (1968), p. 190
- [213] R. Zavin, I. Vorobeichik and N. Moiseyev. *Motions of wave-packets using the smooth-exterior-scaling complex potential*. Chemical Physics Letters **288** (1998), p. 413

Acknowledgements

At the end of this dissertation, I would like to thank all people which made this work possible.

Above all, I am greatly indebted to my doctoral advisor Klaus Richter for his infinite patience. His advice regarding this work has been very helpful. The constant support given by him benefited me greatly. Also his whole research group was highly enjoyable and stimulating.

I would like to express my gratitude to the head of the BEC subgroup Peter Schlagheck for introducing me into the topic of cold atoms. He shared his invaluable insight into semiclassics and the physics of BECs with me. Also, I would like to thank the rest of the BEC subgroup Michael Hartung and Tobias Paul and the semiclassical crowd Cyril Petitjean, Josef Michl and Juan-Diego Urbina. They provided insightful discussions into the scientific and physical aspects of this work.

I would like to thank Michael Hartung, Michael Wimmer, Christopher Eltschka and Viktor Krüchl for helping me with programming and technical issues.

I specially have to give proper respect to my coworkers Josef Michl, Thomas Wellens, Cyril Petitjean, Juan-Diego Urbina and Peter Schlagheck whose heroic efforts culminated in the semiclassical theory of the non-linear weak localization effect.

I would like to thank my officemates Michael Hartung, Michael Wimmer, Matthias Scheid, Tobias Dollinger and Jan Bundesmann for providing a pleasant working atmosphere.

Thanks are due to Josef Michl, Juan-Diego Urbina and Jan Bundesmann for proofreading parts of this thesis.

Finally I want to thank my parents Karin and Jürgen.

I also acknowledge financial support of the FOR760.